

Numerical and Experimental Studies of IFE  
Target Layering in a Cryogenic Fluidized Bed

**Kurt-Julian Boehm**

May 14<sup>th</sup>, 2009



UNIVERSITY OF CALIFORNIA, SAN DIEGO

Numerical and Experimental Studies of IFE Target Layering in a Cryogenic  
Fluidized Bed

A dissertation submitted in partial satisfaction of the requirements for the degree Doctor  
of Philosophy

in

Engineering Sciences (Mechanical Engineering)

by

Kurt Julian Boehm

Committee in charge:

A. René Raffray, Chair  
Farrokh Najmabadi  
Sutanu Sarkar  
Jan Talbot  
George Tynan

2009

Copyright

Kurt Julian Boehm, 2009

All rights reserved.

The Dissertation of Kurt Julian Boehm is approved, and it is acceptable in quality and form for publication on microfilm and electronically:

---

---

---

---

---

Chair

University of California, San Diego

2009

## TABLE OF CONTENTS

Signature Page .....	iii
Table of Contents.....	iv
List of Figures .....	viii
List of Tables.....	xiv
Nomenclature.....	xvi
Subscripts.....	xxi
Superscripts .....	xxi
Acknowledgements.....	xxii
Vita.....	xxiv
Abstract .....	xxv
1. Introduction .....	1
1.1. Technical Motivation.....	1
1.2. The Target Layering Process.....	3
1.3. Fluidized Bed Layering.....	5
1.4. The “Mass Production Layering Experiment (MPLX)”.....	7
1.5. Research Goals.....	9
1.6. Numerical Approach.....	10

2. Modeling a Fluidized Bed.....	13
2.1. Solid-Gas Flow Models.....	14
2.2. Outline of a new Model.....	17
2.3. The LUPSBE model (Large unbalanced particles in small bed).....	22
2.3.1. The Granular Part.....	22
2.3.2. The Fluid-Particle Interaction.....	32
2.3.3. Determining the Void Fraction.....	36
2.3.4. Overview over LUPSBE.....	39
2.4. Validation.....	40
2.4.1. Granular Model.....	40
2.4.2. Verification of the Unbalanced Bounce.....	53
2.4.3. System Parameters.....	56
2.4.4. Fluid Particle Interaction.....	68
2.4.5. Compare Spin and Circulation Rates with Experiments.....	76
2.4.6. Surface Damage Analysis in Fluidization Experiments.....	78
2.5. Relevant Model Output.....	80
2.5.1. Collision Damage Analysis.....	81
2.5.2. Time averaged Spin and Circulation Rates.....	83
3. Modeling the Layering Process.....	90
3.1. Importance of the Layering Process.....	90
3.2. Theoretical Analysis of Redistribution Rates.....	91

3.2.1. Literature Review.....	91
3.2.2. Physical Description of Layering Process.....	92
3.3. Establishing the need for a Two Dimensional Model.....	96
3.4. Development of a 2-D Model.....	98
3.4.1. 2-D Equations and Boundary Conditions for Fixed Grids.....	101
3.4.2. Computing the Location of the Interface.....	104
3.4.3. Adjustment of the Stencils to the Presence of the Interface.....	109
3.4.4. Implementation of the Outer Interface Boundary Condition .....	115
3.4.5. The Gas-Solid Boundary Condition at the Inner Surface.....	117
3.4.6. Moving the Interface and Computing Mechanical Properties .....	120
3.4.7. Initial Conditions.....	125
3.4.8. Concluding Remarks about the model.....	126
3.5. Model Validation .....	129
3.5.1. Convergence for Decreasing Time Step.....	129
3.5.2. Balance of Mass and Energy .....	130
3.5.3. Testing Model computation of Volume of Void, Mass Moment of Inertia and Center of Gravity .....	135
3.5.4. Model Verification by Comparison to Theoretical Results .....	137
3.5.5. Model Verification by Comparison to Experimental Results .....	139
3.5.5.1. Experimental Setup.....	140
3.5.5.2. Modeling Results from Mass Redistribution Experiment.....	148
3.6. Summary of the Layering model and Example Results.....	153

4. Combining the Two Models to Simulate MPLX Layering Experiments .....	158
4.1. Relation between average Orientation of the Particle and the Local Heat Transfer Coefficient .....	160
4.2. Modeling the MPLX.....	164
4.3. Example Results for iterating between the two models.....	167
4.4. Final Remarks about modeling DT Layering.....	177
5. Conclusion .....	180
6. Appendices.....	189
6.1. Appendix A – Quantification of the surface damage.....	189
6.2. Appendix B – Estimating Hertzian contact stress during collision.....	193
6.3. Appendix C – Time step restriction in a special choice of damping Coefficient.....	194
6.4. Appendix D – Error estimates for experimental results.....	197
6.5. Appendix E – Influence of a non-participating gas species in the gaseous void (theory and experiment) .....	201
6.6. Appendix F – MPLX Hardware.....	216
6.7. Appendix G – Influence of the tangential drag force induced by the gas in the fluidized bed.....	220
7. References .....	222
8. Bibliography.....	228

## LIST OF FIGURES

Figure 1.1:	Schematic of the baseline target structure as specified by the National Research Laboratories <sup>2</sup> .....	2
Figure 2.1:	Simplified depiction of the drag on a sphere computed in relation to the void fraction in a cell, if the cell and the sphere are of about the same size.....	20
Figure 2.2:	Simulation of contact between two spheres by a spring-damper for normal contact and by a spring damper slider for tangential contact.....	31
Figure 2.3:	Effect of particle unbalance on the resulting forces. It becomes clear that the position of the particle with respect to the contact point influences the resulting force.....	31
Figure 2.4:	The volume of influence around a sphere is defined by a slice of the fluidized bed, one particle diameter in thickness.....	37
Figure 2.5:	The flow chart of the LUPSBE model.....	39
Figure 2.6:	History of total kinetic energy of a system of 200 spheres.....	44
Figure 2.7:	History of the total energy of all particles in the system. Since the system is undamped, the total energy in the system remains constant.....	45
Figure 2.8:	History of the deviation of total energy from the initial energy..	45
Figure 2.9:	Decay in kinetic energy due to the damped collisions for different damping coefficients ( $c_{eff}$ ) and number of time steps during contact ( $N$ ).....	46
Figure 2.10:	Overall coefficient of restitution as a function of angle of impact for different damping coefficients.....	48
Figure 2.11:	Dimensionless tangential velocity after the impact as a function of the dimensionless tangential velocity before the impact for different contact angles.....	49
Figure 2.12:	Spin rate of the particle after the collision as a function of impact angle for different time steps.....	50

Figure 2.13:	Outgoing velocities as a function of impact angle for different time steps.....	50
Figure 2.14:	Effective coefficient of restitution as a function of angle of impact for different time steps.....	51
Figure 2.15:	Histories of kinetic energy due to damping and frictional collisions for different time step sizes.....	52
Figure 2.16:	Histories of rotational energy during a granular collapse for different time step sizes.....	52
Figure 2.17:	Schematic of the unbalanced foam ball and two frames from the high speed videos illustrating the unbalanced bounce validation experiments.....	54
Figure 2.18:	Angle measurements as a function of time (from which the spin before and after the contact can be computed).....	54
Figure 2.19:	Histories of incoming and outgoing particle position for a single particle collision.....	61
Figure 2.20:	Dimensionless tangential velocity after a rolling impact as a function of incoming tangential velocity for two values of the $\gamma$ coefficient.....	65
Figure 2.21:	Coefficient of restitution as a function of impact angle for two different values of the $\gamma$ coefficient.....	65
Figure 2.22:	Experimental setup with nitrogen as a fluidizing medium.....	70
Figure 2.23:	Pressure drop through the bed as a function of flow speed estimated from the experimental results and computed from Ergun's Equation (Eq.(36)), and from the time-step model.....	72
Figure 2.24:	Flow speed as a function of void fraction for homogeneous fluidized bed based on empirical, experimental and numerical predictions.....	73
Figure 2.25:	Flow speed as a function of void fraction for non-homogeneous fluidized bed operation based on experimental and numerical predictions.....	74

Figure 2.26:	Circulation frequencies and spin rate computed from the model and observed in the experiments as a function of bed expansion.....	77
Figure 2.27:	SEM pictures showing the target surface with a 5000x magnification before and after 16 hrs of fluidization at different temperatures.....	79
Figure 2.28:	Number of collisions at different impact velocities during a 10 second fluidization period for different bed expansions.....	82
Figure 2.29:	Orientation vector of the pellets for different degree of unbalance and bed expansions.....	88
Figure 2.30:	Ratio of standard deviation in time-averaged particle surface temperature to average particle temperature in the bed for different bed expansions (flow rates).....	88
Figure 3.1:	1-D schematic illustrating the temperature distribution during layering.....	92
Figure 3.2:	Schematic of the two dimensional layering problem.....	103
Figure 3.3:	Schematic illustrating how the surface normal through each grid point is found to determine whether a grid point lies in the solid or the gaseous domain.....	108
Figure 3.4:	Schematic illustrating a segment of the interface, the markers of which are represented by the blue squares.....	111
Figure 3.5:	Schematic illustrating the temperature distribution computed along the surface normal in order to relate the heat flux from the cooling gas outside the shell to the surface temperature of the shell.....	117
Figure 3.6:	Approximating the area in the solid phase with simple geometric forms to calculate the fraction of gas volume in a cell with solid and gaseous domains.....	122
Figure 3.7:	Schematic illustrating the computation of the mass moments of inertia for an un-layered sphere.....	125

Figure 3.8:	Two different initial conditions implemented in the model for preliminary testing.....	126
Figure 3.9:	Ratio of change in number of moles in the system as a function of time.....	132
Figure 3.10:	Layering process for two different initial conditions.....	133
Figure 3.11:	Histories of the computed system unbalance and of the difference in layer thickness (from the thickest and the thinnest part at 0° and 180° from the bottom in figure 3.10) for an assumed case with $q'''=200\text{mW/cm}^3$ .....	138
Figure 3.12:	Experimental setup used to perform a water surrogate layering experiment.....	141
Figure 3.13:	Tailoring of emitted light from the IR halogen light source to retain only wavelengths in which the absorption of water provides volumetric heating.....	142
Figure 3.14:	Phase diagram of H <sub>2</sub> O showing the operating point of the water redistribution experiment.....	145
Figure 3.15:	Photographs of cuvette from water layering experiment at time=0 to time=64 hours. Redistribution of the water in the cuvette can be observed as shown also in the schematics.....	147
Figure 3.16:	Numerical results of the mass redistribution of ice in a gas cooled cylindrical cuvette. ....	150
Figure 3.17:	Pictures from the water layering experiment at time=0 and time = 64 hours.....	151
Figure 3.18:	Temperature distribution from the simulation of water layering experiment.....	152
Figure 3.19:	Mass moment of inertia of the system during the layering process for two layering cases with the same void volume.....	155
Figure 3.20:	Temperature field of the fuel layer shown as a color coded 3-D plot. Areas of elevated temperatures can be seen in thicker parts of the layer, while colder areas can be identified close to the cooled surface.....	155

Figure 3.21:	Influence of non-uniform local heat transfer coefficient on layering thickness for a single stationary sphere in a cooling gas stream.....	157
Figure 4.1:	Local heat transfer coefficient as a function of angular position for different average orientation of the shells.....	162
Figure 4.2:	Local heat flux coefficient on the outer surface of a stationary shell for two different Reynolds numbers.....	163
Figure 4.3:	Time & particle-averaged magnitude of the dot product of the vector between the center of gravity and the center of the spheres with the negative z-axis for different degrees of unbalance and fluidization parameters.....	165
Figure 4.4:	Standard deviation for average orientation of each individual particle for a 50-particle bed operating at two different bed expansions.....	169
Figure 4.5:	History of time & particle-averaged value of the orientation vector for two different bed expansions over time.....	170
Figure 4.6:	Standard deviation of the time-averaged gas temperature around each particle as a function of time.....	171
Figure 4.7:	Distance between the center of gravity and the center of the sphere as a function of time for the two cases chosen in this analysis and the limiting case of a stationary sphere in a packed bed. ....	175
Figure 4.8:	Number of collisions during a 10 s fluidization period at different impact velocities in both normal and tangential direction for two different bed expansions.....	176
Figure 4.9:	1/e layering time for 4 mm HAPL shells at 19.65 K as a function of the concentration of <sup>3</sup> He in the void space.....	178
Figure A-1:	The criterion for isolated point defect on the target surface for NIF (National Ignition Facility) <sup>16, 47</sup> .....	192
Figure C-1:	In the case of an unfavorably chosen combination of damping coefficient, stiffness and time step size, the system might become unstable although unexpected.....	195

Figure C-2:	The only difference between this case and the one depicted in C-1 is a smaller damping coefficient.....	196
Figure E-1:	Speed of interface movement towards equilibrium calculated from the two models as a function of tritium age.....	210
Figure E-2:	Ice layering progress over the course of 90 hours.....	214
Figure E-3:	Influence of an increase in partial pressure of the nitrogen on the ice layering time.....	215
Figure F-1:	MPLX experimental setup.....	216
Figure F-2:	Inside of the bottom chamber after removing the vacuum dome. ....	216
Figure F-3:	Fluidized bed consisting of a vertically mounted glass tube.....	217
Figure F-4:	High pressure filling system added to the fluidized bed loop...	218
Figure F-5:	Syringe pump used to slowly increase the pressure during the filling process, and to control the pressure in the permeation cell during the cool down.....	219
Figure F-6:	IR heating system consisting of three IR filaments.....	219

## LIST OF TABLES

Table 2.1:	System parameters used in the bounce experiments with the unbalanced foam ball.....	55
Table 2.2:	Comparison of measured and simulated post-impact velocities.	56
Table 2.3:	Coefficients of restitution determined from video of particle bounce experiment.....	60
Table 2.4:	Comparison between the computed and measured output parameters for several high speed videos.....	63
Table 2.5:	Parameters used in the code to simulate cases relevant to IFE layering in a fluidized bed.....	67
Table 2.6:	Time step sizes for different number of time steps during collision contact ( $N$ ).....	67
Table 2.7:	Comparison of parameters for He @ 18 K and N <sub>2</sub> at RT.....	69
Table 2.8:	The input parameters for the exemplified fluidization simulation presented in section 2.5.2 .....	89
Table 3.1:	Input parameters for conservation of mass and energy tests.....	131
Table 3.2:	Comparison of geometric parameters calculated analytically and from the model computations for 2 cases.....	136
Table 3.3:	Input parameters and properties for $DT$ , $D_2$ and water layering.....	143
Table 4.1:	Values used in the parametric layering simulation .....	172
Table 4.2:	Test results for layering at 1.6 and 2.0 bed expansions using both models iteratively.....	174
Table A-1:	Measurements of the fraction of the damaged surface on shells exposed to several different fluidization scenarios and surface over-coat based on visual inspection of at least five photographs.....	189

Table A-2:	Example cases for the increase in radiative heat flux on the target surface for different degree of surface damage.....	190
Table A-3:	Diameter of the largest point damage measured in each picture along with a count of smaller defects seen on the target surface.	191
Table D-1:	Different types of errors in the flow speed analysis.....	198
Table E-1:	Parameters used in the analysis of the increase in layering time due to the accumulation of $^3\text{He}$ in a HAPL size target.....	211
Table E-2:	Parameters used in computing the influence of air as a non-participating gas on the layering time in an ice layering experiment.....	214

## NOMENCLATURE

<b><u>Symbol</u></b>	<b><u>Description</u></b>
$a$	Slope of the function $y=ax+b$
$a_{diff}, b_{diff}$	Coefficients for the computation of the diffusion coefficient
$A$	Surface area over which the phase change occurs
$\mathbf{A}, \mathbf{A}^T$	Rotation matrix and its transpose
$A_s$	Surface area of the particle
$Ar$	Archimedes Number
$\mathbf{b}$ and $\mathbf{c}$	Third and fourth time derivative of position vector $\mathbf{s}$
$c$	Molar density in the void
$c_{A,h1}, c_{A,h2}, c_{B,h1}, c_{B,h2}$	Molar concentration of species A and B at locations h1 and h2
$c_1, c_2, c_3, c_4$	Gear coefficients for corrector step
$C_1, C_2, C_3, C_4$	Constants of integration
$C_{diff}$	Diffusion coefficient
$c_{eff}$	Effective damping coefficient in elastic contact
$C_{p,gas}$	Specific heat capacity of the gas
$C_{p,part}$	Specific heat capacity of the particle
$C_{p,s}$	Specific heat capacity of the solid
$CG_{void}$	Center of gravity of the void
$d$	equilibrium layer thickness
$d_{gap}$	Gap width in figure 2.3 and Eq. (44b)
$D$	Diameter of the pipes in Hagen- Poiseuille flow
$D_{AB}$	Diffusion coefficient of species A through species B
$D_e$	Effective diameter of the pipes in Hagen- Poiseuille flow
$d_p$	Diameter of the particle
$d_{bed}$	Diameter of the bed
$e$	Coefficient of restitution
$\mathbf{e}^b$	Body fixed coordinate system
$\dot{\mathbf{e}}^b$	Time derivative of the body fixed coordinates
$\mathbf{e}^s$	Space fixed coordinate system
$\dot{\mathbf{e}}^s$	Time derivative of the space fixed coordinates
$E_{Kin}, E_{Pot}, E_{Rot}, E_{Elastic}$	Kinetic, potential, rotational and elastic Energy
$E_{Tot}$	Total Energy in the system
$E_{init}$	Initial total energy of the system

$\Delta E$	Variation in total energy
$f$	Friction factor
$f_d$	Magnitude of drag force on a single particle
$\mathbf{F}$	Force vector
$\mathbf{F}_{buoyancy}$	Buoyancy force vector
$\mathbf{F}_n$	Normal Force vector
$\mathbf{F}_t$	Tangential Force vector
$\mathbf{F}_{tot}$	Total Force acting on the particle during collision
$\mathbf{F}_g$	Gravitational force
$\mathbf{g}, g$	Gravitational constant as vector and scalar
$h$	Heat transfer coefficient
$H$	Fluidized bed height
$h_1, h_2$	Time dependant layer thicknesses, see figure 3.1
$\Delta H_s$	Heat of sublimation
$I$	Value of the mass moment of inertia
$I_{xx}, I_{yy}, I_{zz}$	Values of the mass moment of inertia tensor around principle axes
$k, k_{ice}$	Thermal conductivity of the solid
$k_{gas}$	Thermal conductivity of the fluidizing gas
$k_{eff}$	Effective spring constant in elastic collision
$K_D$	Permeability
$k_{ice}$	Thermal conductivity of ice
$k_{vapor}$	Thermal conductivity of vapor
$L$	Distance of separation of the two surfaces
$m, m_p$	Mass of particle
$\dot{m}_{FB}^{gas}$	Mass flux of the gas through the bed
$\dot{m}_{void}^{gas}$	Mass flux into the void
$M_A, M_B$	Molecular mass of species A and species B
$n$	Coordinate normal to the surface
$n_{DT,fill}, n_{3He}$	Number of moles of DT at filling, and of $^3\text{He}$
$\mathbf{N}$	Surface normal vector
$N$	Coefficient to determine time step sizes during convergence demonstration
$\Delta n$	Increment along surface normal
$N_A, N_B$	Molecular flux of species A and species B
$Nu$	Nusselt Number

$\mathbf{o}$	Offset vector
$P$	Pressure
$P, P_T$	Total pressure in the vapor space
$P_{A,h1}, P_{A,h2}$	Partial pressure of species A at the interfaces h1 and h2
$P_{crit}$	Critical pressure
$P_{fill}$	Fill pressure
$P_g$	Pressure in the gas phase
$P_{3He}$	Partial pressure of $^3\text{He}$
$P_v, P_{v,DT}$	Temperature-dependent vapor pressure over solid (of DT)
$\Delta P$	Pressure drop
Pr	Prandtl Number
$q$	Surface heat flux
$\underline{Q}$	Total heat transferred between the particle and the gas
$\dot{q}''$	Volumetric heating rate
$q_0, q_1, q_2, q_3$	The four components of a quaternion
$\dot{q}_0, \dot{q}_1, \dot{q}_2, \dot{q}_3$	First time derivatives of the four components of a quaternion
$r$	Radial coordinate
$R$	(Outer) radius of the sphere
$R_{gas}$	Universal gas constant
$R_i$	Inner radius of spherical enclosure
$r_{i, cg}$	radial coordinate of the center of gravity of the gaseous portion at grid point $(r_i, z_j)$
$r_0$	Outer radius of spherical enclosure
$\Delta r$	Increment in radial direction
Re	Reynolds number (general)
$Re_p$	Particle Reynolds number
$Re_t$	Particle Reynolds number at terminal velocity
$s$	Coordinate along the interface
$\mathbf{s}, \dot{\mathbf{s}}, \ddot{\mathbf{s}}$	Position vector, velocity and acceleration
$S$	Distance between the centers of the inner and outer sphere
$SR, SZ$	Coordinate along the interface that intersects with a grid line in Z and R direction
$t$	Time
$t_{1/2}$	Tritium half life
$\Delta t$	Time step size
$T$	Temperature
$T_{crit}$	Critical temperature

$T_{fill}$	Fill temperature
$T_g, T_{gas}$	Temperature of the gas
$T_h, T_{h1}, T_{h2}$	Temperature of the inner interface
$T_0$	Outer surface temperature
$T_\infty$	Temperature of the cooling gas
$\Delta T_{gas}$	Raise of the temperature in the gas
$\Delta T_{part}$	Change of the target surface temperature
$T_{surface}$	Temperature of the pellet surface
$\mathbf{u}$	Unit vector
$U$	Fluid velocity (y-direction)
$U_t$	Terminal velocity of particle ( absolute value)
$\dot{\mathbf{s}}_t, \dot{\mathbf{s}}_n$	Tangent and normal components of target velocity
$V$	Volume
$V_n$	Velocity of the interface (normal to the interface)
$V_{Outer Sphere}$	Volume of a sphere of radius R
$V_{total void}$	Total volume of the void
$\Delta V$	Change in volume of the void
$\mathbf{v}_a$ and $\mathbf{v}_b$	Particle velocity before and after collision
$\mathbf{w}_{effective}$	Effective weight
$x, \hat{x}, x^*$	Space variable, see figure 1
$x_A, x_B$	Mole fraction of species A and B
$\Delta X$	Distance between center of gravity and center of the sphere
$z$	Axial coordinate
$Z_{cg}$	Axial coordinate of the overall center of gravity
$z_{j, cg}$	Axial coordinate of the center of gravity of the gaseous fraction at grid point $(r_i, z_j)$
$\Delta z$	Increment of axial coordinate
$\gamma$	Coefficient of viscous friction
$\alpha$	Parameter defined in Eq. (47)
$\delta$	Difference between equilibrium layer thickness and actual layer thickness
$\dot{\delta}$	Speed of the interface
$\delta_0, \delta_1$	Difference between equilibrium layer thickness and actual layer thickness at time =0 and time = t1
$\varepsilon$	Void fraction

$\epsilon_A, \epsilon_B, \epsilon_{AB} \frac{\epsilon_{AB}}{R_{gas}}$	Lennard Jones Parameters
$\kappa$	Parameter defined in Eq. (47)
$\mu$	Coefficient of friction
$\mu_f$	Fluid viscosity
$\nu$	Richardson Zaki Coefficient
$\rho_f$	Density of the fluidizing fluid
$\rho_s$	Density of the solid
$\rho_g$	Density of the gas phase
$\rho_p$	Density of the particle
$\sigma_{DT}, \sigma_{He}, \sigma_{AB}, \sigma_A, \sigma_B$	Lennard Jones Parameters
$\tau$	Total layering time constant
$\tau_3$	Layering time constant due to non-participating gas effects
$\tau_{perm}$	Permeation time constant for nitrogen through the PAMS shell
$\tau_{tritium}$	Time constant of tritium decay
$\tau^b$	Torque on the target in body coordinates
$\tau^s$	Torque on the target in space coordinates
$\dot{\omega}^b$	Time derivate of the particle's spin in body fixed coordinates
$\omega^s$	Particle's spin in space coordinates
$\psi_{in}, \psi_{out}$	Dimensionless tangential velocity (absolute value) before and after collision
$\Omega_{D_{AB}}$	Coefficient related to Lennard Jones potential
$\Theta_n$	Oscillation frequency

## SUBSCRIPTS

The following subscripts are used in this work (unless specified otherwise in the text):

cg	Quantity with respect to the center of gravity
cs	Quantity with respect to the center of the sphere
i,j	Chapter 2: Refers to the $i^{\text{th}}$ and $j^{\text{th}}$ particle
i,j	Chapter 3: Refers to the $i^{\text{th}}$ point in radial and $j^{\text{th}}$ point in axial direction
k	Refers to the $k^{\text{th}}$ marker point
n, n+1, n-1	Refers to the $n^{\text{th}}$ , $n+1^{\text{st}}$ , $n-1^{\text{th}}$ time step (in chapter 2)
N	Refers to a position along the interface between markers
r	Refers to the radial component of a vector
z	Refers to the axial component of a vector (in chapter 3)
x, y and z	x, y, and z component of a vector (in chapter 2)
SZ, SR	Refers to a position along the interface that intersects with the gridlines Z and R, respectively
N1, N2	Refers to a position along the surface normal
$D_2$ , DT, $H_2O$	Deuterium, deuterium-tritium mixture, water
“Celsius“	Use temperature value in degrees Celsius
“Kelvin“	Use temperature value in degrees Kelvin

## SUPERSCRIPTS

The following superscripts are used in this work (unless specified otherwise in the text):

b	Refers to the body fixed coordinate frame
c	Refers to the corrector step
in, out	Refers to quantities before and after a collision
n	Refers to the $n^{\text{th}}$ time step (in chapter 3)
p	Refers to the predictor step
s	Refers to the space fixed coordinate frame

## ACKNOWLEDGEMENTS

I would like to acknowledge Dr. A. Rene Raffray not only for his support as the chair of my committee, but also for guiding my research and focusing my efforts into a fruitful path with exceptional scientific knowledge and near fatherly patience. Through continuous support provided in countless meetings my interest in fusion technology was nourished proving his guidance to be invaluable on so many levels.

My sincere gratitude goes to my committee members, Professors F. Najmabadi, S. Sarkar, J. Talbot, and G. Tynan for their helpful suggestions and recommendations.

I would also like to acknowledge the financial support I have received from General Atomics through my Masters and my PhD studies. In addition, all the help I have received from the Inertial Fusion Energy Group at General Atomics, CA, especially the scientists, technicians and engineering staff in Building 22 contributed to this work in an immeasurable way.

I am deeply indebted to Kate, as she provided inspiration and encouragement through her sometimes inexplicable confidence in my abilities, keeping me motivated and ambitious. Besides that, she filled my life with happiness through a healthy balance of work and various kinds of recreational activities. Thanks to my parents for all the sacrifices they have shouldered to get me to this point, the lessons they taught me from early on, which helped shape my character, work ethics and moral standards. Last but not least, I would like to express my thanks to all coaches, colleagues and friends, who touched my life, completing the “non-academic education”.

Chapter 2, in part, has been accepted for publication in Fusion Science and Technology Special Issue (18th Topical on the Technology of Fusion Energy), K. Boehm and A.R Raffray, 2009. The dissertation author was the primary investigator and author of this material.

## VITA

- 2000-2001 Friedrich Alexander Universität, Erlangen- Nürnberg
- 2004 Bachelor of Science, University of Hawaii, Manōa
- 2004-2006 Research Assistant, Center for Energy Research, University of California, San Diego
- 2006 Master of Science, University of California, San Diego
- 2006 Teaching Assistant, Department of Mechanical Engineering, University of California, San Diego
- 2006-2009 Research Assistant, Center for Energy Research, University of California, San Diego
- 2009 Doctor of Philosophy, University of California, San Diego

## PUBLICATIONS

*“Time dependent Thermo-mechanical modeling including Phase Changes in Direct Drive Inertial Fusion Energy Targets”*, submitted in partial satisfaction of the requirements for the degree Master of Science, 2006.

K-J. Boehm, A.R. Raffray. *“Transient thermo-mechanical behavior of a direct-drive target during injection in an inertial fusion energy chamber”*. Fusion Engineering and Design, 82, 3, 2007.

*“Numerical Studies of a Fluidized Bed for IFE Target Layering”*. Presentation given at the HAPL project meeting, Santa Fe, NM. 2008.

*“Status of Cryogenic Fluidized Bed Experiment and Companion Modeling Results”*. Presentation given at the HAPL program meeting, Madison, WI. 2008.

K-J. Boehm, A.R. Raffray. *“Numerical and Experimental Analysis of a Fluidized bed for IFE Target Layering”*. Fusion Science and Technology Special Issue (18th Topical on the Technology of Fusion Energy), 2009 (accepted and in print).

## ABSTRACT OF THE DISSERTATION

### Numerical and Experimental Studies of IFE Target Layering in a Cryogenic Fluidized Bed

by

Kurt Julian Boehm

Doctor of Philosophy in Engineering Sciences (Mechanical Engineering)

University of California, San Diego, 2009

A. René Raffray, Chair

The redistribution of deuterium (DD) or a deuterium-tritium mixture (DT) to form a layer on the inside of spherical inertial fusion energy (IFE) capsules is a challenging problem because of the symmetry requirements of the fuel layer thickness, the smoothness requirement of the outside target surface, the number of targets required, and the time restriction on the production process.

Several physical processes have been identified to interact with each other to influence the outcome of the layering process in a fluidized bed. These include the gas-

flow-speed-dependent movement of unbalanced spheres through a fluidized bed and the resulting local heat transfer coefficient on the target surface from the cooling gas. The mass redistribution speed of the fuel inside the shell towards a uniform layer and the final layer thickness uniformity depend on the variation in time-averaged local heat transfer coefficient along the outer target surface. While a high gas flow rate through the bed would lead to more uniform time-averaged heat transfer coefficients, the high-Z layer covering the outer target surface has been observed to deteriorate through collisions at high impact velocities which occur during fluidization at high bed expansions.

The focus of this work was to develop numerical tools to help model and understand the physics involved in the fluidized bed layering and to assess the influence of key parameters on the layering outcome. Two separate models have been developed independently for particle behavior in a fluidized bed and for the coupled mass and heat transfer processes governing the layering process; these models include unique boundary conditions, beyond the capability of currently found commercial software. The models were validated through comparison with theoretical results and laboratory-scale experiments. They were then combined to model the entire layering process and used for parametric analyses. From these analyses, a window of operating parameters was identified at which a prototypic layering experiment is likely to be successful.

# **1. Introduction**

## **1.1 Technical Motivation**

Fusion energy has been identified as a clean, efficient and abundant source of energy for the future. The underlying physical concepts have been discussed at large and are well accepted within the scientific community. However on the technical side, much work is required towards the design and realization of a steadily, reliably, and safely operating economic power plant. For the engineers, this means the integration of technologies from many different disciplines.

This study is based on the inertial fusion energy (IFE) approach utilizing multiple laser beams to implode a direct drive (DD) spherical fuel pellet containing a deuterium tritium (DT) mixture. At a frequency of 5 – 10 Hz, a target will be injected into the reaction chamber and hit in flight by laser beams causing a continuous sequence of fusion events. The system parameters and specifications relevant for this research will be presented in this study, while the full technical details of the baseline design can be found in the High Average Power Laser meeting archives<sup>1</sup> or in the publications of Sethian et al. (2003)<sup>2</sup> and Meier et al. (2006)<sup>3</sup>.

One of the major technical challenges for IFE technology lies in the production of the fuel pellets. In order to provide enough power for an economic power plant, about 500 000 shells need to be produced per day. For a high gain fusion event to be successful, these targets must fulfill very strict symmetry and surface finish requirements. In the high average power laser (HAPL) study, the baseline design of the fuel pellets consists of a foam shell, containing a thick layer of frozen DT with a

gaseous DT core in the center<sup>1-3</sup>. The design includes a thin high Z coating (Au or Au-Pd) on the outer surface of the target to reduce the heat transfer onto the target during injection into the reactor chamber. A schematic of the target structure is shown in fig. 1.1. The production process of the fuel pellets must provide a high level of confidence that the targets meet the symmetry specifications for every target, since only a fraction of them can be inspected before injection. As part of the safety considerations for a full size power plant, the total tritium inventory must be kept to a minimum, which limits the available time for target filling and layering. In addition, the quality of the fuel deteriorates over time due to tritium decay, which also calls for a fast production method.

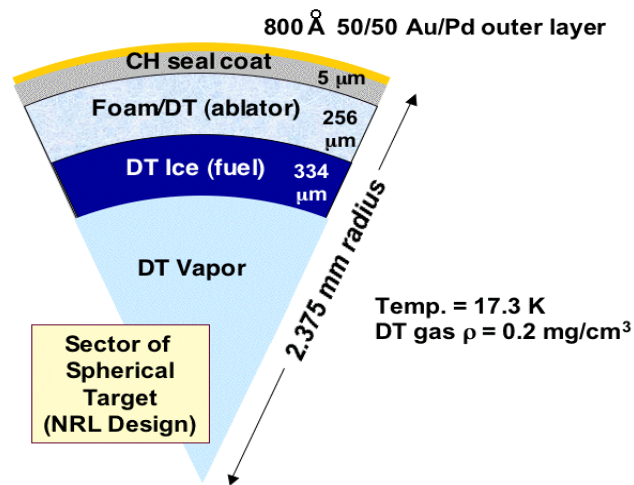


Figure 1.1: Schematic of the baseline target structure as specified by the National Research Laboratories<sup>2</sup>

## 1.2 The Target Layering Process

The underlying physics of mass redistribution towards a spherical layer inside a hollow sphere, a process called layering, has been described theoretically by A.J. Martin and R.J. Simms (1987)<sup>4</sup>. This analysis shows that if the surface of spherical targets, filled with frozen DT, is kept in a highly isothermal environment, the volumetric heating from the beta decay ( $\sim 0.05\text{W/cc}$  for solid DT at triple point) of the tritium can drive non-uniform DT ice layers towards uniformity. The bulk heating will induce sublimation of fuel into the gas phase at the inner surface of thicker parts and condensation of gaseous fuel on the inner surface of thinner layers. The speed of this process depends on the magnitude of the bulk heating. These authors were confident that the beta heating in DT shells is sufficient for the use of this process in mass production of reactor size targets in the required quantities. A derivation of the underlying equations and their expansion for the two dimensional case is shown in chapter 3. In general, we can conclude that, given a constant temperature environment and a uniform volumetric heating of the solid fuel, the symmetry requirements of the targets are theoretically considered feasible.

Harding (2006)<sup>5</sup> demonstrated experimentally that in principle the production of spherical deuterium ice layers for direct drive targets is possible. In these experiments, the targets were placed in the center of a copper layering sphere to provide spherical isotherms. In the absence of tritium, whose radioactivity makes it difficult to handle, an infra-red (IR) heating source was used to produce volumetric heating in the deuterium.

The wavelength of the IR light is matched with the absorption spectrum of deuterium to provide uniform volumetric heating. The target support in this experimental setup was made out of 4 micron diameter spider silk. Both the exact target positioning in the center of the copper sphere as well as the effects of the target support on the layer uniformity made this approach impractical for IFE target production; however, many of the results presented in this work (cooling rates vs. crystal growth rates and non uniformities resulting from temperature differences) can help in the design of a mass production process. In particular, a very precise temperature control ( $< 1.0$  mK) is essential for successful target layering. In addition, it has been shown that the smoothness of the inner surface can be improved by applying extremely slow cooling/freezing rates.

Several ways have been studied in the literature in order to increase the temperature gradients at the inner surface of the ice layer. Larger temperature gradients would lead to faster layering times. These concepts include the use of an additional volumetric heat source in the DT case (IR-lamp) or by electrically heating the gas inside the target. C.M. Chen, T. Norimatsu et al. (1993, 1995)<sup>6,7</sup> as well as E.R. Mapoles et al. (1996)<sup>8</sup> published results indicating that very fast layering times and very smooth layers could be the result of heating by a microwave discharge plasma.

Earlier research dedicated to efficient mass production of uniformly layered targets occurred in the LAPLAS experiments and the HAPL program. E.R. Koresheva (2006)<sup>9</sup> and Aleksandrova (2004)<sup>10</sup> presented the Free-Standing-Technology proposed as part of the LAPLAS experiments. The core element of this technology is a 3mm steel tube of about 1.5 m length, which is coiled around a cryo-cooled copper cylinder. The

shells are dropped into the tube, and as they roll down, they are rapidly cooled to approximately 15K. The rotation of the shells is expected to cause the growth of a symmetric layer. The non-uniformity and inner surface roughness results published lie far below the requirements for successful target implosion. The second approach, which will be the focus of this research, utilizes a fluidized bed for mass production of IFE targets (Alexander, 2003)<sup>11</sup>. Provided good bed fluidization is maintained, the “time-averaged” temperature environment of the spheres is expected to be very uniform. Different heating apparatus (microwave discharge and IR heating) can be tested in an experimental setup; however the fluidized bed parameters have to be adjusted to provide optimal “time-averaged” quantities, without jeopardizing other characteristics like surface finish or cracking the thin walled shells.

### **1.3 Fluidized Bed Layering**

For many reasons, a fluidized bed is a very promising idea for large scale target layering. Large beds can be filled with many targets, a reasonable temperature rise through a precisely controlled gas stream seems feasible, and the operation parameters of the bed are expected to be adjustable to render random target movement and spin throughout the bed, imposing a “time-averaged” uniform temperature field onto the targets. In a series of experiments, the proof of principle of this layering technique was given using a Neopentyl Alcohol as a surrogate for hydrogen (Alexander, 2003)<sup>11</sup>, however the fluidizing parameters were not optimized, and the requirements on layer uniformities were not satisfied.

Some restrictions narrow the parameter space of successful fluidized bed operation. The gas pressure in the bed has to be low enough not to crush the thin walled targets. It has also been observed that high impact collisions damage the surface of the outermost high – Z layer limiting the bed expansion at which the bed can be operated which ultimately limits the gas speed at the bottom inlet. With an upper bound for the operating pressure and the gas speed, the heat transfer between the gas and the shells is restricted. This leads to a significant temperature gradient throughout the bed, since the shells deposit heat into the upstreaming gas. Through “time-averaged” temperature variation in target position inside the fluidized bed, the necessary uniform temperature environment in the immediate vicinity of the target shell can be provided by choosing the appropriate operating point. Analysis of the particles’ motion through the bed and rotation around random axes while applying different fluidizing parameters is the key to determine the outcome of this process.

Preliminary calculations using empirical fluidized bed relations (Rowe, 1971)<sup>12</sup> show that the particles’ circulation frequency (movement of the particle from the bottom of the bed to the top and back down) can be expected to have a value of 1.6 Hz for spheres of similar size and weight to the HAPL size targets<sup>13-15</sup>, when fluidized in helium. An estimate for the resulting non-uniformity shows that under these circumstances, a target would lie within the HAPL specs after 16 hours of fluidization<sup>14</sup>. In the proposed process, shells are gas filled at room temperature and then cooled in a constant-volume-process (the amount of gas in the shell and the shell volume remain constant during the cooling process). After condensing and freezing, the mass of the fuel will be accumulated on the bottom of the shells. This leaves the spheres strongly

unbalanced which impacts the bed's behavior at the beginning of the fluidization and layering phase.

While the behavior of a fluidized bed with spherical target is well described in the literature, an attempt to compare and quantify the spheres' motion for unbalanced spheres during fluidization has not been done, not even empirically.

#### **1.4 The “Mass Production Layering Experiment (MPLX)”**

To extend the proof of principle of a layering technology based on a fluidized bed from surrogate layering (around room temperature) to cryogenic deuterium layering, a prototypic experiment is being set up by the Inertial Confinement Fusion (ICF) group at General Atomics. After demonstrating the functionality of this mass production process in a fluidized bed, which will operate at around 18K (the triple point of deuterium), the prototype can be scaled up from laboratory size to full size power plants.

In this setup, 100 – 200 targets (Poly Alpha Methyl Styrene (PAMS) 4mm in diameter, 35  $\mu\text{m}$  in wall thickness) are filled in a high pressure permeation cell. Due to symmetry constraints the targets cannot be punctured with a fill tube, and need to be filled by a permeation process. The pressurization is done at room temperature, since permeability of the shells drops significantly at cryogenic temperatures. In order to fill the shells to volume fractions of ~ 43 % solid fuel and 57% gaseous fuel, the shells need to be pressurized to ~1150 atm (17 ksi) at room temperature. This process and the hardware necessary are described in Appendix F. After the shells are filled with gas,

they are cooled while still under pressure past the critical point. Once the gas starts condensing, it will be gathering at the bottom of the shell as the shells are immobile in the high pressure cell. Once cooled down past the triple point (18.69 K)<sup>16</sup>, the excess gas surrounding the shells is evacuated. As a next step the shells containing are transferred into a glass tube (about 2.54 cm in diameter) where they are fluidized by a gaseous helium stream. At the beginning of the layering process, the fuel is frozen to the bottom of the shells. In order to simulate the volumetric heating from the beta decay, an IR light source will be used (Alexander, Bittner, Boehm et al., 2006)<sup>13-15</sup>, however the use of a microwave discharge plasma could be explored. When cooled by the fluidizing gas and simultaneously volumetrically heated, the layers are expected to grow uniform according to the layering theory.

Due to the cost involved in this experiment, and the difficulties associated with every single run as well as the time it takes to fill the shells, pump the system to vacuum, cool it down to 18 K and transfer the shells (which is a very delicate process as can be seen from Appendix F), it would be a great advantage if the range of parameters for an optimized outcome could be determined a priori. This would limit the number of experimental runs needed to successfully demonstrate target layering and would help to drastically reduce research cost.

## 1.5 Research Goals

The goals of this research endeavor are: 1) to help understand the multiple interacting physical processes governing the layering process in a fluidized bed under the unique cryogenic conditions; 2) to develop numerical models simulating these processes; 3) to apply the models in order to assess to what extent a uniformly layering target can be achieved in a fluidized bed, and 4) to perform parametric studies in order to provide pre-experimental recommendations on the setup of the proposed MPLX experiment (in particular regarding the parameter space which would increase the likelihood of successful target layering).

Numerical tools to simulate the combination of physical processes would allow us to find a set of optimized fluidization parameters, in which fast layering can happen while the outer surface quality is conserved. Input parameters include the flow speed, flow field, inlet temperature and pressure of the gas, and the heating rate applied to the shells. The relevant output parameters include the expected layering time, the maximum layer uniformity that can be expected and an estimate of the surface damage from possible violent collisions in the bed. Severe damage on the outer high-Z layer has been reported (Boehm, Carlson)<sup>16,17</sup> for fluidized bed operating at both room temperature and at cryogenic temperatures, as discussed in Section 2.4. The numerical models need to be tested and validated before being used for parametric studies.

## 1.6 Numerical Approach

Since the behavior of strongly unbalanced spheres in a fluidized bed has not been described and analyzed in the literature, a numerical tool was created to simulate this issue. In this model the position, velocity and orientation of all shells is followed over time. From this information, the time averaged heat transfer from the gas to the shells and the time averaged local temperature on the outside of each shells can be determined.

In a second model, the influence of the local heat transfer coefficient on the layer formation needs to be assessed. Since the shells are unbalanced, we can expect that, at least for small gas flow rates, the shells will develop a preferential position in the gas stream. Based on this preferential position, the local heat transfer on the outer shell will be non-uniform for each shell.

As a final result, the influence of the bed behavior on the final layer quality is assessed along with parameters like layering time and expected surface damage. Some example cases are being explored for an MPLX-like setup.

The benefit of a numerical model is that the global behavior of a fluidized bed with unbalanced spheres can be explored for different flow parameters. The movement of the individual targets can also be followed, and an estimate of the time-averaged temperature field and heat transfer coefficient can be given. Apart from gas flow parameters and geometric dimensions, the influence of the unbalance (the distance between the center of mass and the geometrical center) on target movement through the bed, and impact velocity during collisions can be studied parametrically.

Before applying this model to the MPLX case, various validation steps needed to be performed by comparing model results to theoretical, empirical and experimental results. The laboratory-scale experiments that were designed and operated as part of this work include a room-temperature fluidized bed set-up to help understand the bed behavior under conditions simulating as best possible prototypical operation, and to help benchmark the model.

A layering model was developed in order to relate the time averaged heat transfer coefficient and temperature field around a shell computed in the fluidized bed model to a prediction regarding the layer formation inside the capsule. Since under certain circumstances the heat transfer around the sphere could be non-uniform, a two dimensional model was developed based on the one dimensional considerations published by Martin et al<sup>4</sup>. While layer non-uniformities could result from a non-uniform heat flux around the shell, the redistribution of the layer inside the shell will affect its mechanical characteristics (mainly the center of gravity and the mass moments of inertia around two different axes) which can then be used in the fluidized bed model. Based on the new unbalance, information about a new (non-uniform) heat flux around the shell can be determined by the fluidized bed model.

This layering model also allows us to study the development of the shape of the inner layer surface; during the layering process, the growth of surface instabilities is observed, which has been reported in HAPL program meetings by Sheliak<sup>18</sup>, but has yet to be studied in detail.

A bench-top layering experiment with water as a surrogate was conducted in order to verify the mass transfer predictions of the code. This experiment, performed under controlled and simplified conditions, is used to benchmark the layering model.

## 2. Modeling a Fluidized Bed

Understanding and simulating the specific set of physical processes coming into play in a fluidized bed layering experiment calls for a unique sort of model, especially since the combination of processes and parameters lie outside the limiting cases that can be studied with conventional models or commercially available software. In this case, we are interested in the motion of fluidized unbalanced spheres (center of mass and geometrical center of a sphere do not coincide), which has not been studied specifically in the literature. In addition, the size of the spheres in relation to the bed diameter poses an extra challenge in modeling the system, as will be discussed in this section.

It is of particular interest when studying the layering process, to know the time average position and orientation of each sphere over a period of time, which is very long compared to the average time between collisions, but short compared to the layering time (~10 – 60 s). High-speed video analysis of a fluidized bed, as has been demonstrated by Warr<sup>19</sup> in a vibrating bed setup, could give an insight of the motion of the target as it moves along one side of the glass wall of the bed. However, once the shells move away from the glass wall, they can't be seen in videos, and assumptions have to be made about their movement through the center of the bed. As it has been observed that the strongest impulses for rotation are given by particle-to-wall collisions, it is possible that the shells strictly do not rotate once they move away from the wall.

During the layering experiment, the setup is not freely accessible and the analysis and characterization of the shells will be difficult. Thus, studying the behavior

of the pellets numerically for different bed setups and fluidization parameters will reduce the number of experimental attempts before successful layering is demonstrated. As a first step in defining the most promising parameter space, a numerical model describing a fluidized bed of matching geometry to the MPLX experiment with unbalanced spheres has been developed. The details of this model will be presented in the next section. Later the model results are compared to empirical and theoretical results, as well as room temperature fluidization experiments.

## **2.1 Solid - Gas Flow Models**

The numerical description of a multiphase flow model consists of two parts. First, a granular model describes the particle-to-particle and particle-to-wall interactions, and second, a fluid flow model describes the interaction between the fluid and the solid particles. The analysis should include the motion of the particles (translation and rotation) as well as fluidized bed characteristics like pressure drop, flow rate and bed expansion as well as the heat transfer between the gas and the solid phase along with the temperature distribution of the gas throughout the bed and the time average of the particles' surface temperature.

Analytical, experimental and numerical analyses of fluidized bed behavior have been attempted since the early 1950's ranging from empirical results from experimental observations to very extensive direct numerical simulations.

In the early literature, the behavior of fluidized beds as a whole was analyzed as opposed to studying the motion of each individual particle; for example, Ergun (1952)<sup>20</sup>

started by estimating the pressure drop close to minimum fluidization gas velocity of various systems. However, the dynamic behavior of discrete particles was neglected, and transient forces acting on the individual particles during fluidization could not be determined both of which most likely influence the multiphase flow behavior significantly.

As a next step in the development of fluidized bed modeling, the local averaging, or continuum approach was developed (Anderson and Jackson, 1967)<sup>21</sup> in which gas and solids are modeled as interpenetrating continua. Later computational cell averages of the void and particle fractions (as opposed to counting the number of particles in each fluid cell at each time step and computing the actual void and particle fraction in the cell) were used in the Navier Stokes equations (one set for each phase), which are solved by CFD methods (Gidaspow, 1994)<sup>22</sup>. An empirical interaction term is applied in the Navier Stokes equations to account for inter phase momentum transfer. The discrete flow patterns for individual particles can not be resolved in this method, since the cell average of the void and particle fraction was applied, but the model was useful to globally describe multiphase flow systems with very small particles (e.g. sand-water systems).

Cundall and Strack (1979)<sup>23</sup> proposed a method referred to as distinct element method (DEM), or discrete particle method (DPM)<sup>24</sup> as a model for the interaction between particles (granular model). The fluid-particle interaction was added later by Tsuji<sup>25</sup> as described below. In the DEM model, the motion of the particles is computed on the basis of Newton's second law. The forces resulting from gravity, particle-to-particle and particle-to-wall interactions are added, resulting in acceleration or

deceleration of the particle. In the soft sphere model, elastic collisions are represented with a spring – damper or spring – damper – slider system. This could lead to very small time steps in the simulation in order to keep the solution stable. For very dilute flows, the kinematics of hard sphere collisions was applied by Hoomans et al. (1996)<sup>26</sup>. The particles are assumed to experience instantaneous collisions and straight path travel between collisions. However, simultaneous multi-particle contacts cannot be resolved.

Tsuji et al. (1992)<sup>25</sup> added a 1-D fluid interaction force (drag force) to this granular model, turning it into a two-phase flow simulation. The two-phase flow region is discretized into volume segments; then the Ergun equation<sup>20</sup> is used to compute the pressure drop through each computational cell based on the gas to solid fraction in that cell. This pressure drop gives information about the drag force induced on the particles inside this cell.

In later developments, Xu and Yu (1997)<sup>24</sup> and well as Tsuji (1993)<sup>27</sup> and Gera (1998)<sup>28</sup> modeled a 2-D fluidized bed by combining the DEM model with the local averaging technique to solve for the fluid flow. In the DEM model, the granular part of the code used an empirical drag relation in order to combine the fluid and the granular code (DiFelice<sup>29</sup>, Richardson and Zaki<sup>30</sup>). These fluid – particle interactions relate the drag force on a sphere due to the relative velocity of sphere and fluid to the void fraction of the gas in the area around the sphere.

Based on this approach, Pannala et al.<sup>31</sup> developed a full 3-D gas-solid simulation code (MFIx). Reasonable results for the formation of clusters and bubbles have been described if the control volumes over which the fluid equations are solved contain more than about 15 particles.

To circumvent the problem of empirical relations, a brute force direct numerical simulation (DNS) has been developed by Pan et al. (2001)<sup>32</sup>. In this simulation the grid is chosen small enough such that a large number of points are within the physical domain of one particle. Then the Navier-Stokes equations are solved exactly for each step, while a distributed Lagrange multiplier is making sure that the volume covered by the sphere is restricted to rotational and translational motion. This DNS approach requires very extensive computer resources.

## **2.2 Outline of a New Model**

As mentioned above, a two phase fluidized bed flow model consists of two components. First, the behavior of the particles needs to be described. Second, an interaction coefficient between the particles and the fluid flow must be introduced to relate the momentum transfer between the fluid and the solid particles. Our interest in the motion of individual particles calls for a DEM approach. Following the literature research above and since the particles in dense flow systems (gas fractions below ~60%) often exhibit simultaneous contacts with other particles, a soft sphere model is considered.

In addition to studying the time- and particle-averaged spin and velocity, we also need to analyze the behavior of unbalanced spheres, since the condensation and freezing of the fuel inside the shell leads to a separation between the center of gravity

and the center of the spheres which evolves during the layering process. The effect of this unbalance on the particle movement will be studied.

In this unbalanced case, the force on the particle due to collisions and fluid particle interaction depends on the orientation of the ‘offset vector’ (vector between center of mass and geometrical center) in the 3 dimensional space of the fluidized bed. The effect of these forces (angular and translational acceleration) must be applied in the coordinate system of the sphere. This means that we must keep track of the Euler angles of each sphere during the simulation and switch back and forth between coordinate system of the individual sphere and the coordinate system of the fluidized bed. Following the molecular dynamics model described by Allen (1987)<sup>33</sup>, Quaternions can be used for the coordinate transformation. The details of this procedure are described in the following section.

The standard method for modeling the fluid-particle interaction uses volume-averaged parameters of many particles in a single fluid cell<sup>31</sup>. The fluid equations are then solved by a fluid solver. The size of the particles determines the minimum size of the fluid cells. When modeling the proposed MPLX fluidized bed, the ratio of pellet diameter (~4mm) over diameter of the (cylindrical) fluidized bed (34mm) is about 0.12. For reasonable results, at least 10 spheres are required to fit in one fluid cell at maximum packing fraction. In the case of the MPLX and its 100-400 spheres, the bed would need to be partitioned in 10-40 cells, which leaves 3-4 cells in each of the three dimensions. A numerical solver for such a coarse system would be possible, but wouldn't be reasonable. Standard codes like the freely accessible MFIX<sup>31</sup> or other

multiphase flow solvers (CFX, Fluent) cannot be applied for this particular system geometry.

A DNS approach as suggested and implemented by T.-W.Pan and D.D. Joseph<sup>32</sup> would result in an expensive computational effort. The most difficult part of a DNS approach is that the flow around each sphere has to be computed on a fine enough grid to describe the flow around each sphere, leading to millions of grid points for a relatively small geometrical domain.

Alternatively, the granular Navier-Stokes equations could be solved if the spheres were bigger than the grid. In this case the void fraction inside the cells that are covered by the sphere must be computed. The drag force needs to be determined by a weighted average of all cells affecting one sphere. A different fluid-solid interaction coefficient needs to be found. This interaction coefficient would be difficult to define, since the drag on a particle should not depend on its position on the grid.

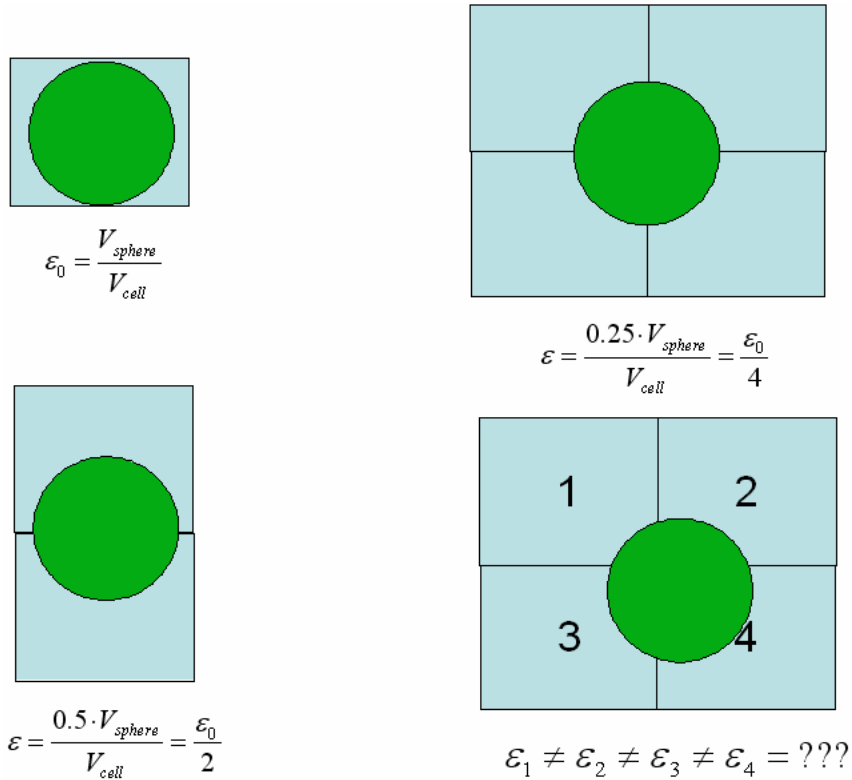


Figure 2.1: Simplified depiction of the drag on a sphere computed in relation to the void fraction in a cell, if the cell and the sphere are of about the same size. In all four cases, the overall drag on the particle should be the same (as it should be independent of the grid)

For example, if a sphere moves through space, the void fraction of the cells around the sphere changes; however, in the absence of other particles, the drag on the sphere should remain the same (see fig. 2.1). Since the drag is a nonlinear function of the void fraction, a simple addition of drag forces imposed by all cells covered by a sphere will rarely lead to the same result.

In absence of a good standard model for the MPLX simulation, a pseudo 1-D Lagrangian model is proposed, which computes the void fraction within a certain volume of interest around the particle. This volume of interest is applied to every single

particle, and it moves with the particles as the time is incremented forward. From the void fraction within this slice of interest, a drag force can be computed that also depends on the particle's relative speed to the gas. Different drag models can be applied at this point. The details of the model are described in the following chapter.

Once the position of each particle in the entire bed is known over a certain period of time, the time-averaged heat transfer to each sphere can be computed. The choice of the length of the time interval has to be long enough to result in a meaningful time-average, but short compared to the layering time scale. In general, the time interval is chosen to be two magnitudes higher than the average time between collisions, and two orders of magnitude lower than the  $1/e$  layering time (in our case  $\sim 10 - 20$  s). Combined with the heating inside the shell, the effectiveness of the layering mechanism in the fluidized bed can be studied. The layer redistribution based on a certain temperature field around the shell is discussed in section 3. The influence of certain fluidizing parameters on the resulting layer quality is presented in section 4.

The surface damage induced by the collisions can be numerically estimated by counting the number of collisions that happen with a certain velocity difference. This analysis will be shown at the end of this chapter.

## 2.3 The LUPSBE (Large Unbalanced Particle in Small Bed) Model

### 2.3.1 The Granular Part

In this part of the model, the motion of each sphere is computed on the basis of Newton's second law. The forces and torques resulting from particle-to-particle and particle-to-wall interactions are added up, resulting in linear and angular acceleration and deceleration of the particle. Similar to the discrete particle method presented by Cundall and Stack<sup>23</sup>, all contacts are converted into sets of forces and moments using spring, damper, and slider elements.

Different approaches to solve the resulting initial value problems for strongly nonlinear ODE's (like the ones found in a system describing a large number of elastic spheres) have been proposed over the years. These include the Euler method (single step extrapolation), multistep methods (Adams-Bashforth), fractional step methods (implicit and explicit Runge-Kutta) and multivalued methods (Gear predictor-corrector method)<sup>33</sup>. Despite the stability issues of the explicit Euler method Eq. (1), it has been successfully implemented for instance in the MFI code<sup>34</sup>.

$$\mathbf{s}_{n+1} = \mathbf{s}_n + \Delta t \cdot \dot{\mathbf{s}}_n \quad (1)$$

An implicit Gauss Legendre Runge Kutta scheme has been tested for a molecular dynamics application by Janezic<sup>35</sup>. One big shortfall of fractional step methods in this context is that determining the forces is computationally very expensive. The implicit scheme described in [35] requires several iterations of each time step until convergence, which renders this method inadequate for this purpose.

When applying an explicit Runge Kutta scheme only one iteration of each time step would be required, however we would still require several force calculations per time step.

The molecular code outlined by Allen<sup>33</sup> serves as the foundation for the granular code used in this model. The translational motion follows exactly the Gear5 predictor corrector method described in the literature<sup>36, 37</sup>, and adapted by many researchers dealing with highly nonlinear systems (Volfson and Tsimring (2003)<sup>38</sup>, Dorbolo et al (2005)<sup>39</sup>). In this case, the position, velocity, acceleration and two more time derivatives are used; the gear parameters are chosen such that the Taylor series is followed as closely as possible (to 5<sup>th</sup> order).

This method, referred to as Gear predictor –corrector method allows relatively large time steps and generally only one force computation per time step. The different steps of the algorithm are explained below. Eq. (2) is solved for the case of linear motion.

$$\mathbf{F}_i = m_i \cdot \ddot{\mathbf{s}}_i \quad (2)$$

The predictor step is basically an explicit time step, using the values of the position and the first four derivatives at the current time step to predict the position of the particle and the first four derivatives at the next time step, following the Taylor series expansion, as shown in Eqs. (3).

$$\mathbf{s}^p(t + \Delta t) = \mathbf{s}(t) + \Delta t \cdot \dot{\mathbf{s}}(t) + \frac{1}{2}(\Delta t)^2 \cdot \ddot{\mathbf{s}}(t) + \frac{1}{6}(\Delta t)^3 \cdot \mathbf{b}(t) + \frac{1}{24}(\Delta t)^4 \cdot \mathbf{c}(t) \quad (3a)$$

$$\dot{\mathbf{s}}^p(t + \Delta t) = \dot{\mathbf{s}}(t) + \Delta t \cdot \ddot{\mathbf{s}}(t) + \frac{1}{2}(\Delta t)^2 \cdot \mathbf{b}(t) + \frac{1}{6}(\Delta t)^3 \cdot \mathbf{c}(t) \quad (3b)$$

$$\ddot{\mathbf{s}}^p(t + \Delta t) = \ddot{\mathbf{s}}(t) + \Delta t \cdot \mathbf{b}(t) + \frac{1}{2}(\Delta t)^2 \cdot \mathbf{c}(t) \quad (3c)$$

$$\mathbf{b}^p(t + \Delta t) = \mathbf{b}(t) + \Delta t \cdot \mathbf{c}(t) \quad (3d)$$

$$\mathbf{c}^p(t + \Delta t) = \mathbf{c}(t) + \dots \quad (3e)$$

After these values have been predicted, the forces at the predicted position are computed. The difference between the predicted acceleration and the actual acceleration at the point are calculated from Eq. (4).

$$\Delta \ddot{\mathbf{s}}(t + \Delta t) = \ddot{\mathbf{s}}^c(t + \Delta t) - \ddot{\mathbf{s}}^p(t + \Delta t) \quad (4)$$

Using the difference between the values for the acceleration, a better prediction can be made using Eqs. (5).

$$\begin{aligned} \mathbf{s}^c(t + \Delta t) &= \mathbf{s}^p(t + \Delta t) + c_0 \cdot \Delta \ddot{\mathbf{s}}(t + \Delta t) \\ \dot{\mathbf{s}}^c(t + \Delta t) &= \dot{\mathbf{s}}^p(t + \Delta t) + c_1 \cdot \Delta \ddot{\mathbf{s}}(t + \Delta t) \\ \ddot{\mathbf{s}}^c(t + \Delta t) &= \ddot{\mathbf{s}}^p(t + \Delta t) + c_2 \cdot \Delta \ddot{\mathbf{s}}(t + \Delta t) \\ \mathbf{b}^c(t + \Delta t) &= \mathbf{b}^p(t + \Delta t) + c_3 \cdot \Delta \ddot{\mathbf{s}}(t + \Delta t) \\ \mathbf{c}^c(t + \Delta t) &= \mathbf{c}^p(t + \Delta t) + c_4 \cdot \Delta \ddot{\mathbf{s}}(t + \Delta t) \end{aligned} \quad (5)$$

The differential equation shown in Eq. (2) will be exactly solved if the difference between the predicted acceleration and the actual acceleration becomes zero. Several iterations of corrections might be applied; however, for most applications, one iteration gives sufficient accuracy for a molecular dynamics simulation<sup>33</sup>.

When it comes to the angular displacement, the spheres are handled as non-spherical bodies since they could be unbalanced in the case of interest. The individual orientation of all bodies needs to be described in relation of the space-fixed coordinate

system  $\mathbf{e}^s$  (in the coordinates of the fluidized bed). The inertia tensor of the  $i^{\text{th}}$  sphere stays constant in the body-fixed coordinate system  $\mathbf{e}^{b,i}$  of the individual sphere. These two coordinate systems ( $\mathbf{e}^s$  and  $\mathbf{e}^{b,i}$ ) are related by a rotation matrix  $\mathbf{A}$  Eq. (6), which can be computed from the three Euler angles.

In order to compute the spin rates of the particles, the change of orientation of the coordinate system of the individual particle  $\mathbf{e}^{b,i}$  with respect to the space fixed coordinate system  $\mathbf{e}^s$  needs to be tracked. The time derivatives of both coordinate systems behave according to Eq. (7).

$$\mathbf{e}^b = \mathbf{A} \cdot \mathbf{e}^s \quad (6)$$

$$\dot{\mathbf{e}}^s = \dot{\mathbf{e}}^b + \boldsymbol{\omega}^s \times \mathbf{e}^s \quad (7)$$

If a torque acts on the sphere, for example due to a collision with a wall, it will be computed in space fixed coordinates. Since this torque needs to be applied to the sphere in body fixed coordinates (see Eq. (9)), the rotation matrix needs to be applied to the torque

$$\boldsymbol{\tau}^b = \mathbf{A} \cdot \boldsymbol{\tau}^s \quad (8)$$

Once we know the components of the torque in body fixed coordinates, we can compute the resulting angular acceleration using Eq. (9) where  $I_{xx}$ ,  $I_{yy}$  and  $I_{zz}$  are the three principal moments of inertia.

$$\begin{aligned}
\dot{\omega}_x^b &= \frac{\tau_x^b}{I_{xx}} + \left( \frac{I_{yy} - I_{zz}}{I_{xx}} \right) \omega_y^b \omega_z^b \\
\dot{\omega}_y^b &= \frac{\tau_y^b}{I_{yy}} + \left( \frac{I_{zz} - I_{xx}}{I_{yy}} \right) \omega_z^b \omega_x^b \\
\dot{\omega}_z^b &= \frac{\tau_z^b}{I_{zz}} + \left( \frac{I_{xx} - I_{yy}}{I_{zz}} \right) \omega_x^b \omega_y^b
\end{aligned} \tag{9}$$

When computing the rotation matrix using the Euler angle description, a  $\sin \theta$  - term appears in the numerator (see Allen<sup>33</sup>). This leads to serious problems as  $\theta$  approaches 0 or  $\pi$ . One way around this problem is the use of the quaternion description.

A quaternion represents the angular rotation around a vector ( $q_1, q_2$  and  $q_3$ ) by a quantity of  $q_0$  as long as the square of the four components of the Quaternion add up to one, see Eq. (10). For example, a rotation of  $\theta$  radians about a unit axis  $\mathbf{u}$  is

represented by the unit quaternion  $\left[ \cos\left(\frac{\theta}{2}\right), \sin\left(\frac{\theta}{2}\right) \cdot \mathbf{u} \right]$  (Baraff, 1997)<sup>40</sup>.

$$\sqrt{q_0^2 + q_1^2 + q_2^2 + q_3^2} = 1 \tag{10}$$

In this case, the rotation matrix  $A$  can be found applying:

$$\mathbf{A} = \begin{pmatrix} q_0^2 + q_1^2 - q_2^2 - q_3^2 & 2(q_1q_2 + q_0q_3) & 2(q_1q_3 - q_0q_2) \\ 2(q_1q_2 - q_0q_3) & q_0^2 - q_1^2 + q_2^2 - q_3^2 & 2(q_2q_3 + q_0q_1) \\ 2(q_1q_3 + q_0q_2) & 2(q_2q_3 - q_0q_1) & q_0^2 - q_1^2 - q_2^2 + q_3^2 \end{pmatrix} \tag{11}$$

The quaternions of each sphere satisfy the following equation of motion:

$$\begin{pmatrix} \dot{q}_0 \\ \dot{q}_1 \\ \dot{q}_2 \\ \dot{q}_3 \end{pmatrix} = \frac{1}{2} \begin{pmatrix} q_0 & -q_1 & -q_2 & -q_3 \\ q_1 & q_0 & -q_3 & q_2 \\ q_2 & q_3 & q_0 & -q_1 \\ q_3 & -q_2 & q_1 & q_0 \end{pmatrix} \begin{pmatrix} 0 \\ \omega_x^b \\ \omega_y^b \\ \omega_z^b \end{pmatrix} \quad (12)$$

The system of Eq. (9) and Eq. (12), while using the rotation matrix in Eq. (11), gives a system of two first order differential equations, which can be solved using the Gear predictor corrector method. In this method, we determine the torque in space coordinates and convert it into body coordinates. Next, we update the angular acceleration in body coordinates and update the angular velocities. Once these are known, the first time derivative of the quaternions can be determined leading to updated values for the quaternions themselves. It is noteworthy that the Gear parameters used for the angular equations are different from the ones used for the translational equations, since they are represented as two first order ODE's Eq. (9) and Eq. (12) instead of one second order ODE Eq. (2).

To close this set of equations, the particle-to-particle and particle-to-wall contacts need to be represented by a set of forces and torques. In the original model by Cundall et al.<sup>23</sup>, these collisions are modeled with a spring – damper system for normal contact or a damper-slider system for tangential contact (fig 2.2). However, the calculation of forces needs to be modified to account for the particles' unbalances as the force on the particle depends on the orientation of the vector connecting the center of mass to the geometrical center (fig. 2.3). The following steps need to be taken to determine the forces resulting from a collision between particle i and j. The force calculation is done in the space-fixed coordinate system.

First, we need to compute the distance between the two centers of the two spheres. If this distance is smaller than the sum of the two radii, we have a collision. Then, Eq. ( 13) is applied to find the vector between the center of the sphere and the contact point ( $\bar{\mathbf{s}}_{csi}^s$ ).

$$\mathbf{s}_{csi}^s = R_i \cdot \frac{\mathbf{s}_i^s - \mathbf{s}_j^s}{|\mathbf{s}_i^s - \mathbf{s}_j^s|} \quad (13)$$

Next, we need to find two vectors between the two centers of mass and the contact point ( $\mathbf{s}_{cgi}^s$  and  $\mathbf{s}_{cgj}^s$ ) by

$$\mathbf{s}_{cgi}^s = \mathbf{s}_{csi}^s - \mathbf{A}_i^T \cdot \boldsymbol{\omega}_i^b \quad (14a)$$

$$\mathbf{s}_{cgj}^s = \mathbf{s}_{csj}^s - \mathbf{A}_j^T \cdot \boldsymbol{\omega}_j^b \quad (14b)$$

We need to convert the spin rates of the two particles, computed by the molecular dynamics algorithm in the body-fixed coordinate system, into the space-fixed coordinates.

$$\boldsymbol{\omega}_i^s = \mathbf{A}_i^T \cdot \boldsymbol{\omega}_i^b \quad (15a)$$

$$\boldsymbol{\omega}_j^s = \mathbf{A}_j^T \cdot \boldsymbol{\omega}_j^b \quad (15b)$$

Now the contact point velocities ( $\dot{\mathbf{s}}_{cpi}^s$  and  $\dot{\mathbf{s}}_{cpj}^s$ ) can be found by

$$\dot{\mathbf{s}}_{cpi}^s = \boldsymbol{\omega}_i^s \times \mathbf{s}_{cgi}^s + \dot{\mathbf{s}}_i^s \quad (16a)$$

$$\dot{\mathbf{s}}_{cpj}^s = \boldsymbol{\omega}_j^s \times \mathbf{s}_{cgj}^s + \dot{\mathbf{s}}_j^s \quad (16a).$$

We are interested in the difference between the two contact point velocities ( $\dot{\mathbf{s}}_{cp}^s$ ) and their respective tangential and normal components ( $\dot{\mathbf{s}}_{cp,n}^s$  and  $\dot{\mathbf{s}}_{cp,t}^s$ ) Eq. (17) and Eq. (18).

$$\dot{\mathbf{s}}_{cp}^s = \dot{\mathbf{s}}_{cp_i}^s - \dot{\mathbf{s}}_{cp_j}^s \quad (17)$$

$$\dot{\mathbf{s}}_{cp,n}^s = \dot{\mathbf{s}}_{cp}^s \cdot \frac{\mathbf{s}_i^s - \mathbf{s}_j^s}{|\mathbf{s}_i^s - \mathbf{s}_j^s|} \quad (18a)$$

$$\dot{\mathbf{s}}_{cp,t}^s = \dot{\mathbf{s}}_{cp}^s - \dot{\mathbf{s}}_{cp,n}^s \quad (18b)$$

The different components can now be utilized to determine the force on the particle due to this collision Eq. (19) and Eq. (22). The normal force ( $\mathbf{F}_n^s$ ) follows the spring damper model:

$$\mathbf{F}_n^s = \left[ \left( |\mathbf{s}_i^s - \mathbf{s}_j^s| - (R_i + R_j) \right) \cdot k_{eff} \right] \cdot \frac{(\mathbf{s}_j^s - \mathbf{s}_i^s)}{|\mathbf{s}_j^s - \mathbf{s}_i^s|} - c_{eff} \cdot \dot{\mathbf{s}}_{cp,n}^s \quad (19)$$

When computing the tangential force ( $\mathbf{F}_t^s$ ), one of the models presented by Schaefer et al.<sup>41</sup> has been applied. Since applying solely the Coulomb Law of friction Eq. (20) leads to a discontinuity during a rolling contact ( $\dot{\mathbf{s}}_{cp,t}=0$ ), it has been combined with a viscous friction term Eq. (21). The  $\gamma$  value, which doesn't have a real physical interpretation, has to be chosen large enough in order for the simulation to return a good model of the physics behind an oblique impact, but small enough to resolve the discontinuity. In the model, the smaller of the two forces is applied to compute the tangential force during the impact Eq. (22).

$$\mathbf{F}_t^s = \left| \boldsymbol{\mu} \cdot \mathbf{F}_n^s \right| \cdot \frac{\left( -\dot{\mathbf{s}}_{cp,t}^s \right)}{\left| \dot{\mathbf{s}}_{cp,t}^s \right|} \quad (20)$$

$$\mathbf{F}_t^s = -\gamma \cdot \dot{\mathbf{s}}_{cp,t}^s \quad (21)$$

$$\mathbf{F}_t^s = -\min\left(\left| \boldsymbol{\mu} \cdot \mathbf{F}_n^s \right|, \left| \gamma \cdot \dot{\mathbf{s}}_{cp,t}^s \right|\right) \cdot \frac{\left( \dot{\mathbf{s}}_{cp,t}^s \right)}{\left| \dot{\mathbf{s}}_{cp,t}^s \right|} \quad (22)$$

The total force ( $\mathbf{F}_{tot}^s$ ) during the impact is then computed as the sum of the normal and the tangential force:

$$\mathbf{F}_{tot}^s = \mathbf{F}_n^s + \mathbf{F}_t^s \quad (23)$$

As a last step, the torque will be computed (in space fixed coordinates):

$$\boldsymbol{\tau}_i^s = \mathbf{s}_{cg,i}^s \times \mathbf{F}_{tot}^s \quad (24)$$

The main difference of this model and the standard models is that in the computation of the contact point velocity we need to account for the orientation of the unbalance Eq. (14). In contrast to spherical and completely balanced spheres, the unbalanced spheres rotate around their center of mass, not the center of the sphere. As a result of this, we need to record the rotational motion in body fixed coordinates. The offset of the center of mass also causes additional set of forces and moments that need to be added to the torque and force vectors (see figs. 2.2 and 2.3 along with Eq. (13) through Eq. (16) and Eq. (25).

The different parameters modeling the contact, namely the spring constant and the coefficient of friction, will be found by analyzing videos of single bounces and isolated particle – particle interactions. This will be subject of section 2.4.

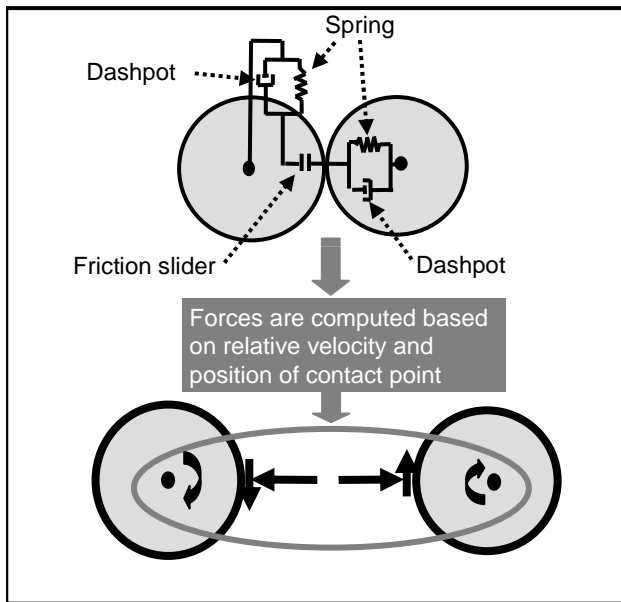


Figure 2.2: Simulation of contact between two spheres by a spring-damper for normal contact and by a spring damper slider for tangential contact.

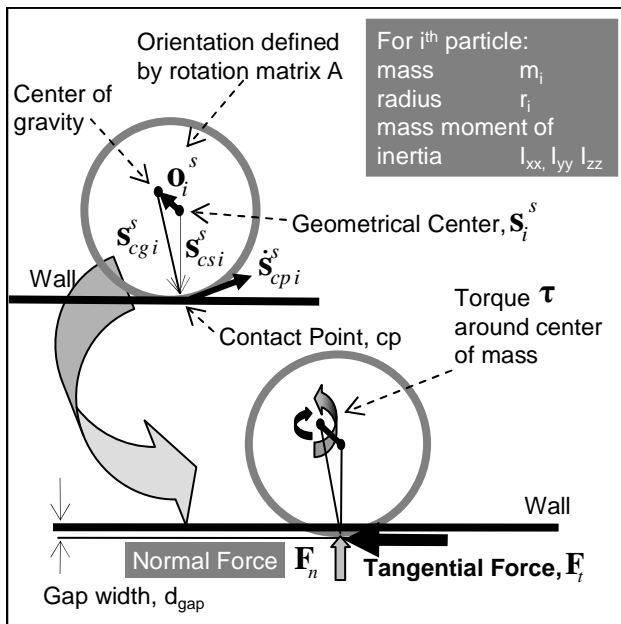


Figure 2.3: Effect of particle unbalance on the resulting forces. It becomes clear that the position of the particle with respect to the contact point influences the resulting force.

### 2.3.2 The Fluid- Particle Interaction

In this section, we will describe the forces acting on the particles due to the gas flow, namely the gravitational force and the drag force (interaction between the gas and the gas flow). These will be added to the force terms from the elastic contacts presented in the previous section.

The influence of the neighboring spheres on the gravitational force is first considered. The weight of the particle is reduced by buoyancy effects, from its dead weight to an effective weight, as shown in Eq. (26) and Eq. (27).

$$\begin{aligned}\mathbf{F}_g &= -m \cdot \mathbf{g} \\ m &= \rho_p \cdot V \\ V &= \frac{4\pi}{3} R^3\end{aligned}\tag{25}$$

$$\begin{aligned}\mathbf{F}_g &= -\frac{4\pi}{3} R^3 \cdot \rho_p \cdot \mathbf{g} \\ \mathbf{F}_{buoyancy} &= \frac{4\pi}{3} R^3 \cdot \rho (\varepsilon \rho_f + (1 - \varepsilon) \rho_p) \cdot \mathbf{g}\end{aligned}\tag{26}$$

$$\mathbf{w}_{effective} = \mathbf{F}_g + \mathbf{F}_{buoyancy} = -\frac{4\pi}{3} R^3 \cdot \mathbf{g} \cdot \varepsilon \cdot (\rho_p - \rho_f)\tag{27}$$

For the drag force on the particle, two different drag models were considered. The first one splits the drag force into a viscous and an inertial term. The derivation is demonstrated for the most part in Gibilaro (1997)<sup>42</sup>.

The viscous term is found starting out from the Darcy equation Eq. (28) and the Hagen-Poiseuille Equation (Eq. (29)), and estimating the pressure drop by viscous flow

through many small diameter pipes. An expression for the permeability or the effective diameter is then needed to model the pressure drop through a sphere packed bed.

$$\Delta P = K_D \mu_F H U \quad (28)$$

$$\Delta P = \frac{32}{D^2} \mu_F H U \quad (29)$$

If the flow through a sphere packed bed was not to be approximated by the flow through small diameter cylinders, Eq. (30) could be used to find the effective diameter, which can be applied in Eq. (29).

$$D_e = 4 \cdot \frac{\text{void volume}}{\text{internal surface area}} \quad (30)$$

A unit volume contains  $\frac{6(1-\varepsilon)}{\pi d_p^3}$  spheres.

This leads to an internal surface of  $\frac{6(1-\varepsilon)}{d_p}$ .

Knowing the void volume fraction  $\varepsilon$ , the effective diameter is  $D_e = \frac{2}{3} \frac{d_p \varepsilon}{(1-\varepsilon)}$ .

Using this result and the observation that the flow velocity  $U$  around the particle increases as  $1/\varepsilon$ , the Blake – Kozeny equation Eq. (31) can be derived (with a modified coefficient of 150).

$$\Delta P = 150 \frac{\mu_F H U}{d_p^2} \frac{(1-\varepsilon)^2}{\varepsilon^3} \quad (31)$$

The pressure drop for the inertial case can be computed following similar reasoning. The pressure drop for inertial pipe flow depends on a friction factor  $f$ , which stays constant at high Reynolds number flows.

$$\Delta P = 4f \frac{H \rho_f U^2}{D} \frac{1}{2} \quad (32)$$

Applying the effective diameter, the flow speed dependence on  $1/\varepsilon$ , and the value of  $3f=1.75$  for the friction factor, leads to:

$$\Delta P = 1.75 \frac{H \rho_f U^2 (1-\varepsilon)}{d_p \varepsilon^3} \quad (33)$$

Adding the two components of the pressure drop from Eq. (33) and Eq. (31) leads to the well-known Ergun Equation<sup>20</sup>.

$$\Delta P = 150 \frac{\mu_f H U (1-\varepsilon)^2}{d_p^2 \varepsilon^3} + 1.75 \frac{H \rho_f U^2 (1-\varepsilon)}{d_p \varepsilon^3} \quad (34)$$

For expanded beds, the path length  $H$  (bed height) also increases with  $1/\varepsilon$ , increasing the power of the  $\varepsilon$  in the numerator by one. Setting the friction factor  $f$  proportional to the particle concentration ( $f \sim (1-\varepsilon)$ ) the void fraction dependence in the viscous and the inertial term are similar. Using a numerical approximation for the void fraction dependence (the term that only depends on  $\varepsilon$ ), the pressure drop can be described in terms of the revised Ergun equation:

$$\Delta P = 18 \frac{\mu_f H U (1-\varepsilon)}{d_p^2 \varepsilon^{4.8}} + 0.33 \frac{H \rho_f U^2 (1-\varepsilon)}{d_p \varepsilon^{4.8}} \quad (35)$$

In terms of the Reynolds number, Eq. (35) can be written as Eq. (36).

$$\text{Re} = \frac{d_p \rho_f U}{\mu_f}$$

$$\Delta P = \left( \frac{18}{\text{Re}_p} + 0.33 \right) \frac{H \rho_f U^2 (1-\varepsilon)}{d_p \varepsilon^{4.8}} \quad (36)$$

The unrecoverable pressure drop basically describes the sum of the drag forces acting on each individual particle; by considering all spheres within a unit volume, one can use Eq. (36) to determine the drag on a sphere based on the flow velocity and the void fraction.

$$f_d = \frac{\pi d_p^3 \varepsilon}{6H(1-\varepsilon)} \cdot \Delta P \quad (37)$$

$$f_d = \pi d_p U \varepsilon^{-3.8} (3\mu_f + 0.055\rho_f d_p U) \quad (38)$$

The second alternative to determine drag on the spheres in a fluidized bed is founded on the Richardson Zaki relation, and the observation that the void fraction and the inlet velocity are related by Eq. (39).

$$U = U_t \varepsilon^v$$

$$\frac{4.8 - v}{v - 2.4} = 0.043 Ar^{0.57} \quad (39)$$

The velocity  $u_t$  is the terminal velocity. A free falling sphere would have this velocity in absence of other spheres. It can be computed using the Dallavalle drag relation also used by Gibilaro<sup>42</sup> Eq. (40) through Eq. (42). The Archimedes number, which appears in these equations, is a dimensionless number representing the ratio of gravitational force to viscous force in a two phase system.

$$Re_t = \left( -3.809 + (3.809^2 + 1.832 Ar^{0.5})^{0.5} \right)^2 \quad (40)$$

$$Ar = \frac{g d_p^3 \rho_f (\rho_p - \rho_f)}{\mu_f^2} \quad (41)$$

$$Re_t = \frac{d_p \rho_f}{\mu_f} U_t \quad (42)$$

Based on the assumption that the drag force and the particle's effective weight are equal and opposite in an equilibrium condition, Eqs. (40-42) and (27) give Eq. (43) as a drag force relation.

$$f_d = \frac{\pi d_p^3}{6} (\rho_p - \rho_f) g \left( \frac{U}{U_t} \right)^{\frac{4.8}{v}} \varepsilon^{-3.8} \quad (43)$$

As a result, we found two different models, with which we can determine the drag force on a sphere knowing the void fraction of the volume surrounding the sphere.

### 2.3.3 Determining the Void Fraction

The most common volume-averaging technique cannot be applied since the particles are too big in comparison with the bed diameter (see section 2.2). Thus, a different flow model is proposed based on the following assumptions: the most valuable information we are trying to get from the model is the particle velocity, position, orientation, and its angular spin rate. We were able to see in experiments that the spin rate is mainly induced by collisions, not by fluid interaction. This can be verified by computing the angular drag on a rotating sphere, which would not reduce the spin rate of the particle significantly in the time between two collisions. An exact analysis of the flow around the shell is thus less important than the primary effect it has on the sphere: namely to apply a drag force to levitate the sphere, counteracting gravity and cause agitation leading to collisions with the wall and other particles. The drag force should depend on the flow speed of the gas relative to the particle and have some dependence on the proximity of other particles.

In the proposed model, the void fraction in the vicinity of the particle is computed by adding up the partial volumes of the spheres that penetrate a certain volume of influence. This volume of influence has been defined as a slice with a radius equal to the whole fluidized bed, and limited by two planes one particle radius away from the center of the particle in both directions (up and down). This volume of influence is computed for every single sphere (as the y-position of each sphere is different) and moves with the particle, as the y-position of the particles change with time (see fig. 2.4).

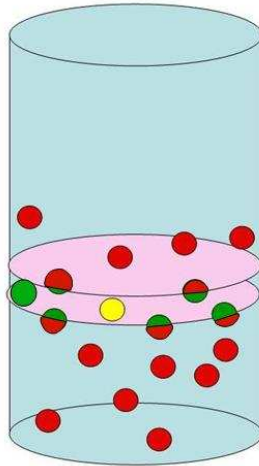


Figure 2.4: Volume of influence around a sphere defined by a slice of the fluidized bed, one particle diameter in thickness. The void fraction is computed by summing the partial volumes of the spheres inside this volume.

From the void fraction calculation within this volume of interest, the drag force and effective weight of the particle can be computed as described in the previous section. With this model in place, all the forces acting on the particles can be computed, completing the description of the model.

As part of the model, the position and orientation of each particle is written to an output file. Visualization of the results is arranged by creating pictures of the positions of the targets in the fluidized bed using raster 3-d<sup>43</sup>. In addition, these pictures have been compiled to movie files to show the dynamics of the fluidization using ffmpeg<sup>44</sup>. Some of the movies have been made available online under <http://iacs5.ucsd.edu/~kuboehm>.

### 2.3.4 Overview over LUPSBE

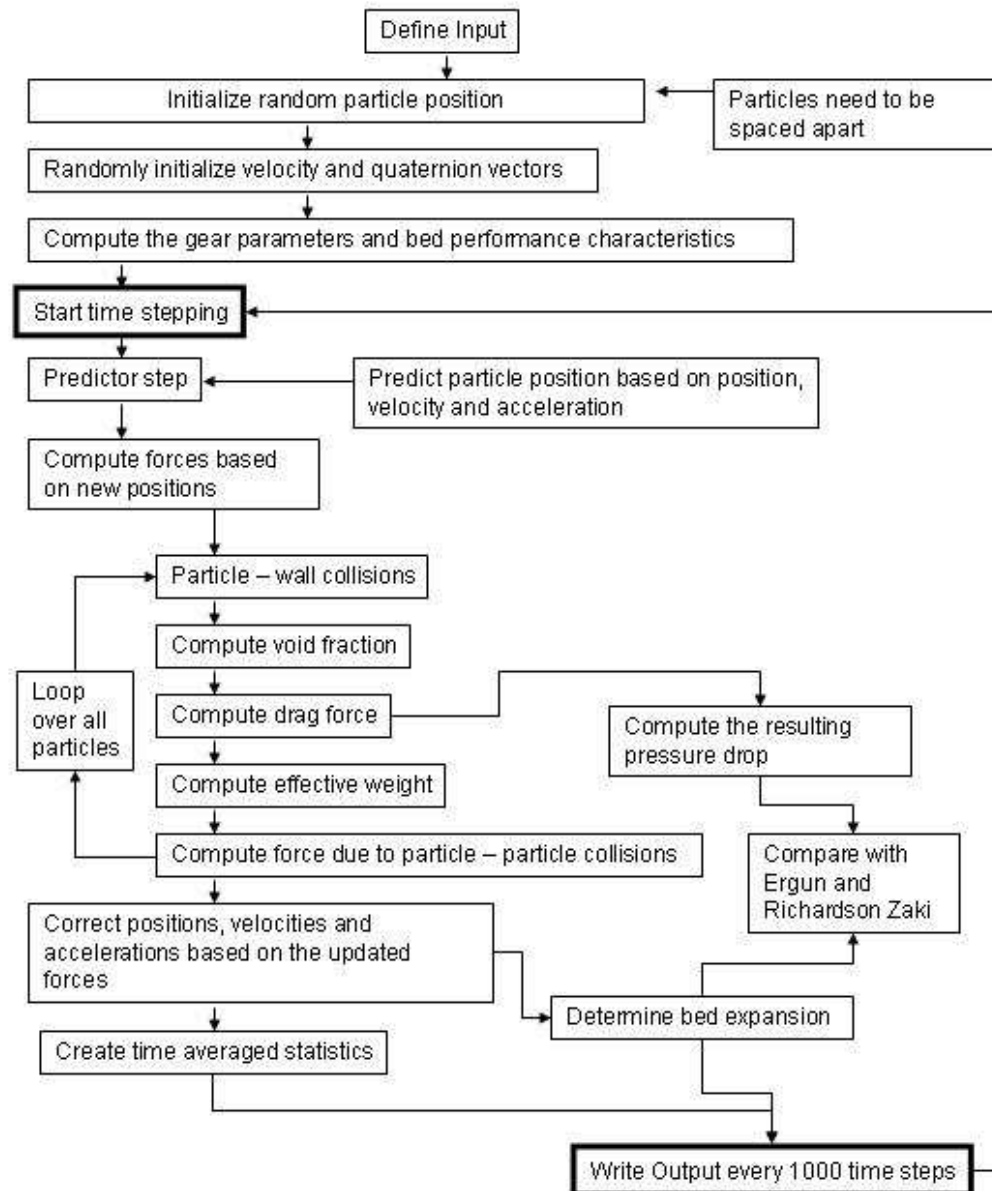


Figure 2.5: The flow chart of the LUPSBE model.

## 2.4 Validation

Before the results from the code can be used for prototypical simulation, the validity of the results needs to be established. The model needs to be verified by comparison to theoretical results, other models in the literature, as well as direct comparison with (room temperature) experiments.

### 2.4.1 Granular Model

The validation of the granular code has been done following different steps. To show that the method is stable and converges, cases with known behavior and with increasing complexity were modeled, starting with a simple undamped, frictionless bounce of one elastic sphere and ending in the simulation of a granular collapse of hundreds of unbalanced spheres.

A system is considered converging if the deviation of the simulated particle paths from the real, experimental or analytical particle paths becomes smaller with decreasing time step size. Since the particle behavior of hundreds of particles cannot be determined analytically and is hard to characterize experimentally, we introduce the total energy and the total kinetic energy of the system as stability criteria. The total energy of the system will be computed by summing the total energy of each individual particle in the system following Eqs. (44) and compared over the entire duration of a simulation.

$$E_{Tot} = E_{Kin} + E_{Rot} + E_{Pot} + E_{Elastic} \quad (44 \text{ a})$$

$$\begin{aligned}
E_{kin} &= \frac{1}{2} \cdot m \cdot \dot{\mathbf{s}} \cdot \dot{\mathbf{s}} \\
E_{rot} &= \frac{1}{2} \cdot I \cdot \boldsymbol{\omega} \cdot \boldsymbol{\omega} \\
E_{pot} &= m \cdot g \cdot s_y \\
E_{elastic} &= \frac{1}{2} \cdot k_{eff} \cdot d_{gap}^2
\end{aligned} \tag{44 b}$$

An estimate of the largest possible time step to be used can be computed by regarding a particle bounce as a purely oscillatory motion and looking at its natural frequency<sup>23</sup>. The oscillation period can be determined by Eq. (45).

$$\Theta_n = 2\pi \sqrt{\frac{m}{k_{eff}}} \tag{45}$$

The time step applied to the model follows Eq. (46); in order to show convergence and stability, N is increased from 4 to 50, where N defines the number of time steps during which the contact occurs.

$$\Delta t = \frac{\Theta_n}{2N} \tag{46}$$

The system parameters describing the elastic contact of the spheres, namely the stiffness of the sphere, ( $k_{eff}$ ), the damping coefficient ( $c_{eff}$ ), and the parameters describing the tangential contact ( $\gamma$  and  $\mu$ ), were determined through experiments which are subject of section 2.4.2. In order to test the code the measured values shown in Tabs. 2.5 and 2.6 (section 2.4.2) are chosen.

The first series of tests consists of modeling an undamped and frictionless case; the model can be considered stable if the deviation of the total energy of the system from the initial energy of the system remains small.

The first test performed on the model was a single, undamped, frictionless, and spherical particle bouncing on a flat surface. The particle has been placed at a certain height within the modeled bed and exposed to only the gravitational field. The code returned an acceleration of the particle towards the bottom of the bed, a bounce, and a continuous oscillating (bouncing) motion with close to constant amplitude. Since this model only performs one single predictor - corrector iteration, the analytical solution will not be followed exactly; however, with decreasing time step, the deviation from the analytical solution (exactly constant height at zero velocity at the highest point) becomes arbitrarily small. Since no friction is applied, the rotational energy of the particle remains constant zero during this test.

In a second test, the un-damped, frictionless particle was given an initial lateral motion. The particle's path was now occasionally obstructed by the bounding walls keeping the particle inside the fluidized bed container; without damping, the total energy of the system remained constant for small enough time steps ( $N > 5$ ).

In the next test, a damping factor has been introduced. In this case, since energy is being taken out of the system during every bounce, the amount of energy in the system will not be constant, but will decay at a rate proportional to the damping factor. This case was used later in section 2.4.2 to verify the experimentally measured damping coefficient by comparing the decay of particle kinetic energy from the model to the experimental observations.

The damping coefficient,  $c_{eff}$ , is related to the coefficient of restitution, Eq. (47), as discussed in the literature<sup>26</sup>. The coefficient of restitution will be determined by

the ratio of the velocity of the shell after and before the collision. For our PAMS shells, this was done experimentally as discussed in section 2.4.2. The relation between the coefficient of restitution and the damping factor is shown in Eqs. (47) and (48)<sup>27</sup>.

$$c_{eff} = 2\kappa\sqrt{m \cdot k_{eff}}$$

$$\kappa = \frac{\alpha}{\sqrt{1+\alpha}} \quad (47)$$

$$\alpha = -\left(\frac{1}{\pi} \ln e\right)$$

$$e = \frac{|\mathbf{v}_a|}{|\mathbf{v}_b|} \quad (48)$$

As a next step, a system of multiple particles has been considered. Initially, three particles were placed in the same x and z coordinates but with different y- coordinates (directly on top of each other). This leads to a one dimensional test of multiple collisions. Some of them occur simultaneously if the center particle collides with the bottom and the top particle at the same time. The energy balance for this test returned a constant value, the sum of the particles' initial potential energies, in the undamped case. In the damped case, the particles were at rest at the bottom of the bed after some time. This time scale is proportional to the rate, at which energy is taken out of the system, namely to the damping coefficient.

As a next step, the number of particles was increased to 200. All particles were initially uniformly spaced from each other and at rest and then were exposed to the gravitational field. The following analysis has been performed for the test cases: (A) the kinetic energy of the system has been computed as a function of time using different time step sizes in the solution as shown in fig. 2.6; (B) similarly, the total energy of the

system has been computed for different time step sizes as shown in fig. 2.7; and (C) the deviation of the system's energy from the initial energy has been calculated from Eq. (49) and plotted in fig.2.8.

$$\frac{\Delta E}{E_{init}} = \frac{\sqrt{\left(\sum_i E_{tot,i} - E_{init}\right)^2}}{E_{init}} \quad (49)$$

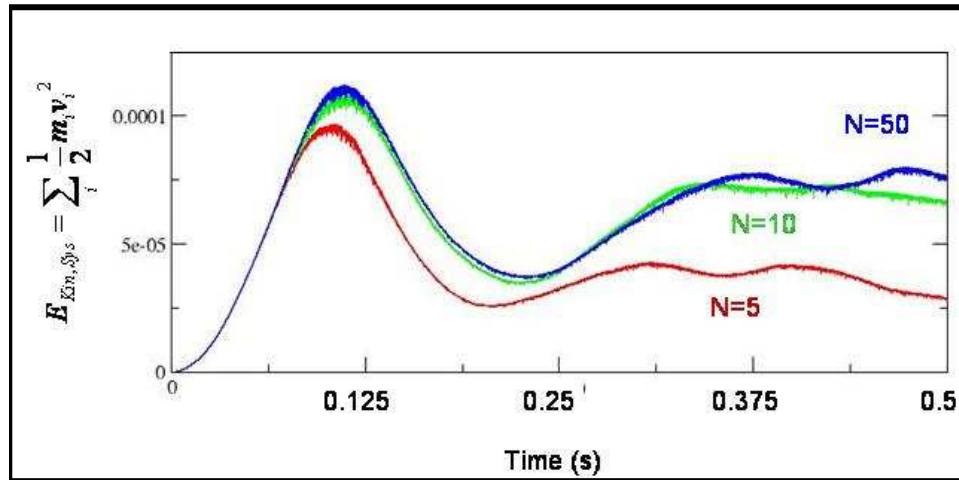


Figure 2.6: History of total kinetic energy of a system of 200 spheres. Due to the initial conditions (all particles at rest and all particles are equally spaced from their neighbors, we see an increase in kinetic energy from zero. Once the system is totally random, we should see only little fluctuation in total kinetic energy.

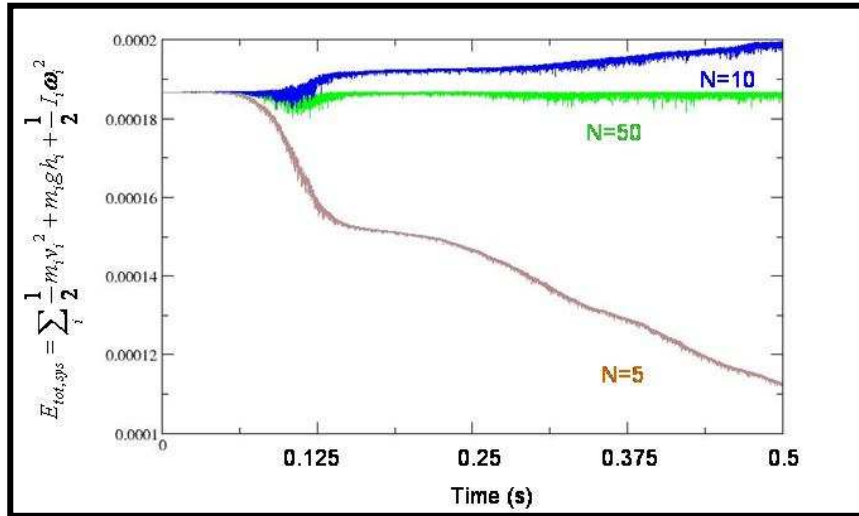


Figure 2.7: History of the total energy of all particles in an un-damped system. Since the system is undamped, the total energy in the system remains constant. As expected, the solution converges as the time step size decreases.

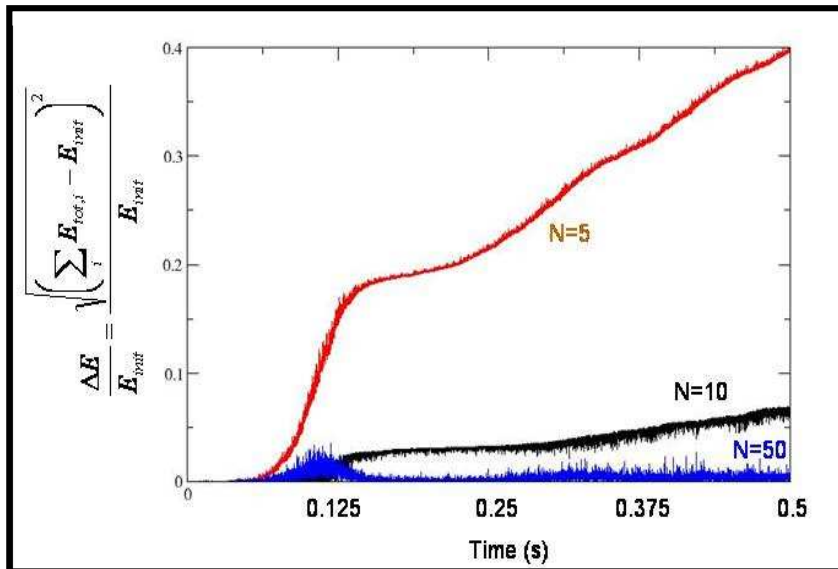


Figure 2.8: History of the deviation of total energy from the initial energy. This can be regarded as a measure of accuracy of the method. In addition it becomes clear, that the method satisfies stability and convergence.

We can see that the method converges and that it is stable if the time steps are chosen to be sufficiently small, such that  $N > 10$ .

As a next test, a damped case has been modeled. The initial conditions are the same as the previous test, but now energy is taken out of the system at each bounce by adding the dashpot damper in the collision model. Following the reasoning of Tsuji<sup>27</sup>, this test can also be used as a stability criterion. The kinetic energy has been plotted against time for different time step sizes (fig. 2.9). Since this case is still kept frictionless for tangential contacts, the rotational energy of the system remains zero.

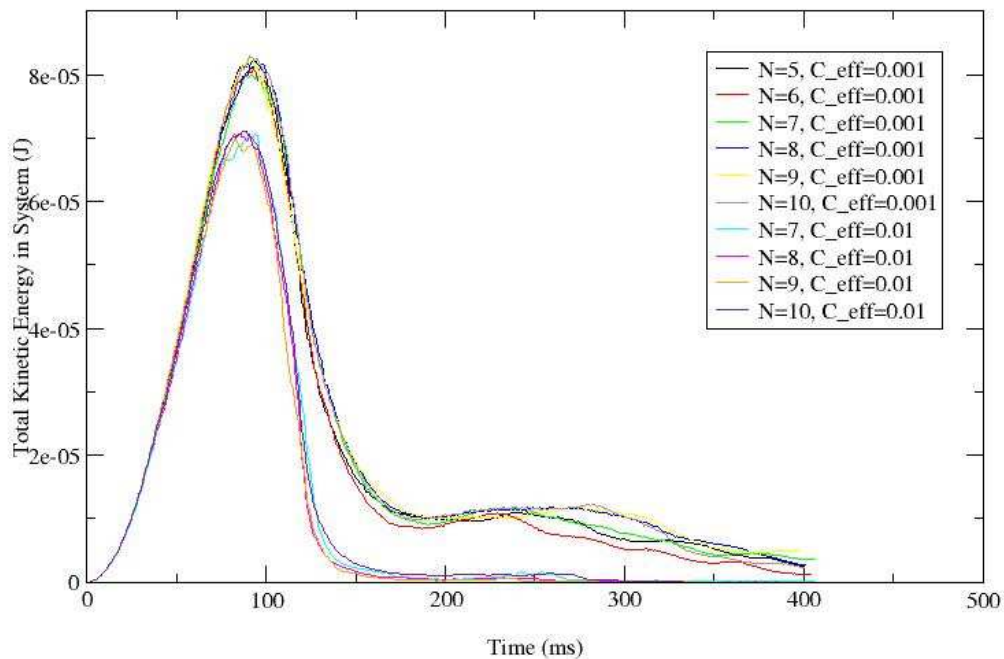


Figure 2.9: Decay in kinetic energy due to the damped collisions for different damping coefficients ( $c_{eff}$ ) and number of time steps during contact ( $N$ ). Stability is achieved at a lower  $N$  values than in the undamped case. In addition, the effect of different damping coefficients can be seen. Clearly, the energy is dissipated faster, if a higher damping coefficient is chosen.

The influence of different coefficients of restitution on the simulation of the granular collapse has been explored. Not surprisingly, by using a larger damping coefficient, the system reaches faster the state of complete rest. Tab. 2.7 in section 2.4.2 shows the time step sizes used in this simulation. We propose to use an N value of 10 in the simulations based on these results.

This series of tests, leading to a description of a granular collapse, shows that the model works satisfactorily as long as the time step restrictions are followed. By choosing an N value of 10, the behavior characteristic to spring-damper contacts described in Appendix C is avoided. This behavior was noticed for N values between 4 and 6, and it leads to a discontinuity in the energy balance.

As a next test, single particle bounces with a nonzero coefficient of friction have been analyzed. As described by Schaefer et. al<sup>41</sup> and demonstrated here, the frictional collisional contact makes the conservation of energy impossible, even if the damping coefficient for the normal contact is set to zero (see fig. 2.10).

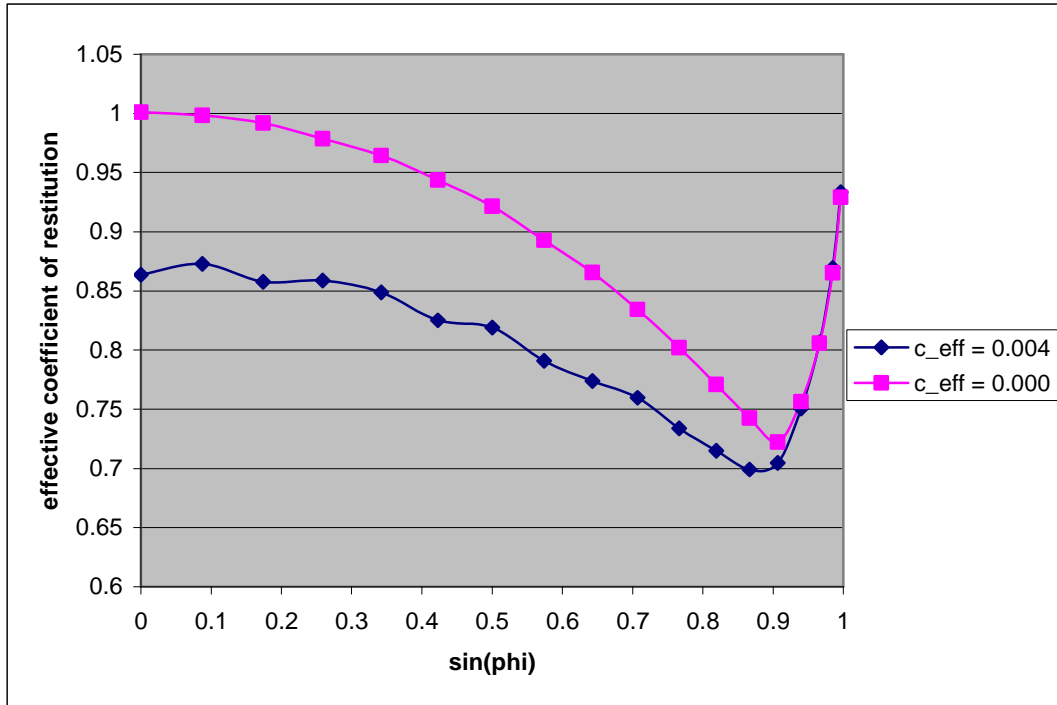


Figure 2.10: Overall coefficient of restitution as a function of angle of impact for different damping coefficients. It is clear, that even for an undamped case, the total energy in the system will not be conserved as soon as oblique impacts happen.

The effective coefficient of restitution for an oblique impact is defined by Eq. (50)<sup>41</sup>. The angle of impact is taken as the deviation from the vector normal to the impact surface.

$$e = \sqrt{\frac{E_{kin}^{out} + E_{rot}^{out}}{E_{kin}^{in} + E_{kin}^{in}}} \quad (50)$$

The results shown in fig. 2.11 compare well with the results presented by Schaefer et al<sup>41</sup>. The results comparing the dimensionless tangential velocities Eq. (51) before and after the impact look similar to the ones presented in the literature. We are therefore confident that the tangential collision model works accurately. The parameters chosen in this simulation can be found in section 2.4.2.

$$\psi_{in} = \frac{\dot{s}_t^{in}}{\dot{s}_n^{in}}, \quad \psi_{out} = \frac{\dot{s}_t^{out}}{\dot{s}_n^{out}} \quad (51)$$

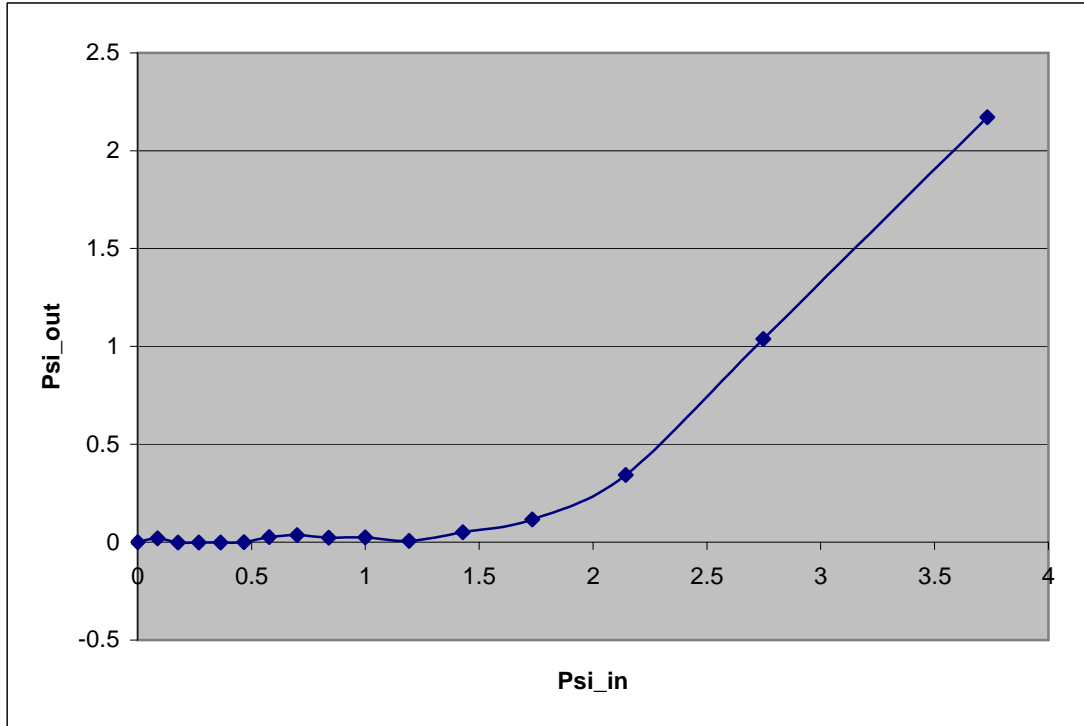


Figure 2.11: Dimensionless tangential velocity after the impact as a function of the dimensionless tangential velocity before the impact for different contact angles. The (close to) zero velocity of the contact point after the impact indicates that the particle achieved a rolling contact with the surface.

The velocities and the spin rate of the particle after the contact have been computed for different impact angles using different time step sizes to demonstrate convergence of the frictional tangential contact model.

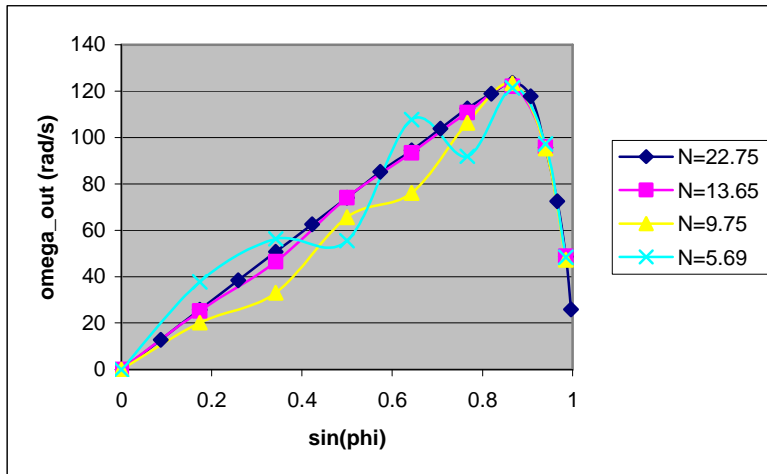


Figure 2.12: Spin rate of the particle after the collision as a function of impact angle for different time steps. Due to the more involved physics of this contact model as compared to the normal compression (non-frictional), at least ten time steps per contact seem to be required for accurate results.

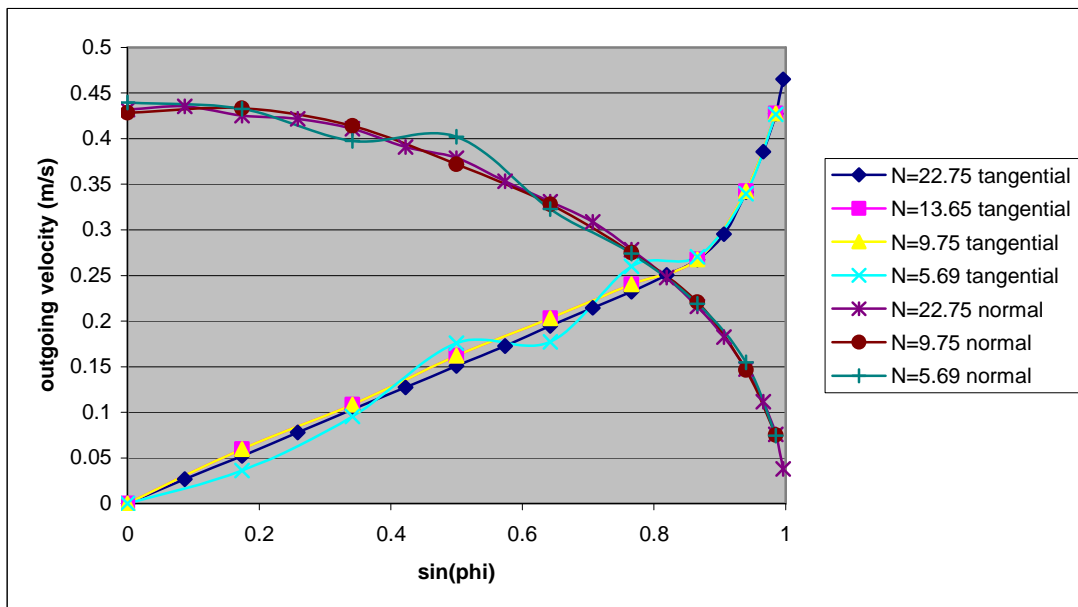


Figure 2.13: Outgoing velocities as a function of impact angle for different time steps. The desired accuracy is achieved for an N-value greater than 10.

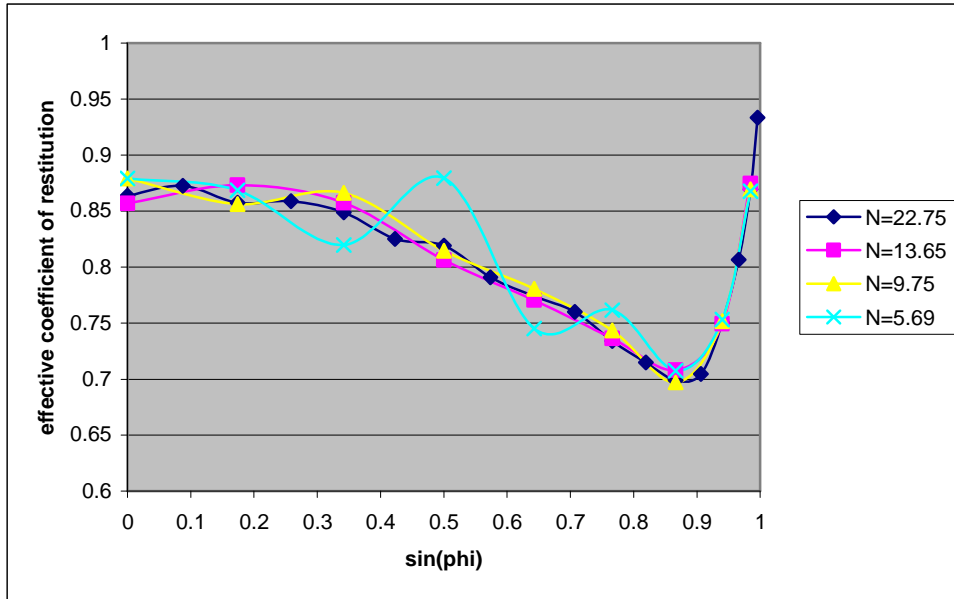


Figure 2.14: Effective coefficient of restitution as a function of angle of impact for different time steps. The results approach each other as the time step size is decreased.

As a first result from this analysis we can see, that the time step size chosen for frictional contact is required to be smaller than in the frictionless case (see fig. 2.14).

(The  $N$  value for convergence is larger here than it was in the frictionless case).

However, choosing an  $N$ -value of about 20 seems to give converged results.

Next, the granular collapse of 200 particles with frictional contact was tested. As in the frictionless case presented earlier, the particles were placed at rest into the fluidized bed. This gives the particles an initial potential energy. Since the frictional contacts have been shown to take energy out of the system, we expect the granular collapse to come to rest quicker than in the frictionless case. The dissipation of kinetic- and rotational energy during the collapse can be seen in figs. 2.15 and 2.16. Again, for time steps sufficiently small, the model converges as indicated by congruent time-energy curves for both the rotational and translational (kinetic) energies.

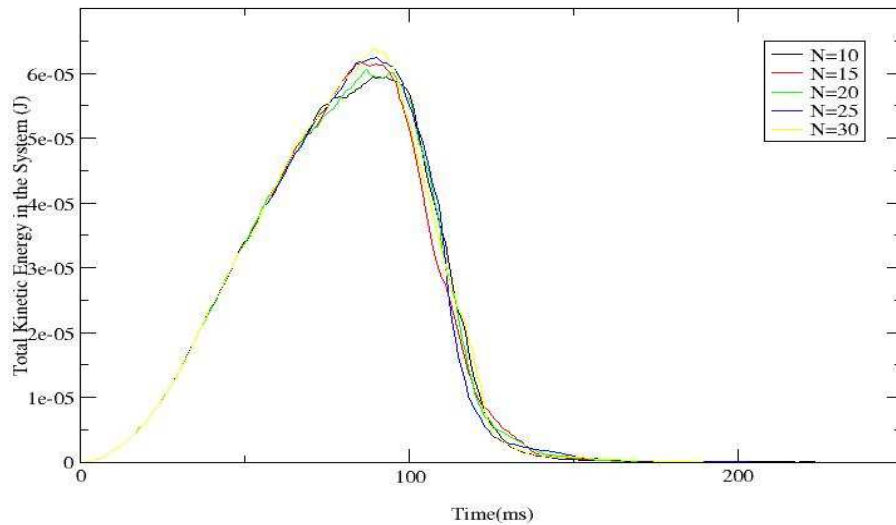


Figure 2.15: Histories of kinetic energy due to damping and frictional collisions for different time step sizes. The model predicts the same behavior for different step sizes indicating that the model has converged.

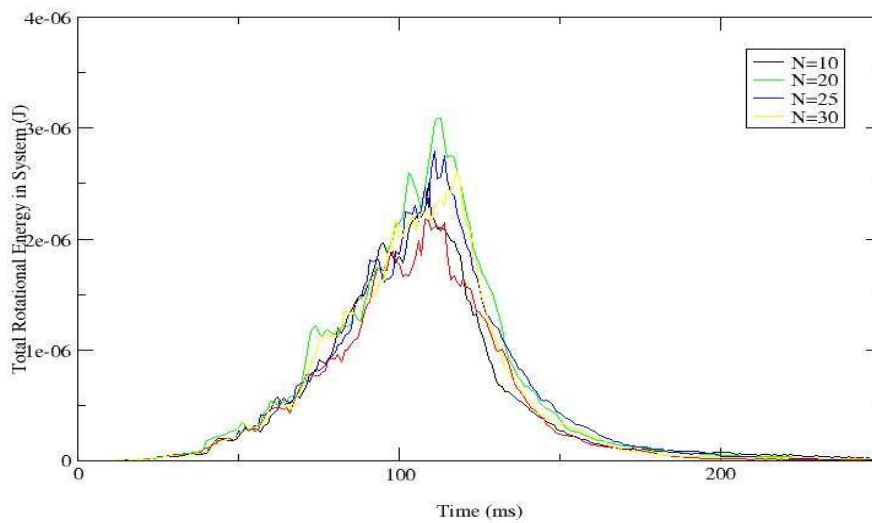


Figure 2.16: Histories of rotational energy during a granular collapse for different time step sizes. Although a weak influence of the behavior of the system can be identified, the overall behavior including the system's maximum rotational energy and the time it takes to dissipate that energy out is the same, independent of the time step size.

### 2.4.2 Verification of the Unbalanced Bounce

The model's correct representation of an unbalanced bounce needed to be confirmed. This is an essential part of the validation and has been done by comparing modeling results to high speed videos of unbalanced single particle bounces.

We attempted to shoot high speed videos with an unbalanced sphere (a hollow sphere filled with glue on one side to make it lopsided). However, since the mass distribution in a small (4mm diameter) shell filled with an unknown amount of glue was not expected to be anything better than a rough estimate, we deviated from the geometry we are ultimately trying to model, and scaled the experiment up for validation purposes.

In this experiment, a foam tennis ball (radius 0.0446 m and mass 0.04273 kg) was cut on the surface, and a stainless steel nut (radius 0.00685 m and mass 0.05018 kg) was inserted and glued into place ( $\sim 0.0102$  m from the center of the sphere). After gluing the foam sphere closed again, we ended up with a strongly unbalanced sphere with known parameters. After computing its center of gravity, the mass moment of inertia in all three main axes could be determined applying the parallel axis theorem. Markers on the sphere surface indicate the location of the nut, and give a reference point when analyzing its orientation in space in high speed videos (see figs. 2.17 and 2.18).

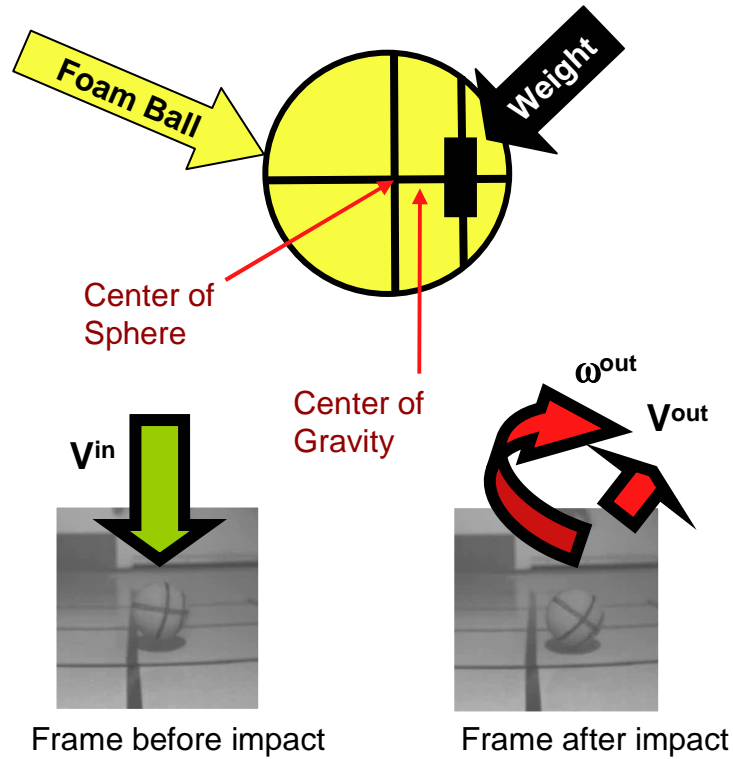


Figure 2.17: Schematic of the unbalanced foam ball and two frames from the high speed videos illustrating the unbalanced bounce validation experiments.

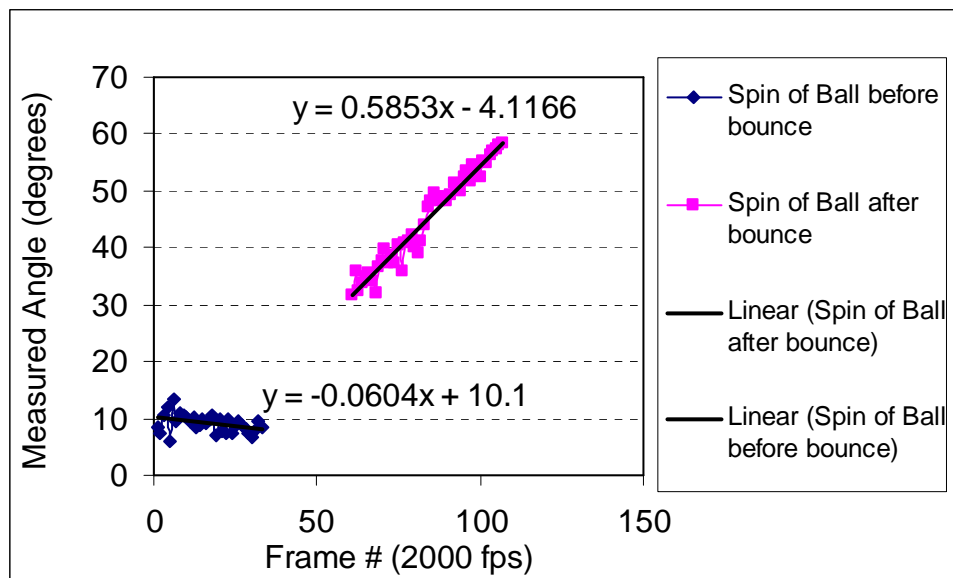


Figure 2.18: Angle measurements as a function of time (from which the spin before and after the contact can be computed).

Six different high-speed videos were taken with different contact angles and incoming velocities. The seemingly completely random post-bounce velocities and spin rates were analyzed post experimentally on a frame by frame basis ready to be compared to the calculated values from the model.

Before the model could be applied to simulate these experiments, all the other values describing the system needed to be assessed. These include the stiffness parameter ( $k_{\text{eff}}$ ), the damping parameter ( $c_{\text{eff}}$ ) and the parameters describing the tangential contact,  $\mu$  and  $\gamma$ . All these parameters have been found in a methodology similar to the one described below for the PAMS shell parameters (in section 2.4.3). Tab. 2.1 shows the parameters used in this simulation. Tab. 2.2 shows a comparison of the results from the experimental analysis to the values calculated by applying the same initial conditions.

Table 2.1: System parameters used in the bounce experiments with the unbalanced foam ball

Radius	0.0446	m
Mass	0.09291	kg
$K_{\text{eff}}$ (stiffness parameter)	4330	
$C_{\text{eff}}$ (damping parameter)	1.32	
Mass moment of Inertia Y, Z	$4.000 \times 10^{-6}$	kg m <sup>2</sup>
Mass moment of Inertia X	$6.025 \times 10^{-6}$	kg m <sup>2</sup>
Unbalance	0.0102	m
$\mu$	0.5	
$\gamma$	2.5	
Time Step size	$1 \times 10^{-4}$	s

During this analysis, it became obvious, that the results are strongly dependent on knowing the exact contact angle. Slight shifts would lead to a spin or a linear displacement in the third dimension (perpendicular to the plain of view of the camera),

which is not captured by the camera, leading to a sizeable measurement uncertainty. Despite the fact that at times, there is a significant difference between the measured and the computed values, when comparing the respective values to the pre-collision velocities, it becomes clear, that the trend of the experimental system (e.g. significant increase in x-velocity, slight decrease in spin rate) are followed within the uncertainties of the measurements. Taking these considerations into account, we demonstrated that we are able to reproduce several different scenarios of a single bounce of an unbalanced sphere, increasing our confidence in the physical description applied in this model.

Table 2.2: Comparison of measured and simulated post-impact velocities.

Case	<b>x-vel IN</b>	x-vel out meas.	x-vel out comp.	<b>y- vel IN</b>	y-vel out meas.	y-vel out comp.	<b>Omega IN</b>	omega out meas.	omega out comp.
1	<b>-0.05</b>	0.80	1.58	<b>-2.89</b>	1.57	2.164	<b>-5.37</b>	-31.5	-28.17
2	<b>-0.18</b>	-1.17	-1.68	<b>-3.46</b>	1.78	1.92	<b>-2.11</b>	42.00	20.43
3	<b>-0.17</b>	-1.06	-0.54	<b>-3.98</b>	2.67	3.0	<b>3.07</b>	32.00	25.00
4	<b>-0.01</b>	-0.48	-0.59	<b>-2.61</b>	0.98	1.46	<b>23.45</b>	13.6	4.75
5	<b>-0.04</b>	-0.96	-1.25	<b>-1.67</b>	0.98	0.85	<b>0.60</b>	27.6	32.46
6	<b>-0.86</b>	0.91	0.54	<b>-1.23</b>	2.92	3.0	<b>7.80</b>	26.9	25.0

### 2.4.3 System Parameters

The system parameters describing the spheres (mass, radius, mass moment of inertia, and distance between center of mass and center of the sphere) as well as the parameters describing the normal and tangential collision (stiffness of the sphere  $k_{eff}$ , damping coefficient  $c_{eff}$ , coefficients of static and dynamic friction  $\mu$  and  $\gamma$ ) have to be determined, so that the code can model the experimental setup accurately. Different

approaches have been used to find the different parameters characterizing the system. This section will explain what values have been used in the code, how they have been determined, and the size of the error expected from the measurement.

#### **2.4.3.1 Mass of the Sphere**

Since we are using the shells created in the prototypic shell production process, we cannot be sure that the shells have a uniform weight. Due to the small mass of the shells (and the lack of an accurate enough scale), the shells have been weighed in groups of 30 to 40. The final mass of the shells has been determined to be the statistical mean with a certain standard deviation.

Two groups of shells have been used for the room temperature bed. In particular, to test the fluid-particle interaction (see section 2.4.3), shells of different radii and masses were used in the testing. The two masses were found to be  $1.89 \times 10^{-6}$  kg and  $0.677 \times 10^{-6}$  kg with a standard deviation of  $9.2 \times 10^{-8}$  kg and  $4.45 \times 10^{-8}$  kg, respectively.

#### **2.4.3.2 Radius of the Sphere**

Unfortunately, the production process mentioned above typically does not yield shells with exactly identical radius. Thus, the radius of a number of spheres has been measured under a microscope, sampling 20 shells out of a batch of about 400. From the measurements, the statistic mean and standard deviation have been found. For the group of lighter and smaller shells, this analysis gave a mean diameter of 2.112 mm with a standard deviation of 0.287mm. This uncertainty of 13.5 % leads to very inconclusive results, especially, since this means that the volume of the spheres cannot be determined

to within 40%. When using this diameter to determine the void fraction, this error in the measurement leads to a large uncertainty in the void fraction calculation (see Appendix D). Alternatively, a known number of shells were held under water. The increase in volume was measured and related to the average radius of the shells. This measurement was more accurate, although the uncertainty of the graduated cylinder was taken into consideration. A collection of 200 of the larger shells were found to have a volume of 6.4 ml (+/- 0.15 ml), 490 of the smaller shells were measured at 3.4 ml (+/- 0.15). This translates into diameters of 3.939 (+/- 0.030) mm and 2.367 (+/- 0.033) mm as shown in the error analysis in Appendix D.

#### **2.4.3.3 Stiffness of the Sphere**

The stiffness of the shells ( $k_{eff}$ ) determines the contact time of a bounce. During the bounce, the kinetic energy of the shell is transferred into elastic deformation energy until the shell comes to rest (assuming a perpendicular incoming velocity). After that the shell is accelerated away from the object and some of this deformation energy is converted back into kinetic energy. In the undamped case, the kinetic energy of the particle approaching the object is equal to its kinetic energy departing from the object. Since the kinetic energy is just reversed in orientation, the only influence the stiffness has on the behavior of the system is the contact time.

Analyzing high speed videos of a perpendicular bounce of a 4mm PAMS shell target, the contact time was found to lie between 1/6000 s and 1/10000 s. Videos of higher speed than the ones taken (6000 and 10000 frames per second) would be

required for a more accurate measurement. This contact time converts into stiffness following equations Eqs. (52) when applied the equations of oscillatory motion.

The time for one half of a period (contact is only half of a period):

$$\Theta_{n/2} = \pi \sqrt{\frac{m_p}{k_{eff}}} \quad (52.a)$$

The shell's stiffness can be computed from the contact time:

$$k_{eff} = \frac{\pi^2 m_p}{\Theta_{n/2}^2} \quad (52.b)$$

Based on contact time between 1/6000 and 1/10000 seconds ( $k_{eff} = 672$  N/m and 1865 N/m) the stiffness has been set to 1000 N/m in the model.

#### 2.4.3.4 Damping Factor during Collision

The damping factor has been found by analyzing several videos of single particle bounces. These videos cover up to four bounces, an average coefficient of restitution has been found from them. The velocity of the particles after each bounce has been determined by measuring the time between two bouncing contacts and applying the simple equations of motion (assuming a frictionless case). See tab. 2.3 for the details of the measurements. To check this approach, in which the air drag might play a distorting role, a different approach has been taken in one case. The y-position (height) of a particle has been determined (using National Instrument's Vision program) for each frame during a collision. Knowing the frame rate the video was taken at, the speed of the particle before and after the bounce could be determined.

The coefficient of restitution was computed from the absolute value of the velocity before and after the collision (Eq. (53a)), while the velocity is computed from Eq (53b), knowing the time between collisions.

$$e = \frac{v_a}{v_b} \quad (53a)$$

$$\dot{s} = 9.81 \cdot \frac{\Delta t}{2} \quad (53b)$$

Table 2.3: Coefficients of restitution determined from video of particle bounce experiment.

Video #	Bounce #	Time between bounces (s)	Impact Velocity (m/s)	Coefficient of restitution
1	1	0.1562	0.76	-
	2	0.1160	0.569	0.749
	3	0.0897	0.440	0.773
2	1	0.106	0.52	-
	2	0.093	0.456	0.877
	3	0.056	0.275	0.603
	4	0.040	0.196	0.713
3	1	0.108	0.53	-
	2	0.086	0.422	0.796
	3	0.076	0.373	0.884
	4	0.064	0.314	0.842
Mean:		0.780	Standard Deviation	0.093

The height vs. time plot for a single particle bounce is given in fig. 2.19.

Considering that the total duration of plotted time here is rather short, the influence of the gravitational force is neglected, and the trend line was approximated linearly. The incoming velocity of 0.65 m/s and an outgoing velocity of 0.41 m/s have been determined (the velocity error added by gravitation in this time period is of the order of  $10^{-5}$  m/s). The coefficient of restitution found this way was 0.63, which is a little bit lower than the one found with the first methodology.

During this and other experiments we have found, that at times the particles obtain a static charge, which interferes with the bounce and causes the particle to stick to the bottom. This observation suggests that a value on the high side of these measurements ( $e = 0.75$ ) should be used. In order to study the influence of different coefficients of restitution on the system, the values of 0.96 ( $c_{eff} = 0.001$ ) and 0.68 ( $c_{eff} = 0.01$ ) have been chosen to be used in the code during the validation process. However, it is suggested to use a value between 0.75 and 0.85 when modeling the experimental setup. This difference results from the fact that the coefficient of restitution depends on the thickness of the pellet wall, and the pellet's radius and mass; all of these parameters vary from particle to particle, affecting the coefficient of restitution.

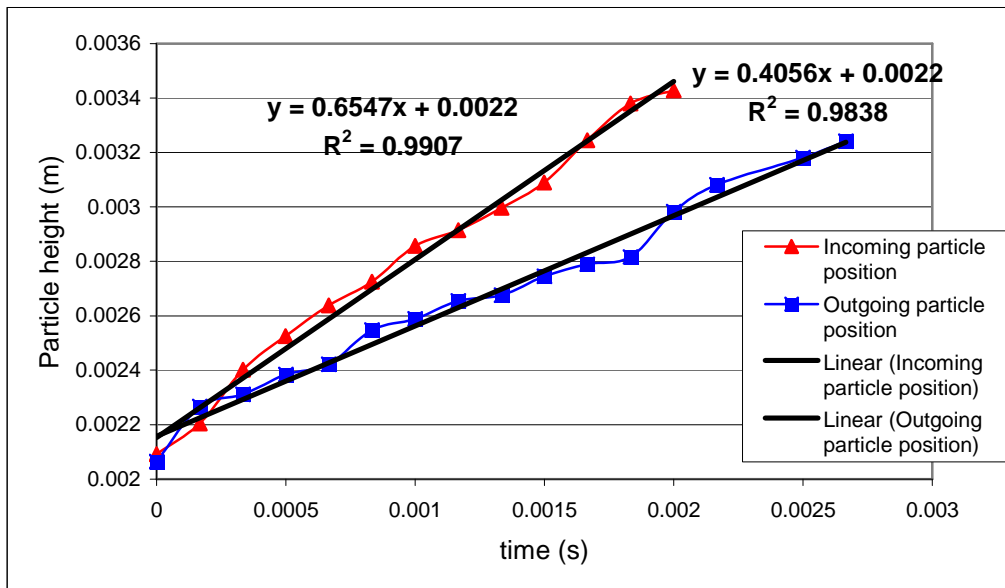


Figure 2.19: Histories of incoming and outgoing particle position for a single particle collision. The incoming particle velocity has been inverted in time to simplify comparison. The particle's velocity can be read from the linear fit through the points.

#### 2.4.3.5 The Coefficient of Friction and the $\gamma$ -Coefficient

The transition of energy between translational and rotational depends on the coefficient of friction  $\mu$  and the coefficient  $\gamma$  in Eq. (22). Both parameters are related to each other, as they both determine the tangential forces acting on a particle based on the contact velocity. While the coefficient of friction could be determined by dragging a sphere over a surface and measuring the drag force in relation to the normal force applied to the particle, the  $\gamma$  coefficient does not have a real physical meaning, and as such is hard to determine. As Schaefer<sup>41</sup> explains, this coefficient has to be chosen high enough to not interfere with the collision model, and low enough to resolve the discontinuity that a rolling contact would impose to the force calculation. It was the focus of this study to find the parameters that most accurately describe the effect of contact in terms of velocity and spin of the sphere before and after a collision. One way to narrow the parameter space for both coefficients was to record high speed videos of a collision of a sphere with a flat plate at a certain angle and the collision of two shells and measure the velocities and spin rates of both spheres before and after the contact using by a frame by frame analysis. Later the same initial conditions (in terms of positions, speeds and spins of both particles) are modeled with different  $\mu$  and  $\gamma$  parameters. The velocities and spin rates after the simulated contacts can then be compared with the results from the high speed video analysis.

However, as the high speed video could only give us information in two of the three dimensions of the contact, an exact replication of the velocities and spin rates could not be expected. Particularly in the collision between two spheres, the results

could vary largely if the point of contact and the two centers of the spheres are not in the plane perpendicular to the camera. Adjusting the values of the  $\mu$  and  $\gamma$  parameters to best fit the measured experiments gave the post-collision velocities shown tab. 2.4.

Table 2.4: Comparison between the computed and measured output parameters for several high speed videos

Video #1 Single Sphere Units: m/s (linear) or 1/s (angular)	Incoming Parameters	Outcoming Parameters MEASURED	Outcoming Parameters CALCULATED
Vx	-0.3486	-0.3519	-0.365
Vy	-0.67447	0.586	0.580
Omega	223	173	192

Video #2 Single Sphere Units: m/s (linear) or 1/s (angular)	Incoming Parameters	Outcoming Parameters MEASURED	Outcoming Parameters CALCULATED
Vx	-0.3453	-0.3409	-0.387
Vy	-0.7064	0.5949	0.609
Omega	218	115	151

Video #3 Two Spheres Units: m/s (linear) or 1/s (angular)	Incoming Parameters	Outcoming Parameters MEASURED	Outcoming Parameters CALCULATED
Vx (Sphere 1)	0.0119	0.2027	0.188
Vy (Sphere 1)	-0.5703	0.3598	0.344
-----	--	--	--
Vx (Sphere 2)	0.00	-0.0279	0.186
Vy (Sphere 2)	0.00	0.1977	0.157

The spin rates in the case of the particle-to-particle collision could not be determined, as the spin after the bounce was clearly not along the axis perpendicular to the plane of view. The parameters that could best reproduce both particle-to-wall and particle-to-particle contacts were  $\gamma = 0.05$  and  $\mu = 0.42$ . The results were satisfying, since the window of parameters for which the results from the numerical model matched the experimental results within the measurement errors was fairly large ( $0.1 < \gamma < 0.01$  and  $0.35 < \mu < 0.5$ ).

Applying a sensitivity study, it was determined, that by choosing a  $\gamma$ -value in Eq. (21) between 0.050 and 0.025 the discontinuity, that evolves from applying only Eq. (20) in the case of a rolling contact<sup>41</sup>, gets resolved (for  $N > 10$ ). This discontinuity appears as the tangential force computed in Eq. (21) oscillates between a negative and a positive value for contact velocities close to zero, and it is resolved by including Eq. (21) in Eq. (22). Figs. 2.20 and 2.21 show the influence of the  $\gamma$  coefficient on the dimensionless tangential contact point velocity and the effective coefficient of restitution.

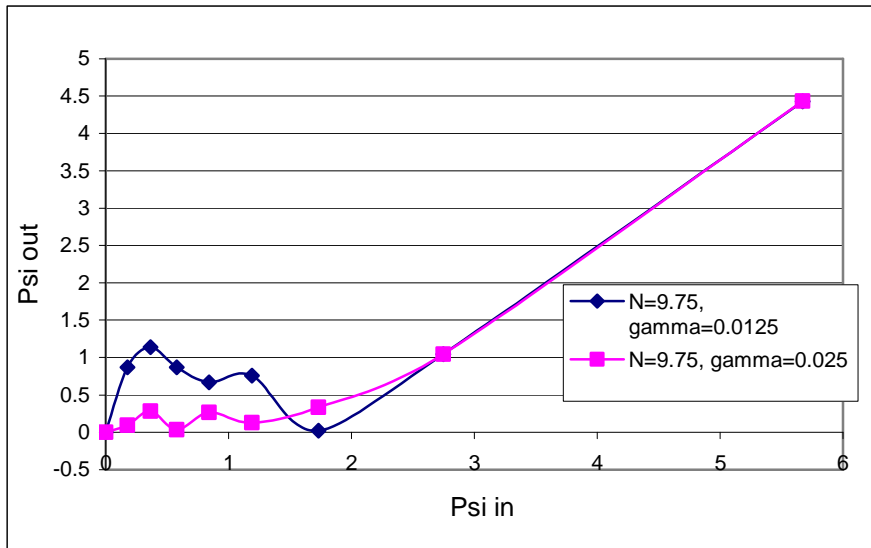


Figure 2.20: Dimensionless tangential velocity after a rolling impact as a function of incoming tangential velocity for two values of the  $\gamma$  coefficient. The large tangential velocity after the contact at low incoming tangential velocities is a result of the force jumping between a (fairly large) positive and negative value. This jumping indicates, that the discontinuity is affecting the system.

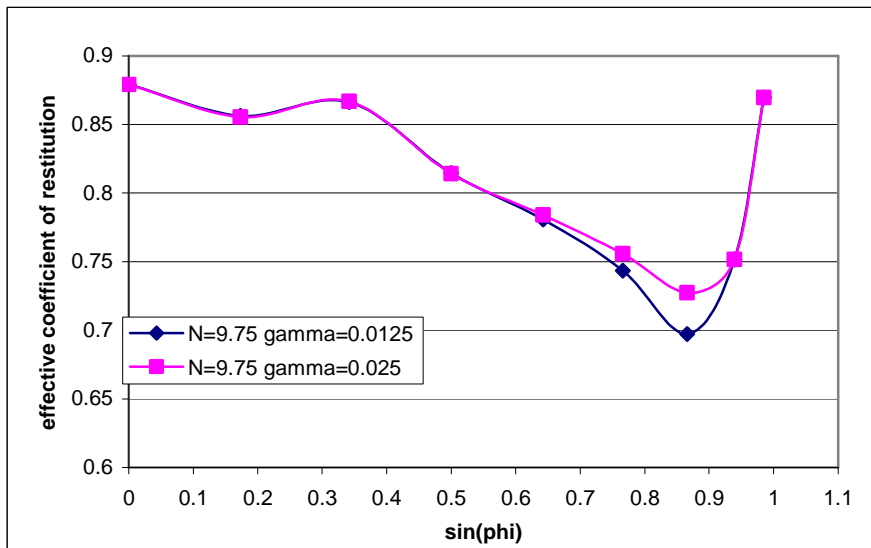


Figure 2.21: Coefficient of restitution as a function of impact angle for two different values of the  $\gamma$  coefficient. For the two chosen values the only noticeable difference occurs for fairly large impact angles.

#### **2.4.3.6 Mass Moment of Inertia and Unbalance**

Knowing the particle's mass, radius and shape, the only parameter missing to fully describe the system is the mass moment of inertia in the three main axes of the body fixed coordinate system. For a balanced sphere, this is a straightforward task, however, this computation becomes a little more complicated if unlayered or partially layered shells are considered. In addition, the distance between the center of mass and the center of gravity needs to be assessed. These parameters were computed for different inner layer shapes in the layering model (described in chapter 3).

#### **2.4.3.7 Summarizing the System Parameters**

Tab. 2.5 shows a summary of the system parameters determined in this section and used to simulate granular part of the fluidized bed model. Slightly different values will be used depending on the case that is being modeled (e.g. particle mass depends on how much fuel it contains). Apart from the computations of the mass moment of inertia, the values have been determined for empty shells. Once experiments are being conducted with filled shells, the values will be determined in a similar fashion than the one described above.

Based on these values, the time step size and number of time steps for a simulation of a certain time period can be determined. These values are given below in tab. 2.6.

Table 2.5: Parameters used in the code to simulate cases relevant to IFE layering in a fluidized bed

Parameter	Symbol	Value	Unit
Mass of PAMS shell	$m_p$	$1.89 \times 10^{-6}$	$kg$
Moment of Inertia of an unfilled target	$I$	$5.00 \times 10^{-12}$	$kg \cdot m^2$
Moment of Inertia of a filled target during layering	$I$	$0.8 - 1.0 \times 10^{-11}$	$kg \cdot m^2$
Distance between center of mass and center of sphere (offset)	$o$	$0.00 - 5 \times 10^{-4}$	$m$
Radius	$R$	$1.5 \times 10^{-3} - 2.00 \times 10^{-3}$	$m$
Stiffness value	$k_{eff}$	$1.00 \times 10^3$	$\frac{N}{m}$
Damping coefficient	$c_{eff}$	$1.00 \times 10^{-3}$	$\frac{N \cdot s}{m}$
Coefficient of static friction	$\mu$	0.4	$n/a$
Coefficient of dynamic friction	$\gamma$	0.025 - 0.05	$\frac{N \cdot s}{m}$

Table 2.6: Time step sizes for different number of time steps during collision contact ( $N$ ). The total time of simulation was 0.4 seconds; samples were taken every 0.001 seconds.

$\Delta t$ (s)	$\Theta_{n/2}$ (s)	N	# of steps	Steps between samples
$3.38 \times 10^{-5}$	$2.7 \times 10^{-4}$	4	11851	30
$2.70 \times 10^{-5}$	$2.7 \times 10^{-4}$	5	14812	37
$2.25 \times 10^{-5}$	$2.7 \times 10^{-4}$	6	17778	44
$1.93 \times 10^{-5}$	$2.7 \times 10^{-4}$	7	20725	51
$1.69 \times 10^{-5}$	$2.7 \times 10^{-4}$	8	23668	59
$1.50 \times 10^{-5}$	$2.7 \times 10^{-4}$	9	26667	67
$1.35 \times 10^{-5}$	$2.7 \times 10^{-4}$	10	29630	74
$0.90 \times 10^{-5}$	$2.7 \times 10^{-4}$	15	44444	111
$0.675 \times 10^{-5}$	$2.7 \times 10^{-4}$	20	59259	148
$0.54 \times 10^{-5}$	$2.7 \times 10^{-4}$	25	74074	185
$0.45 \times 10^{-5}$	$2.7 \times 10^{-4}$	30	88889	222

#### 2.4.4 Fluid- Particle Interaction

The fluid-particle interaction predicted by the model was compared with empirical relations and experimental observations. Since the flow conditions for the actual layering experiment (performed with helium at about 0.5 atm and at temperatures below 19 K) are difficult to sustain practically in a laboratory environment, and the analysis of such a system would be somewhat challenging, a room-temperature, standard-pressure fluidized bed was set up to experimentally observe the motion of the particles in the bed with different configurations. The purpose of this analysis is to benchmark the model with an easier setup than required for layering conditions, and ultimately confidently apply the model to study the layering process under cryogenic conditions. Then a window in the parametric operating space can be defined, in which the layering experiment can be expected to be successful. Tab. 2.7 compares the most important parameters for nitrogen at the room-temperature (RT) and for cryogenic helium as a fluidizing gas.

Table 2.7: Comparison of parameters for He @ 18 K and N<sub>2</sub> at RT

		Helium @ 18 K, 0.5 atm <sup>45</sup>	Nitrogen @ RT, 1.0 atm <sup>46</sup>	Units
$\mu_f$	Viscosity of fluid	$0.33 \times 10^{-5}$	$1.82 \times 10^{-5}$	$Pa \cdot s$
$\rho_f$	Density of fluid	1.337	1.293	$\frac{kg}{m^3}$
$C_{p,gas}$	Specific heat of fluid	5200	1005	$\frac{J}{Kg \cdot K}$
$k_{gas}$	Thermal diffusivity	0.026	0.0257	$\frac{W}{m \cdot K}$
Pr	Prandtl Number	0.733	0.707	n/a
$d_p$	Particle diameter	2.36-4.00	4.00	$mm$
$m_p$	Mass of particle (empty)	$1.89 \times 10^{-6}$	$1.89 \times 10^{-6}$	$Kg$
Ar	Archimedes number	$8.18 \times 10^6$	$1.4 \times 10^5$	n/a
$Re_{pellet}$	Reynolds number pellet in free fall	3439	519	n/a
$U_t$	Free fall particle speed	2.91	1.82	$\frac{m}{s}$
$H$	Bed height	~0.05	~0.05	$m$
$d_{bed}$	Bed diameter	0.025	0.025	$m$
$N_{Sph}$	Number of shells	~100 - 400	~100 - 400	n/a
$\nu$	Richardson Zaki Exponent	2.406	2.41	n/a

In this setup, the fluidized bed consists of a 2.54 cm (1 inch) ID tube of 45.72 cm (18 inches) length. A distributor plate, or “frit”, is mounted at the bottom of the tube to provide a shelf for the shells, to impose a uniform gas flow velocity across the cross sectional area of the bed, and to provide a pressure drop which is significantly higher than the pressure drop through the fluidized bed (see fig. 2.22). The tube was filled with

shells with a range of sizes and weights to study the influence of these parameters on the overall bed behavior.

Several different sphere sets were used, including 100-150 PAMS shells (3mm in diameter), 200 PAMS shells (4mm in diameter), 350 solid nylon spheres (3.98 mm in diameter), and 900 solid nylon spheres (3.175 mm in diameter). As a fluidizing medium, nitrogen or water was pushed through the bed in a vertically upward direction.

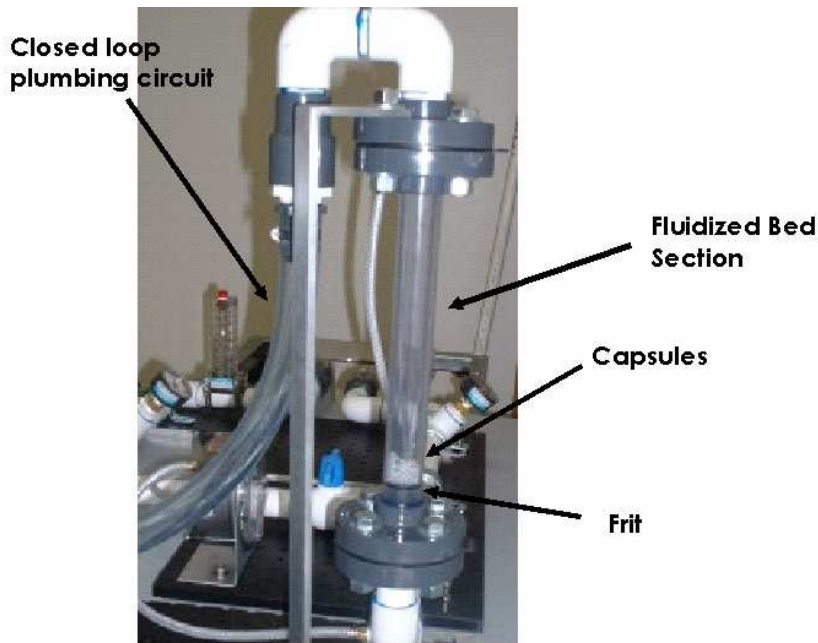


Figure 2.22: Experimental setup with nitrogen as a fluidizing medium.

As a first test, the unrecoverable pressure drop, computed by summing up the drag forces of all the particles, is compared to the pressure drop predicted by the Ergun equation<sup>20</sup>, applied over the bed as a whole. Despite being based on simple assumptions, the revised Ergun equation has been widely accepted as a very good approximation. The pressure drop has been measured in the room temperature experiments and is compared

with the values resulting from directly applying the Ergun equation on the entire bed domain.

The application of the Ergun equation is restricted to cases in which the particles are immobile and the void fraction is fixed and homogeneous over the entire bed domain. Thus, it is only reasonable to compare pressure drop values for fluid velocity values below the minimum fluidization velocity. We know that the void fraction in the case of a packed bed is around 0.40. Once the gas flow fluidizes all the particles, the pressure drop through the bed should increase slower as the drag on the spheres, in average, is equal to the particles effective weight which only varies weakly with the void fraction. Due to their low density, the PAMS shells are fluidized at very low flow velocities. Thus, in the first test, the bed was filled with 900 solid nylon shells. Their density ( $\sim 1370 \text{ kg/m}^3$ ) allow us to measure the pressure drop for a larger range of flow velocities. Fig. 2.23 shows a comparison of the experimental results, the Ergun equation prediction and the time-stepped model simulation. The underlying considerations for the error estimates are presented in Appendix D.

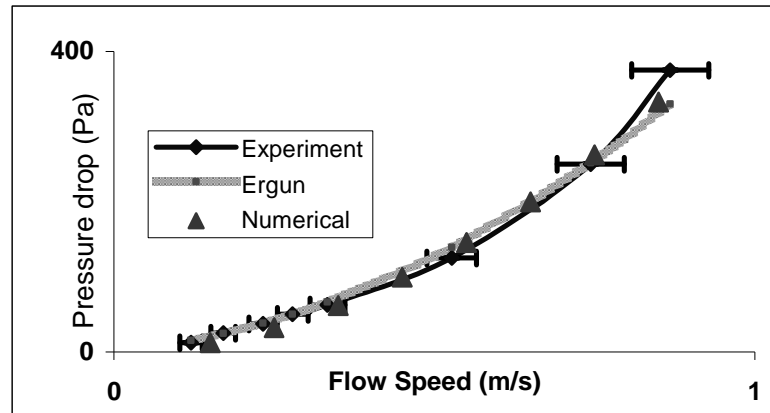


Figure 2.23: Pressure drop through the bed as a function of flow speed estimated from the experimental results and computed from Ergun's Equation (Eq.(36)), and from the time-step model.

Now that we established evidence that the drag force leading to the unrecoverable pressure drop is modeled correctly for gas speeds below the minimum fluidization velocity, the next step is to check the relationship between the flow speed and the bed expansion after fluidization is achieved as well as the general behavior of the bed.

The predictions from the Richardson-Zaki relation (applied to the bed globally) could be compared with the time-stepped numerical model. However, the Richardson Zaki relation is based on the assumption of homogeneous fluidization.

In general, most gas-solid fluidized beds show a bubbling or chugging behavior (inhomogeneous fluidization), whereas in liquid-solid systems, homogeneous fluidization is to be expected. By defining and comparing the kinematic and dynamic wave velocity, Gibilaro<sup>42</sup> shows that Eq. (54) can be used as a predictive measure of the likelihood of homogeneous fluidization. If the expression on the right hand side is positive, we can expect homogeneous fluidization, if it is negative, bubbling behavior

(inhomogeneous fluidization) can be predicted. The void fraction is the only free parameter of the system, and it can be shown that over the entire porosity range ( $0.4 < \epsilon < 1.0$ ), the stability criterion predicts bubbling behavior for the case of PAMS and nylon shells fluidized in nitrogen.

$$\frac{1.79}{\nu} \cdot \left( \frac{g \cdot d_p}{U_t^2} \right)^{0.5} \left( \frac{\rho_p - \rho_f}{\rho_p} \right)^{0.5} \left( \frac{\epsilon^{1-n}}{(1-\epsilon)^{0.5}} \right)^{-1} = 0 \quad (54)$$

After these considerations, we decided to fluidize nylon shells with water, as Eq. (54) predicts homogeneous fluidization for this case of liquid-solid fluidization. This is an important step in the validation process, as it allows us to compare experimental results to the Richardson-Zaki predictions (which are only valid for homogeneous fluidization) and modeling results, as depicted in fig. 2.24. Although the fluidization of ultimate interest for the layering experiment involves gaseous helium, which leads to inhomogeneous fluidization, we can use this case as an additional case to verify the model predictions.

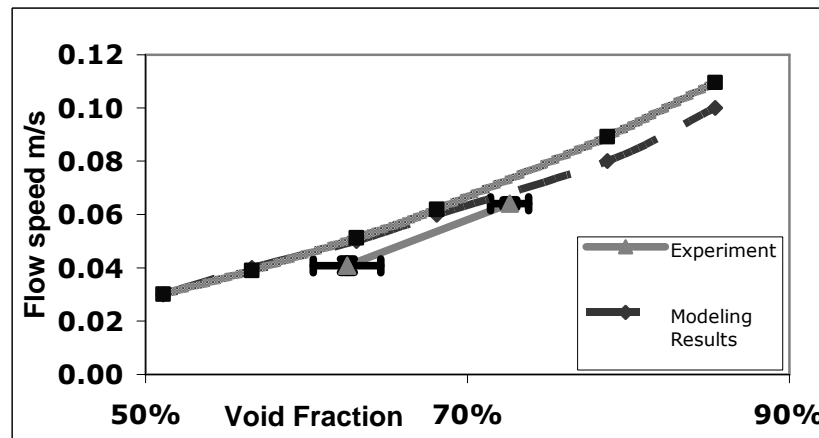


Figure 2.24: Flow speed as a function of void fraction for homogeneous fluidized bed operation of 350 particles in water based on empirical, experimental and numerical predictions.

Good agreement can be seen between the experimental results, the model predictions and the appropriate empirical relation.

As a final step in benchmarking the model, we compared the model predictions directly to the experimental observation in the case of inhomogeneous fluidization. In this case, we observe bubbling or chugging behavior both experimentally and numerically. Different videos of these behaviors as well as from the experiments are posted on the web ([www.iacs5.ucsd.edu/~kuboehm](http://www.iacs5.ucsd.edu/~kuboehm)).

In a fluidized state which is governed by bubbling behavior, the prediction of the bed expansion is a little bit more complicated; in the model, the average of the highest ten shells is used to report the bed height. Fig. 2.25 shows the average void fraction based on the overall bed expansion observed in the experiment and predicted by the code for the case of 200 PAMS 4mm PAMS shells fluidized in nitrogen.

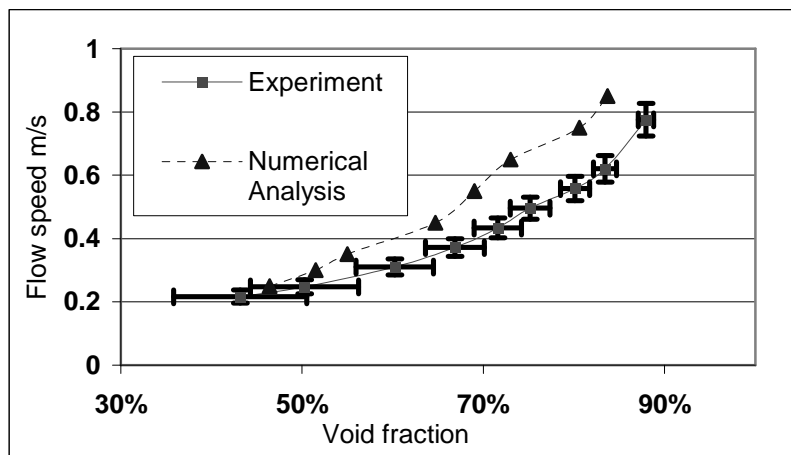


Figure 2.25: Flow speed as a function of void fraction for non-homogeneous fluidized bed operation using nitrogen based on experimental and numerical predictions.

The error bars in this figure include the uncertainties in the measurement of the relevant parameters (particle radius, flow speed, etc.) under steady state conditions. The uncertainties resulting from difficulties in measuring the time-averaged bed height of a bubbling bed are not included in this figure, and a comparison to the time-averaged bed height of the mean y-position of the ten highest particles as done in the numerical case is not expected to match the experimental findings perfectly.

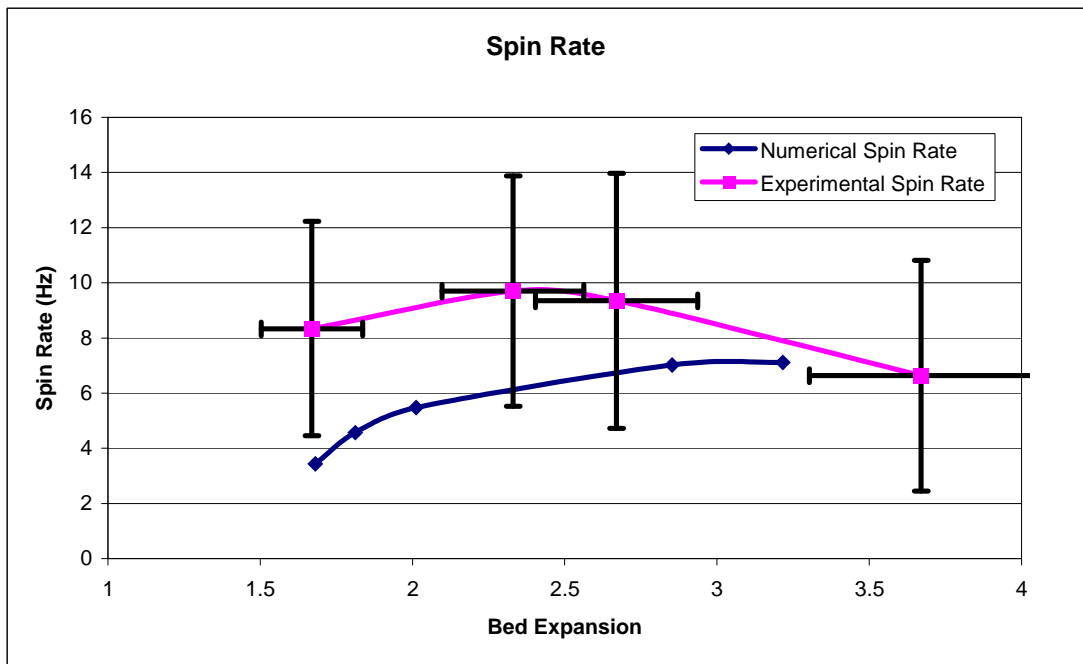
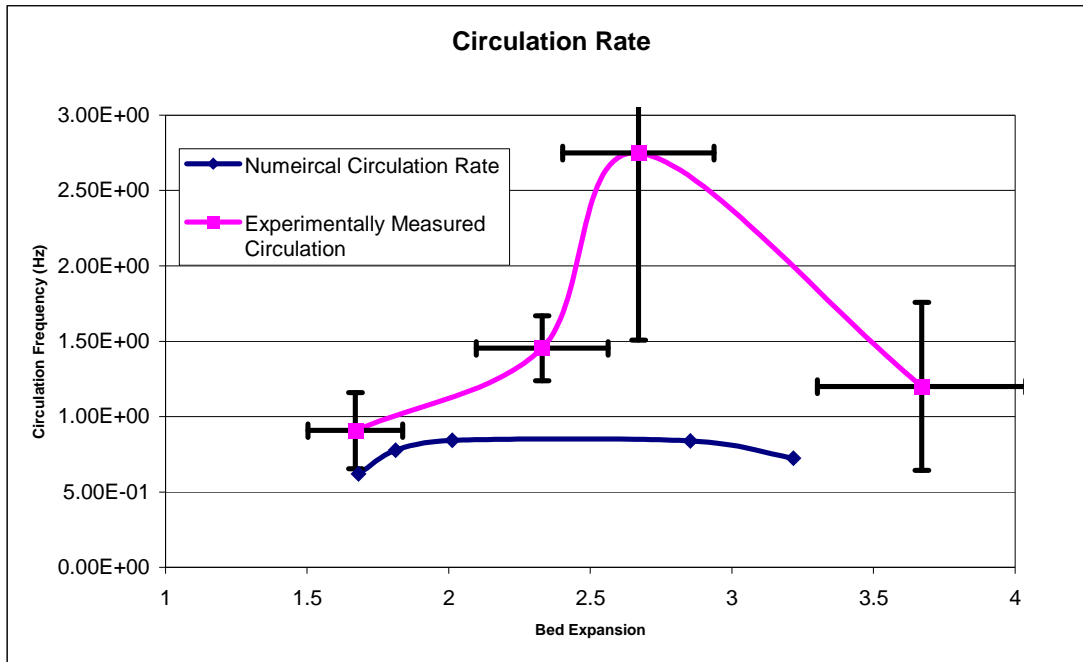
The results, mainly the prediction of the bubbling bed behavior with a bubbling frequency close to the one observed in the experiment ( $\sim 3\text{-}6$  Hz), and the relation of bed height vs. flow speed (Fig. 225), while considering the large measurement error for the bed height in the experimental case, give confidence that both the granular model and the fluid-particle interaction model can predict the behavior of the cryogenic fluidized bed with satisfying accuracy.

#### **2.4.5 Compare Spin and Circulation Rates with Experiments**

The overall bed behavior predicted by this model is close to the bed behavior observed in the experiment and similar to the one predicted by theory. The resulting agitation of the shells leads to certain average spin rates and particle velocities.

The analysis of the particle behavior has been done by post-experimentally examining high speed videos of the room temperature experimental fluidization. For tracking purposes a white foam shell is inserted to the bed which can be easily distinguished from the clear PAMS shells. Rotating motion can be tracked by following a line pattern marked on the target. These videos can be analyzed frame by frame using the FASTCAM software; knowing the frame rate at which the video is taken (usually around 500 fps) and the distance the pellet moved between two frames, the translational and rotational speed can be determined.

The spin rates computed from the high speed video analysis are compared with results from the fluidized bed model. Fig. 2.26 shows that the observed spin rates in the experiment are slightly higher than the results from the “time-averaged” numerical computation. This is due to the fact that the particle rotation is induced by its interaction with the wall, while particles in the center of the bed are expected to have lower spin since they don’t interact with the wall. As a result of this observation, the measurements on the particles’ spin rate are biased, as measurements are made on particles close to the wall, since they are easier to see.



Figures 2.26: Circulation frequencies and spin rate computed from the model and observed in the experiments as a function of bed expansion.

#### 2.4.6 Surface Damage Analysis in Fluidization Experiments

The conservation of the surface finish has been of main concern because of the demanding requirements for target implosion physics<sup>47</sup>. A thin, a gold or gold-palladium alloy overcoat needs to fully and uniformly cover the surface of the target to reflect radiation during injection as well as to help with the implosion of the target. A method was developed, that creates a smooth and very uniform layer of gold or gold - palladium around the outside of the shells. Using a sputter coater and a rotating dish design, layers with a thickness of 30-50 nm and a surface smooth enough to meet HAPL surface specifications could be produced.

One of the parameters that will determine the success of the layering apparatus is the condition of the outer surface of the shell at the end of the layering process. While being fluidized, the shells will experience a large number of collisions with a range of impact velocities, which has been shown to deteriorate the thin reflective overcoat.

Through experimental analysis, the damage on the target surface induced by a fluidized bed operating at roughly two bed expansions was assessed. SEM images taken after the shells have been fluidized for 16 hrs (the maximum time that we expect layering to take) at room temperature and temperatures around 18 K indicate severe surface degradation from the collisions. These observations (shown in Fig. 2.27, and further discussed in Appendix A and B) indicate that the Au-Pd layer is peeled off due to particle – particle collisions at both operation temperatures, although a stronger effect is seen at room temperatures than at 18 K. There was reason to believe that the surface damage could be reduced by over-coating the shells with an additional layer of thin

plastic (glow discharge polymer, GDP) as direct gold on gold contact can be avoided this way. GDP over-coated shells were produced and fluidized for 16 hours both at room temperature and at 18 K. Visual analysis of the SEM images taken after the fluidization indicates that the surface damage could be reduced, but not eliminated. Fig. 2.27 summarizes the results. The surface damage on the pure gold-palladium layer, which was very severe at room temperatures, was slightly alleviated in the cryogenic case. The GDP overcoat could protect the underlying high Z layer in the room temperature case, but damage in the overcoat was induced by fluidization in the cryogenic case.

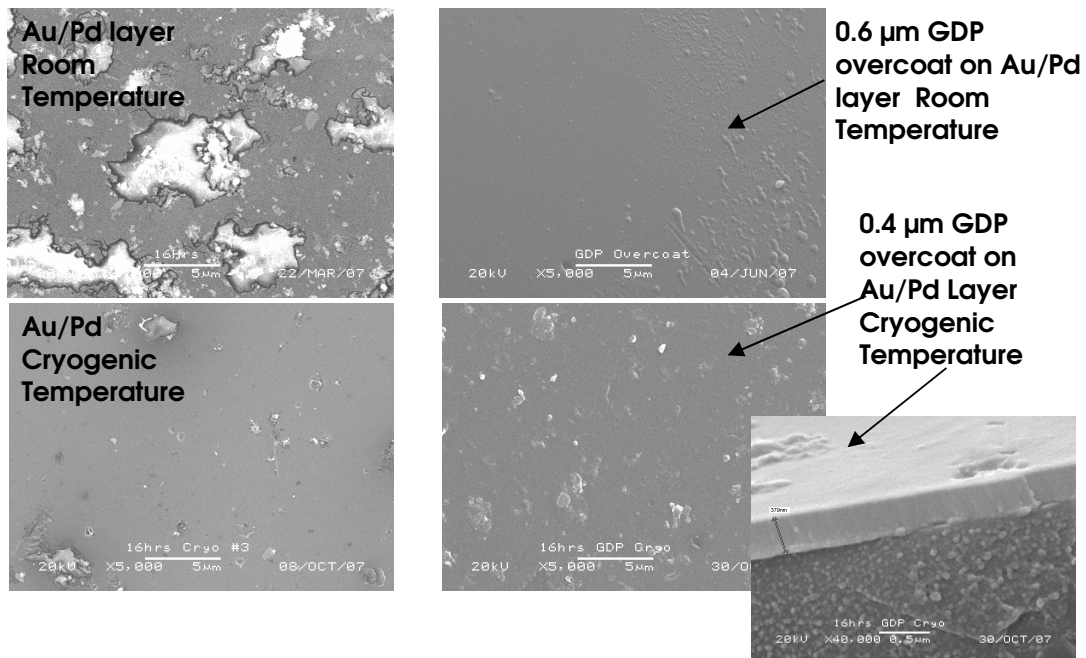


Figure 2.27: SEM pictures showing the target surface with a 5000x magnification before and after 16 hrs of fluidization at different temperatures.

After analyzing these results, a study was performed (and presented as a Master's Thesis by Landon Carlson, Dec 2008 at UC San Diego)<sup>17</sup> to further analyze

the surface damage mechanisms and to explore methods to create a more durable high Z layer. It was shown that stronger coatings could be produced by changing the sputtering parameters. Research is in progress to analyze whether a threshold on the impact velocity or the number of impacts at a given velocity that leads to acceptable surface finish could be defined.

It will be shown in the next section how the fluidized bed model could be applied to help minimize the surface damage.

## **2.5 Relevant Model Output**

Through preliminary calculations<sup>13-14</sup>, the following parameters have been identified as being the most important in order to achieve a uniform deuterium ice layer: the time that one particle takes to move from the top to the bottom of the bed and back to the top (speed of circulation); and the frequency at which the particle spins around its own axis in the bed. Additionally, the direction of the spin needs to be randomized. These parameters influence the temperature distribution around a single pellet, and the difference in temperatures imposed on one shell as compared to another; at the same time, the spinning motion counteracts a permanent temperature difference between the top and the bottom of the shell.

The optimized fluidized bed design would have to not only provide the required “time-averaged” uniform temperature, but also minimize the surface damage on the targets. In this section, the relevant model output to find an optimized fluidized bed design will be presented.

We will start with the requirements on the system for outer surface damage and then cover the heat transfer and temperature uniformity.

### **2.5.1 Collision Damage Analysis**

As an example of how the model will help in optimizing the layering process, it is shown here how the outer surface damage specification can limit the available fluidization parameters. By recording the normal and tangential impact velocity of each collision during fluidization, statistical data can be extracted from the model, which can help in estimating the surface damage resulting from certain fluidization parameters

Fig. 2.28 shows the number of collisions at different normal impact velocities for different bed expansions during a 10 second fluidization period. These statistics indicate that the higher the fluidizing gas velocity (higher bed expansion), the higher the number of collisions at large impact velocities. Although it is qualitatively an obvious result that a more violent bed would induce a higher average impact velocity, the model is able to quantify the difference in average impact velocity (tangential and normal). In addition the model can provide an upper limit of collision velocity, above which only a very small number of collisions occur for a certain gas speed at the bed inlet.

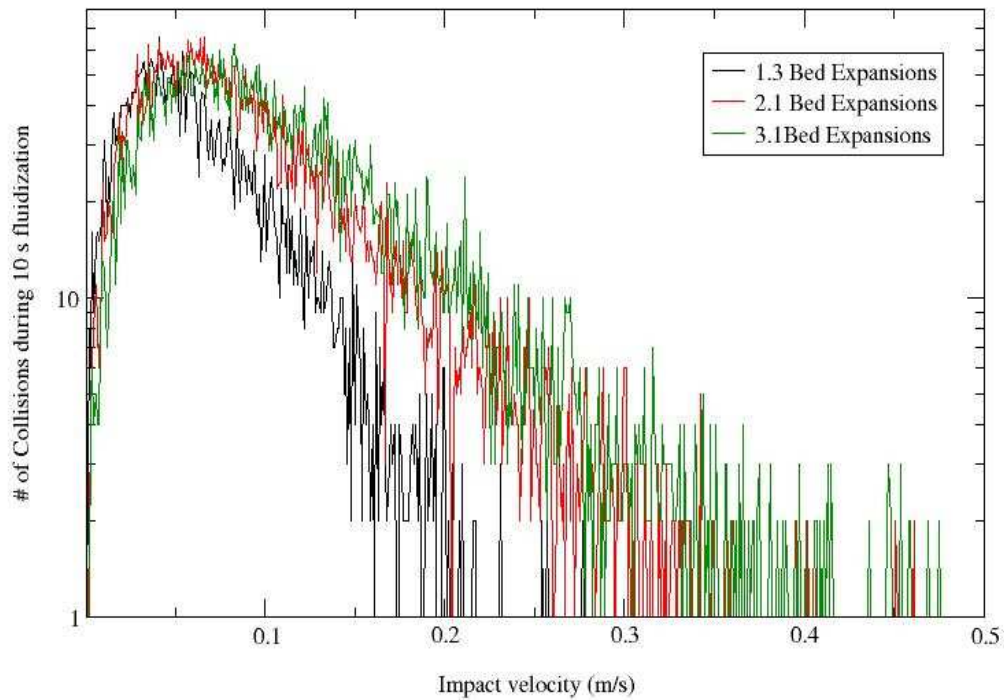


Figure 2.28: Number of collisions at different impact velocities during a 10 s fluidization period for different bed expansions.

Although the severity of the surface damage resulting from a certain number of collisions at a certain impact velocity still needs to be assessed, the influence of changing the bed expansion on the impact velocity can be addressed. The model output relevant to this analysis is: 1) the number of total collisions that occur during a given time interval (collisions per 10 s); 2) the number of total collisions that fall within a pre-set velocity interval, as shown in fig. 2.28 (the collisions occurring at normal impact velocities within a 0.001 m/s interval are counted, similarly the tangential velocity can be plotted for different bed expansions and degrees of unbalance); and 3) the collision frequency spectrum for each individual pellet computed by recording the time between

collisions for each particle or for the overall bed. All these statistical values are used to quantify the collision impact induced surface damage as presented in section 4.

Based on the research presented here and the by Carlson<sup>17</sup> we could conclude that the surface damage to the Au-Pd layer at 2.0 BE was very severe. If a threshold for the maximum allowable impact velocity can be found, that limits the surface damage induced by collisions at this velocity to an acceptable level, (as indicated in the previous section), the results from the fluidized bed model could be used to provide an upper limit for the bed expansion at which the pellets' surface damage is kept to an acceptable limit. So far, the results from the research on this field allows the conclusion that the a bed expansion of 2.0 will damage the surface.

### **2.5.2 Time averaged spin and circulation rates**

Two main factors define the thermal environment of the shell in the bed. First, the pellets spin rate around its own axis, and second the pellets circulation speed, or movement throughout the bed. While the spin of the particle influences the temperature difference imposed on the target on opposite sides of the shell, the circulation rate gives a measure of the time-averaged gas temperature to which the pellet is exposed. In this section we will show how the values of these two quantities are determined from the simulation and how they are influenced by the bed parameters.

The spin rate around the three main axes of each shell is computed during the simulation, a time-averaged output file containing the spin rate and the particles' average orientation is created. For completely balanced spheres, the values of the spin

rate in all three directions should be very similar. As the distance between the center of mass and the center of the sphere is increased, the spin rates will vary between the axis along which the center of mass is moved away from the center of the sphere, and the other two, which are now parallel to the body fixed coordinate system, but shifted to pass through the center of gravity (CG) instead of the center of the sphere (CS). At this point, it is important to realize, that while the spin rate is important, we also need to take the average orientation of the particle into account. This average orientation is computed by applying the rotation matrix Eq. (11) to the vector (1,0,0). This leads to a maximum value of -1, if the x-axis is pointed straight down, and a value of +1, if the body fixed x-axis is parallel to the system fixed y-axis. During a long enough fluidization period of a perfectly balanced sphere, this quantity should assume a very small value, as the orientation of the particle in the system should be completely random. With increasing degree of unbalance, the spheres are expected to orient themselves in the bed with their x-axis pointing down (for small fluidizing gas speeds, since they would be top-heavy otherwise). As an output from the simulation, the model is programmed to give this value (which we will refer to as “average orientation vector”) for each individual particle as well as for the entire bed.

The circulation speed is difficult to compute, as the particles do not literally circulate though the bed. One measure is to take the time-averaged velocity of the target in the bed and divide it by twice the bed height. This way we assume that the particles are moving straight up and down in the bed. Alternatively, the gas temperature can be taken as a measure of the mixing of the particles. The gas temperature is modeled to increase as it flows through the bed. The time-averaged temperature in the gas

surrounding each individual shell is written to file. The standard deviation in the data set including the time-averaged temperature around each shell provides information about the degree of mixing and circulation that is happening in the bed during fluidization.

A good approximation is needed when computing the rise in temperature of the gas as it passes each shell as the gas flow is only modeled in one dimension. In addition, the heat transfer coefficient will depend on the target surface temperature, which needs to be computed from the layering model presented in the following chapter. However, the following argument can be made for this particular case.

A certain amount of heat is released from each particle to the gas. This heat will depend on the speed of the gas with respect to the particle, and the respective temperatures. As the pellet moves through the bed, that gas temperature that surrounds the pellet will change, and is unknown. Thus, the pellets are sorted by y-position (height in the bed). Then, the Reynolds number for each individual particle is determined. Knowing the properties of the gas, the Prandtl number is given as a constant for a particular system. From these two non-dimensional numbers, the Nusselt number can be determined by

$$Nu = \left( 2.0 + 1.8 \cdot Re^{1/2} Pr^{1/3} \right) \quad (55).$$

This empirical result is well accepted in the literature for the particle-gas heat transfer in a fluidized system operating at Reynolds numbers higher than  $10^{48}$  such as expected to occur in the planned experiments. From the Nusselt number, the heat

transfer coefficient (averaged over the entire surface of one particle) can be computed by

$$h = \frac{Nu \cdot k_{gas}}{2 \cdot R} \quad (56).$$

The total amount of heat transferred between the solid and the gas can then be computed for each particle by assuming as an initial guess that both the particle and the gas temperature at the current time step are the same as the previous time step.

$$Q = h(4\pi R^2)[T_{surface} - T_{gas}] \quad (57)$$

As a result, the temperature rise of the gas caused by each shell can be computed from the mass flow rate and the specific heat

$$\Delta T_{gas} = \frac{Q}{\dot{m}_{FB}^{gas} C_{p,gas}} \quad (58)$$

The local temperature of the gas around the shell can be found by adding all the temperature rises due to the particles below the pellet in question. This temperature is recorded along with the surface temperature.

The surface temperature of the pellet can be computed from the difference between the amount of heat produced by the volumetric heat inside the shell and the amount of heat released to the gas.

$$\Delta T_{part}^i = \frac{(\dot{q}'' \cdot V \cdot \Delta t - Q)}{C_{p,part} \cdot m_p} \quad (59)$$

After these calculations, the pellets have to be sorted according to their original numbering to avoid confusion. The sorting in ascending height before and ascending number after the temperature calculations has been done by a straight insertion

method<sup>49</sup>. The outlet gas temperature can be found after the temperature raise from all particles has been considered.

Next, example results are presented from the application of this model to a few specific test cases to demonstrate how the information calculated by this model could affect the layering parameters. A set of simulations was performed assuming a certain set of conditions (see tab. 2.8). The geometric constraints of the bed were kept constant, while the flow speed of the gas at the inlet and the distance between the center of gravity and the center of the sphere were independently varied. The mass moments of inertia around the three main axes were adjusted accordingly.

Two quantities were chosen to estimate the average temperature field imposed on the pellets. One is the scalar product of the x-axis in body-fixed coordinate and the negative y-axis in system-fixed coordinates. From fig. 2.29 we can see that at low bed expansions the time-averaged orientation of the particle is very strongly biased to face down if strongly unbalanced particles are being fluidized at low bed expansions. At higher gas flow rates or lower degree of unbalance, the orientation of the particle becomes more and more random (indicated by a small scalar product). The other quantity computed by the model describing the temperature environment of the particle is the standard deviation of the time-averaged particle surface temperature. The ratio between the standard deviation and the average particle temperature is used as a parameter describing the mixing in the bed. Fig. 2.30 shows that a higher degree of mixing is expected for higher gas flow rates.

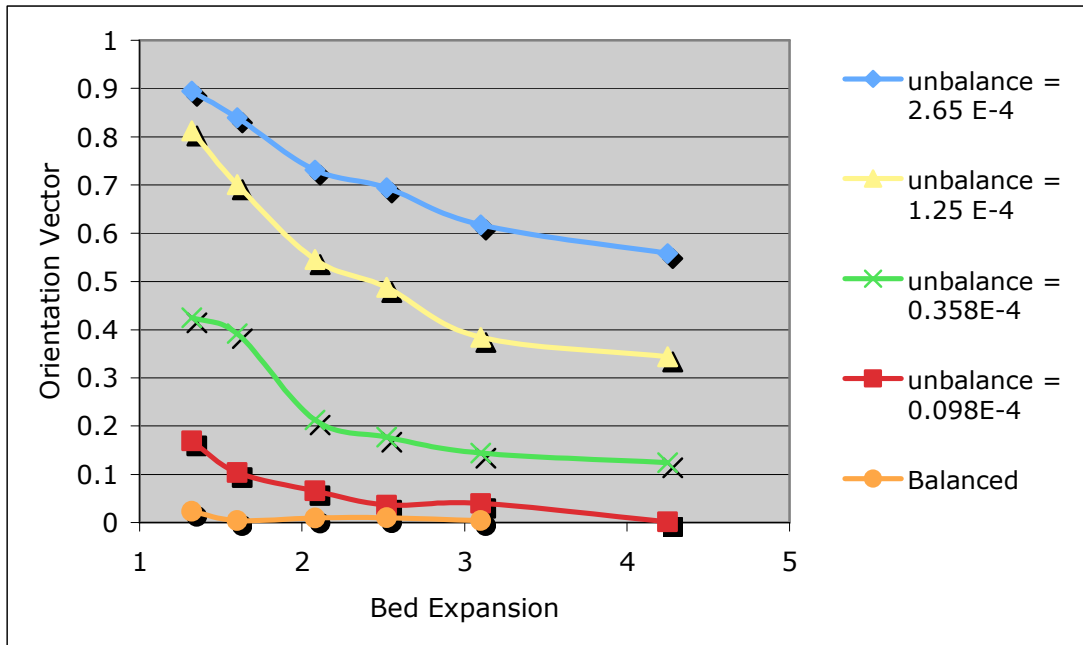


Figure 2.29: Orientation vector of the pellets for different degree of unbalance and bed expansions.

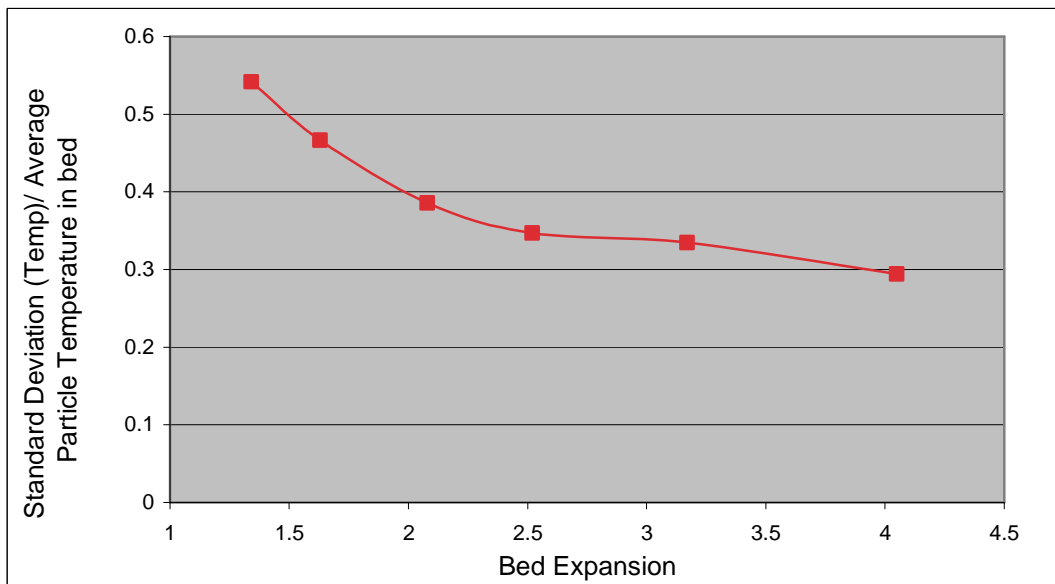


Figure 2.30: Ratio of standard deviation in time-averaged particle surface temperature to average particle temperature in the bed for different bed expansions (flow rates). The smaller this value is, the more mixing will be seen in the bed. If the simulation is carried on for longer periods of time, the value is expected to drop, but for comparison purposes, the simulated fluidization time is kept at a constant 10 s. The degree of unbalance was shown to have only little effect on the mixing of the shells.

Table 2.8: The input parameters for the exemplified fluidization simulation presented in section 2.5.2 (see Reference 45)

Radius of Fluidized Bed Cylinder	CYL_RAD	0.01	m
Temperature of the gas at inlet	T_GAS_IN	18.5	K
Viscosity of Helium Gas	MU_F	$0.33 \times 10^{-5}$	Pa-s
Density of Helium Gas at inlet	RHO_F	1.337	$\text{kg/m}^3$
Specific Heat of the Gas	CP_F	5200	J/kg-K
Thermal Conductivity of the gas	KK	0.026	W/m-K
Number of spheres	N_SPH	50	--
Mass of particles	M_PART	$3.6 \times 10^{-6}$	kg
Radius of sphere	R	0.002	m
Volumetric heat in particle	Q_VOL	$5 \times 10^4$	$\text{W/m}^3$
# of timesteps	T_STEPS	$1 \times 10^6$	--
Time step size	DT	$1 \times 10^{-5}$	s
Coefficient of elastic contact	K_EFF	1000	
Damping in elastic contact	C_EFF	$4 \times 10^{-3}$	
Friction parameter	MU	0.4	
Gamma-coefficient	GAMMA	0.05	

Preliminary analysis showed that at low bed expansion and large unbalance, the particles do not turn over. It will be part of the combined fluidization – layering model (Chapter 4 of this work), to study the bed expansion necessary to overturn shells of different degrees of unbalance.

### **3. Modeling the Layering Process**

This chapter will elucidate the relevance of the layering process and its position in the sequence from target production to injection and engagement. A brief literature review reveals the underlying physics of the layering process in the one dimensional case. After highlighting the advantages of studying a two-dimensional case, the details of the development of a 2-D description are presented. Before using this model to predict the layer formation in shells inside a fluidized bed, several test cases have been studied in order to validate and verify the model output.

A benchmark experiment has been set up using water as a surrogate in a cuvette, providing practical results of a controlled test case.

#### **3.1 Importance of the Layering Process**

In the proposed production process, plastic or foam capsules are filled with gaseous deuterium (DD) or deuterium-tritium (DT) at room temperature, and then cooled past the triple point. When the gas is condensed inside stationary shells, the fuel will be gathered at the bottom of the shell. Spherical symmetry of the fuel layer thickness inside the target has been established as a requirement by target implosion physicists to minimize Rayleigh Taylor instabilities<sup>1-2</sup>. This uniformity in the layer thickness will be achieved by a mass redistribution process after the fuel has been frozen at the bottom of the shell. Success in presenting a feasible pathway to mass-produce IFE capsules, in which the DT is frozen uniformly on the inside of the pellet,

depends on the reliability and predictability of the layering process. After redistributing the fuel into a uniform layer, the targets need to be immediately transferred to an injection system and shot into the reaction chamber for implosion.

## **3.2 Theoretical Analysis of Redistribution Rates**

### **3.2.1. Literature Review**

As mentioned in section 1.3, the redistribution mechanism of DT fuel in an ICF capsule based on the heat released during the tritium decay has been analyzed theoretically by A.J. Martin et al.<sup>4</sup> and later by T.P. Bernat et al.<sup>51</sup> and experimentally confirmed by Hoffer and Foreman<sup>52</sup>. Starting with the general heat diffusion equation in both cases, the main points of their derivation are highlighted here and will be the starting point of the development of a 2-D layering model.

The main difference between the two authors [4] and [51] lies in the modeling of the movement of the gas inside the gaseous void. If the time between filling the capsule and layering is long enough, the buildup of helium-3 from the tritium decay during filling and layering of the capsules would result in the movement of the DT-gas through the helium-3 in the void, becoming a two-species diffusion problem. Appendix E analyzes the two theories behind the two models, compares the results from one specific DT layering case. In addition, some experimental analysis of the multi-species problem is presented in Appendix E.

The present work focuses on the heat transfer aspect of the redistribution process, not considering the mass transfer problem presented in [4] and [51]. Such a



Integrating twice leads to

$$T(x) = -\frac{\dot{q}''}{2k_{ice}}x^2 + C_1x + C_2 \quad (61a)$$

The boundary conditions that will be applied at the inner and outer surfaces are

$$\frac{dT}{dx} = -\frac{N_A\Delta H_s}{k_{ice}} \quad \text{Evaporation flux at the interface } x=h_1, \text{ and} \quad (62a)$$

$$T = T_0 \quad \text{at } x=0. \quad (62b)$$

Applying the constant temperature boundary condition at the outer surface Eq.

(62b) to the general solution of the heat equation Eq. (61) leads to:

$$C_2 = T_0, \text{ and } T(x) = T_0 - \frac{\dot{q}''}{2k_{ice}}x^2 + C_1x \quad (63)$$

The heat flux boundary condition based on the evaporative mass flux at  $x=h_1$

leads to:

$$\left. \frac{dT}{dx} \right)_{x=h_1} = -\frac{\dot{q}''}{k_{ice}}h_1 + C_1 = -\frac{N_A\Delta H_s}{k_{ice}}$$

This leads to Eq. (64) in general, and to Eq. (65a) for the conditions at the inner surface

$$T(x) = T_0 - \frac{\dot{q}''}{2k_{ice}}x^2 + \left( -\frac{N_A\Delta H_s}{k_{ice}} + \frac{\dot{q}''}{k_{ice}}h_1 \right)x \quad (64)$$

$$T_{h_1} - T_0 = -\frac{\dot{q}''}{2k_{ice}}h_1^2 - \frac{N_A\Delta H_s}{k_{ice}}h_1 + \frac{\dot{q}''}{k_{ice}}h_1^2$$

$$T_{h_1} - T_0 = -\frac{N_A\Delta H_s}{k_{ice}}h_1 + \frac{\dot{q}''}{2k_{ice}}h_1^2 \quad (65a)$$

In order to compute the temperature at the opposing surface ( $x=h_2$ ), Eq. (61b) is solved similarly, and the corresponding boundary conditions at the interfaces are applied (Eqs. (62c) and (62d)).

$$T(x^*) = -\frac{\dot{q}''}{2 \cdot k_{ice}} x^{*2} + C_3 x^* + C_4 \quad (61b)$$

$$\frac{dT}{dx^*} = \frac{N_A \Delta H_s}{k_{ice}} \quad \text{Condensation flux at the interface } x^*=h_2 \quad (62c)$$

$$T = T_0 \quad \text{at } x^*=0 \quad (62d)$$

As a result, equation (65b) can be used to find the temperature at the inner interface.

$$T_{h_2} - T_0 = \frac{N_A \Delta H_s}{k_{ice}} h_2 + \frac{\dot{q}''}{2k_{ice}} h_2^2 \quad (65b)$$

Subtracting (65b) from (65a) leads to:

$$T_{h_1} - T_{h_2} = -\frac{N_A \Delta H_s}{k_{ice}} (h_1 + h_2) + \frac{\dot{q}''}{2k_{ice}} (h_1^2 - h_2^2) \quad (66)$$

Using the following notation for the uniform layer thickness  $d$  and the nonuniformity  $\delta$ , we get:

$$\begin{aligned} (h_1 + h_2) &= 2d & (h_1 - h_2) &= 2\delta \\ T_{h_1} - T_{h_2} &= \left( -\frac{N_A \cdot \Delta H_s}{k_{ice}} \cdot 2d + \frac{\dot{q}''}{k_{ice}} 2d\delta \right) \end{aligned} \quad (67)$$

The movement of the interface  $\dot{\delta}$  can be related to the molar flux and the molar density Eq. (68), which in combination with Eq. (67) leads to Eq. (69).

$$\dot{\delta} = -\frac{N_A}{\rho_s} \quad (68)$$

$$T_{h1} - T_{h2} = \frac{2d}{k_{ice}} (\dot{\delta} \rho_s \Delta H_s + \dot{q}'' \delta) \quad (69)$$

Assuming no temperature difference between the two walls, (idealized scenario), the movement of the interface can be determined by Eq. (70)

$$\begin{aligned} (\dot{\delta} \rho_s \Delta H_s + \dot{q}'' \delta) &= 0 \\ \dot{\delta} &= -\frac{\dot{q}''}{\rho_s \Delta H_s} \delta \end{aligned} \quad (70)$$

Eq. (70) is a 1<sup>st</sup> order ODE with the solution:

$$\delta(t) = \delta(0) \exp\left(-\frac{\dot{q}''}{\rho_s \Delta H_s} t\right) \quad (71)$$

In this special case, a very small temperature difference between the two interfaces (assumed to be exactly zero for the calculations above) is the driving force for the molecules to move through the vapor space. This is a good approximation, if there is pure fuel vapor present in the gas phase. The gas molecules are assumed to flow through the vapor space instantaneously. This is a valid assumption, since the pressure of the gas close to the interface (in steady state) is very close to the vapor pressure at the surface temperature. In a small void as the one in question, large pressure differences resulting from large temperature differences would equalize in a time frame of the order of the speed of sound and the diameter of the shell (which is very small). This results in sublimation or re-sublimation mass flux at the surface until the equilibrium temperature is reached ( $T_0 = T(P_v)$ ). Both the characteristic time of the evaporation and sublimation flux at the surface and characteristic time resulting from the speed of sound in the gas in

comparison with the size of the void are very small compared to the layering times making this assumption acceptable.

However, if a nonparticipating gas species is present, the flow of vapor molecules will be slowed down. The total pressure in the gas will be constant in the entire void, but the values of the two partial pressures will be different at the surface depending on the surface temperature. The speed of redistribution for this case will depend on the conditions of the nonparticipating gas species as well. The problem becomes both a heat transfer and mass transfer problem. The mass diffusion of species A (fuel) through species B (nonparticipating gas) needs to be accounted for. This difference in partial pressure can be computed by solving both mass and heat equation simultaneously. Two different models have been applied for this case<sup>4, 51</sup>. In Appendix E both models are presented and their results are compared, in addition a simple experiment was set up to further verify their validity.

In the following analysis the influence of a non-participating gas has not been taken into account for the reasons presented in section 3.2.1. The model should then be valid, when layering pure deuterium under IR irradiation.

### **3.3 Establishing the Need for a Two Dimensional Model**

Information on the layering process found in the literature comprises only the one-dimensional case. However, there is a substantial advantage in studying the effects of the second dimension on the layering process. Since small spherical shells are being layered, the approximation of looking at two infinite thin plates in Cartesian coordinates,

as taken in the theoretical analysis<sup>4, 51-52</sup>, is expected to break down as two dimensional effects become more and more important. In addition, some of the surface-roughening phenomena observed by Sheliak<sup>18</sup> likely result from 2-D effects. These surface features have been studied in solid-liquid systems<sup>53</sup> but have yet to be analyzed in the context of the layering mechanism. While numerical descriptions of solid-liquid phase changes can easily be found in the literature<sup>53-55</sup>, a two dimensional description of a solid to gas phase transformation could not be found. The main reason for this lies in the limited application of a sublimation and re-condensation system. Furthermore, since the total volume of the system is limited to the volume of the shell, the large density changes between the gas and the solid phase make the boundary condition at the inside surface difficult to apply.

Additional reasons for studying this problem in two dimensions come from the time-dependent local heat transfer coefficient at the outer surface of the sphere imposed on the shells in a fluidized bed, as the pellets are exposed to the cooling gas stream. This temporal and local change in heat transfer coefficient as well as the influence of a preferential position of the pellet in the bed can only be studied by looking at a two dimensional case. A preferential position can be expected at low to moderate gas velocities of the fluidizing gas due to the pellets' unbalance. Since there is no easy theoretical solution for the two dimensional layering problem (as there is in 1D), the heat conduction equation Eq. (72) is solved numerically to study the influence of different outer boundary conditions on the resulting mass redistribution on the inside of the shell.

The preceding literature review and its conclusions, in combination with the experiments described by Harding<sup>5</sup> (summarized in section 1.2) and earlier by Hoffer and Foreman<sup>52</sup>, identified the physical concepts that can be applied to describe the layering process.

If the temperature and the molar density of the gas phase throughout the void are taken to be nearly uniform and a function of the inner surface temperature, solving the heat conduction equation in the solidified portion of the fuel will suffice to describe the physics of layering. Of course the proper boundary conditions need to be applied: conservation of mass in the gaseous void, combined with the appropriate boundary conditions at the inner and outer surface of the fuel.

In this work, an attempt was made to develop a two dimensional description of this problem. After implementing this model, a number of model tests have been performed showing that the conservation laws are respected. Comparisons to the one dimensional case were then studied. Before using the model to analyze the influence of the local and temporal variations of the heat transfer coefficient that result from different operating parameters of the fluidized bed, a controlled experiment was performed to provide a test case for the second dimension of the model.

### **3.4 Development of a 2-D Layering Model**

Solving the heat conduction equation in two dimensions (Eq.(72)) is in principle a straightforward task. A Gauss Red Black algorithm had been developed and tested successfully in previous work on target survival studies<sup>56</sup>. Similar to the target survival

studies, the response of the temperature field in the fuel layer to different heat flux scenarios will be studied. However, the treatment of the inner and outer boundaries will be significantly more complicated, as the comparatively long time frame studied in this case will cause the inner surface to change its shape. As a result, the entire fuel layer needs to be studied as the targets are not spherically symmetric as has been assumed in previous work.

The main obstacle in developing the two dimensional layering model is the treatment of the solid-gas boundary. Several concepts to model a moving boundary are presented in Minkowycz<sup>54</sup>, including refining a fixed grid close to the interface (Eulerian approach), moving the grid with the position of the interface (Lagrangian approach) or a combination of the two descriptions. One of the mixed Eulerian-Lagrangian models, the “Immersed-boundary Technique”, presented by Udaykumar et al.<sup>55</sup>, was chosen to describe the layering process as we are interested in the exact position of the interface and large movements of the position of the interface are expected. In this description, the heat equation is solved on a fixed grid, while the interface is treated as a sharp discontinuity that is moving through the grid and tracked by recording the coordinates of a number of markers along the interface. These markers are treated in a Lagrangian frame, while the field equations are solved on an Eulerian grid. The stencils of grid points which will be affected by the interface are adjusted accordingly. The advantage over pure Eulerian description is that the interface boundary condition is applied exactly at the location of the interface, which leads to a more accurate description of the phase boundary and its influence on the temperature field on the neighboring grid points. In contrast to the Lagrangian description, large

deformations of the interface can easily be modeled without introducing large errors when moving the grid to locations where the temperature needs to be estimated. In addition, re-computing the grid after every time step to adjust to the new location of the interface is computationally very expensive.

Udaykumar et al.<sup>53,55</sup> illustrate the advantages of this “sharp interface description” and compare the results for liquid solidification to other sources. These authors also show, that the method is globally second order accurate, since the number of grid points the stencils of which are adjusted (leaving them first order accurate) are few compared to the overall number of grid points.

It was decided to follow the outline presented in [55], while certain modifications to the model had to be implemented in order to describe the specifics of the layering process. These modifications include describing a solid-gas boundary instead of a solid-liquid boundary, the main difference of which lies in the density change in the gas-solid case, which is much larger than in the solid-liquid case. Other differences include the heat flux boundary condition applied on the outer shell surface implementing temperature-dependent coefficients, and writing the model in cylindrical coordinates in order to describe the entire sphere.

In this chapter, the main features of the moving phase front on a fixed grid are pointed out; the modifications to the boundary conditions are then described such that the layering process can be simulated.

### 3.4.1 2-D Equations and Boundary Conditions for Fixed Grids

As discussed in section 3.3, the layering process can be modeled by solving the energy transport equation (72) in the solid part of the fuel while applying the boundary conditions Eq. (73) on the inner and Eq. (74) on the outer boundary. It is worth noticing that Eq. (72) accounts for temperature-dependent thermal conductivity, since this value changes significantly for DD or DT close to the triple point, see [Souers<sup>57</sup>, and tab. 3.2]. In this sublimation and re-sublimation problem, the interface velocity is computed directly from the Stefan condition and the normal gradient of the temperature normal to the interface Eq. (73), while a known heat flux is imposed on the outer boundary. In contrast to Udaykumar et al.<sup>55</sup>, these boundary conditions must be fulfilled while simultaneously conserving the total mass in the system, which means that the sum of sublimation and re-condensation at the interface, and the accumulation of mass in the void must be balanced. A small change in solid volume will cause a significant increase in pressure in the void. This change in pressure, in turn, affects the sublimation flux at the surface. These conditions, originating from the fact that we are modeling an enclosed void containing a pure species, are subject of section 3.4.5.

The starting point of modeling the layering process in a sphere is a rectangular grid representing the volume containing the sphere. Two interfaces enclose the solid fuel domain in this volume. The outer surface describes the location of the thin plastic shell containing the fuel. This interface is fixed on the grid, only the heat flux or surface temperature applied on the surface will vary. The inner surface represents the solid-gas boundary, and it is free to move through the grid as the mass redistribution is modeled.

The location of both interfaces is described by two sets of markers along the interfaces, which record the coordinates of the interfaces in certain intervals.

Fig. 3.2 shows the geometrical details of the model; note that the entire sphere is being modeled by applying cylindrical coordinates with the axis of rotation along the centerline of the circle. In applying this equation, some assumptions are being made about the symmetry of the initial layer shape, but they seem reasonable considering the complexity of modeling a 3-D sphere and the small benefit one could get out of such a model.

$$\frac{\partial T}{\partial t} = \frac{1}{\rho_s C_{p,s}} \left( \frac{1}{r} \cdot \frac{\partial}{\partial r} \left( k_{ice} r \frac{\partial T}{\partial r} \right) + \frac{\partial}{\partial z} k_{ice} \frac{\partial T}{\partial z} + \frac{\dot{q}''}{\rho_s C_{p,s}} \right) \quad (72)$$

$$V_n = \frac{1}{\rho_s \Delta H_s} \left( k_{ice} \left( \frac{\partial T}{\partial n} \right)_s - k_{gas} \left( \frac{\partial T}{\partial n} \right)_g \right) \quad (73)$$

$$k_{ice} \frac{\partial T}{\partial n} = h(T_0 - T_\infty) \quad (74)$$

In applying cylindrical coordinates, zero gradient boundary conditions have to be imposed in the radial direction at the origin. We also impose that the interface crosses the z-axis perpendicular.

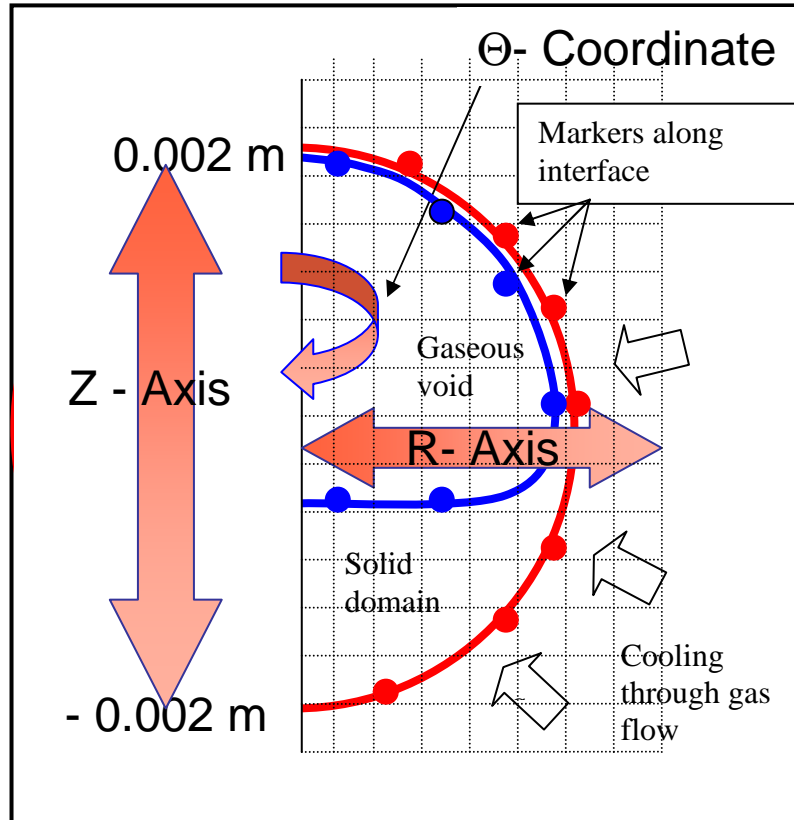


Figure 3.2: Schematic of the two dimensional layering problem. The blue markers represent the inner layer (initial condition), which will move through the grid. The red markers represent the outer (shell) boundary, which are immobile; however the cooling from the gas stream is applied here.

The temperature field of the gas around the shell is not being computed. Instead, a certain heat flux is applied on the outer surface, which is assumed to be due to the convective cooling on the outer surface, which is ultimately determined by the position and orientation of the pellet in the fluidized bed (see previous and following chapter). The temperature of the vapor inside the pellet is considered homogenous throughout the void, but it does depend on the temperature of the inner surface. Eq. (72) is only solved for grid points in the solid domain. These grid points can be divided between those whose stencils are affected by the interfaces and those whose stencils are not affected.

As a general form for grid points not affected by the interface, Eq. (72) can be discretized according to the rules of numerical differentiation using finite difference formulation for pure implicit solution of the problem, resulting in

$$\frac{T_{i,j}^{n+1} - T_{i,j}^n}{\Delta t} = \frac{1}{\rho_s C_{p,s}} \left[ \begin{aligned} & k_{i,j}^n \left( \frac{T_{i,j+1}^{n+1} + T_{i,j-1}^{n+1} - 2T_{i,j}^{n+1}}{\Delta z^2} + \frac{T_{i+1,j}^{n+1} + T_{i-1,j}^{n+1} - 2T_{i,j}^{n+1}}{\Delta r^2} \right) + \\ & \left( \frac{T_{i,j+1}^{n+1} - T_{i,j-1}^{n+1}}{2\Delta z} \right) \cdot \left( \frac{k_{i,j+1}^{n+1} - k_{i,j-1}^{n+1}}{2\Delta z} \right) + \\ & \left( \frac{T_{i+1,j}^{n+1} - T_{i-1,j}^{n+1}}{2\Delta r} \right) \cdot \left( \frac{k_{i+1,j}^{n+1} - k_{i-1,j}^{n+1}}{2\Delta r} + \frac{k_{i,j}^{n+1}}{R_i} \right) + \\ & (\dot{q}''') \end{aligned} \right] \quad (75)$$

For all the grid points, which are in close proximity to the interface, the stencils are modified to account for the presence of the phase boundary. The following section will describe how this interface is treated.

### 3.4.2 Computing the Location of the Interface

As illustrated in fig. 3.2, and described in the previous section, the inner and outer boundaries are described by recording the coordinates of a number of markers along the interfaces. This results in a mathematical description of the interface of the form  $r(s)$  and  $z(s)$ . The spacing between two markers,  $(r(s_k), z(s_k))$  and  $(r(s_{k+1}), z(s_{k+1}))$ , has to be of the order of the grid spacing, and it is the general convention that the solid lies on the right hand side, as one moves along the interface (from  $k$  to  $k+1$ ). While the inner surface of the layer will move through the grid, the outer interface will just serve to apply the appropriate boundary conditions to the solid domain. It is worth noticing that the markers of the interface do not necessarily coincide

with the grid points. If the position of the interface between two markers is needed, it is computed by interpolation.

In difference to Udaykumar et al.<sup>55</sup>, a cubic spline interpolation was implemented following Bewley<sup>58</sup> since the polynomial description for a high number of marker points are expected to give unsatisfactory results. The values of the second derivative of the cubic spline function  $f''(s_k)$  are computed and saved for each marker point for both the radial and the axial direction. The distance between two markers is taken as one to simplify the equations. As a result, the Eq. (76) gives the radial coordinate of the interface at position  $s_N$ , which lies between markers  $s_k$  and  $s_{k+1}$ , where  $r_k$  and  $r_{k+1}$  are the radial positions of the two markers k and k+1.

$$f(s_N) = r(s_N) = \left[ \begin{array}{l} \frac{f''(s_k)}{6} \left( \frac{(s_{k+1} - s_N)^3}{1} - 1 \cdot (s_{k+1} - s_N) \right) + \\ \frac{f''(s_{k+1})}{6} \left( \frac{(s_N - s_k)^3}{1} - 1 \cdot (s_N - s_k) \right) + \\ r_k \cdot \frac{(s_{k+1} - s_N)}{1} + r_{k+1} \cdot \frac{(s_N - s_k)}{1} \end{array} \right] \quad (76)$$

The derivative  $\frac{\partial r}{\partial s}$  at position SN is found directly from the values of the second

derivative:

$$f'(s_N) = \left. \frac{\partial r}{\partial s} \right|_{s_N} = \left[ \begin{array}{l} \frac{f''(s_k)}{6} (-3 \cdot (s_{k+1} - s_N)^2 + 1) + \\ \frac{f''(s_{k+1})}{6} (3 \cdot (s_N - s_k)^2 - 1) + \\ -r_k + r_{k+1} \end{array} \right] \quad (77)$$

The axial direction is handled analogously.

Now that we can describe the location of the interface in space, we need to relate the position of the interface to the grid.

After identifying all grid points close to the interface, it needs to be determined if each of those grid points  $(r_i, z_j)$  lie in the solid or the gaseous domain (see fig. 3.3). For each grid point we thus need to find the line that passes through  $(r_i, z_j)$  and is perpendicular to the surface. This line has the form  $z = a \cdot r + b$ , the slope  $a$  can be found from Eq. (78). The intersection of the surface normal with the interface is labeled  $s_{SN}$ . Both the slope and the point of intersection have to be determined as has been demonstrated in [55], by solving Eq. (78) using Eq. (77). In difference to [55], when implementing a cubic spline interpolation, these equations can not be solved directly for  $s_{SN}$ . Instead, a pair of consecutive markers bracketing  $s_{SN}$  has to be found by looping Eq. (79) over all markers until a pair (k and k+1) is found, for which the product of  $C_1$  and  $C_2$  is negative. If more than one pair can be found, the one closest two markers to the grid point will be chosen. Then Eq. (79) is used in a bisection method to determine the exact location of the intersection ( $s_{SN}$ ), the markers k and k+1 are taken as the initial bracket, which is being refined to zoom in on the exact location of the intersection.

$$a = -\frac{1}{\left(\frac{dz}{dr}\right)_{SN}} = -\frac{\left(\frac{dr}{ds}\right)_{SN}}{\left(\frac{dz}{ds}\right)_{SN}} = \frac{z_{SN} - z_j}{r_{SN} - r_i} \quad (78)$$

$$\left. \begin{aligned} \left. \left. \left. \frac{dr}{ds} \right)_k \cdot (r_k - r_i) + \frac{dz}{ds} \right)_k \cdot (z_k - z_j) = C_1 \right\} \\ \left. \left. \left. \frac{dr}{ds} \right)_{k+1} \cdot (r_{k+1} - r_i) + \frac{dz}{ds} \right)_{k+1} \cdot (z_{k+1} - z_j) = C_2 \right\} \end{aligned} \right\} \quad (79)$$

Once the intersection of the surface normal and the interface ( $s_{SN}$ ) is found, the scalar product of the vector  $\lambda$  (Eq. (80)) and the surface normal  $\mathbf{n}$  (Eq. (81)) will determine which side of the interface the grid point lies on. Based on the sign convention described above, the point lies outside the solid domain, if that scalar product is positive, and inside, if the scales product is negative. The radial and axial components of  $\vec{\lambda}$  are given by:

$$\lambda_r = \frac{r_{SN} - r_i}{\sqrt{(r_{SN} - r_i)^2 + (z_{SN} - z_j)^2}} \quad \lambda_z = \frac{z_{SN} - z_i}{\sqrt{(r_{SN} - r_i)^2 + (z_{SN} - z_j)^2}} \quad (80)$$

The radial and axial component of the surface normal can be computed by

$$n_r = \frac{-\frac{\partial z}{\partial s}}{\sqrt{\left(\frac{\partial z}{\partial s}\right)^2 + \left(\frac{\partial r}{\partial s}\right)^2}} \quad n_z = \frac{\frac{\partial r}{\partial s}}{\sqrt{\left(\frac{\partial z}{\partial s}\right)^2 + \left(\frac{\partial r}{\partial s}\right)^2}} \quad (81)$$

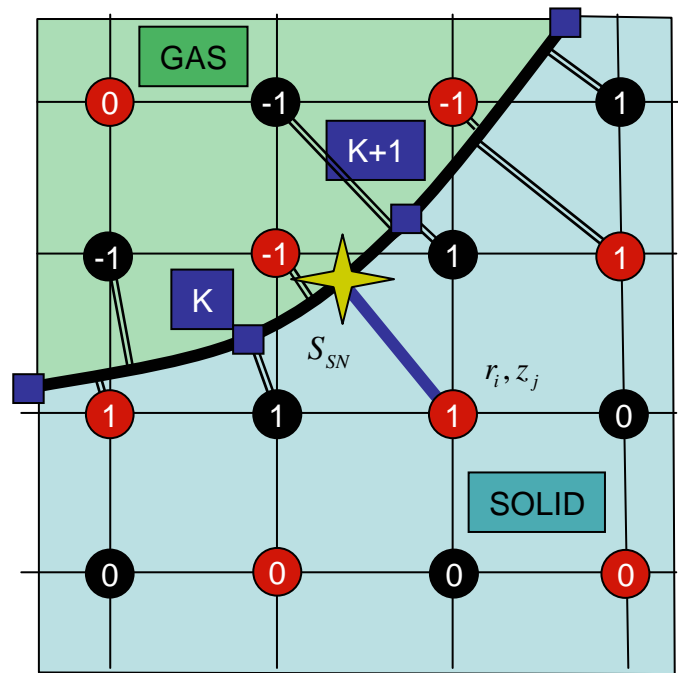


Figure 3.3: Schematic illustrating how the surface normal through each grid point is found to determine whether a grid point lies in the solid or the gaseous domain.

Recording either +1 or -1 depending on the sign of  $\lambda \cdot \mathbf{n}$  for each grid point results in a -1/+1 map of the grid points crowding the interface (see fig. 3.3). As a next step, “true neighbor cells” need to be identified. These are grid points which are separated from at least one direct neighbor by the phase boundary. This procedure is similar to the one presented by Udaykumar et al.<sup>55</sup> and we end up assigning a value of

+1 to all grid points inside the solid domain, while values for the gaseous domain are set back to zero. In contrast to [55] the present work assigns a value of 2 to all true border cells (see fig. 3.4). This way, the distinction between neighbor cells and the rest of the domain will be easier for the 2-D solver.

Overall, the coordinates of  $N$  markers are stored in a two by  $N$  array, the cubic spline coefficients fill an additional two by  $N$  matrix, while the position of the interface on the grid (with  $GR$  grid points in radial direction and  $GZ$  in axial direction) is represented by a  $GR$  by  $GZ$  array, which is referred to as the “interface matrix”, that only carries the values zero, one and two. This is a very economic description of the problem.

### 3.4.3 Adjustment of the Stencils to the Presence of the Interface

When solving the transport equation, Eq. (72), the discretization shown in Eq. (75) is used in a Gauss Red Black (GRB) algorithm<sup>58</sup> to determine the temperature field on every grid point in the solid domain that is not directly affected by the interface (i.e. those with a value of 1 on the interface matrix). The Gauss Red Black algorithm is an iterative scheme, in which the grid points are divided into a checkerboard pattern, as illustrated in fig. 3.4. The temperatures of all grid points of one color (red) are updated solely based on the values of grid points of the other color (black) (see Eq. (75)). After that, the temperatures of the black points are computed based on the updated values of the red points. This method converges fairly quickly, since the values of all the points of one color only depend on the values of the points of the other color (except for the boundary conditions).

All the points with a zero in the interface matrix (gaseous domain and cooling gas) do not need to be solved for (for reasons discussed earlier), leaving us with the true border cells (value 2 in the interface matrix).

In contrast to the unaffected grid points (value of 1 in the interface matrix), the discretization of Eq. (72) for the “true neighbor” grid points will be different from Eq. (75) to accommodate the presence of the interface. The computation of the temperatures of the true neighbor grid points, by applying a modified stencil, is performed after each GRB-iteration.

The modification of the stencils for the true-neighbor grid points is described next.

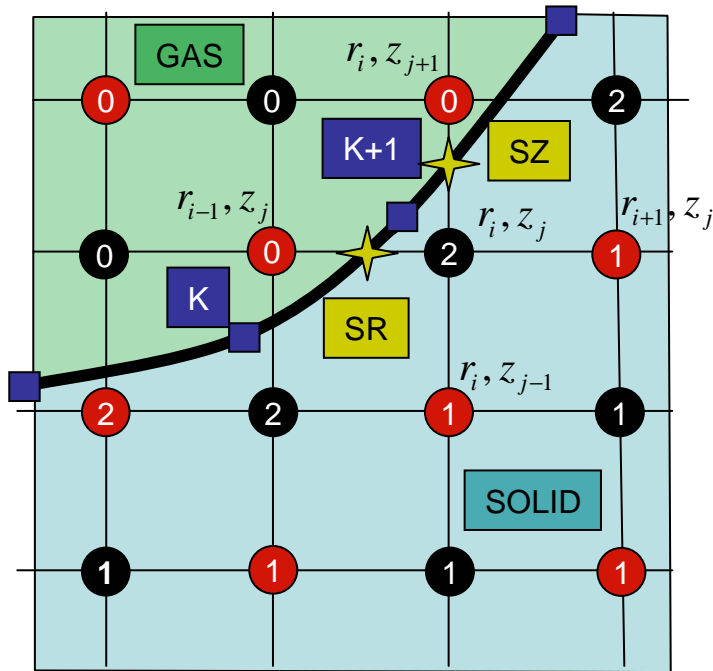


Figure 3.4: Schematic illustrating a segment of the interface, the markers of which are represented by the blue squares. The distinction between the red and black points for the GRB algorithm is depicted along with the classification of the true neighbor points (2) and the regular solid domain (1).

The stencils marked by a ‘2’ in fig. 3.4 will need to be adjusted due to the presence of the interface. Grid point  $(r_i, z_j)$  is chosen as an example to describe the

modifications to the stencil in the r and in the z- direction, since two of its neighbors  $(r_{i-1}, z_j)$  and  $(r_i, z_{j+1})$  lie in the gaseous domain.

When trying to apply the z-component of Eq. (72) to  $(r_i, z_j)$ , it becomes obvious, that, since the point at  $(r_i, z_{j+1})$  lies in the gaseous domain, we need to replace that point by  $(r_i, z_{SZ})$ , the intersection of the grid line with the interface, and the temperature  $T_{i,j+1}$  by  $T_{SZ}$ , the temperature of the interface at the intersection with the grid line. The discretization then follows

$$k \frac{\partial^2 T}{\partial z^2} + \frac{\partial T}{\partial z} \cdot \frac{\partial k}{\partial z} = \left[ \begin{array}{l} 2 \cdot k(T_{i,j}) \cdot \left( \frac{T_{SZ} - T_{i,j}}{z_{SZ} - z_j} - \frac{T_{i,j} - T_{i,j-1}}{z_j - z_{j-1}} \right) + \\ \left( \frac{T_{SZ} - T_{i,j-1}}{z_{SZ} - z_{j-1}} \right) \cdot \left( \frac{k(T_{SZ}) - k(T_{i,j-1})}{z_{SZ} - z_{j-1}} \right) \end{array} \right] \quad (82)$$

The in the r-direction, the discretization looks similar, substituting  $(r_{SR}, z_j)$  for  $(r_{i-1}, z_j)$  and  $T_{SR}$  for  $T_{i-1,j}$  when setting up the stencil:

$$k \frac{\partial^2 T}{\partial r^2} + \frac{\partial T}{\partial r} \cdot \frac{\partial k}{\partial r} = \left[ \begin{array}{l} 2 \cdot k(T_{i,j}) \cdot \left( \frac{T_{i+1,j} - T_{i,j}}{r_{i+1} - r_i} - \frac{T_{i,j} - T_{SR}}{r_i - r_{SR}} \right) + \\ \left( \frac{T_{i+1,j} - T_{SR}}{r_{i+1} - r_{SR}} \right) \cdot \left( \frac{k(T_{i+1,j}) - k(T_{SR})}{r_{i+1} - r_{SR}} + \frac{k(T_{i,j})}{r_i} \right) \end{array} \right] \quad (83)$$

Thus, instead of using the temperature of the neighboring grid point to solve Eq. (72) at the present point, the temperature of the interface at the intersection with the grid line is used.

In order to find the position SR and SZ (in coordinates along the interface) at which the interface intersects the grid lines in the radial and axial direction, respectively,

we need to solve the third order polynomial resulting from substituting  $r_i$  or  $z_j$  on the right hand side of Eq. (76) and solving for the 'SN'. For example, we find SZ, the coordinate along the interface between  $k$  and  $k+1$ , at which the  $r$ -coordinate is equal to  $r_i$  through Eq. (84). Since we can compute the coefficients of the polynomial exactly, we can efficiently solve this problem using Newton Raphson method<sup>58</sup>. Similar to the method described above, Eq. (79) is applied to find a bracketing pair of markers  $k$  and  $k+1$ .

$$r_i = \left[ \begin{array}{l} \frac{f''(s_k)}{6} ((s_{k+1} - SZ)^3 - (s_{k+1} - SZ)) + \\ \frac{f''(s_{k+1})}{6} ((SZ - s_k)^3 - (SZ - s_k)) + \\ r_k \cdot (s_{k+1} - SZ) + r_{k+1} \cdot (SZ - s_k) \end{array} \right] \quad (84)$$

Once SR or SZ is found, we can apply Eq. (76) to compute the values  $r_{SR}$  and  $z_{SZ}$ , and we can set up the stencils in Eqs. (82) and (83).

In summary, Eq. (72) can be solved for a true neighbor grid point  $(r_i, z_j)$  by applying Eqs. (82) and (83). In the case the interface separates the point  $(r_i, z_j)$  in the solid domain from  $(r_i, z_{j-1})$ , in the gaseous domain (in the negative direction), Eq. (82) needs small adjustments, but the underlying discretization would be the same. A similar argument holds true for Eq. (83) and the interface passing between point  $(r_i, z_j)$  (solid) and  $(r_{i-1}, z_j)$  (gas).

In the case where the phase boundary crosses a grid line more than once in the neighborhood of one grid point, attention has to be paid to finding the intersection that

lies in the corresponding direction along the grid line. For instance, if two intersections in the positive and negative  $r$ -direction need to be found, the stencil needs to be modified twice, once in either direction. These grid points are identified by having a value of 2 on the interface matrix and a value of 0 for either neighbor. In this case, both intersections need to be found for proper adjustment of the stencil.

One of the computational issues of this method mentioned by Udaykumar et al.<sup>55</sup> is the assignment of properties to newly emerged grid point. Problems could arise from the sudden change in properties on the grid point as a phase change happens in this point. However, this is only a problem if the transport equation is solved on both sides of the interface. In the case of a gas-solid phase change problem, the abrupt change in properties during phase transitions is accounted for by the special treatment of the solid-gas interface. The newly emerged point is assigned the temperature of the gas phase at the previous time step. This represents a small approximation, as discussed earlier, but large temperature differences between the gas and the interface are not expected. To find the temperature of the newly emerged point by interpolating between temperatures of the closest interface marker points would yield a similar result. This approximation would worsen, if large jumps of the interface would result into a new point emerging deep in the solid domain. In that case, a bilinear interpolation function including the neighboring grid points and interface markers as presented in [55] would become necessary.

Since the transport equation is only solved on the solid side a sudden change in properties is not observed, however special care need to be applied when dealing with the density change as is presented in section 3.4.5.

#### **3.4.4. Implementation of the Outer Interface Boundary Condition**

In order to complete the description of the layering problem, the appropriate boundary conditions need to be implemented at both the inner and the outer interfaces. In the present study, the result of different heat transfer boundary conditions on the outer surface of the pellet will be studied. When applying a local heat transfer coefficient on the outer surface, the outer temperature will also vary. As a first step, a cubic spline interpolation function was implemented to determine the temperature of the interface between marker points.

When using Eqs. (82) and (83) to compute the temperatures of the “true neighbor” grid points, the temperature on the interface is required. However, the temperature along the interface depends on the temperature field of the solid domain AND the heat flux boundary condition on the outer surface. As a result both the temperature field and the heat flux boundary condition have to be computed simultaneously and can be taken to desired levels of convergence by iterating between first computing the temperature field in the solid domain based on the previous temperatures at the interface markers, and second, update the temperatures at the interface markers based on the temperature field. In this work, the temperature at the interface and in the solid domain are obtained iteratively by coupling the computation of the interface temperature into the GRB algorithm.

When computing the temperature gradient normal to the interface at each interface marker, a forward differencing formula is applied using two points along the

surface normal. First, the location of two points at a certain distance from the surface is computed. Second, the temperature at these points is determined through bilinear interpolation of the neighboring grid points. The distance between the two points along the surface normal is chosen to be of the order of the grid spacing, as illustrated in fig. 3.5.

The temperature of the interface marker is then found by applying

$$q = k \frac{\delta T}{\delta n} = k \cdot \left( \frac{4 \cdot T_{N1} - T_{N2} - 3 \cdot T_0}{2 \Delta n} \right) \quad (85a)$$

$$q = h(T_0 - T_\infty) \quad (85b)$$

where  $T_\infty$  is the gas temperature of the cooling gas around the sphere, and  $h$  is the local heat transfer coefficient. The interface temperature can be computed directly by applying:

$$T_0 = T_\infty + \frac{1}{\frac{h}{k} + \frac{3}{2 \cdot \Delta n}} \cdot \left( \frac{4 \cdot T_{N1} - T_{N2}}{2 \Delta n} \right) \quad (86)$$

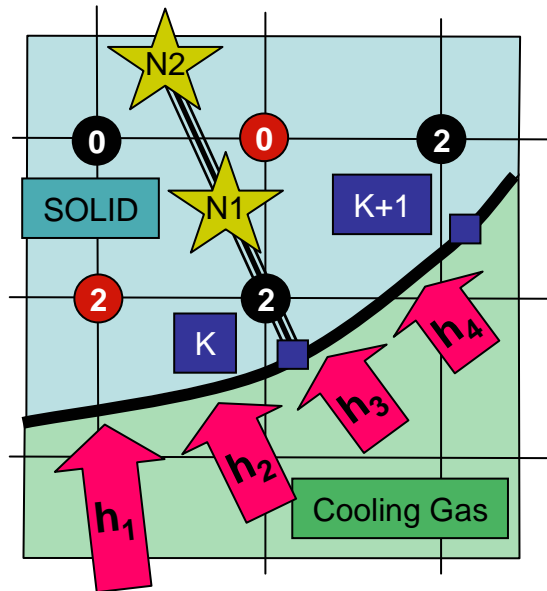


Figure 3.5: Schematic illustrating the temperature distribution computed along the surface normal in order to relate the heat flux from the cooling gas outside the shell to the surface temperature of the shell.

### 3.4.5. The Gas-Solid Boundary Condition at the Inner Surface

The inner boundary poses some complex difficulties, which originate from the geometry of the problem and the nature of the solid-gas phase change we are trying to model. In difference to solidification/melting problem, as modeled by Udaykumar et

al.<sup>53, 55</sup>, the sublimation-condensation problem at hand is accompanied with a large change in density between the two phases. This, in combination with the fact that the gaseous phase is enclosed in a cavity poses a challenging problem: the mass flux at the interface, coupled to the temperature field defined by the Stefan Condition Eq. (73) on the solid side, has to be matched to the condensation and sublimation flux defined by Eq. (87), as described by Collier<sup>59</sup>, on the gas side, and to the physical law of mass conservation. It is the last part, the mass conservation equation, which makes this problem difficult, as it demands, that a net sublimation flux along the entire interface would lead to a pressure increase in the gaseous void (and a net condensation flux would lead to a net decrease in pressure).

$$q = \frac{\Delta H_s}{\sqrt{2\pi M_A R_{gas}}} \left( \frac{P_g}{\sqrt{T_g}} - \frac{P_v(T_h)}{\sqrt{T_h}} \right) \quad (87)$$

Due to the high density difference and the small size of the void, a excess sublimation or condensation of fuel leads to large changes in pressure, which in turn leads to a large change in the sublimation/condensation flux Eq. (87).

This means, Eq. (87) and Eq. (85a) have to be matched for the heat flux across the interface, and this heat flux has to satisfy Eq. (73) (Stefan Condition for the movement of the interface; this movement of the interface has to result in a pressure change, such that Eq. (87) is still satisfied.

As with the outer boundary, this problem is solved iteratively between the GRB-iterations of the main transport equation.

Although the pressure and temperature in the void are subject to changes, it becomes obvious by studying Eq. (87), that the pressure in the void and the vapor pressure at the interface temperature have to be very close to each other.

The following sequence has been implemented in order to satisfy all of the above conditions:

After each GRB-iteration, the temperature at the boundary is found based on the temperature field of the solid domain Eq. (82) and (83). Based on this temperature field, the heat flux at the surface is found Eq. (85). The same forward difference formula in combination with bilinear interpolation as described in the previous section and illustrated in fig. 3.5 has been implemented for this purpose. Then, the velocity of the interface is computed by Eq. (88), noting that the temperature gradient in the gas is assumed to be very small. After that, the net mass flux based on this heat flux is found by applying Eq. (89).

$$V_n = \frac{1}{\rho_s \Delta H_s} \left( k_s \left( \frac{\partial T}{\partial n} \right)_s \right) \quad \text{as} \quad k_g \left( \frac{\partial T}{\partial n} \right)_g \approx 0 \quad (88)$$

$$\dot{m}_{void}^{gas} = V_n \cdot \rho_s \cdot A \quad (89)$$

where  $A$  is the area of the surface over which the phase change occurs. This is found for each marker point  $k$  by computing the length of the interface between  $(k-0.5)$  and  $(k+0.5)$ . This length is then multiplied with the arc length  $(2\pi r_k)$  to get the area.

Knowing the total volume of the void, the change in pressure resulting from the change in mass in the void can now be computed. Ideally, one would use this value in the next iteration (specifically as  $P_g$  in Eq. (87)), however this problem proves to be a

very stiff set of nonlinear differential equation leaving this approach highly unstable. Instead, the pressure is changed after each GRB-iteration, raised by a small value, if the computed change in pressure is positive, and decreased by a small value, if the change is negative. Once the change in pressure switches signs from positive to negative or vice versa, the interval by which the pressure is changed is decreased zooming in to the real value of the pressure. This method, though crude, worked reliably in the simulations. However, it depends on a good initial guess of the temperature and pressure at the interface (within a few degrees K) or a very small time step for the first few seconds of the simulation. In addition this boundary condition imposes a very strong time step restriction on the method. If the time steps are chosen too large, the resulting movement of the interface is too large causing strongly oscillating values for the pressure as the interface temperature is adjusted.

In the end, the pressure in the capsule is found that satisfies both the mass flux boundary condition Eq. (87) and the rise in pressure due to mass accumulation/loss. Simultaneously, the temperature field corresponding to this mass flux is determined.

#### **3.4.6. Moving the Interface and Computing Mechanical Properties**

After each time step, the interface markers are moved according to Eq. (73). The change in total volume is recorded Eq. (90) as it will influence the absolute pressure for the next time step.

$$\Delta V = V_n \cdot \Delta t \cdot A \quad (90)$$

As a last step to close this system of equations, the total volume of the gaseous void needs to be initialized. The change in volume can be computed from the movement of the interface, but the total volume needs to be computed at the beginning of the simulation, as it quantifies the raise in pressure due to a change in the number of moles in the void. The difficulty of computing the volume depends on the initial conditions (IC) to be implemented. If the void is initialized as a shape of known volume (i.e. a sphere or a rectangle) this volume can be used to initialize the total volume. In order to keep the initial conditions (IC) arbitrary (see next section for the IC's used in this model), the volume calculation becomes somewhat complex.

In this model, since the cells covering the solid and the gaseous domain have already been sorted and the true neighbor cells determined, we can use this information to compute the volume of the void, and with that the mass moment of inertia and the overall center of gravity. The information from the interface matrix, along with the cubic spline interpolation coefficients, will be used to compute the area of the gaseous fraction and the coordinates of the center of gravity for each cell. Depending on the position of the interface with respect to the grid, fourteen different shapes have been identified. The approximation implied here is that the interface crosses through the grid point as a straight line. Fig. 3.6 depicts all fourteen different possibilities, each of which calls for a slightly different treatment.

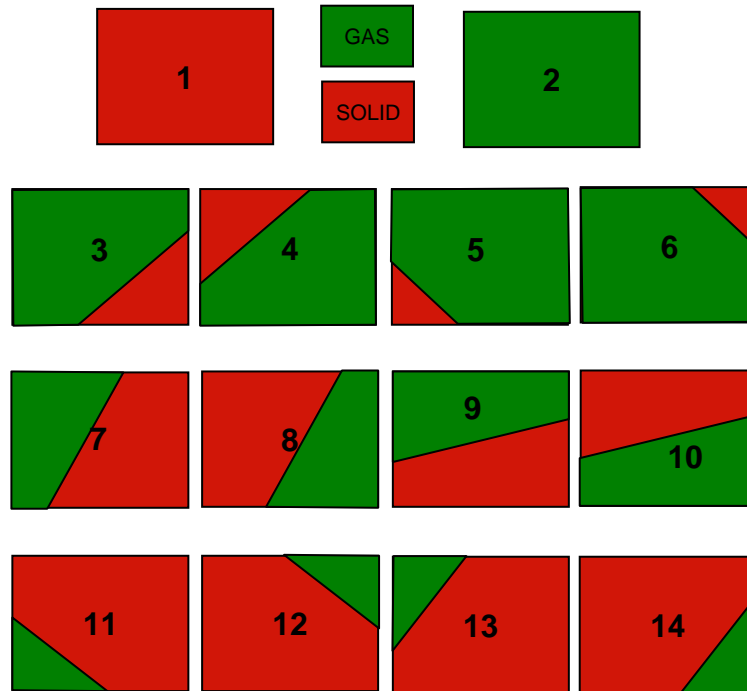


Figure 3.6: Approximating the area in the solid phase with simple geometric forms (triangle, trapezoids, rectangles, and combinations of rectangles and trapezoids) to calculate the fraction of gas volume in a cell with solid and gaseous domains.

The two cases in the first row are trivial, as they represent the case of (1) the cell lies completely in the solid domain, and (2) the cell lies completely in the gaseous domain. In the four cases in the second row (3 through 6), the gaseous phase is approximated to have a triangular shape; in the cases in the third row (7 through 10) trapezoids have been assumed, while for the last row (11 through 14), a combination of rectangle and trapezoid is used to find the approximate area and center of gravity. The coordinates of the intersections with the grid lines are computed the same way as described in Eq. (84).

Now that the center of gravity of the gaseous part of each cell and the respective area are found, we can determine the volume,  $V_{i,j}$ , that this area represents once the symmetry along the centerline of the cylinder is applied:

$$V_{i,j} = 2 \cdot A_{i,j} \cdot \pi \cdot r_{i, cg} \cdot z_{j, cg} \quad (91)$$

where  $r_{i, cg}$  is the radial coordinate of the center of gravity of the gaseous portion at grid point  $(r_i, z_j)$ , and  $A_{i,j}$  is the respective area.

The overall center of gravity of the fuel layer in axial direction,  $Z_{cg}$ , assuming the gas does not contribute to the overall weight, (which is a good approximation considering the large difference in density):

$$Z_{cg} = \frac{\sum_{i,j} (V_{i,j} \cdot z_{j, cg})}{V_{Outer\ Sphere} - V_{total\ void}} \quad (92)$$

where  $z_{j, cg}$  is the axial coordinate of the center of gravity of the gaseous fraction at grid point  $(r_i, z_j)$ ,  $V_{Outer\ Sphere}$  is the total volume of the sphere that is being layered, and  $V_{total\ void}$  is the total volume of the void (determined by summing Eq. (91) over all grid points in the gaseous domain.

Since we would like to feed all mechanical properties of the unbalanced sphere into the fluidized bed model, the mass moment of inertia is computed at this point as well. Two different values for the three different mass moments of inertia of an unbalanced sphere can be found, applying the body fixed, Cartesian coordinate system described in the fluidized bed model. Assuming that the unbalance is in positive x-direction (corresponding to the negative axial direction in the layering model), we can

compute  $I_{xx}$  by Eq. (93), subtracting the moment of inertia of the void from the moment of inertia of the solid sphere. The other two moments ( $I_{zz}$  and  $I_{yy}$ ) are computed by first, determining the moments for the void around the  $x=0$  axis (Eq. (94a)), applying the equation corresponding to the moment of inertia of a ring to each individual area (volume) segment and parallel axis theorem. Second, the moment of the void needs to be subtracted from the moment of the solid sphere and simultaneously the parallel axis theorem needs to be applied (again) to account for the shift in center of gravity away from the center of the sphere Eq. (94b) (see fig. 3.7 for nomenclature). Here, we assume that the geometrical center of the sphere is located at  $z = 0$  in the coordinate system of the layering model, and at the origin in the body fixed Cartesian coordinate system of the sphere when applied in the fluidized bed model.

$$I_{xx} = \frac{8}{15} \rho_s \pi R^5 - \sum_{i,j} \left( V_{i,j} \cdot \rho_{i,j} \cdot r_{i,cg}^2 \right) \quad (93)$$

$$I_{yy,void} = I_{zz,void} = \sum_{i,j} \left( V_{i,j} \cdot \rho_{i,j} \cdot \left( z_{j,cg}^2 + \frac{1}{2} r_{i,cg}^2 \right) \right) \quad (94a)$$

$$I_{yy,zz} = \frac{4}{3} \rho_s \pi R^3 \cdot \left( \frac{2}{5} R^2 + \Delta X^2 \right) - I_{yy/zz,void} - \left( \sum_{i,j} V_{i,j} \rho \right) \cdot \left( 2 \cdot \Delta X \cdot CG_{void} + \Delta X^2 \right) \quad (94b)$$

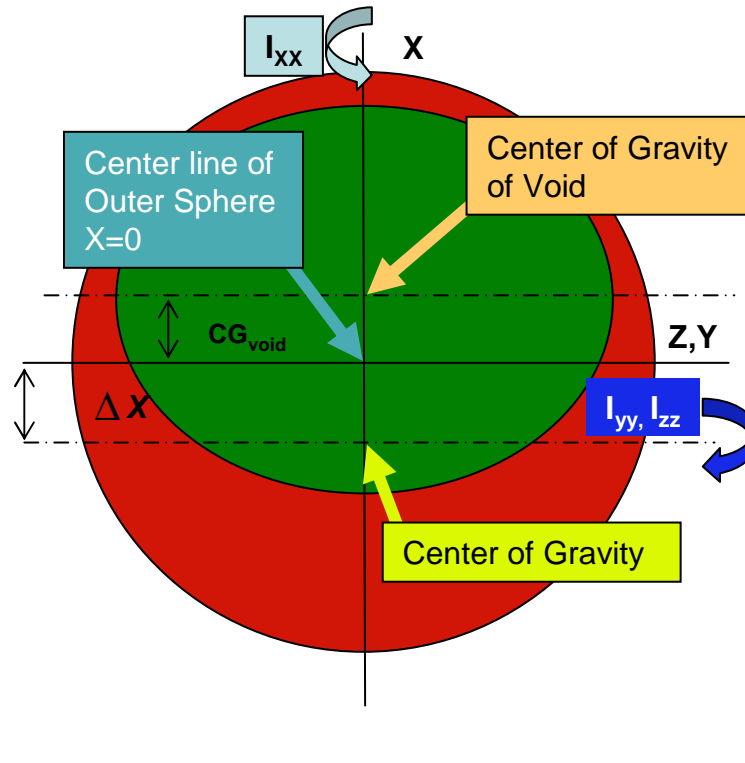


Figure 3.7: Schematic illustrating the computation of the mass moments of inertia for an un-layered sphere. The x-moment is computed around the x-axis (passing through the origin), while the y and z moments are computed around the axes parallel to y and z, but passing through the center of gravity.

### 3.4.7. Initial Conditions

In general any shape of interface can be imposed as an initial condition to the layering problem. As an input, the model requires the coordinates of a certain number of marker points. Two different initial conditions have been implemented for preliminary testing, as depicted in fig. 3.8. The spherical shape is chosen to reproduce redistribution speeds similar to the 1-D case, while the frozen puddle represents more closely the initial conditions after freezing the fuel to the bottom of the shells. Results are discussed in section 3.5. It was reported by Harding<sup>60</sup> that the liquid deuterium or deuterium-tritium mixture will wet the entire inside surface of the shell due to its zero degree

wetting angle. After freezing the resulting initial layer is expected to look similar to the ones represented in fig. 3.8; however, the initial conditions presented here are just suggestions, and can certainly be changed.

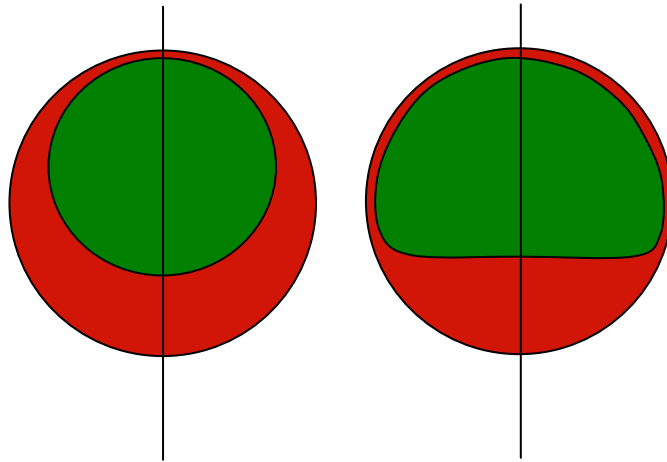


Figure 3.8: Two different initial conditions implemented in the model for preliminary testing. Both assume the presence of a thin film, covering the inside of the plastic shell completely. This approximation can be justified by the zero degree wetting angle reported by Harding<sup>60</sup> in his single sphere layering studies.

### 3.4.8 Concluding remarks about the model

The above described model is believed to be suitable to simulate the layering process under the described assumptions. However, before showing tests case results we wish to say a few words about the model in general:

First, as the interface markers move through the grid more or less independently of each other, the entire interface might change its length, and the distance between two

neighboring markers in comparison to the grid spacing might slide outside of the envelope for which the algorithm is proven to converge (distance between two markers needs to fall between 0.5 and 2.5 times the grid spacing). If these changes are large, periodic reorganization of the interface becomes necessary. This includes adjusting the number of grid points and the space between them (see Udaykumar et al.<sup>55</sup>).

Second, as the movement of the interface through the grid is modeled, we need to have an interface present before the layering begins. This is done by assuming that a layer of finite thickness is present before the layering is initiated. The thickness of this initial layer depends on the grid spacing. Otherwise the freezing and crystal growth would have to be modeled first, which is outside the scope of this study. The zero degree wetting angle of deuterium and deuterium tritium reported in the literature<sup>60</sup> allows the assumption of a thin initial layer.

Third, some problems might arise from tracking the interface explicitly. Using a pure implicit solver for the temperature field mitigates the problem of the explicit interface tracking; alternatively, when moving the interface from one time step to another, the speed of the interface of the present and the previous time step could be combined to stabilize the problem (but it was not necessary in this analysis).

Fourth, in phase change problems the solid-gas interface rarely maintains a planar state as material is deposited or evaporated from the interface. Small perturbations of the surface smoothness tend to grow into bigger disturbances<sup>53, 55, 18</sup>. These disturbances seem to grow at first, but smoothen out again, once the layer is close to equilibrium due to the bulk heating. These disturbances can be explained by the temperature gradient along a surface normal that is only locally normal to the surface,

but not globally due to the initial slight deviation from the planar state. This is not an error or instability of the model, but the result of a physical instability. Ref. [53] shows that local disturbances to the shape of the interface push the isotherms closer together, leading to an increase of the local heat flux. These instabilities lead to the development of inner surface roughness features during the initial layering phase. These features will disappear as the layering process continues. Similar roughening has been observed and reported in freezing and layering experiments at the Los Alamos National Laboratories<sup>18</sup>. In order to avoid numerical difficulties resulting in the development of long fingerlike features in the layering process, the maximum allowable curvature of the interface was limited, following the arguments presented in Udaykumar et al.<sup>53</sup>.

### **3.5 Model Validation**

The first tests after developing the model consisted of convergence for decreasing time steps and grid spacing. Then, a number of simple test were performed to ensure that the basic principles of mass and energy conservation have been followed. After that, we compared the model results to the 1-D case that can be solved analytically. As a final step in the model validation, a mass redistribution experiment was performed providing a test case under controlled conditions.

#### **3.5.1 Convergence for Decreasing Time Step**

As has been discussed in section 3.4.5, the inner boundary condition treating both the phase change and the change in pressure originated from a net flux of gas to or from the void (Eqs. (87) through (90)), imposed a strong time step restriction on the model. Time steps larger than 3.0 s resulted in numerical instabilities when applying the boundary conditions described in section 3.4.5. Thus maximum time step allowed by the solid-gas phase-change boundary condition is significantly smaller than the stability criterion of the thermal model (by almost one order of magnitude). Once a sufficiently small time step size is chosen for the inner boundary to be stable, the resulting plots are indistinguishable for further decreasing time steps.

### 3.5.2 Balance of Mass and Energy

Before applying this model to the test cases for validation and verification or to model the problem of interest, it needed to be assured that the principles of energy and mass conservation are respected.

Because of the strong coupling of net mass flux into the void (from a net evaporative and condensing flux) and the change in pressure, an inaccurate account of the total mass would substantially affect the outcome of the simulation. Small changes of the solid volume lead to large changes in pressure in the void due to the large difference in density and the small size of the void.

It is crucial for the accuracy of the prediction that the sum of all moles in the solid and the gas phase is as close to constant as possible and depends only on the initial condition.

As a first test the inner boundary was initialized to a certain shape. Then the simulation is started using the parameters given in tab. 3.1. The total numbers of moles in the solid and the gas phase were added after each time step and compared to the initial number of moles.

The error in mass was found to be less than four orders of magnitude lower than the total number of moles in the system. These small changes in mass can be attributed to the approximation that the gas temperature is equal to the temperature of the inner surface. The magnitude of this change in temperature depends on the difference in temperature chosen as an initial condition and computed as a final inner surface temperature. The biggest effect of this change in temperature is observed at the beginning of the simulation, changing the number of moles in the system slightly.

Table 3.1: Input parameters for conservation of mass and energy tests. In order to simplify the theoretical computations, a constant heat flux has been applied on the outer surface of the shell.

Parameter	Value	Unit
Heat transfer coefficient	77.8	W/m <sup>2</sup> -K
Outer Radius	0.002	m
Temperature cooling gas	18.9	K
Initial target temperature	19.50	K
Volumetric Heat	200 000	W/m <sup>3</sup>
Latent heat of sublimation	78.471x10 <sup>6</sup>	J/m <sup>3</sup>
Equilibration time	3000	s
Volume of the void	1.71415x10 <sup>-8</sup>	m <sup>3</sup>
Initial offset	0.000140	m
Theoretical temperature difference between the cooling gas and the target surface (assuming spherical geometry)	$\frac{(R^3 - R_{inner}^3) \dot{q}''}{3Rh}$	K

The model does not accommodate the change in solid volume for cases where the curvature of the interface becomes so large, that the surface normal intersects the interface twice within the length of two times the grid spacing. In these cases, the interface needs to be moved to avoid discontinuities, which leads to a variation in total mass in the system of the order of 0.05% of the total mass in the system. In cases, in which the positions of the first and last marker points of the interface need to be moved in order to satisfy the boundary conditions, the total number of moles in the system is also affected, but to a smaller degree (0.01% of the total mass in the system). The model recovers fast from these disturbances to stay below the acceptable limit of  $1 \times 10^{-4}$  of the total mass (see fig. 3.9).

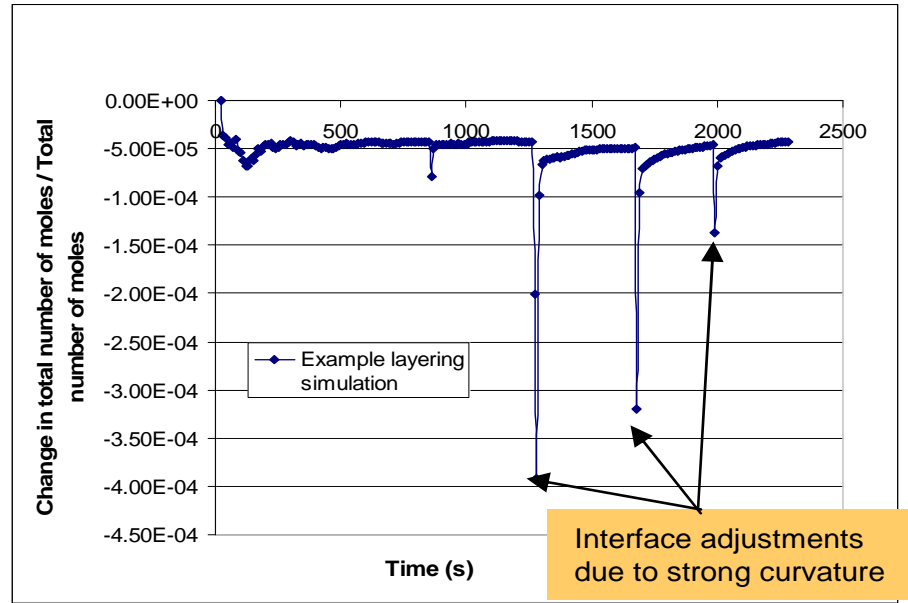


Figure 3.9: Ratio of change in number of moles in the system as a function of time. After equilibrating the temperature of the inner surface in the first few time steps, the mass in the system is conserved. At times, in which the position of individual markers needed adjustment, comparatively large jumps in the total number of moles are observed.

As a second test, the shape of the final layer (in thermal equilibrium) is compared between two cases with different initial conditions. These two cases were chosen such that the total amount of mass in the shells for the two cases was equal. The final outcome of the layer formation should not depend on its initial condition but only on the time it takes to develop the equilibrium position, as can be seen in fig. 3.10. Since a constant heat flux of a given value is imposed on the outer surface in both cases, the equilibrium temperature field and the final location of the inner boundary can be expected to be the same. In addition, the equilibrium layer thickness can be expected to be uniform, as shown in fig. 3.10.

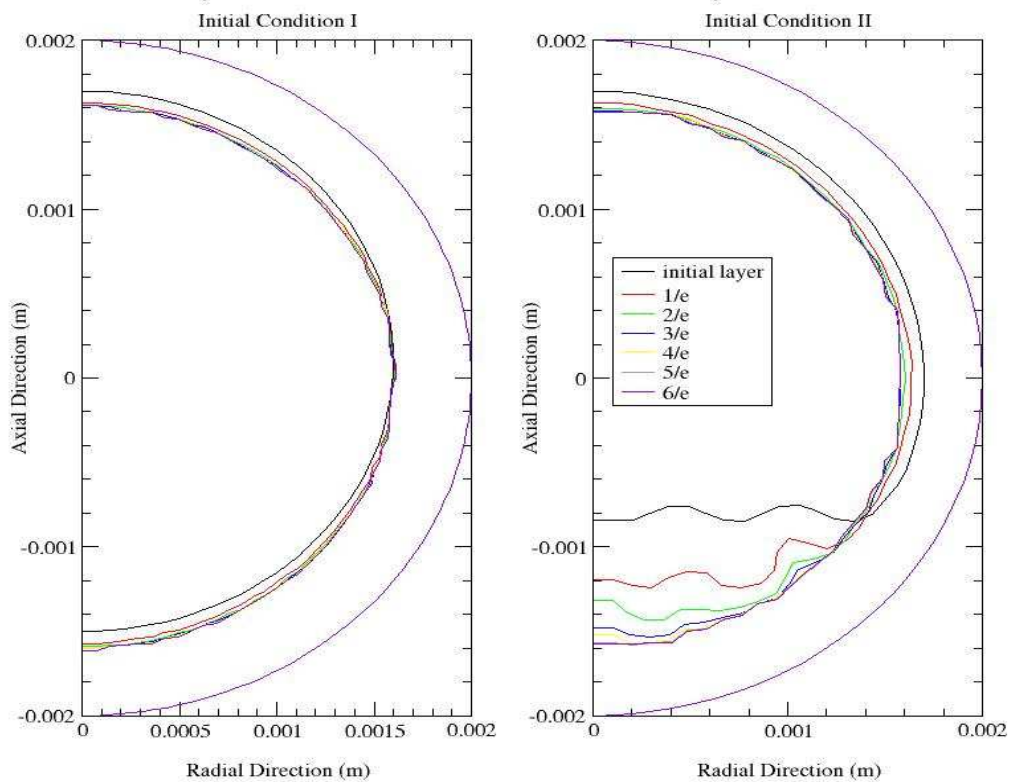


Figure 3.10: Layering process for two different initial conditions. On the left hand side, the initial inner boundary is defined by a non-concentric inner circle (of radius 1.6 mm). On the right hand side, the initial layer is chosen to simulate the frozen fuel gathered at the bottom of the shell. Both initial condition lead to the same final fuel distribution since the shells contain the same amount of fuel, and the same outer boundary conditions (constant heat flux) are applied.

As a third test, the same simulations can be used to verify the global conservation of energy. While applying different values for the heat transfer coefficient,  $h$ , and gas temperature,  $T_\infty$ , on the outer surface, the equilibrium temperature of the system will change. This implies that the inner surface will also slightly change its location.

After equilibrating, the temperature of the outer surface was used in Eq. (95) to determine that the amount of cooling induced by the gas is equal to the total amount of heat produced inside the shell by the volumetric heat.

$$\frac{q}{h} = T_0 - T_\infty$$

$$T_0 = T_\infty + \frac{\dot{q}'' V_{solid\ fuel}}{A_s h} \quad (95)$$

In this equation, the product of the volumetric heat and the solid volume is used to compute the total amount of heat produced in the shell, while the heat flux coefficient and the outer surface area are used to compute the cooling provided by the gas. If the computed final temperature of the shell corresponds to the one computed in Eq. (95), the total amount of heat is balanced, satisfying the conservation of energy. As an example studied within this series of tests, for a volumetric heating of  $2 \times 10^5 \text{ W/m}^3$  in a 43% filled 4 mm shell, the difference in temperature between the cooling gas and the outer surface of the shell in steady state was computed to be 0.83633 K from Eq. (95), and 0.8371 K from the time-step model, indicating that the total energy in the system is balanced.

### 3.5.3 Testing the Model Computation for Volume of the Void, Mass Moments of Inertia and Center of Gravity

As a next test, the model's capabilities to compute the volume of the void, the mass moment of inertia and the distance between the center of mass and the geometrical center were tested. By using a sphere as the initial shape of the void (the radius of the inner sphere had to be sufficiently small for it to fit within the boundaries of the outer sphere, but the two spheres were not concentric) exact equations could be applied to compute the quantities in question by applying global equations of a two body problem. We could then compare these results to the ones computed by the discretized model for validation. In the case of two non-concentric spheres, the volume of the void can be found by computing the volume of the inner sphere, the location of the center of gravity can be computed from Eq. (96). The mass moment of inertia can be calculated from Eq. (97), by applying the parallel axis theorem.

For two spheres, whose centers are separated by  $S$ , the distance between the center of the outer sphere and the center of gravity ( $\Delta X$ ) is

$$\Delta X = -\frac{V_{inner\ sphere} \cdot S}{V_{outer\ sphere} - V_{inner\ sphere}} \quad (96)$$

Based on this result, we can compute the mass moments of inertia using

$$\begin{aligned} I_{xx} &= \frac{8}{15} \pi \rho (R^5 - R_i^5) \\ I_{yy,zz} &= \frac{4}{3} \pi \rho R^3 \left( \frac{2}{5} R^2 + \Delta X^2 \right) - \frac{4}{3} \pi \rho R_i^3 \left( \frac{2}{5} R_i^2 + (\Delta X + S)^2 \right) \end{aligned} \quad (97)$$

The results from this set of tests are presented in tab. 3.2. The decreasing difference between the analytical value and the value computed by the model using spatial discretization with decreasing grid spacing indicates spatial convergence.

Table 3.2: Comparison of geometric parameters calculated analytically and from the model computations for 2 cases with inner and outer radii of 1.6 and 2.0 mm, respectively: (1) two concentric circles; and (2) distance between the two centers of the sphere,  $s=0.2$  mm. For increasing grid points, the model returns values closer and closer to the computed value indicating convergence.

	31x61 Mark 41	61x121 Mark 81	121x241 Mark 161	241x481 Mark 321	Exact Calc.
$\Delta X$ (m)	$4.398 \cdot 10^{-9}$	$2.322 \cdot 10^{-8}$	$6.234 \cdot 10^{-10}$	$4.414 \cdot 10^{-10}$	0.00
Volume of Void ( $\times 10^{-8} \text{m}^3$ )	1.7143	1.7142	1.7156	1.7158	1.7157
$I_{xx}$ $10^{-12} \text{kg m}^2$	9.3816	9.3787	9.3734	9.3721	9.3723
$I_{yy}$ $10^{-12} \text{kg m}^2$	9.3941	9.3832	9.3737	9.3722	9.3723

	31x61 Mark 41	61x121 Mark 81	121x241 Mark 161	241x481 Mark 321	Exact Calc.
$\Delta X$ (m)	$2.114 \cdot 10^{-4}$	$2.095 \cdot 10^{-4}$	$2.096 \cdot 10^{-4}$	$2.10057 \cdot 10^{-4}$	$2.0983 \times 10^{-4}$
Volume of Void ( $\times 10^{-8} \text{m}^3$ )	1.7177	1.7147	1.7154	1.7158	1.7157
$I_{xx}$ $10^{-12} \text{kg m}^2$	9.3841	9.3776	9.3741	9.3720	9.3723
$I_{yy}$ $10^{-12} \text{kg m}^2$	9.0176	9.0155	9.00984	9.00592	9.00669

### 3.5.4 Model Verification by Comparison to Theoretical Results

As mentioned in section 1.2, experimental studies performed by Harding et al.<sup>5</sup> confirm the analytical one-dimensional layering results presented by Martin et. al.<sup>4</sup> for constant local heat transfer coefficients or outer surface temperature. These one-dimensional analytical results were simulated with the new layering model. Due to the difference in geometry between the model (sphere) and the theoretical analysis (planar geometry) the initial condition had to be picked carefully. The results from the model were not expected to perfectly match the theoretical results due to the difference in geometry.

We chose to model the initial inner boundary to have a spherical shape, the center of which is shifted in the positive axial direction. This way, a gradual change in layer thickness is imposed to the model as an initial condition, while the thicknesses at the extreme angles (0 and 180 degrees) assume a maximum and a minimum value. This leads to a distribution of mass between two non-concentric spheres as initial conditions, as shown in fig. 3.10 (left hand side). In order to compare the results, we plotted the difference in layer thickness at the zero and 180 degree angle, see fig. 3.11. The results from the simulated layer redistribution can be compared to the theoretical analysis by finding an exponential fit through the modeling results and comparing the results to the 1-D theoretical predictions

$$\delta(t) = \delta(0) \exp \left[ - \frac{\dot{q}''}{\rho \Delta H_s} \cdot t \right] \quad (71)$$

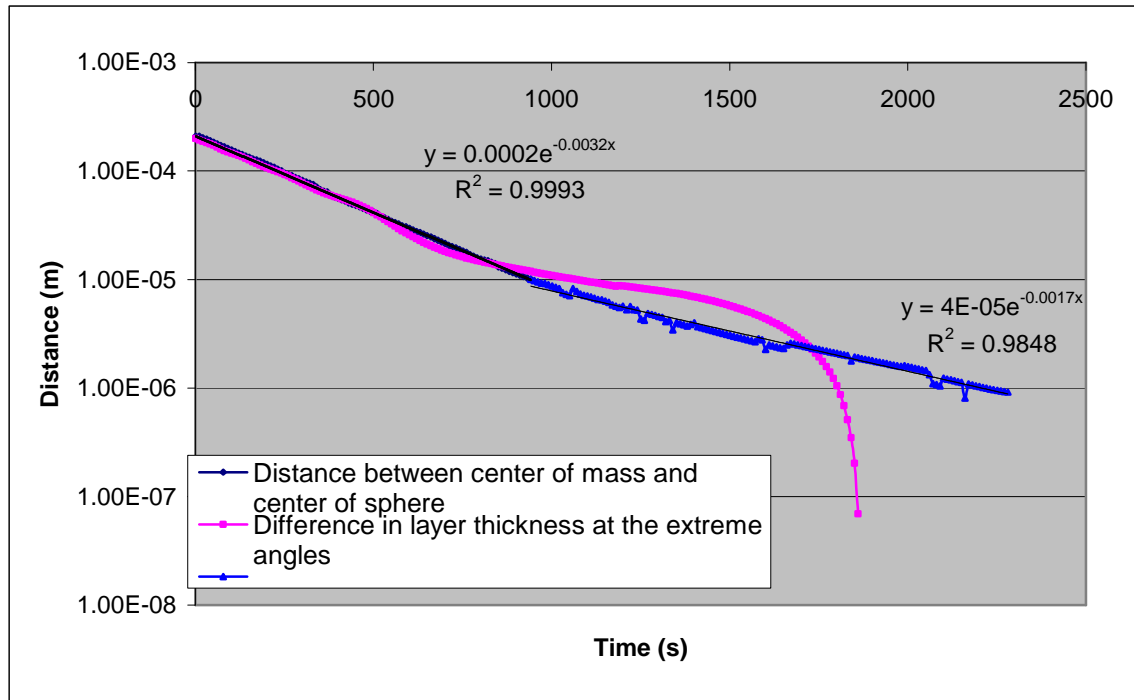


Figure 3.11: Histories of the computed system unbalance (distance between the center of mass of the entire system and the center of the outer sphere) and of the difference in layer thickness (from the thickest and the thinnest part at  $0^\circ$  and  $180^\circ$  from the bottom in figure 3.10) for an assumed case with  $q'''=200\text{mW/cm}^3$ .

The heating rate chosen in this simulation,  $200\text{ mW/cm}^3$  in DT solid fuel, four times higher than the heating from the beta decay, would lead to a theoretical  $1/e$  layering time constant of 384 s. In the simulation, the difference in layer thickness between the zero and the 180 degree angle follow this prediction until a difference of  $\sim 30\text{ }\mu\text{m}$  is reached, and then it slows down. The difference between the center of gravity and the center of the sphere follows this line closely until  $\sim 10\text{ }\mu\text{m}$  (the computed  $1/e$  layering time was 312 s). The deviation of the simulated results from the exponential curve is found to be due to the surface roughness features that develop during the initial stage of the mass redistribution process. These features resolve at a

much slower rate than the overall equilibration, which was also observed experimentally by Sheliak<sup>18</sup>.

Applying lower values for the volumetric heating leads to similar results; in each case, the redistribution speed from the model is slightly faster than the one predicted by the theory. In each case, the equilibration speed slows down significantly once the non-uniformities are of comparable size to the surface roughness features ( $\sim 10\mu\text{m}$ ).

### **3.5.5 Model Verification by Comparison to Experimental Results**

In order to build higher confidence in the modeling results, further redistribution experiments were performed inside the MPLX at General Atomics, providing a controlled test case for the model.

Due to the complexity of the apparatus required to fill PAMS shells with pure species (generally, the shells are filled by permeating gaseous fuel at high pressures into the shells and then cooled past the triple point to reach solid-gas interface), the possibility of using water as a surrogate was investigated. The idea was to observe and quantify the fuel redistribution in a single stationary sphere in a uniform gas stream, as the local heat flux on the outer surface on the sphere under these conditions is well known<sup>61</sup>. For this purpose, the PAMS shells could be punctured filled with water using a syringe, and then glued shut. However, a close look at the properties of ice (in particular the vapor pressure over the solid), in combination with the fact that the shells would contain a water vapor and air mixture, indicate the that influence of a non-participating gas species needs to be addressed. Appendix E presents two models found in the literature<sup>4, 51</sup> applied to the one dimensional case exploring the influence of the

non-participating gas on the layering mechanism. Application of the resulting equation to the water surrogate case indicated a significant influence of the air in the shell on the layering time, eliminating a similar setup as a meaningful test case. However, as described in Appendix E, this setup was used to test the non-participating gas equations resulting from the theoretic analysis in a practical case.

In search for a meaningful test case, we decided to test the redistribution of water in a partially water filled and otherwise evacuated volume.

### **3.5.5.1 Experimental Setup**

Fig. 3.12 shows a schematic of the test stand for the water redistribution experiment. A cuvette is a small tube of square cross-section (1 cm by 1 cm) and ~5 cm in length. It is filled to a level of ~5 mm of pure water and held in place inside a glass tube (2.4 cm in diameter) by a thin steel tube. This steel tube feed through a small hole in a thin 1 cm by 1 cm plate, which is glued to the top of the cuvette sealing the volume of the cuvette and the steel tube from the cooling gas stream. Through the steel tube, the gas (air) in the cuvette can be evacuated. In that experiment, the mass redistribution of water inside the cuvette under IR irradiation can be studied. The cuvette is inserted upright into a glass tube (which will later be the fluidized bed in the deuterium layering experiment) and cooled by a temperature controlled nitrogen gas stream.

Despite its non-spherical geometry, a known, non-uniform heat flux is imposed on the outer surface, and the movement of the interface can be studied experimentally by analyzing pictures of the water level before and after layer redistribution and numerically by applying the corresponding initial and boundary conditions along with

the appropriate geometric constraints as a model input. The results from the experiments and the model will be compared in this section.

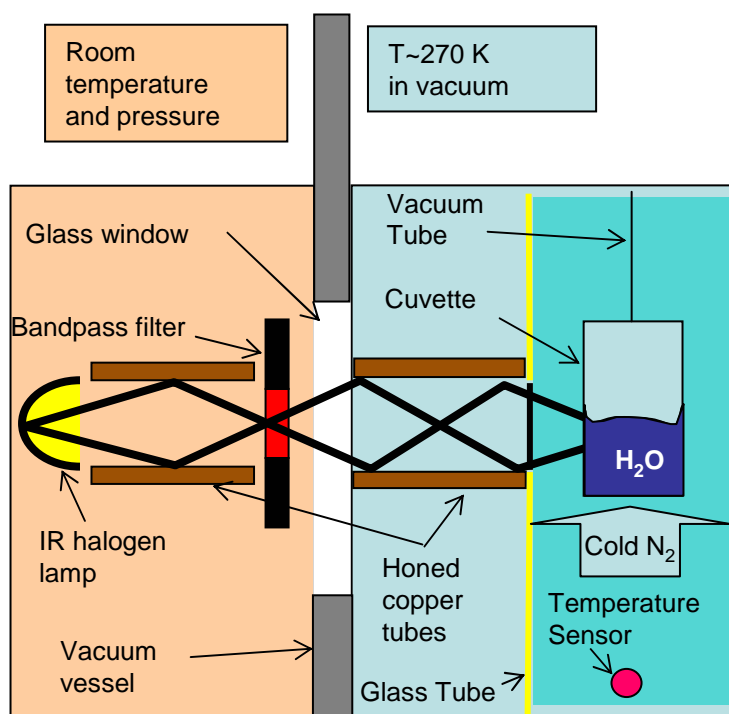


Figure 3.12: Experimental setup used to perform a water surrogate layering experiment.

The heating system providing bulk heating to the water in the cuvette consists of a IR halogen light bulb, which is mounted on the outside of the vacuum vessel. Honed copper tubes act as waveguides to deliver most of the IR radiation directly into the water. A narrow band pass filter is used to limit the incoming radiation to the one that matches the absorption spectrum of water (as shown in fig. 3.13). The broad emission spectrum of the halogen lamp (very close to blackbody emission spectrum at 2950 K) is limited by the band pass filter to wavelength, in which the absorption lies between 1 and  $3 \text{ cm}^{-1}$ . Light at higher absorption coefficients would be absorbed on the surface leading

to surface heating, while the water in the cuvette would be almost transparent to light at lower coefficients<sup>62, 63</sup>.

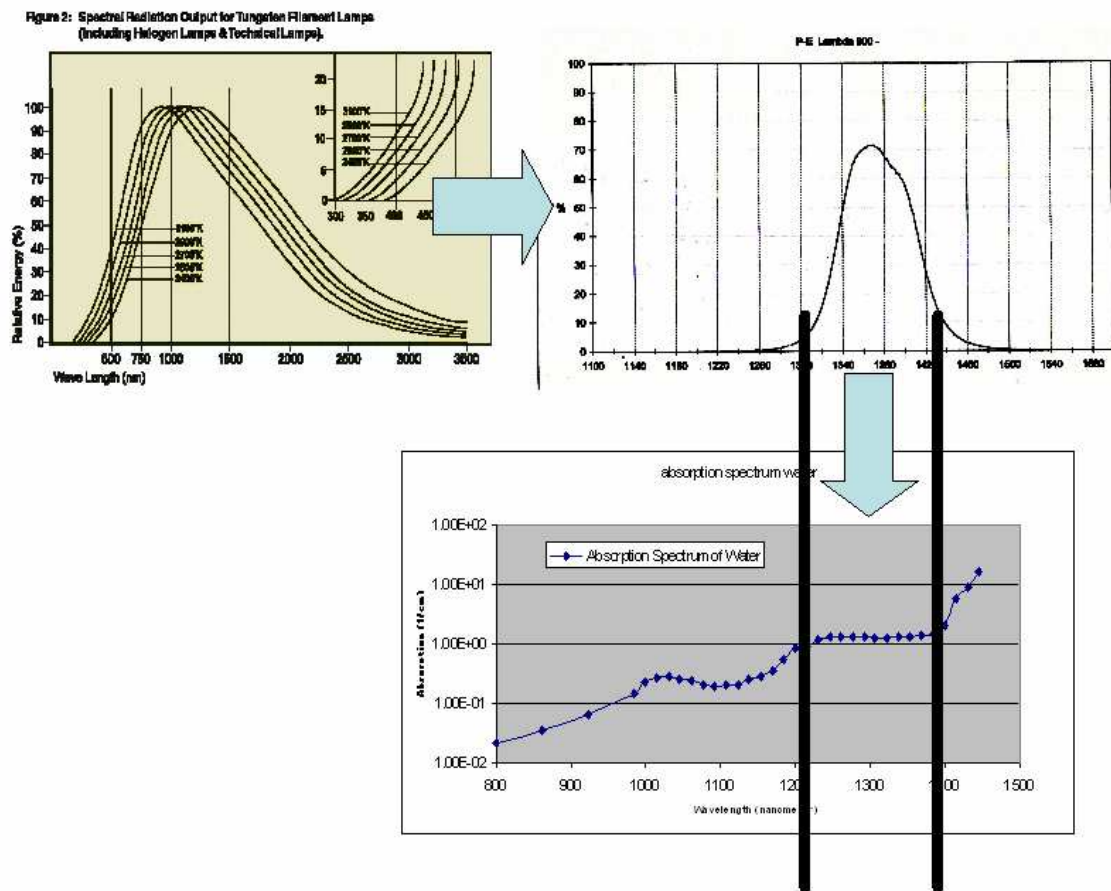


Figure 3.13: Tailoring of emitted light from the IR halogen light source to retain only wavelengths in which the absorption of water provides volumetric heating.

In order to quantify the total heat in the filtered spectrum provided by a 21 Watts halogen IR bulb, the heat flux through the entire setup of waveguides, filters and window glass was measured in front of and behind the water filled cuvette using a power meter. Measuring 13.43 mW in front of the cuvette and 0.902 mW behind the cuvette, the absorbed heat was 9.58 mW over the path length of 1 cm and an area of  $0.785 \text{ cm}^2$  (area of the detector plate). This corresponds to an absorption coefficient of

$2.7 \text{ cm}^{-1}$ , which is in good agreement with the reported absorption coefficient of water<sup>62</sup>,<sup>63</sup> at wavelength  $\lambda = 1382 \text{ nm}$ , and the specifications of the optical filter used in this setup. Thus, the volumetric heating rate was  $0.016 \text{ W/cc}$  in the narrow band around  $1380 \text{ nm}$ .

The remaining properties that describe this experimental setup are presented in tab. 3.3. As a comparison the properties of D2 and DT are also shown.

Table 3.3: Input parameters and properties for DT, D<sub>2</sub> and water layering.

		DT-layering	D <sub>2</sub> -layering	H <sub>2</sub> O-layering
$T_{\infty}$	Temperature of the cooling gas	19.3	18.3	272.3
$\Delta H_s$	Latent heat of fusion	$7.8471 \times 10^7 \text{ J/m}^3$	$7.1917 \times 10^7 \text{ J/m}^3$	$2.5 \times 10^9 \text{ J/m}^3$
$M$	Molecular mass	0.005 kg/mol	0.004 kg/mol	0.018 kg/mol
$\rho_{ice}$	Density of the ice	$\sim 251 \text{ Kg/m}^3$	$\sim 195 \text{ kg/m}^3$	$916.7 \text{ kg/m}^3$
$P_v(T)$	Temperature dependent vapor pressure (see Eqs. (98) and (99))	A = 10.821 B = 150.34 C = 2.2389	A = 10.427 B = 138.31 C = 2.2891	A = $3.665 \times 10^{10}$ B = $-1.309 \times 10^6$ C = - 33793
$\dot{q}''$	Volumetric heat	$\sim 0.049 \text{ W/cm}^3$	--	$0.016 \text{ W/cm}^3$
$k_{ICE}$	Thermal conductivity	$0.31 \text{ W/(m K)}^{16}$	$0.31 \text{ W/(m K)}^{16}$	$2.25 \text{ W/(m K)}^{47}$
$k_{VAPOR}$	Thermal conductivity of vapor	$0.01 \text{ W/(m K)}^{16}$	$0.01 \text{ W/(m K)}^{16}$	$0.024 \text{ W/(m-K)}$
$C_{p,s}$	Specific heat	$\sim 4280 \text{ J / kg-K}$	$2675 \text{ J / kg-K}$	$2050 \text{ J / kg-K}$

$$P_{v,DT-D_2} = \exp\left(A - \frac{B}{T_{Kelvin}} + C \ln(T_{Kelvin})\right) \quad (98)$$

$$P_{v,H_2O}(T) = \left[A + B \cdot T_{Celsius} + C \cdot T_{Celsius}^2\right] \cdot \exp\left(\frac{-6150}{T_{Kelvin}}\right) \quad (\text{in mbar}) \quad (99)$$

The temperature-dependent vapor pressure over the solid are computed from equations (Eqs. (98) and (99)), the coefficients A, B, and C are listed in tab. 3.3.

Due to the significant influence of air as a nonparticipating gas in the void space of the cuvette as analyzed in Appendix E, the experiment was performed under evacuated conditions. A small amount of air will remain in the void space, as complete evacuation also removes the water from the cuvette. In order to evacuate most of the air, the cuvette was initially filled to a height of ~1 cm and then evacuated until the water level in the cuvette dropped to ~0.5 cm thus flushing most of the air out along with part of the water. This way, we can safely assume that the partial pressure of air in the gas phase is lower than the vapor pressure of water at room temperature which reduced the influence of the air as a non-participating gas to negligible levels.

After filling the cuvette with water and evacuating most of the air from the vapor space, the cuvette was cooled to just under the freezing point of water. A temperature sensor was installed in this setup, measuring the temperature of the cooling gas ~ 20 cm below the cuvette. Since these experiments were performed in the MPLX, the existing feedthroughs into the cooling loop were used, although the distance between the location of the temperature measurement and the cuvette was larger than it would have been required for a more accurate temperature reading. The absolute temperature reading of the gas stream at the freezing point of water was 270.3 K. The

freezing point was determined by observing the water inside the cuvette to turn opaque (fast freezing). This absolute temperature reading might be distorted due to the distance of the location of measurement and the point of interest (cuvette), and due to the heat connection between the temperature sensor to the surrounding tube. However, the temperature difference between the freezing point of water and the operating point can be taken to be accurate to within 0.1 K (accuracy of the platinum resistance temperature detector (RTD) is 0.05 K). The operating point for the measured gas temperature for this experiment was chosen to be 0.3 K below the measured temperature of the freezing point. A small heating device in combination with a PID controller is used to keep the temperature at 0.3 K below the value recorded at the freezing point. The temperature control worked to within a  $\pm 20$  mK of the set point.

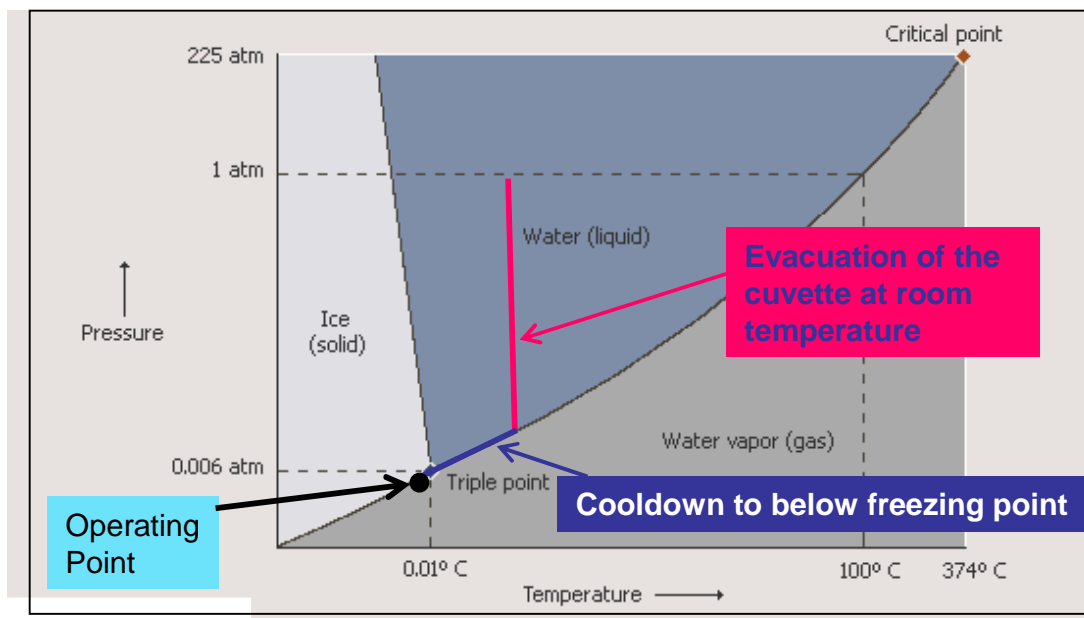


Figure 3.14: Phase diagram of H<sub>2</sub>O showing the operating point of the water redistribution experiment.

The gas stream velocity of the cooling nitrogen was measured beforehand in a separate experiment. The flow speed of the gas can be increased by controlling the rotational speed of the cryogenic blower. In absence of a flow meter (not part of the MPLX design since the flow meter would increase the pressure drop through the gas loop), the flow speed was determined by increasing the blower velocity incrementally until single spherical particles of a certain size and weight are levitated in the gas stream. From these experiments, we determined the gas flow speed to be 6 +/- 0.5 m/s at atmospheric pressure nitrogen.

In order to estimate the approximate time, after which a significant redistribution can be expected, we applied the results from the heat transfer layering equations shown in the previous section for the mass redistribution between two parallel plates under completely evacuated conditions:

$$\delta(t) = \delta_0 \exp\left(-\frac{t}{\tau}\right) \quad (100a)$$

$$\tau = \frac{\Delta H_s \rho_{solid}}{\dot{q}''} = 39.4 \text{ hrs} \quad (100b)$$

Based on these results, a significant mass redistribution will occur within two days, and we arbitrarily picked 64 hrs as our layering time.

The location of the solid-vapor interface inside the cuvette is recorded using a camera with a microscopic lens and a backlight. A significant amount of backlight was required to record an image with the camera, which will also be absorbed in the water. Thus the results would be distorted if the backlight was used too long or too frequently.

Fig. 3.15 shows two images taken at 0hrs and 64 hours of redistribution time. The dark spot below the interface in the solid region in the picture taken after the layering period was a phenomenon we could not explain from this analysis. A cartoon drawing is added to this picture to help interpret the pictures.

We established that the redistribution was indeed due to the IR light by melting and re-freezing the ice and have it being cooled without the IR light. No layer movement was observed.

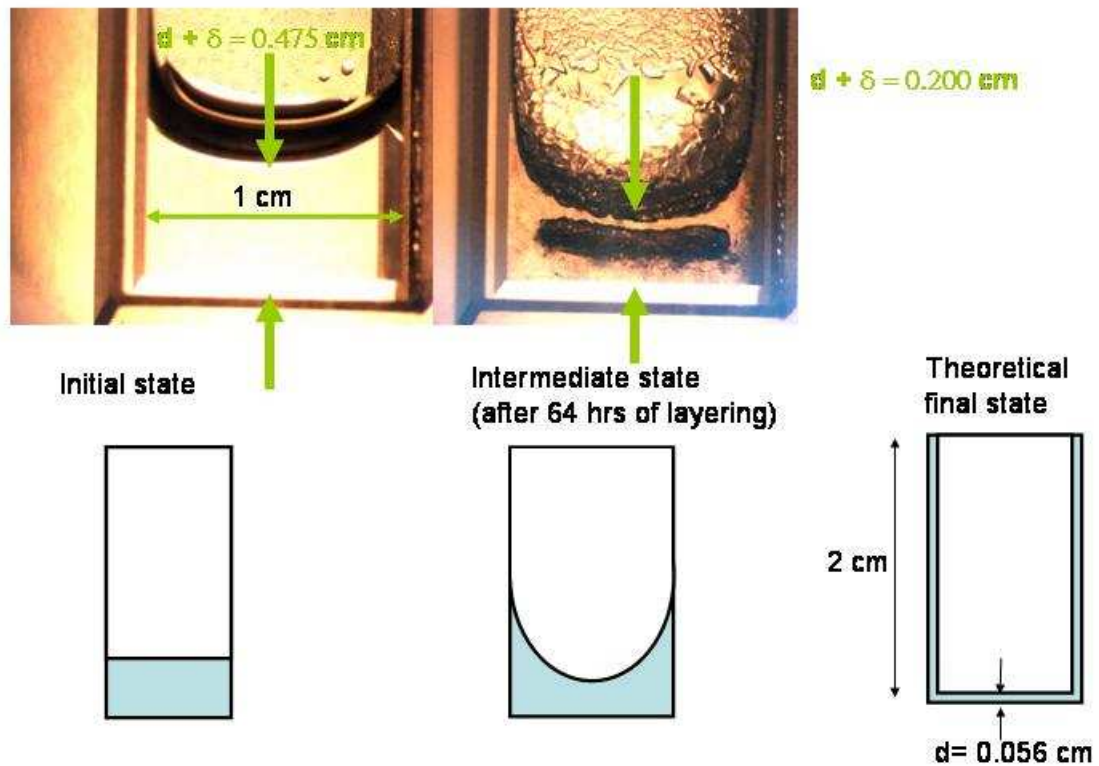


Figure 3.15: Photographs of cuvette from water layering experiment at time=0 to time=64 hours. Redistribution of the water in the cuvette can be observed as shown also in the schematics.

We consider these results satisfactory, as we now have an experimental case for which the parameters and boundary conditions are known with a non-uniform heat flux at the outer surface of the cuvette. Based on the flow information in combination with the gas temperature, the local heat transfer coefficient along the outer surface of the cuvette can be estimated. All other parameters of interest have been determined, and we can now attempt to reproduce these results with our layering model.

### **3.5.5.2 Modeling results from the mass redistribution experiment**

The model presented in section 3.3 is suitable to model the experiment presented in the previous section. However, some modifications needed to be implemented in order to accommodate the altered geometry. Furthermore the properties of the redistributed mass needed to be changed from deuterium or deuterium-tritium- mixture to the water used in the experiment (see tab. 3.3).

In order to limit the changes to the model presented and tested previously, a cylindrical cuvette with round cross-section is modeled instead of the square cross-section used in the experiment. This approximation will distort the final results slightly, but for the benchmarking purpose of this test, the results are expected to be sufficiently accurate. Instead of a complete validation, this simulation rather serves verification purposes than complete validation. However, we can use the modeling results to show that the correct physical laws and processes are modeled.

Fig. 3.16 shows the redistribution of the water from its initial configuration in intervals of 8 hours until the experimental 64 hours are reached. The heat flux boundary condition along the outside surface of the cuvette is approximated to be similar to the

heat transfer found in cooling of a flat plat with laminar flow, and can be found from the local Nusselt number. The Nusselt number as a function of the axial coordinate,  $z$ , follows

$$Nu(z) = 0.332 \cdot \text{Pr}^{\frac{1}{3}} \text{Re}^{\frac{1}{2}} \quad (101a).$$

The local heat transfer coefficient is then

$$h(z) = 0.332 \cdot \text{Pr}^{\frac{1}{3}} \left( \frac{U \cdot \rho_g}{\mu_f \cdot z} \right)^{\frac{1}{2}} \cdot k_{gas} \quad (101b)$$

Comparison of the simulated results in fig. 3.16 to the experimental results in fig. 3.17 shows a reasonably good agreement.

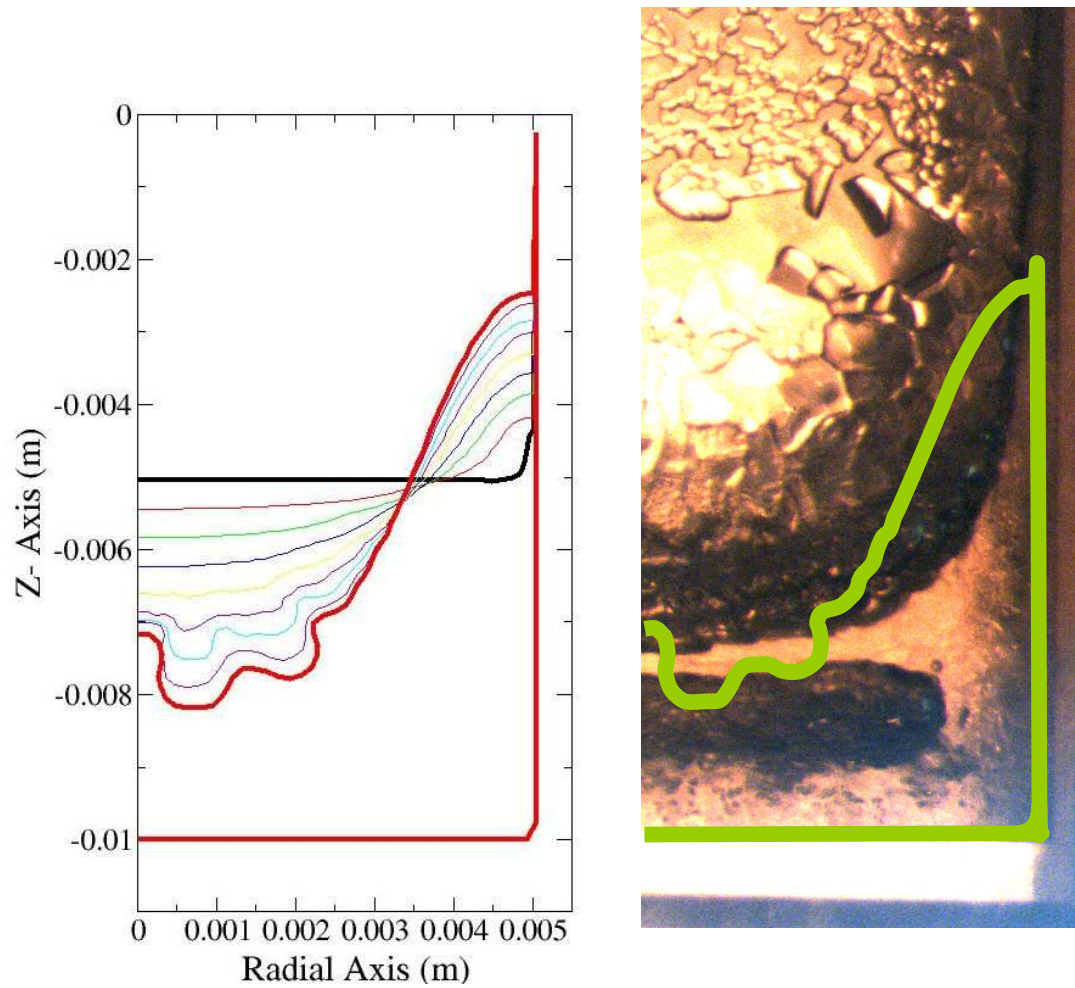


Figure 3.16: Numerical results of the mass redistribution of ice in a gas cooled cylindrical cuvette. Each line on the left represents the location of the interface at layering time intervals of 8 hours. The right hand side shows an overlay of the experimental and the numerical results.

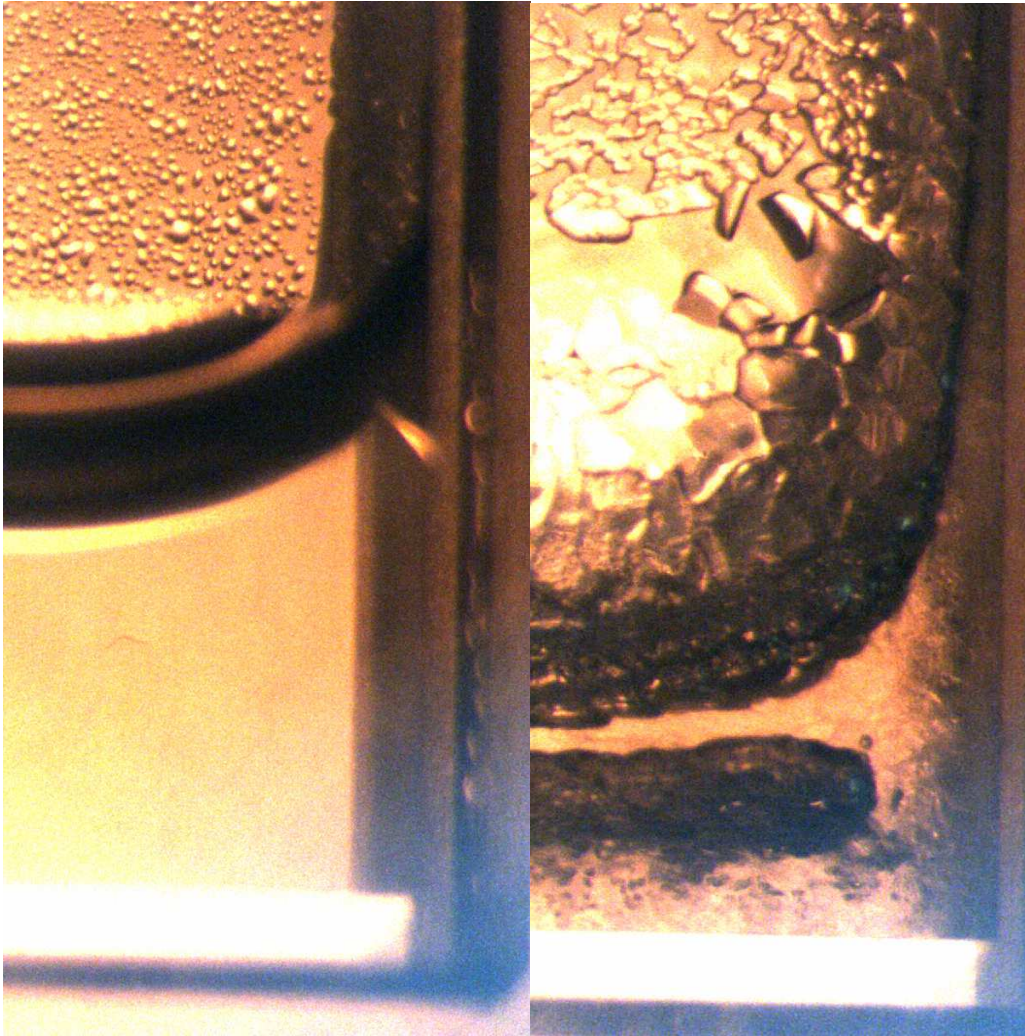


Figure 3.17: Pictures from the water layering experiment at time=0 and time = 64 hours.

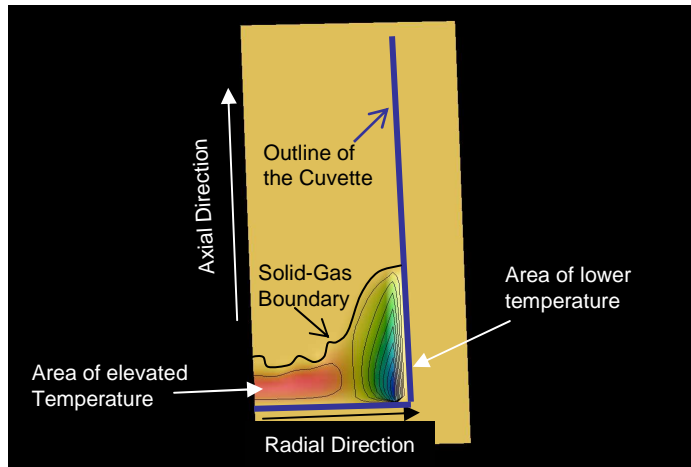


Figure 3.18: Temperature distribution from the simulation of water layering experiment. The sub-cooled region close to the cooled surface is shown in blue, while areas of elevated temperatures are shown in red.

The dark area underneath the surface in the experimental results (see figs. 3.15 and 3.17 right hand side) can now be explained from studying the thermal contour picture shown in fig. 3.18. The region of elevated temperature (shown as a purple contour in fig. 3.18) has the same shape as the dark spot seen experimentally after 64 hours (see fig. 3.17), indicating that the elevated temperature in this region is causing the ice to melt. The experiment was conducted at a temperature very close to the freezing point, thus small increases above (the model predictions are  $\sim 10$  mK) this temperature will certainly lie in the liquid domain. The volume containing the melt forms a rough interface with the ice, causing it to become opaque.

In summary, the attempt to provide a controlled experimental test case for the model under controlled conditions was successful, despite its altered geometry. The model reproduced the mass redistribution fairly well, considering the many unknowns in the experimental setup. The predicted surface roughness features were very coarse (1.5 mm as compared to 0.5 mm in the experimental case), and the peak-to-valley-distances (amplitudes of the surface instabilities) were magnified (0.5 mm as compared to 0.1 mm). This is a result of the coarse grid that needed to be chosen in this test in order to keep the computation time within reasonable margin (<1 day). The difference in global interface shape (see fig. 3.16) is a result of the approximation in the local heat transfer coefficient along the outer surface of the cuvette and the treatment of the interface at the location in contact with the inner surface of the glass.

This test, however, allowed us to understand an experimental observation that could not be clearly explained at first.

### **3.6 Summary of the Layering Model and Example Results**

After confirming that the layering model accurately simulates the physics of layering, a summary of the necessary input and the output computed by this model is presented, keeping in mind that it will be used in combination with the fluidized bed model, as described in section 4.

As an input, the model requires the coordinates of a number of marker points along the inner and outer surfaces, the magnitude of the volumetric heating and some properties of the fuel, like the vapor pressure curve over the solid, the density, latent

heat and molecular mass. In addition the layering time needs to be specified along with the local heat transfer coefficient along the outer target surface and the temperature of the cooling gas. Of course the grid spacing and the size of the overall domain needs to be given as well.

As an output the model returns the position of the markers of the inner interface after a certain number of time steps, along with the coordinates of the center of gravity and the mass moments of inertia. Fig. 3.19 shows the transient mass moment of inertia during an example layering simulation. Besides illustrating the usefulness of the time-step layering model in providing the time-dependant magnitude of the mass moments of inertia at different initial conditions and heat flux scenarios, this test further demonstrates the validity of the model. The transient mass moment of inertia is plotted for the two initial conditions introduced in section 3.4.3 and shown in fig. 3.10, which specified the initial position of the inner boundary: (1) as a sphere (non-concentric to the outer shell); and (2) as a frozen puddle at the bottom of the shell. The mass moments of inertia along the three main axes are shown to converge to the same value, as the final magnitude of the mass moment in any direction of a uniformly layered shell should be the same. As long as the total mass in the system and the outer boundary condition are the same, the final mass moment of inertia should not depend on its initial condition (see fig. 3.19) and the orientation of the axes.

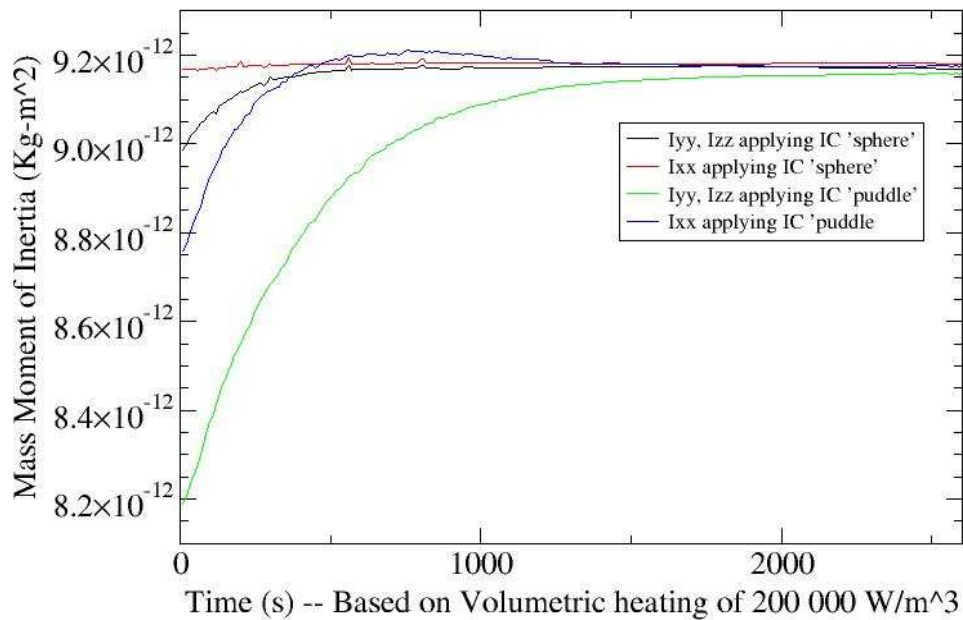


Figure 3.19: Mass moment of inertia of the system during the layering process for two layering cases with the same void volume. As the layer thickness equilibrates to a uniform value, the moments around the different axes become equal in magnitude.

The temperature at the inner and outer surface and the entire temperature field in the fuel layer are part of the output (see fig. 3.20 for an example output showing the temperature field in the solid fuel layer in a 3-D plot).

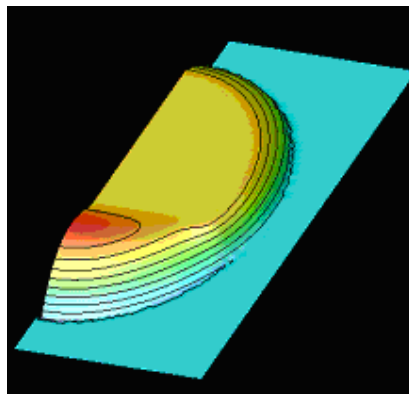


Figure 3.20: Temperature field of the fuel layer shown as a color coded 3-D plot. Areas of elevated temperatures can be seen in thicker parts of the layer, while colder areas can be identified close to the cooled surface.

Furthermore, histories of the vapor pressure in the void and of the change in total number of moles in the system are part of the output. These last two output files (pressure v. time and  $\frac{\# \text{ of moles}(\text{time}) - \# \text{ of moles}(t = 0)}{\# \text{ of moles}(t = 0)}$  v. time) are used after a simulation to verify that the total mass has been conserved in this simulation. Large changes in total mass during a simulation (e.g. when the time step chosen is too large leading to an over-prediction of the movement of the interface and ultimately to a misrepresentation of the layering physics) need to be recognized and avoided before the results are used.

The model can be used to determine the equilibrium layer distribution for a specific case with non-uniform heat flux. Fig. 3.21 shows an example for a non-uniform heat flux around a stationary sphere in a cooling gas stream. The local heat flux around the sphere as a function of the distance from the leading edge was based on Ref. [61]. The results show that in thermal equilibrium, a non-uniform layer thickness results from the non-uniform heat flux. The distance between the center of mass and the center of the sphere can also be attributed to the non-uniform heat flux profile around the sphere, for which two corresponding mass moments of inertia can be found.

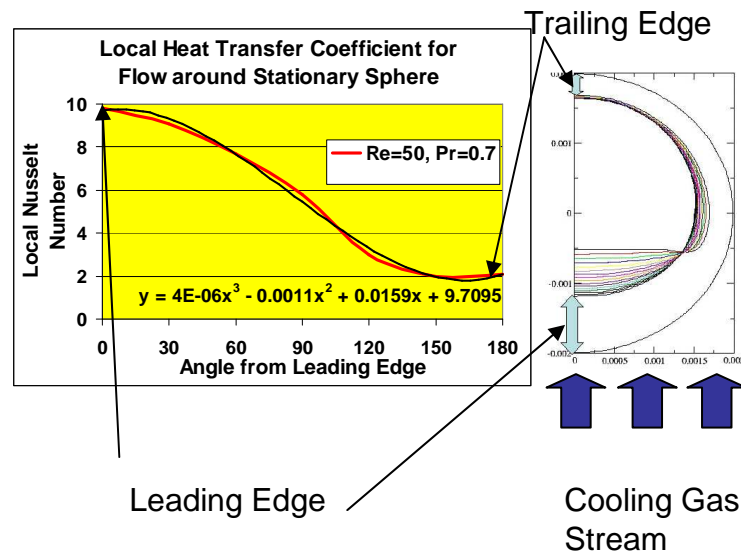


Figure 3.21: Influence of non-uniform local heat transfer coefficient on layering thickness for a single stationary sphere in a cooling gas stream.

#### **4. Combining the Two Models to Simulate the MPLX Layering Experiment**

Two models have been presented in the previous two chapters, each of which can be used to simulate one aspect of fluidized bed layering. The first model simulates the behavior of the particles in the bed and computes the resulting thermal environment based on certain flow parameters and pellet characteristics, while the second model uses the resulting local heat transfer coefficient from the fluidized bed operation and predicts the mass redistribution in the shell. The final result that will be presented in this chapter concerns the transient layer formation that is induced by a specific fluidized bed design operating under controlled gas flow parameters within a given time frame. Some information about the anticipated outer surface damage will be given for each set of operating parameters.

The two models could not be fully combined to simulate the entire fluidized bed layering process, as it would be a computationally very expensive task to track the interface of ~200 shells for 16 hours of fluidization since the time step size of the fluidization has to be of the order of  $1.0 \times 10^{-5}$  seconds. This time step restriction is described in section 2.4 and it is required in order to achieve a stable solution when modeling an elastic contact. Much bigger time step sizes are allowed in the layering model (~1.0 s, as described in section 3.5), since the time scale of the mass redistribution process is about five orders of magnitude slower than the time scale of the particles' elastic collision contact. Simulating the fluidization during the entire layering process (a 1/e layer uniformity improvement is expected every 26 minutes in a beta

layering scenario) would not only take a long time computationally, but it is also redundant, as a converged statistic for time- and particle averaged orientation vector as well as impact collision and collision frequency for a specific fluidization case can be computed by modeling 5-30 seconds (see following section). Over such a short period of time, the layer movement will not be significant. Thus, some assumptions can be made to relate the time-averaged temperature field that is imposed on the outer target surface to the mass transfer inside of the pellet. The fluidized bed parameters (including the pellet characteristics like the distance between the center of gravity and the center of the sphere along with the corresponding mass moments of inertia, and the bed characteristics namely the gas flow speed, and temperature as well as the size of the bed) are applied to the model for a period of time, which is chosen such that the time- and particle-averaged statistics for orientation vector as well as impact collision velocities and collision frequencies converge (typically of the order to 10-60 s, as described in section 4.3). The average heat transfer and particle orientation, along with its spin, linear velocity, bed expansion, gas temperature etc. are then computed. These values are then inserted into the layering model to compute the mass transfer under these boundary conditions. After applying these conditions to the mass transfer model for a time that is short compared to the total layering time, but long as compared to the fluidized bed operation (a few minutes), the new degree of unbalance along with updated values for the mass moment of inertia are computed and used as input for the fluidized bed model to compute the new thermal environment of the sphere. These iterations continue until the layering process is completed. Finally, an estimate on the

surface damage can be inferred for different bed designs based on the statistics of the impact collisions encountered during the layering process.

#### 4.1 Relation between average Orientation of the Particle and Local Heat Transfer Coefficient

Before starting the first series of simulations, the relation between the time-averaged orientation vector (as defined in chapter 2), the gas flow speed, and the local heat transfer coefficient has to be defined. In this argument, we start out by analyzing the local heat transfer coefficients in the two extreme cases. Consider first the case in which the average orientation vector is zero. In this case, the time averaged local heat transfer coefficient is constant, and can be computed from empirical relations for pellet to gas heat transfer in a fluidized bed found in the literature (e.g. Refs. [48] and [64]). These sources show that the particle to gas heat transfer coefficient in fluidized bed systems operating at Reynolds numbers higher than  $\sim 10$  can be estimated from the following equation:

$$Nu_{gp} = \frac{2 \cdot h_{gp} R}{k_{gas}} = 2 + (0.6 \sim 1.8) Re_p^{1/2} Pr_g^{1/3} \quad (102)$$

In this equation,  $h_{gp}$  stands for the heat transfer coefficient describing the heat transfer between the particle and the gas, the corresponding Nusselt number is symbolized by  $Nu_{gp}$ ,  $R$  is the radius of the particle,  $k_{gas}$  is the thermal conductivity of the gas, while  $Re$  and  $Pr$  describes the Reynolds and the Prandl number, respectively. This equation indicates that the particle to gas heat transfer in a fluidized bed falls in a

range of values limited by the equation for the heat transfer in a single sphere (0.6 as a factor in the second term) and the heat transfer for a fixed bed with large isometric spheres (1.8 as a factor in the second term) <sup>64</sup>.

In our fluidized bed simulation, we chose a factor of 1.2 for the second term coefficient in Eq. (102) since the mode of operation of our fluidized bed lies between these two limiting cases. Thus, the constant heat transfer coefficient imposed on the outer target surface is computed by Eq. (102) using 1.2 as a factor for the case where the time-averaged particle orientation is completely random and the particle spin rate is fast enough ( $\sim 5$  Hz estimated by Alexander<sup>11</sup>)

The second limiting case deals with the local heat transfer coefficient applied to a sphere whose average orientation vector is exactly one. In this case, the sphere can be modeled as a stationary sphere in a uniform gas stream. The local heat transfer coefficient on the outer target surface is well described in the literature (e.g. Refs. [61] and [65]). The change in local heat transfer coefficient along the outer surface from the leading edge depends on the Reynolds number and the flow regime. In the case of the fluidization of deuterium-filled 4 mm shells in cold helium ( $\sim 18$  K), the flow regime falls into the “subcritical regime”. This regime is defined by  $400 < \text{Re}_D = \frac{d_p U}{\nu} < 10^5$  [61] and is applicable to our fluidized bed experiments (Reynolds numbers between  $\sim 1200$  and  $3000$ ). In this region the vortices are shed and the flow behind the sphere oscillates. The angular variation in heat transfer coefficient is taken from Kaviany<sup>61</sup> and is approximated by two third order polynomials to simplify the implementation to the layering model. The polynomial coefficients need to be computed for each Reynolds

number; as an example for a slow flow over a sphere, the computed coefficients for a Reynolds number of 50 is given in fig. 3.21, for higher Reynolds numbers ( $Re > 400$ ), two polynomials are computed as shown in tab. 4.1 for  $Re=1296$  and  $Re=1620$ .

Lastly, the heat transfer coefficient imposed on the target surface for arbitrary orientation vectors needs to be defined. In this case, a combination of the two limiting cases has been applied, as is illustrated in fig. 4.1. The orientation vector is applied as a measure by which the variation in local heat flux is imposed on the target surface. The average heat flux applied to the target's outer surface is chosen to satisfy Eq. (102); only the variation in local heat transfer coefficient will change.

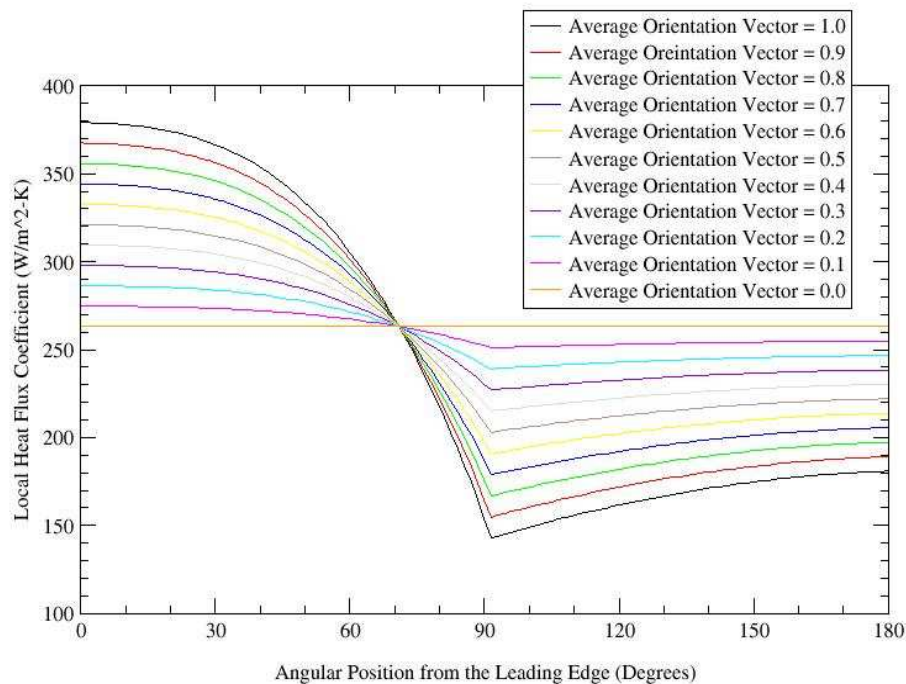


Figure 4.1: Local heat transfer coefficient as a function of angular position for different average orientation of the shells.

The Nusselt number for two different gas flow speed scenarios is shown in fig. 4.2. The gas flow speed at the fluidized bed inlet in combination with the fluid density defines the Reynolds number, which in turn defines the bed expansion at which the bed operates. Two different values of Reynolds numbers have been chosen in such a way, that the resulting bed expansions are 1.6 and 2.0, by varying the gas velocities (0.8 and 1.0 m/s) and keeping the density constant (0.5 atm).

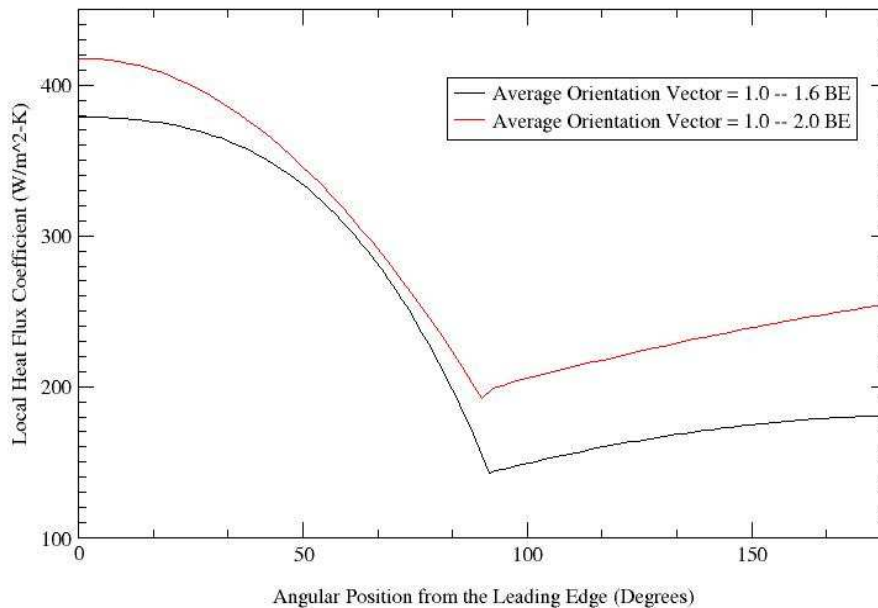


Figure 4.2: Local heat flux coefficient on the outer surface of a stationary shell for two different Reynolds numbers (1296 and 1620). Increasing the Reynold number implies a higher gas speed and a higher bed expansion of the fluidized bed. The average orientation vector is chosen as unity for both cases.

The particle to bed surface heat transfer is not considered in this model, as the fluidized bed is operating in vacuum chamber. The heat transfer in the bed in radial direction is expected to be very small in comparison to the one imposed by the helium

flow in the axial direction. The radiation from the thermal shield in the experimental setup leads to an estimated heat flux of  $\sim 0.5 \text{ W/m}^2$  on the outside surface of the fluidized bed, while the heat flux on the shell surface has to be of the order of  $30 \text{ W/m}^2$  in order to account for the volumetric heating.

## 4.2 Modeling the MPLX

As a last step before modeling deuterium layering experiments inside the MPLX, the input parameters for the fluidizing gas need to be changed from room temperature nitrogen to helium at  $\sim 18 \text{ K}$ . Tab. 2.7 identifies the parameters that change in the transition from using room temperature air as a fluidizing gas (which served as a reference case in the room temperature experiments) to helium at cryogenic temperatures. Tab. 3.2 identifies the parameters that change when deuterium is being layered instead of water, which was used in the validation case.

As an initial step, we investigated how the average position vector of an unbalanced sphere varies as a function of the unbalance and the flow speed. The results from this analysis are shown in fig. 4.3.

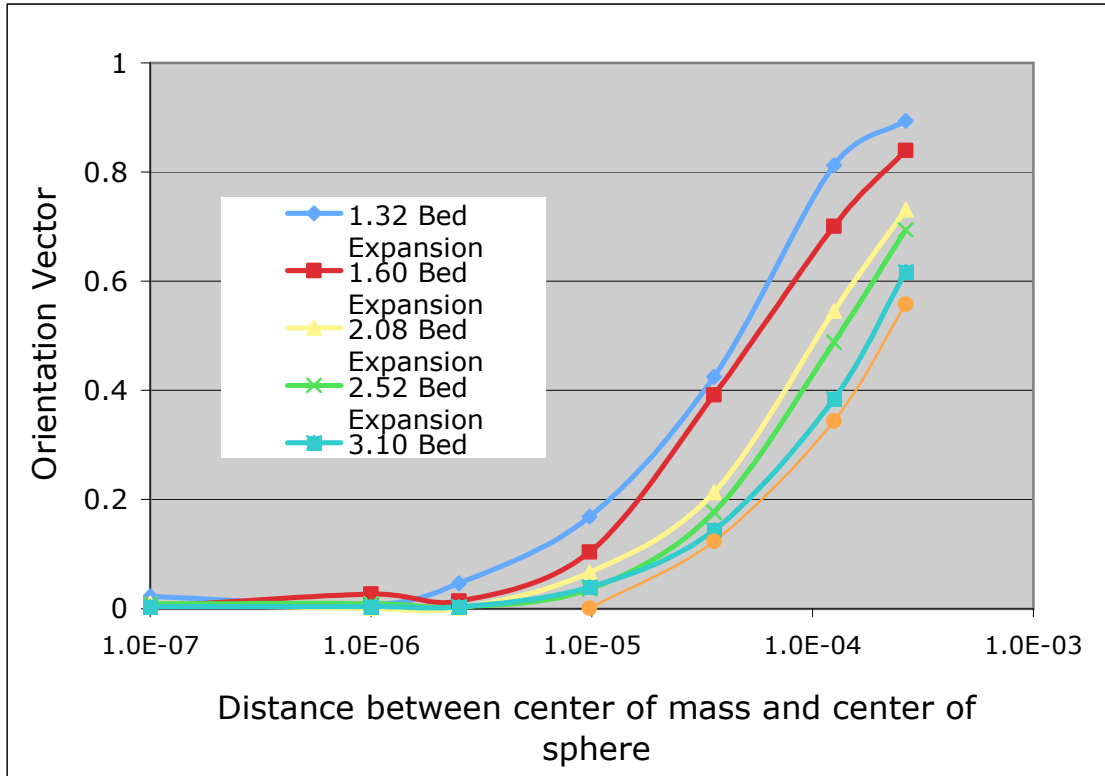


Figure 4.3: Time & particle-averaged magnitude of the dot product of the vector between the center of gravity and the center of the spheres with the negative z-axis for different degrees of unbalance and fluidization parameters.

Higher values in bed expansion than the ones presented here are expected to not only induce surface damage to the shells, but perhaps even to actually break them. For lower values than the ones presented here, no circulation could be observed experimentally and numerically. From this preliminary analysis we determined:

- 1 For a high degree of unbalance, the drag imposed on the targets by the gas stream in the fluidized bed (which acts at the center of the particle) orients all targets in such a way that the heavy part is pointing down.
- 2 As the particles are stirred with a higher gas speed, the average orientation becomes more random.

- 3 This effect is alleviated for lower degree of unbalance at all gas flow speeds.
- 4 For a distance between the center of the sphere (CS) and the center of gravity (CG) of  $\sim 10 \mu\text{m}$ , the particles' orientation can be completely randomized for a bed expansion of 4.25.
- 5 For a distance between CS and CG of the order of  $3 \mu\text{m}$ , the orientation can be randomized even at very low bed expansions.

From our layer formation analysis (Chapter 3), we know that during the layering process, certain inner surface roughnesses can be expected. We were able to compute the influence of these roughness features on the unbalance of the sphere, computing a value of the order of a few  $\mu\text{m}$  for the distance between the center of the sphere and the center of gravity. This in combination with point #5 above shows, that once the particle is layered to the point at which surface features, and not a global layer non-uniformity contribute to the unbalance, any fluidization gas velocity will induce a temperature field uniform enough to smoothen these features. The 1/e improvement for these features has been shown to be larger than the global layering time<sup>18</sup> ( $\sim 4$  hours for a 1/e improvement as opposed to 26 min in the natural DT layering case). This means that once the global layering process is finished, the smoothening of the inner surface will not yet be completed, as the surface smoothening will take longer by a factor of about 8. During this time the particles can assumed to be spherical and the fluidizing gas speed can be chosen to be very low, as a bed expansion of 1.3 is sufficient to randomly spin the particle in the bed, without the development of a preferential position.

### 4.3 Example results for iterating between the two models

As a next test, we analyzed the layer formation in a fluidized bed by iterating between the two models. From the analysis depicted in fig. 4.3, we chose two limiting cases for this set of tests, one at a bed expansion of  $\sim 2.0$  and one at  $\sim 1.6$ . Higher bed expansions are shown to provide a more uniform temperature field, but are also expected to cause unacceptable surface damage, while the lower bed expansion is expected to preserve the outer surface quality, but might not be able to provide a uniform thermal environment.

The analysis is performed in a particle-averaged manner. We assume that all temperature and orientation statistics are the same for all targets in the bed. This is a valid assumption as the bed is being operated for comparatively long periods of time, but the simulation is only run for a few seconds. While the pellets' average temperature environment and average position could be biased based on where it was located at the beginning of the simulation if it is only run for a few seconds, this bias will disappear, as the fluidization time is of the order of several minutes as it is in the MPLX case. Modeling the layer redistribution for all 200 shells in the bed individually because of slight variations in statistical data from the fluidized bed analysis seems unnecessary. This assumption is supported by computing the standard deviation in average orientation and local gas temperature around the target for increasing layering times. For this case, we fluidized 50 particles for one minute and recorded the time average orientation of all particles. At each time step, the standard deviation of the individual particle orientation is computed. From results shown in fig. 4.4, we can conclude, that

the time-averaged orientation vector of the individual target lies within 5 % of the time- and particle averaged orientation vector computed over a 20 s fluidization interval, and within less than 2.5 % after one minute, indicating that the pellets will experience a similar local heat flux variation. This means that the layer formation computed for a single particle based on the particle- and time averaged orientation vector is representative for all particles in the bed.

Next, we needed to estimate how long of a fluidization period needed to be modeled in order to find meaningful statistics e.g. of average particle orientation and helium gas temperature. Fig. 4.5 shows the history of the time & particle -averaged value of the orientation vector during a 60 s simulation of 50 particles. Based on these results, we chose to model 10 seconds of fluidized bed operation since the statistics don't change significantly after that.

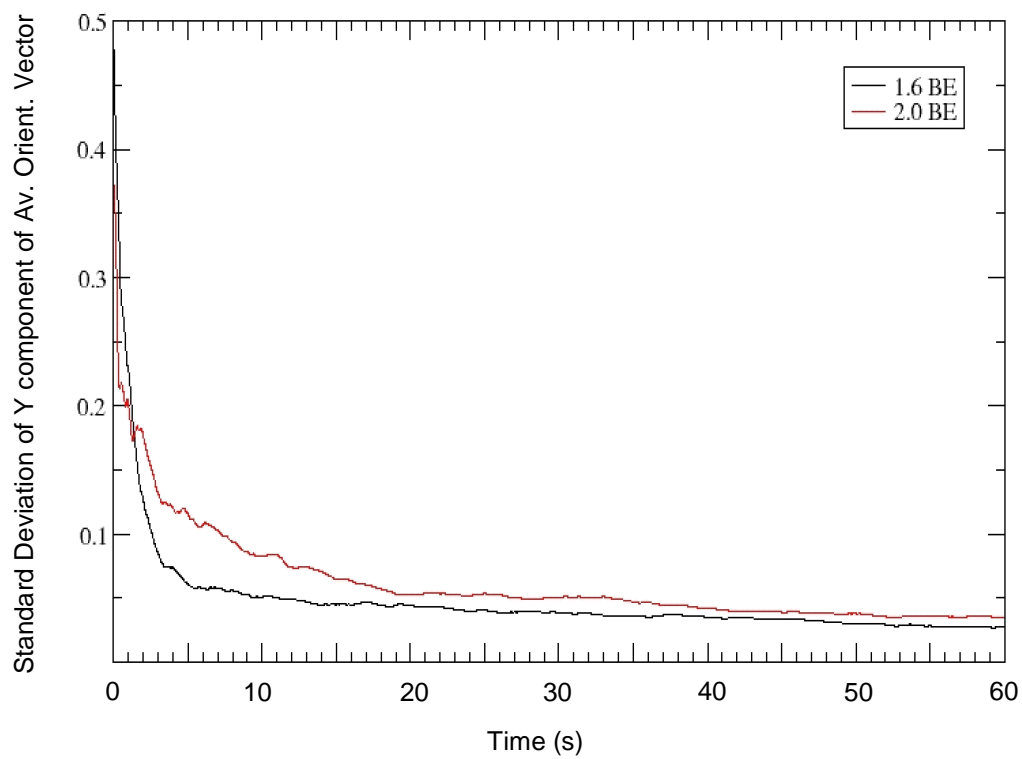


Figure 4.4: Standard deviation for time-averaged orientation of each individual particle for a 50-particle bed operating at two different bed expansions. After 60 seconds of simulated fluidized bed operation, this standard deviation falls below 0.05, indicating that the time averaged orientation does not vary greatly from one particle to another.

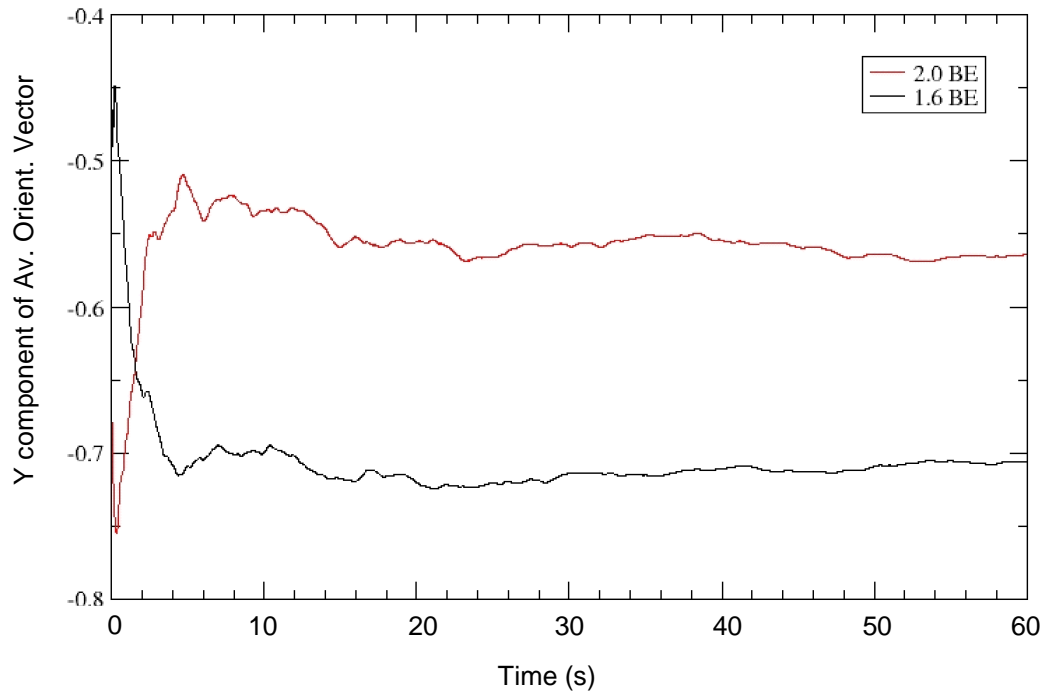


Figure 4.5: History of time & particle-averaged value of the orientation vector for two different bed expansions over time. Due to the rather large unbalance of the spheres in this simulation, the particles have a preferential orientation signified by a non-zero value of their average orientation vector. Despite the fact that different bed expansions result in a different value in the average orientation vector, 8-10 seconds of simulated fluidization seem to be long enough to compute meaningful statistics.

Following the same line of argument, the standard deviation for the value of the gas temperature surrounding the target was computed. These results are shown in fig. 4.6, indicating that the error of using a time & particle-averaged value for the gas temperature around the shell induces an error of  $\sim 1-3$  mK. Besides giving an insight on the error induced by using a particle and time averaged value for the gas temperature when computing the local heat flux around the sphere, this value gives a good indication about the mixing observed in these cases. The better the bed mixes the

particles, the lower the standard deviation of the time averaged gas temperatures for the individual particles.

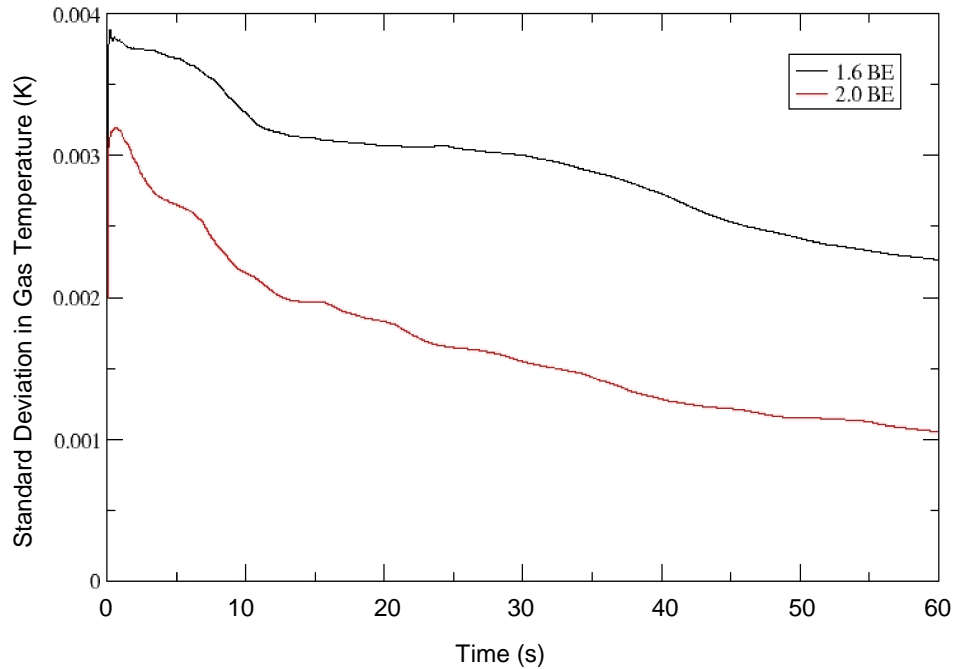


Figure 4.6: Standard deviation of the time-averaged gas temperature around each particle as a function of time. As the bed mixes the particles, this value decreases. The higher overall value of the standard deviation at the lower bed expansion can be explained by a lower degree of mixing observed at low bed expansions.

After these considerations, the analysis for the two cases was started by computing the time & particle-average gas temperature and y- coordinate of the orientation vector for a fluidized bed containing 200 particles, filled with unlayered deuterium. The degree of unbalance and mass moment of inertia was computed by the layering model, the initial condition used in this case described the inner boundary with a spherical shape. The initial distance between the two centers of the spheres was

assumed as 200  $\mu\text{m}$ . The initial conditions and other parameters used in this simulation are given in tab. 4.1.

Table 4.1 Values used in the parametric layering simulation

Parameter	1.6 Bed Expansion		2.0 Bed Expansion	
Flow Speed	0.8 m/s		1.0 m/s	
Gas Pressure	0.5 atm		0.5 atm	
Reynolds Number	1296		1620	
Average Nusselt Number	38.0		44.5	
Polynomial Approximation Local Nusselt Number	Angle<90	Angle>90	Angle<90	Angle>90
	A = $-4 \times 10^{-5}$	A = 0.00	A = $6 \times 10^{-4}$	A=0.00
	B = $-6 \times 10^{-4}$	B = $-6 \times 10^{-4}$	B = -0.005	B = $-3 \times 10^{-4}$
	C = -0.0111	C = 0.23	C = 0.011	C = 0.18
	D = 59	D = 6.2	D = 65	D = 16.95
Mass of Particle	$3.206 \times 10^{-6}$ kg		$3.206 \times 10^{-6}$ kg	
Bed height at rest	$2.5243 \times 10^{-2}$ m		$2.5243 \times 10^{-2}$ m	
Volumetric heat	50 000 W/m <sup>3</sup>		50 000 W/m <sup>3</sup>	
Radius of sphere	0.002 m		0.002 m	
Number of spheres in bed	200		200	
Viscosity of helium	$0.33 \times 10^{-5}$ Pa – s		$0.33 \times 10^{-5}$ Pa – s	
Density of helium	1.333 kg/m <sup>3</sup>		1.333 kg/m <sup>3</sup>	
Heat capacity helium	5200 J/ mol – K		5200 J/mol – K	
Thermal conductivity helium	0.26 W/ m – K		0.26 W/ m – K	
Radius of fluidized bed	0.012 m		0.012 m	
Temperature of gas @ inlet	18.5 K		18.5 K	
Latent heat of deuterium	$71.917 \times 10^6$ J/m <sup>3</sup>		$71.917 \times 10^6$ J/m <sup>3</sup>	
Molecular mass deuterium	0.004 kg/mol		0.004 kg/mol	
Initial Void Volume	$1.7154 \times 10^{-8}$ m <sup>3</sup>		$1.7154 \times 10^{-8}$ m <sup>3</sup>	

The local heat transfer coefficient resulting from the time & particle-averaged orientation and gas temperature determined by the fluidized bed model was imposed on the outer surface; the layering model was then used to compute the change in layer distribution caused by this heat flux. The layering model was applied for ten minutes before the new degree of unbalance and mass moment of inertia was computed and then used as an input for the fluidized bed model to compute updated values on the temperature field.

Fig. 4.7 shows the histories of the distance between the center of the sphere and the center of gravity for the two cases chosen for this analysis and the limiting case of a stationary sphere in a packed bed. Due to the particles' preferential positions in the bed, the times it takes to develop a uniform layer are higher than the ones computed in the case of a constant local heat transfer coefficient (section 3.4.4). In the case of the stationary sphere in the packed bed, the heat flux non-uniformity of the outside surface prevents a layer uniformity better than 30  $\mu\text{m}$ . However, in the cases in which the shells are fluidized, in spite of being exposed to a non-uniform heat flux, the redistribution of mass towards a uniform layer slowly causes the shells to spin more randomly in the bed. This in turn causes the shells to have a more uniform heat flux on the outer surface, which ultimately leads to a layer movement closer and closer to uniformity. Even in the case of very low bed expansions, in which case we have shown that the particles barely leave their preferential position, the heavy side of the shell pointing down, the heat flux imposed by the gas causes a mass redistribution towards uniformity.

Tab. 4.2 shows the values of the average orientation computed in each fluidized bed iteration combined with the resulting distance between center of gravity and center of the sphere as computed by the layering model.

Table 4.2a: Test results for layering at 1.6 bed expansion using both models iteratively

It.	Layering Model Results				Fluidized Bed Model Results			
	time (s)	Distance Between CG and CS ( $\times 10^{-4}$ m)	Ixx ( $\times 10^{-12}$ kg m <sup>2</sup> )	Iyy ( $\times 10^{-12}$ kg m <sup>2</sup> )	Average Orientation Vector	Spin X rad/s	Spin Y rad/s	Spin Z rad/s
0	0.00	2.0918	7.0600	6.7959	0.7170	7.63	8.91	8.97
1	3000	0.4140	7.0969	7.1171	0.3159	7.91	8.14	8.16
2	3600	0.3062	7.0586	7.0615	0.2545	7.91	7.93	7.98
3	4200	0.2240	7.0591	7.0644	0.1870	7.87	7.84	7.88
4	4800	0.1594	7.0585	7.0681	0.1373	7.83	7.72	7.79
5	5400	0.1333	7.0577	7.0618	0.1072	7.87	7.89	7.80
6	6000	0.0959	7.0634	7.0705	0.0919	7.80	7.78	7.84
7	6600	0.0802	7.067	7.075	0.0846	8.02	7.96	7.98
8	7200	0.0723	7.065	7.071	0.0517	8.06	8.08	8.04
9	7800	0.0435	7.059	7.064				

Table 4.2b: Test results for layering at 2.0 bed expansion using both models iteratively

Iteration	Layering Model Results				Fluidized Bed Model Results			
	Time (s)	Distance Between CG and CS ( $\times 10^{-4}$ m)	Ixx ( $\times 10^{-12}$ kg m <sup>2</sup> )	Iyy ( $\times 10^{-12}$ kg m <sup>2</sup> )	Average Orientation Vector	Spin Z rad/s	Spin X rad/s	Spin Y rad/s
0	0.00	2.0918	7.0600	6.7959	0.6130	11.5	10.3	11.4
1	1200	0.8659	7.0448	7.0357	0.3636	11.1	10.5	11.3
2	1800	0.5678	7.049	7.061	0.2700	10.9	10.6	10.8
3	2400	0.3701	7.0543	7.073	0.1740	11.0	10.8	11.0
4	3000	0.242	7.0560	7.074	0.1270	11.0	10.9	11.0
5	3600	0.159	7.0607	7.0773	0.0809	10.9	10.8	10.9
6	4200	0.116	7.0630	7.0770	0.0589	10.6	10.7	10.6
7	4800	0.081	7.0619	7.0715	0.0325	10.5	10.6	10.7
8	5400	0.0587	7.0696	7.0709				

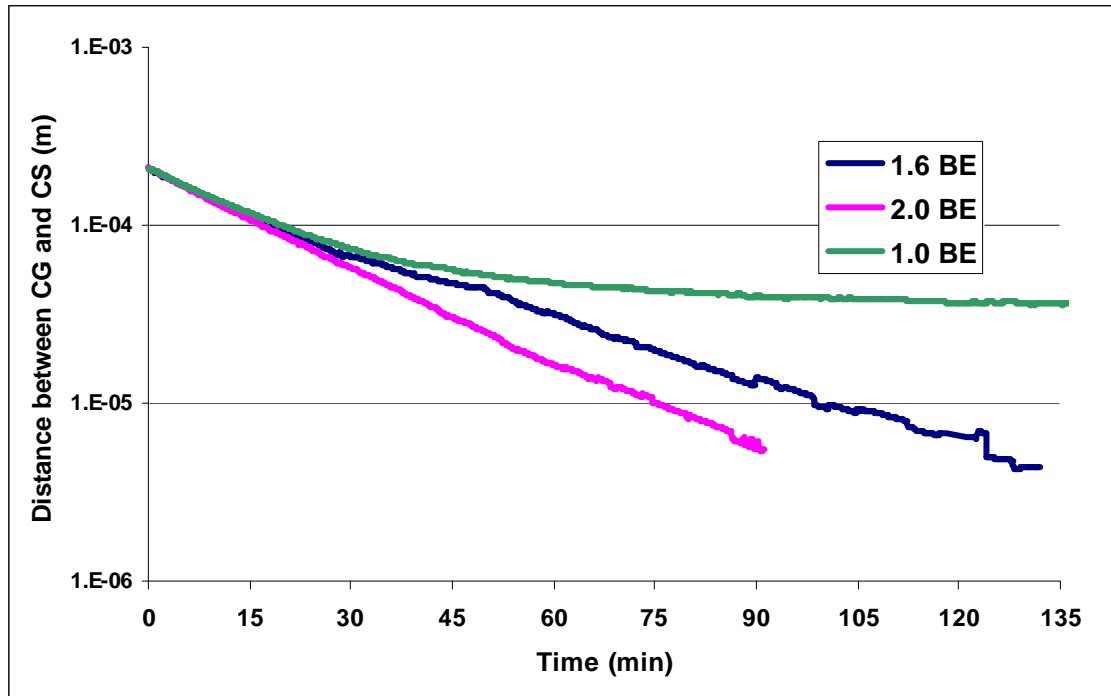


Figure 4.7: Distance between the center of gravity and the center of the sphere as a function of time for the two cases chosen in this analysis and the limiting case of a stationary sphere in a packed bed. The more random spin of the particles in the case of higher bed expansion causes a faster layering time. The simulations are discontinued at  $5 \mu\text{m}$ , as that is the length scale of the surface roughness features. The fluidization at this unbalance imposes a very uniform heat environment and will not cause the pellet to develop a preferential position in the bed.

In order to complete these example test cases, we need to analyze the average impact velocity of particle-to-particle collisions in both cases. Fig. 4.8 shows by analyzing a 10 s fluidization period that the number of collisions at elevated velocities is decreased for both the normal and tangential contact when the bed is operated at a lower gas speed. However, to determine the overall effect on the shell surface, the reduction in average impact velocity for lower bed expansion must be considered in combination with the  $\sim 30\%$  increase in layering time, which increases the number of total collisions.

Despite indicating a lower impact velocity, these statistics obscure the actual surface damage on the shell by the fluidization. This analysis reveals that the average impact velocity can be reduced; however the ~30% increase in layering time increases the number of total collisions which might affect the results disadvantageously.

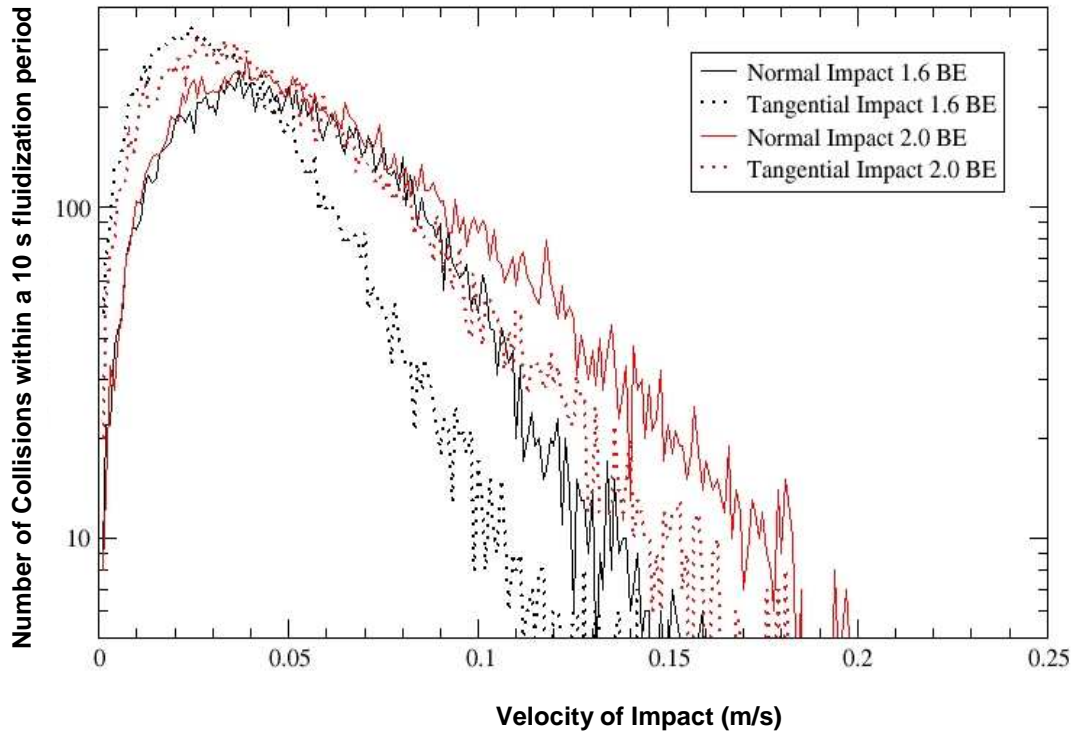


Figure 4.8: Number of collisions during a 10 s fluidization period at different impact velocities in both normal and tangential direction for two different bed expansions. Clearly, the impact velocity is reduced in the case of a lower bed expansion.

The analysis presented in this chapter illustrates that, at low bed expansion and large offset between center of mass and geometrical center, the particles in the bed barely move from their preferential position. However, the layer thickness uniformity can be increased at low bed expansions even if the pellets do not turn over based on the local heat transfer coefficient over an almost stationary sphere. Once this has occurred,

it might become advisable to operate the bed at a higher bed expansion to provide a more uniform heat flux on the outer shell through a more random orientation and to continue the equilibration process. It is essential to know what bed expansion is necessary to overturn shells of this unbalance in order to keep moving the layer towards a uniform thickness. We have shown in the previous example that the bed could be operated at bed expansions as low as 1.6 while conserving the surface quality by reducing the average impact velocity of the particle-to-particle collisions. The penalty paid by this approach is a longer redistribution time as the particles are not exposed to a uniform thermal environment at first.

As the bed is fluidized with higher gas flow rates, causing the pellets to have a more randomized orientation from the beginning of the layering phase they ultimately achieve the layer symmetry faster. Once layer uniformity within a few microns is reached it is possible to run the bed at lower bed expansions conserving the surface quality. This could lead to a time-dependent flow speed profile, which results in a fast layering time and an improved surface quality.

#### **4.4 Final remarks about modeling DT layering**

Although the models have only been applied to the deuterium layering case encountered during the MPLX experiments so far, they can be used to predict the formation of DT layers. However, this model loses accuracy as the  $^3\text{He}$  gas builds up in the void space from tritium decay. The layering process will be slowed down as the mass movement of the gas through the void is impeded by the  $^3\text{He}$  gas in the void,

which is described in Appendix E. From this analysis, a 1-D estimate of the impact of non-participating gas on the DT diffusion and, ultimately, on the layering time can be made. The results are shown in fig. 4.9. From this figure we can conclude that, if the  $^3\text{He}$  concentration in the DT can be maintained within about 5%, its impact on DT diffusion would be small. For the geometry studied in these example cases, the increase in layering time due to a 5%  $^3\text{He}$  buildup in the void would be about 2 minutes per day, which is small compared to the 26 minutes natural layering time for pure DT (provided the total number of days between target filling and layering is kept low). In terms of tritium decay a 5%  $^3\text{He}$  concentration corresponds to a fill and cool-down time of 3 days. This would require improvement in the current fill and cool down process considered for the MPLX (~1-2 weeks).

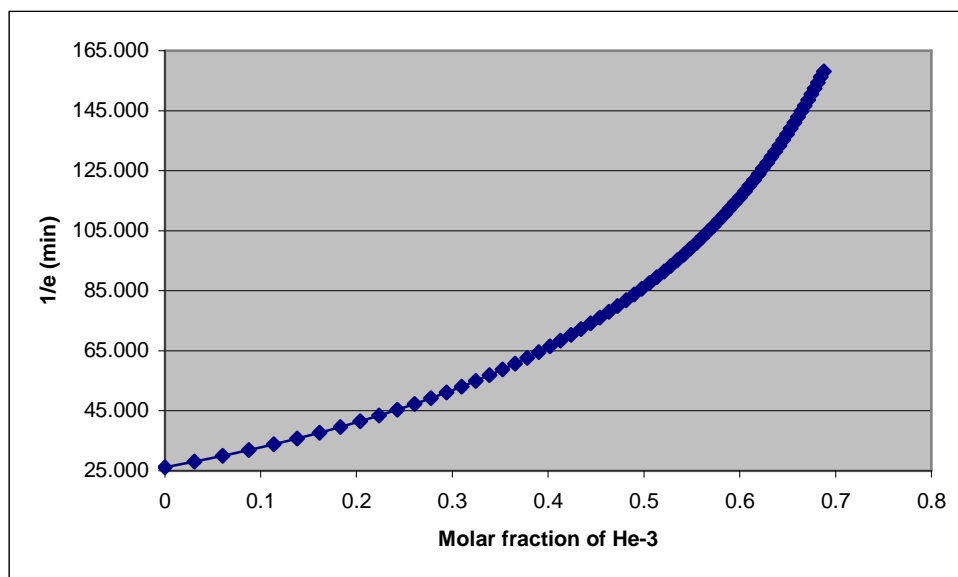


Figure 4.9: 1/e layering time for 4 mm HAPL shells at 19.65 K as a function of the concentration of  $^3\text{He}$  in the void space. These results were based on a one-dimensional analysis presented by Hoffer and Foreman<sup>52</sup>, and are further explained in Appendix E. Clearly, in the concentration is kept below about 5%, the influence of the non-participating gas is very small, increasing the layering time by 6 minutes (from 26 to 32 minutes). In this figure, each square represents an increase in tritium age by one day.

If long fill times cannot be avoided, this model could still be used to estimate the layering progress by using a non-dimensional layering time (normalized to a time constant obtained from figure 4.9), in which case the time constant can be found from fig. 4.9. Alternatively, the layering model needs to be expanded to solve the heat and the mass diffusion equation simultaneously for a case with significant non-participating gas.

## 5. Conclusion

The focus of this research was to help understand and simulate the key physical processes coming into play during layering of an IFE target in a cryogenic fluidized bed. Numerical tools were developed to advance this endeavor, including a model for the fluidized bed behavior and another one for the processes occurring during layering in a fluidized sphere.

The first model combines a 1-D Lagrangian description for the fluid phase and a 3-D discrete particle model for the solid phase into a two phase flow model to describe a fluidized bed with very large particles. This method was validated using experimental and theoretical analysis. The model was then expanded to predict the unique behavior of unbalanced spheres expected initially in a fluidized bed proposed to produce highly uniform IFE fuel pellets.

The “time-averaged” temperature environment inside a fluidized bed is expected to turn initially non-symmetric deuterium or deuterium-tritium targets into highly uniform targets by a layering process. This mass redistribution process has been modeled numerically in two dimensions; the computational algorithm was verified by comparison to 1-D results presented in the literature and to a water layering experiment performed as part of this study. This second model delivers information about the layer formation in a sphere, which is exposed to a certain local heat flux distribution on the outer surface and which is partially filled with a volumetrically heated solid.

The two models were then combined to simulate the integrated overall layering progress in a fluidized bed.

Key findings from this study are summarized below:

#### FLUIDIZED BED MODEL AND RELATED EXPERIMENTS

- Treating the fluid phase in the numerical model in one dimension only, while resolving the granular part in three dimensions resulted in a simulated bed behavior which is in good agreement with the theoretical results and experimental observations, for homogeneous and inhomogeneous fluidization. In addition the computation of the pressure drop through the bed was computed accurately as established by comparison to theoretical results for a limiting case with particles at rest.
- Statistics of the normal and tangential impact velocities for particle-to-particle and particle-to-wall collisions could be computed as a function of the bed expansion of the fluidized bed through numerical simulations. This provides valuable information on the expected surface damage induced by the collisions on the outer surface of the shell, which has been shown to be a key issue in the evaluation of using a fluidized bed for IFE target layering.
- The time-averaged spin rates could be determined for all particles in the bed, which proves to be essential in assessing the time-averaged heat transfer coefficient on the outer surface of the pellet.
- Including the unbalance of the particles to the granular model enabled us to analyze test cases with the following results:
  - o The bed expansion at which the fluidized bed operates is not influenced by the unbalance of the spheres for constant gas flow speeds.

- The collision frequency is not significantly influenced by the unbalance of the spheres.
- The magnitude of tangential impact velocities during particle-to-particle and particle-to-wall contacts increases with increasing unbalance, while the magnitude of the normal impact velocities show only little difference.
- The particles develop a preferential orientation in the bed, even for small degree of unbalance. We were able to quantify in how far the bed expansion at which the fluidized bed operates can influence the preferential position as a function of the degree of unbalance. These are key observations influencing the evaluation of a fluidized bed for IFE target layering, since the targets' preferential position affects the time-averaged uniformity of the local heat flux on the outer surface.

#### LAYERING MODEL AND RELATED EXPERIMENTS

- The influence of a non-participating gas species in the void space of an unlayered target has been studied through literature research. Furthermore, a set of laboratory-scale experiments was set up to show that the problem could be generalized from DT diffusion through  $^3\text{He}$  to water vapor diffusion through air.
- The two-dimensional numerical description of a solid-gas interface poses a challenge due to the significant change in density across the interface. Through careful application of the basic principles of physics (in particular

the conservation of mass and energy), a model derived in the literature describing a solid-liquid phase change could be adapted to describe the sublimation and re-sublimation problem encountered in this application.

- The influence of the non-participating gas in the gaseous void was not included in this model; however, the limits within which the model is applicable have been defined. A number of relevant experiments and possible IFE prototypical conditions lie within these limits, making this model a unique and valuable tool in advancing the study of the layering process.
- By applying cylindrical coordinates in two dimensions, the movement of the interface in a spherical target could be modeled. The layering times computed in this analysis could be compared to the 1-D theoretical results, which assumed planar geometry.
- The expansion of the layering model to the second dimension enabled the analysis of the influence of a non-uniform heat flux on the outer shell of the target. The equilibrium layer thickness non-uniformity for a certain non-uniform heat flux applied on the outer surface could be found.
- The development of inner surface roughness features, previously reported in single sphere layering experiments could be demonstrated and explained from the simulations, arising from the unstable growth of small surface perturbations. However, these roughness features subside resulting ultimately in a smooth inner surface, which is an important target physics requirement. The formation and history of these roughness features

developing at the inner surface cannot be modeled when considering only one dimension.

- A water surrogate layering experiment was used to verify the mass redistribution predictions from the layering model. The modeling results for this case could also be used in explaining the occurrence of dark spots in the ice layer observed in the experiments.

#### COMBINING THE TWO MODELS

- By combining the fluidized bed and the layering model, the redistribution of fuel in the shell could be modeled based on the local heat flux imposed on the shell based on certain fluidization conditions. As the mass in the shell forms a more and more uniform layer on the inside of the shell, the degree of unbalance of the target decreases. This influences the orientation preference of the particle in the bed and thus the variation in local heat transfer coefficient on the surface of the shell.
- By integrating the two models, important information on the influence of certain fluidization parameters on the layering process could be explored, and recommendations depending on the demands of the layering process could be given.
- For example, the model provides the flexibility of assessing operation over a range of parameters to maintain surface damage within allowable limits, including flow speed, bed expansion, number of spheres and layering time.

- An example case was focused on low gas flow fluidization since particle-to-particle collisions in a bed, operating at bed expansions around two have been reported to damage the outermost surface of the shells severely. For low bed expansions, the results indicated that the shells were having a preferential position in the bed, with the heavier side of the particles pointing in the direction of the gas stream. This leads to a higher heat flux on the leading edge than on the trailing edge, affecting the layer formation inside the shell. However, the layer moves towards uniformity from the initial condition despite the non-uniform heat flux. This changes the degree of unbalance in the sphere and causes an assimilation of all three moments of inertia, leading to a more random orientation of the particles when fluidized at the same low bed expansion.
- The models were applied for parametric studies simulating the conditions expected in the MPLX experiments. In these experiments, pure deuterium is planned to be layered inside PAMS shells under IR irradiation. The example cases chosen in the simulation show how the models can be applied to gain valuable information on the application of a cryogenic fluidized bed for IFE target layering.

The model was then used to simulate deuterium layering under the range of expected conditions in the MPLX experiments. Major results include:

- At a high gas flow speed (or bed expansion), the randomness of the particles' orientations and the rate at which the particles spin lead to a more uniform time-

averaged temperature field, resulting in a layering time close to the simple estimate for a completely uniform heat flux. For example, for fluidization with two bed expansions (with a gas flow speed of  $\sim 1.0$  m/s), it took  $\sim 90$  minutes of simulated layering time for the fuel to reach a layer non-uniformity which was of the order of the surface perturbations (of the order of  $5 \mu\text{m}$ ); this corresponds to a  $1/e$  layering time of 25.2 minutes, which is in good agreement with the theoretical result based on the 1-D layering equations assuming a completely uniform heat flux on the outer surface.

- Decreasing the flow speed (or bed expansion) would reduce the number of collisions at high impact velocity (and the corresponding surface damage); however, this would result in a longer layering time. For example, reducing the gas flow speed at the inlet from 1.0 m/s to 0.8 m/s (at a pressure of 0.5 atm) decreases the bed expansion from  $\sim 2$  to  $\sim 1.6$ . The layering time constant increases from 25.2 to 35.6 min for a  $1/e$  improvement of the layer uniformity, increasing the layering time to  $\sim 125$  min until the pellets' unbalance is governed by the surface perturbations. The analysis showed that this increase in layering time due to lower gas velocities is the penalty for significantly reducing the number of collisions at impact velocities greater than 0.15 m/s. The analysis also showed that once the unbalance of the target is of the order of  $5 \mu\text{m}$ , the pellets lose their tendency to develop a preferential position, even at 1.6 bed expansions. This means that the layering process can be continued at 1.6 bed

expansions under a time-averaged isothermal environment until the surface roughness features are smoothed out.

- More information about collision damage, inner surface roughness requirements, layer uniformity requirements and potential volumetric heating devices would be required to provide more specific guidance in planning for the MPLX experiment.

The results from this study are very encouraging regarding the understanding of the integrated behavior of DT layering in a cryogenic fluidized bed. However, some issues remain which could be addressed by the following R&D as a complementary effort to the research presented here:

- It would be useful, once the MPLX experiment (using deuterium and an IR light) is underway, to compare the initial experimental results to the model predictions as a final confirmation of the accuracy and range of application of the model predictions.
- Depending on possible shortcomings observed in the initial results from this experiment (in particular regarding damage to the resulting surface finish, total layering time, final layer uniformity, or variation in layer quality between targets), the model would then be used to scan the range of available parameters and provide specific recommendations for improving the experimental setup and guiding future test campaigns.
- Further improvement to the layering model should include the capability to model the diffusion mechanism of D-T in the presence of a non-participating

gas ( $^3\text{He}$ ). Including this element will increase the accuracy of simulations for cases where the DT fill time of the targets exceeds the limit of application of the current model (about three days, as described in section 4.4).

- The fluidized bed model could be expanded to include different frit configurations. By including the possibility of applying different gas flow vectors to at the inlet of the bed, the impact of these changes on the bed behavior and the expected outcome on the layer formation could be quantified numerically.

At the time this research was done, to the knowledge of the author, development of a fluidized bed model with transient sphere parameters (including changes in the unbalance and mass moments of inertia of particles) had not yet been attempted. In addition, previous numerical attempts on multi-dimensional modeling of a solid-gas phase change in an enclosed volume could not be found. Thus, this work is groundbreaking in, for the first time, integrating the various physical phenomena of fluid mechanics, fluidization dynamics, thermodynamics, mass transfer, phase change, interface dynamics to develop an optimized numerical tool to understand the complex DT layering process under the unique set of cryogenic fluidized bed conditions.

## 6. Appendices

### APPENDIX A: Quantification of surface damage

The damage on the shell surface due to fluidization has been evaluated by post processing SEM pictures. The first visual inspections lead to the result that the surface is not necessarily roughened, but that the Au-Pd overcoat has been peeled off during hard particle-to-particle collisions. Utilizing National Instrument's Vision the area fraction of the pull out has been estimated, see tab. A-1. Example pictures of this analysis are shown in fig. 2.27.

Table A-1.: Measurements of the fraction of the damaged surface on shells exposed to several different fluidization scenarios and surface over-coat based on visual inspection of at least five photographs

	<u>0 Hour Au-Pd</u>	<u>16 Hours RT Au-Pd</u>	<u>0 Hour GDP</u>	<u>16 Hours RT GPD</u>
<u>Mean (in %)</u>	0.18	34.14	0.973	1.367
<u>St. Dev. (in %)</u>	0.0336	2.309	0.290	n/a

	<u>8 Hours cryo Au-Pd</u>	<u>16 Hours cryo Au-Pd</u>
<u>Mean (in %)</u>	2.255	4.799
<u>St. Dev. (in %)</u>	0.336	1.515

To quantify the additional heat flux reaching the shell due to damage in the reflective coating, the following considerations have been followed, where  $q_{rad}$  is the radiative heat flux and  $\sigma$  is the Stefan Boltzman constant.

$$q_{rad} = (1 - reflectivity)(\sigma T^4) \quad (A-1)$$

Assuming that the reflectivity of the undamaged surface is about 96 %, and the damaged surface doesn't reflect at all (0.0%), the heat flux can be computed by:

$$q_{rad} = [1 - (1 - damage) \cdot 0.96](\sigma T^4) \quad (A-2)$$

In approximation, since the difference between the undamaged and damaged surface is about 1, we can say, that the increase in heat flux is equal to the damage. See tab. A-2 for examples:

Table A-2: Example cases for the increase in radiative heat flux on the target surface for different degree of surface damage.

Damage	Heat flux formula	Heat flux	$\Delta q_{rad}$
0.00	$q_{rad} = (1 - 0.96)(\sigma T^4)$	$q_{rad} = 0.04 \cdot (\sigma T^4)$	0.00
0.02	$q_{rad} = (1 - (1 - 0.02) \cdot 0.96)(\sigma T^4)$	$q_{rad} = 0.0592 \cdot (\sigma T^4)$	$0.0192 * (\sigma T^4)$
0.04	$q_{rad} = (1 - (1 - 0.04) \cdot 0.96)(\sigma T^4)$	$q_{rad} = 0.0784 \cdot (\sigma T^4)$	$0.0384 * (\sigma T^4)$
0.08	$q_{rad} = (1 - (1 - 0.08) \cdot 0.96)(\sigma T^4)$	$q_{rad} = 0.1168 \cdot (\sigma T^4)$	$0.0768 * (\sigma T^4)$
0.16	$q_{rad} = (1 - (1 - 0.16) \cdot 0.96)(\sigma T^4)$	$q_{rad} = 0.1936 \cdot (\sigma T^4)$	$0.1536 * (\sigma T^4)$
0.32	$q_{rad} = (1 - (1 - 0.32) \cdot 0.96)(\sigma T^4)$	$q_{rad} = 0.3472 \cdot (\sigma T^4)$	$0.3072 * (\sigma T^4)$

Seeing that we start with a reflectivity of 96%, any multiple of 4% of damage double the incident heat flux. The importance of the additional heat flux depends on the magnitude of the radiative heat flux to the heat flux from the chamber walls and the background gas. Depending on the chamber parameters (wall temperature, gas temperature, gas species, injection velocity) the ratio of radiation/convection ranges between 1.5 to 0.3 W/m<sup>2</sup>.

## Point Damage Specifications

A different criterion for estimating whether the target surface will be acceptable for an IFE application can be taken from the “point design spec”. For this purpose the size of the damages and the number of damages within a certain size range have been estimated (again using Vision)

One should keep in mind that the size of the patch under the SEM might not be representative of the entire shell. Depending on the magnification factor of the SEM, the patch on the picture has a size of 25 um x 15.5 um (5000x) or 62 um x 38 um (2000x). That means, that we have 133 000 of these patches (5000x case) or 20 700 (2000x) on the entire 4mm shell.

This damage analysis needs to be considered under a statistical perspective, but the few dozen pictures available don't seem to be able to provide a statistic that is representative of the whole sphere surface. Tab. A-3 shows the largest damage for each picture.

Table A-3: Diameter of the largest point damage measured in each picture along with a count of smaller defects seen on the target surface

<b>8 hrs cryo Au-Pd</b>						
<b>5000x</b>						
	Smaller than 1um		1.0um < Size < 5.0um		Size > 5.0 um	
	#	Max size	#	Max size	#	Max size
1-1	4	0.89	0	-	0	-
2-1	6	0.98	0	-	0	-
3-1	2	-	3	-	1	5.27um
4-1	3	0.63	0	-	0	-
5-1	4	-	3	3.11	0	-

<b>8 hrs cryo Au-Pd</b>						
<b>2000x</b>						
	Smaller than 1um		1.0um < Size < 5.0um		Size > 5.0 um	
	#	Max size	#	Max size	#	Max size
1-2	n/a	-	3	2.72	0	-
2-2	n/a	-	3	2.98	0	-
3-2	n/a	-	11	3.60	0	-
4-2	n/a	-	2	2.24	0	-
5-2	n/a	-	6	-	2	8.1

<b>16hrs cryo Au-Pd</b>						
<b>5000x</b>						
	Smaller than 1um		1.0um < Size < 5.0um		Size > 5.0 um	
	#	Max size	#	Max size	#	Max size
1-1	5	-	4	1.58	0	-
2-1	9	-	4	1.80	0	-
3-1	4	-	1	2.74	0	-
4-1	2	-	5	3.02	0	-
5-1	10	-	3	2.86	0	-

<b>16hrs cryo Au-Pd</b>						
<b>2000x</b>						
	Smaller than 1um		1.0um < Size < 5.0um		Size > 5.0 um	
	#	Max size	#	Max size	#	Max size
1-2	n/a	-	4	4.82	0	-
2-2	n/a	-	16	2.69	0	-
3-2	n/a	-	10	-	2	5.889
4-2	n/a	-	6	-	3	5.865
5-2	n/a	-	12	2.74	0	-

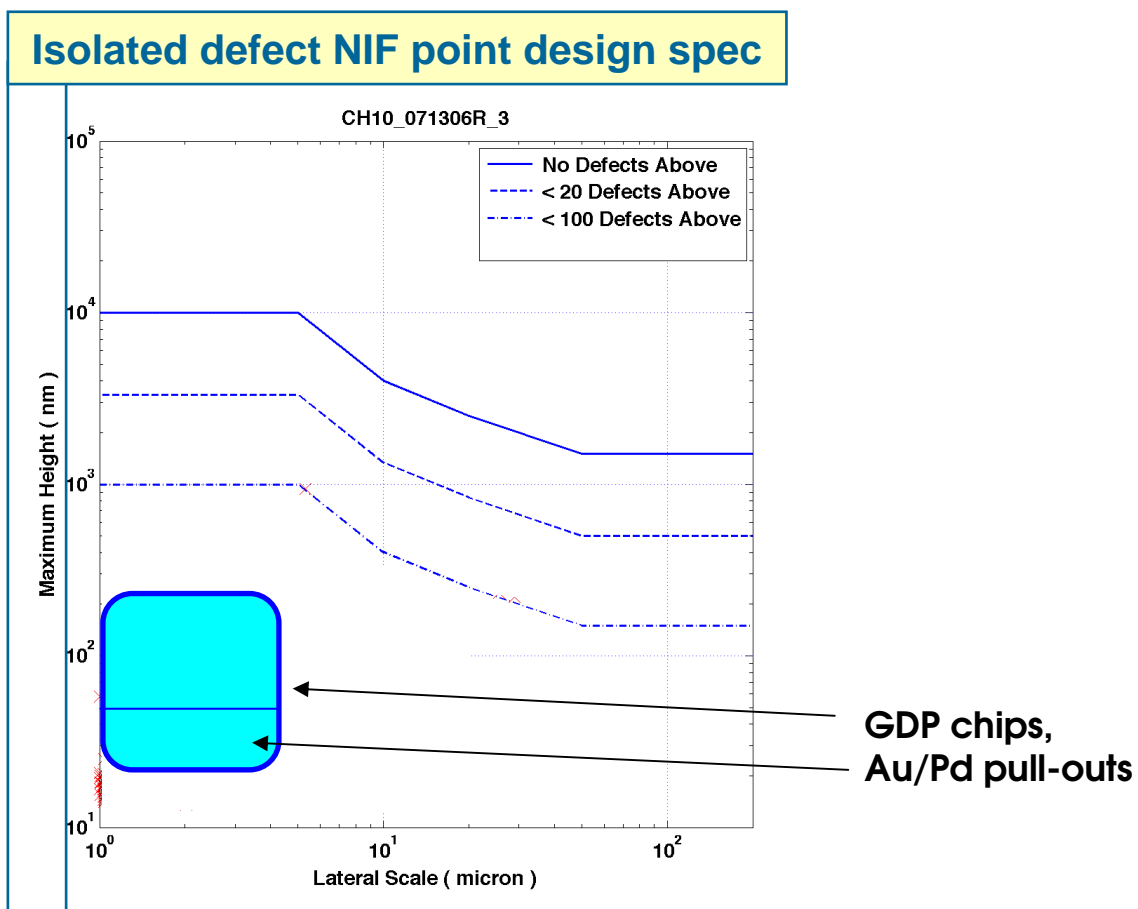


Figure A-1: The criterion for isolated point defect on the target surface for NIF (National Ignition Facility)<sup>16, 47</sup>. A similar analysis from an implosion physics point of view has yet to be done for HAPL targets, but these results can be used to show that the surface damage induced to the surface at two bed expansion might be acceptable.

## APPENDIX B: Estimating the Hertzian contact stress during collision

As a follow up to the discussion in Appendix A of the surface damage due to collisions during fluidization, this appendix describes estimates of the force applied on a surface due to a collision at a certain speed. This is especially interesting when analyzing the defects in the GDP over-coated PAMS shells since the SEM show a damage resembling failure following Hertzian contact stress. This sort of failure is characterized by breaking small conical chips out of the surface of a sphere. The equations follow Ugural and Fenster<sup>68</sup>.

The maximum stress due to the contact pressure  $\sigma_c$  is given by Eq. (B-1):

$$\sigma_c = 1.5 \frac{F}{\pi a^2} \quad (\text{B-1})$$

In this case,  $F$  is the force of contact and  $a$  is the contact area given by Eq. (B-2).  $E$  represents the Young's Modulus and  $r_1$  and  $r_2$  the radii of the two spheres.

$$a = 0.88 \left[ \frac{F (E_1 + E_2) r_1 r_2}{E_1 E_2 (r_1 + r_2)} \right]^{\frac{1}{3}} \quad (\text{B-2})$$

For two spheres with the same radius  $r$  and the same material, this simplifies to Eq. (B.3).

$$a = 0.88 \left[ \frac{F \cdot r}{E} \right]^{\frac{1}{3}} \quad (\text{B-3})$$

This leads to a contact stress following Eq. (B.4):

$$\sigma_c = 0.62 \left( \frac{F E^2}{r^2} \right)^{\frac{1}{3}} \quad (\text{B-4})$$

The time averaged impact force during the collision can be approximated by:

$$F_{av} = \frac{m \Delta v}{\Delta t} \quad (\text{B-5})$$

Using some approximate values shows that a failure in contact stress of the GDP overcoat is possible:

$$\Delta v = 1 \text{ m/s}, \quad \Delta t = \frac{1}{6000} \text{ s}, \quad m = 2 \cdot 10^{-6} \text{ Kg}, \quad E = 150 \text{ GPa} \rightarrow$$

$$\sigma_c = 250 \text{ MPa}$$

The assumed values of the Young's Modulus (150 GPa) and the maximum tensile strength for the GDP layer at cryogenic temperatures (250 MPa) are only estimates.

The fluidized bed model can provide an estimate of the average velocity difference of the collision contacts at different bed expansions and/or frit designs.

## APPENDIX C: Time step restriction in a special choice of damping coefficient

During the test of the numerical model, it has been noted that the choice of damping factor impairs the stability of the method (see figs. C-1 and C-2). Since this seemed counterintuitive at first, the following analysis has been performed to bring light into the subject.

First, the shift in resonance frequency due to the damping factor was explored, since this shift might alter the N-value that is being used in the convergence argument. The N-value is a measure of the number of time steps during which a collision contact occurs; this value is computed based on the natural frequency of the system and the time step size (see Eq. (C-5)). Clearly, an increase in the resonance frequency of the system (decrease in oscillation period) will result in a smaller number of time steps during the elastic contact for the same time step size which will change the convergence argument.

For this analysis, we need to compute the critical damping coefficient,  $c_c$ , defined in Eq.(C-1) and the natural frequency, defined in Eq.(C-2)

$$c_c = 2\sqrt{km} \quad (C-1)$$

$$\Theta_n = \sqrt{\frac{k}{m}} \quad (C-2)$$

Using the definition in Eq. (C-3), the resonance frequency of the damped system can be computed by Eq. (C-4).

$$\xi = \frac{c}{c_c} \quad (C-3)$$

$$\Theta_d = \Theta_n \sqrt{1 - \xi^2} \quad (C-4)$$

An overdamped system ( $\xi > 1$ ) in this model would be unphysical since it would lead to the shells not bouncing at all. Thus, we only consider underdamped cases ( $\xi < 1$ ). From Eq. (C-4) we can see that the oscillation frequency will become smaller for higher damping coefficients (as  $\xi$  assumes a value closer to 1). For the same value of the time step size,  $\Delta t$ , this means that larger N values are achieved when the damping coefficient is increased (see Eq.(C-5)).

$$N = \frac{\pi}{\Theta \Delta t} \quad (C-5)$$

As a result, the shift in the natural frequency of the damped system due to increased damping coefficient is not expected to cause any instabilities in the model.

Second, the ratio of energy taken out of the system in one time step due to damping (from the damping force shown in Eq. (C-7)) and the distance traveled estimated in Eq. (C-8)) and the total kinetic energy in the system (see Eq. (C-6)) can be estimated from Eq. (C-9).

$$E_{Kin} = \frac{1}{2}mv^2 \rightarrow v = \sqrt{\frac{2E_{Kin}}{m}} \quad (C-6)$$

$$F_{Damping} = v \cdot c_{eff} = \sqrt{\frac{2E_{Kin}}{m}} \cdot c_{eff} \quad (C-7)$$

$$s = \sqrt{\frac{2E_{Kin}}{m}} \cdot \Delta t \quad (C-8)$$

$$\frac{\Delta E}{E_{Kin}} \approx \frac{F_{Damping} \cdot s}{E_{Kin}} = \frac{2}{m} \cdot \Delta t \cdot c_{eff} \quad (C-9)$$

For the values used in this simulation (see tab. 2.5) the ratio reaches a value as high as 26% for  $c_{eff} = 0.01$ . This leads to the instabilities shown in fig. C-1 as compared to the smoother results shown in fig. C-2., in which the only value that changed was the  $c_{eff}$ .

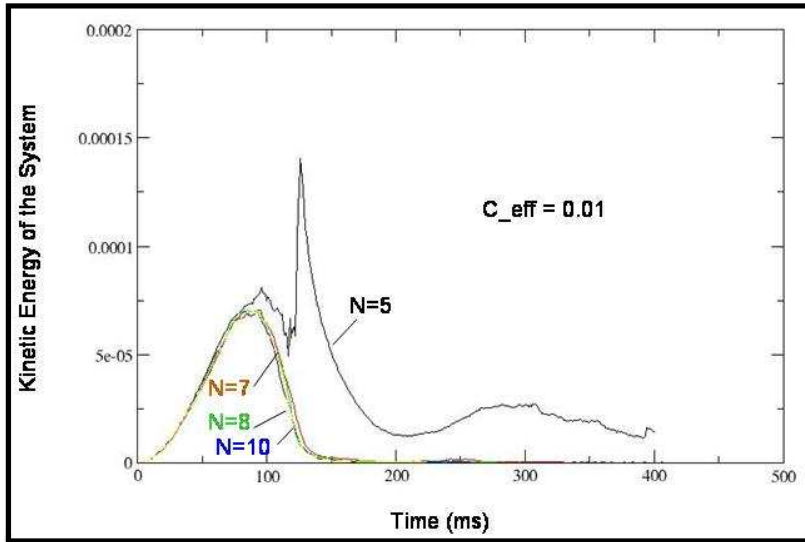


Figure C-1: In the case of an unfavorably chosen combination of damping coefficient, stiffness and time step size, the system might become unstable although unexpected.

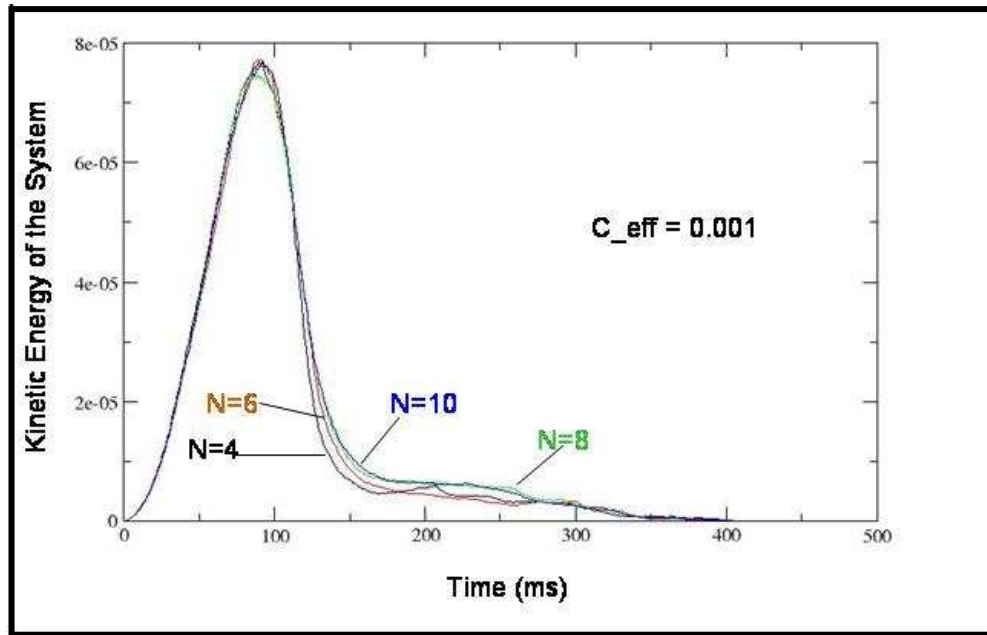


Figure C-2: The only difference between this case and the one depicted in C-1 is a smaller damping coefficient. With this choice of parameters, the system is stable for lower values of  $N$  than in the above case.

## APPENDIX D: Error estimates for the experimental results

Whenever experimental results are being quoted, an estimate of the error must be given along with the data. This section describes the error sources which have been considered in the experiments and shows estimated values for the overall errors.

### Error Estimates on Room Temperature Spin and Circulation Rates

The error of the room temperature spin- and circulation rate computation is shown in form of error bars in figs 2.26, 2.32 and 2.33.

In the spinning case, a rotation (mostly between 45 to 90 degrees) has been determined experimentally by following a marking on the shell over several frames of a high speed video. Knowing the number of frames it takes for the particle to spin a certain angle one can compute the spin rate. The main value reported is the mean of four to six measurements made at each bed expansion.

Two different error sources have been considered for the spin rate. The first one comes from the spread of the measurements; we consider one standard deviation  $\sigma$  to estimate the size of that uncertainty. The other error considered comes from the uncertainty of knowing the exact angle rotation within the number of frames we counted. This error is being accounted for by adding an uncertainty of  $\pm 1$  frame for every 45 degree spin following Eqs. (D-1) and (D-2).

$$\text{Number of frames for a 45 degree (1/8) rotation} = \frac{\text{frame rate}}{\text{spin rate}} \times \frac{1}{8} \quad (\text{D-1})$$

The uncertainty in the spin rate due to counting frames ( $\Delta\omega_{\text{frame}}$ ) can then be found depending on the average spin rate  $\bar{\omega}$ .

$$\Delta\omega_{\text{frame}} = \bar{\omega} - \frac{\text{frame rate}}{8 \cdot \left( \frac{\text{frame rate}}{8 \cdot \bar{\omega}} \pm 1 \right)} \quad (\text{D-2})$$

The total error is the computed by Eq. (D.3) following<sup>67</sup>.

$$\Delta\omega_{\text{tot}} = \sqrt{\Delta\omega_{\text{frame}}^2 + \sigma^2} \quad (\text{D-3})$$

The error on the bed expansion measurement has been determined to be 10%. For most videos, the interface between the gas and the gas-solid mixture falls within 10% of the mean value. The main reason for this uncertainty is the fact that this interface constantly moves and that it can't be clearly defined (e.g. it could be based on the position of the highest particle in the bed or on the average of the highest four).

The circulation rate has been determined by measuring the time (counting frames) it takes for the particle to move from the bottom of the bed to the top and back down to the bottom. The error bars for the circulation speed have been computed in a similar fashion than the spin rate, using the standard deviation and Eqs. (D-1) through (D-3). Since the circulation speed has a lower value than the spin rate, the error from counting the frames is less important. In addition, the position of the shell inside the bed is easier to determine than its orientation.

### **Error Estimates on Pressure Drop vs. Flow Rate Plot**

In fig. 2.23, the pressure drop throughout the bed is plotted for different flow speeds. The uncertainty analysis for this plot is mainly based on the measurement instrument error and the standard deviation of the measurements. However, since the flow speed cannot be measured directly, the effect of the measured parameters on the error of the flow speed has to be estimated by the error propagation formula, shown in Eqs. (D-4)<sup>67</sup>. This formula determined the error of a variable  $R$  based on errors of variables  $x_i$ , and is based on the Taylor series expansion of a multivariable function  $R = f(x_1, x_2, x_3, \dots, x_L)$ .

$$\theta_i = \frac{\delta R}{\delta x_i} \quad (\text{D-4a})$$

$$u_R = \pm \left[ \sum_{i=1}^L (\theta_i u_{x_i})^2 \right]^{\frac{1}{2}} \quad (\text{D-4b})$$

When determining the flow speed, the measured variables are the volumetric flow speed and the cross sectional area of the tube. The errors in the volumetric flow speed are given in tab. D-1, the error in the cross sectional area is computed from the manufacturer's tolerance in the radius.

Table D-1: Different types of errors in the flow speed analysis.

Value measured:	volumetric flow rate
- resolution uncertainty:	0.5 resolution = 1 SCFH
- repeatability:	3% of measured value (given by manufacturer)
- accuracy	6% of measured value (given by manufacturer)
Conversion from volumetric flow rate to flow speed:	
- cross sectional area of the tube:	$A = \pi r^2$
- error in radius:	1%

The total error for the volumetric flow rate can be computed by the RSS method Eq. (D-5). The individual errors  $e_k$  are the ones given in tab. D-1

$$u_x = \pm \sqrt{\sum_{k=1}^K (e_k)^2} \quad (\text{D-5})$$

The error for the flow speed is then computed by Eqs. (D-6))

$$v = \frac{\dot{V}}{A} = \frac{\dot{V}}{\pi r^2} \quad (\text{D-6})$$

$$\Delta v = \pm \sqrt{\left(\frac{1}{\pi r^2} \Delta \dot{V}\right)^2 + \left(-\frac{2 \dot{V}}{\pi r^3} \Delta r\right)^2}$$

In this case, the error contribution from the cross sectional area (or radius of the tube) is one order of magnitude smaller than the error from the volumetric flow rate uncertainty.

The pressure drop can be measured directly. In this case, the individual errors (resolution error, instrument error and standard deviation) have to be considered when computing the total error through Eq. (D.5). Since separate measurements for the pressure drop at a given flow rate are taken, the standard deviation is considered to account for that uncertainty.

The calculation resulting in the error bars shown in figs. 2.24 and 2.25 (fluidization experiments are compared with numerical computations and empirical results) are covered next. The uncertainty in the flow speed for the nitrogen case (fig. 2.25) is determined as described above.

When the system of Delrin spheres was fluidized with water (fig. 2.24), a different method was applied to measure the flow speed of the water. In this case, the fluidization was performed for one minute, and the water was collected in a beaker. This way provided accurate account of the flow rate. Applying Eq. (D-4b) to compute the error in the water flow rate measurements, results in Eq. (D-7).

$$v = \frac{\dot{V}}{A} = \frac{\dot{V}}{\pi r^2} = \frac{V_{\text{collected}}}{t_{\text{elapsed}}} \cdot \frac{1}{\pi r^2} \quad (\text{D-7})$$

$$\Delta v = \pm \sqrt{\left(\frac{\Delta V_{\text{collected}}}{t_{\text{elapsed}} \pi r^2}\right)^2 + \left(\frac{V}{t_{\text{elapsed}}^2} \frac{\Delta t}{\pi r^2}\right)^2 + \left(\frac{2V_{\text{collected}}}{t_{\text{elapsed}} \cdot \pi r^3} \Delta r\right)^2}$$

The error in the void fraction is equal to the error in the particle fraction, since:

$$1 = \varepsilon_p + \varepsilon_v \quad (\text{D-8})$$

The particle fraction is computed from Eq. (D-9).

$$\varepsilon_p = \frac{\text{Volume of particles}}{\text{Bed area} \cdot \text{Bed height}} \quad (\text{D-9})$$

The bed height is read on the metric scale attached to the side of the bed. Due to the bubbling behavior of the bed (as shown in fig. 2.25 for the case of gas fluidization), the uncertainty in determining the bed height is fairly large (estimated at 3mm + 5% of the recorded value). In the case of water fluidization, the bed height could be determined more accurately, as the bed height does not fluctuate as much as for a gas fluidized bed.

Applying Eqs.(D-4) to Eq. (D-9), yields the following estimate for the error in particle fraction:

$$\Delta\varepsilon_p = \sqrt{\left(\frac{\Delta V_{\text{particle}}}{\text{Bed area} \cdot \text{Bed height}}\right)^2 + \left(\frac{\Delta \text{Bed height} \cdot V_{\text{particle}}}{\text{Bed area} \cdot \text{Bed height}^2}\right)^2} \quad (\text{D-10})$$

The uncertainty in the volume of the particles has been determined next. In the case of the Delrin spheres, the manufacturer's tolerance in particle diameter could be used leading to a fairly accurate account of the volume of all particles (25  $\mu\text{m}$  in diameter tolerance of a 3.95 mm sphere gives an error of less than 4 %).

In the case of the PAMS shells, the volume of a number of shells was measured by recording the volume of water displaced by the particles, when forced under water. In contrast to the radius measurements, this method of determining the particle volume brought the error down to  $\sim 4.4\%$  (see section 2.4.3).

## APPENDIX E – Influence of a non-participating gas species in the gaseous void (theory and experiment)

In this section, the influence on the layering physics of a non-participating gas in the void space of the IFE targets will be analyzed. First, the theoretical model derived by Martin et al.<sup>4</sup> is presented, where the mass transfer of the fuel through the void space is described with a simple diffusion model. Second, the model derived by T.P. Bernat et al.<sup>51</sup> is presented, in which the same physical process is modeled as a two species diffusion problem following the Stefan flow equations.

Experimental results presented by Hoffer and Foreman<sup>52</sup> indicate confirmation of these equations in the case of a deuterium-tritium (DT) filled target. A gradual buildup of <sup>3</sup>He from the beta-decay in the void space is observed, which impedes the mass transfer of DT through the void space, and increases layering times.

The layering model described in section 3 does not account for the presence of a non-participating gas species. A 2-D description of the diffusion in the void can be added to the model, but has not been done in this work. However, the effect of the presence of the non-participating gas is negligible, if the partial pressure of the <sup>3</sup>He falls below a certain threshold value. The 1-D diffusion equations derived in this section have been used to estimate the age of the DT, up to which the layering model can be applied.

Finally, the diffusion equations are applied to a scenario where the redistribution of water in a 4 mm PAMS shell in the presence of nitrogen (air) is studied. A companion experiment has been set up, the measurements confirming the validity of these equations in the water layering case.

### SIMPLE DIFFUSION MODEL

Martin et al. treat the diffusion of species A through species B like solid state diffusion. In this case, the species B is stationary and acts like an obstacle to the diffusion of species A. Eqs. (E-1) through (E-6) describe this model. Due to the solid state diffusion assumption, only the first term on the right hand side of Eq. (E-1) contributes to the mass diffusion. Please refer to fig. 3.1 for a schematic and the nomenclature at the end of this appendix for an explanation of the symbols used in this derivation.

The molar flux  $N_A$  is found by the diffusion Eq. (E-2).

$$N_A = -cD_{AB} \frac{dx_A}{d\hat{x}} + x_A(N_A + N_B) \quad (\text{E-1})$$

$$N_A = -cD_{AB} \frac{dx_A}{d\hat{x}} \quad (\text{E-2})$$

Assuming that the concentrations of species A and B are known at the interfaces, the boundary conditions are  $\frac{dN_A}{d\hat{x}} = 0$  (everywhere),  $x_A(\hat{x} = 0) = x_{A,h1}$ , and  $x_A(\hat{x} = L) = x_{A,h2}$

$$\rightarrow \text{apply B.C. 1:} \quad -cD_{AB} \frac{dx_A}{d\hat{x}} = C_1$$

$$\frac{dx_A}{d\hat{x}} = -\frac{C_1}{cD_{AB}} \quad x_A(\hat{x}) = -\frac{C_1}{cD_{AB}} \hat{x} + C_2$$

$$\rightarrow \text{apply B.C. 2:} \quad x_A(\hat{x}) = x_{A,h1} - \frac{C_1}{cD_{AB}} \hat{x}$$

$$\rightarrow \text{apply B.C. 3:} \quad x_{A,h2} = x_{A,h1} - \frac{C_1}{cD_{AB}} L$$

$$C_1 = \frac{cD_{AB}(x_{A,h1} - x_{A,h2})}{L}$$

As a final result, we get

$$x_A(\hat{x}) = x_{A,h1} - \frac{\hat{x}}{L}(x_{A,h1} - x_{A,h2}) \quad (\text{E-3})$$

This shows that at steady state, a linear concentration profile can be expected, independent of the diffusion coefficient.

The slope of the concentration profile is:

$$\frac{dx_A}{d\hat{x}} = -\frac{1}{L}(x_{A,h1} - x_{A,h2}) \quad (\text{E-4})$$

Including this result in Eq. (E-2) gives:

$$N_A = -cD_{AB} \frac{dx_A}{d\hat{x}} = \frac{cD_{AB}}{L}(x_{A,h1} - x_{A,h2}) \quad (\text{E-5})$$

Applying the relation between the molecular flux and the movement of the interface, leads to Eq. (E-6)

$$-\dot{\delta} = \frac{N_A}{\rho_s}$$

Per definition:

$$c \cdot x_{A,h1} = c_{A,h1} = \frac{P_{A,h1}}{R_{gas} T_{x=h1}} \quad \text{and} \quad c \cdot x_{A,h2} = c_{A,h2} = \frac{P_{A,h2}}{R_{gas} T_{x=h2}}$$

$$\dot{\delta} = \frac{dh_1}{dt} = -\frac{D_{AB}}{\rho_s R_{gas} L} \left( \frac{P_{A,h1}}{T_{h1}} - \frac{P_{A,h2}}{T_{h2}} \right) \quad (\text{E-6})$$

In this case it is assumed that the partial pressures of species A at the interfaces are equal to the vapor pressures corresponding to the interface temperatures.

The diffusion coefficient needs to be computed for different pressures and temperatures. In the case of DT, the theory of ordinary diffusion in gases at low temperatures<sup>67</sup> is applied to compute the diffusion coefficient from the Lennard Jones potential. The following values have been computed from Souers<sup>57</sup>, for an example temperature of 19.65 K (very close to the triple point 19.79 K).

$$D_{AB} = 0.0018583 \frac{\sqrt{T^3 \left( \frac{1}{M_A} + \frac{1}{M_B} \right)}}{P \sigma_{AB}^2 \Omega_{D_{AB}}} \quad (\text{in cm}^2/\text{s, pressure in atm}) \quad (\text{E-7})$$

$$M_A = 5 \text{ g/mol (for the DT)} \quad M_B = 3 \text{ g/mol (for the } ^3\text{He)}$$

$$\sigma_{AB} = \frac{1}{2} (\sigma_A + \sigma_B) \quad (= 2.752 \text{ \AA for DT in } ^3\text{He}) \quad (\text{E-8a})$$

$$\varepsilon_{AB} = \sqrt{\varepsilon_A \varepsilon_B} \quad (\text{E-8b})$$

$$\frac{R_{gas}}{\varepsilon_{AB}} = 19.4 \text{ K} \quad \text{for DT and } ^3\text{He} \quad (\text{E-8c})$$

$$\Omega_{D_{AB}} \text{ is tabulated for } \frac{R_{gas} T}{\varepsilon_{AB}} \quad (\text{E-8d})$$

$$\Omega_{D_{AB}} \cong 1.430 \quad \text{for DT and } ^3\text{He and 19.65 K} \quad (\text{E-8e})$$

In order to find the speed of the interface at any given time, Eqs. (69) in section 3.2) and (E-6) have to be solved simultaneously. The temperature difference between the two interfaces has to satisfy both the heat and the mass transfer equations. A closed solution for this problem could not be found, but the two equations can be solved numerically.

### THE STEFAN FLOW MODEL

In the second approach to describe the influence of a non-participating gas, the Stefan flow model is applied to combine the heat and mass transfer equations. The starting point is again Eq. (E-1); accounting for the movement of species A and setting the mass flux of the nonparticipating gas to zero ( $N_B = 0$ ) lead to equation (E-9).

$$N_A = -cD_{AB} \frac{dx_A}{d\hat{x}} + x_A N_A \quad (\text{E-9})$$

The boundary conditions are:  $\frac{dN_A}{d\hat{x}} = 0$  (BC 1) over the entire domain,  $x_A(0) = x_{A,h1}$  (BC 2), and  $x_A(L) = x_{A,h2}$  (BC 3).

Applying BC 1 to Eq. (E-9), we get:

$$N_A = \frac{-cD_{AB} \frac{dx_A}{d\hat{x}}}{1 - x_A} = -C_3 \quad (\text{E-10})$$

Integrating:

$$cD_{AB} \int \left( \frac{1}{1 - x_A} \frac{dx_A}{d\hat{x}} \right) d\hat{x} = C_3 \hat{x} + C_4$$

$$cD_{AB} \int \frac{1}{1 - x_A} dx_A = C_3 \hat{x} + C_4$$

$$-cD_{AB} \ln(1 - x_A) = C_3 \hat{x} + C_4 \quad (\text{E-11})$$

Applying BC 2  $\rightarrow C_4 = -cD_{AB} \ln(1 - x_{A,h1})$

$$cD_{AB} \ln\left(\frac{1-x_A}{1-x_{A,h1}}\right) = -C_3 \hat{x} \quad (\text{E-12})$$

$$\text{Applying B.C. 3} \rightarrow -C_3 = \frac{1}{L} cD_{AB} \ln\left(\frac{1-x_{A,h2}}{1-x_{A,h1}}\right) \quad (\text{E-13})$$

$$\ln\left(\frac{1-x_A}{1-x_{A,h1}}\right) = \frac{\hat{x}}{L} \ln\left(\frac{1-x_{A,h2}}{1-x_{A,h1}}\right) \quad (\text{E-14})$$

Inserting Eq. (E-13) in Eq. (E-10) leads to:

$$N_A = -C_3 = \frac{cD_{AB}}{L} \ln\left(\frac{1-x_{A,h2}}{1-x_{A,h1}}\right) \quad (\text{E-15})$$

For binary species, since  $\frac{x_{B,h2}}{c} = c_{B,h2}$  this can be rewritten:

$$N_A = \frac{cD_{AB}}{L} \ln\left(\frac{x_{B,h2}}{x_{B,h1}}\right) = \frac{cD_{AB}}{L} \ln\left(\frac{c_{B,h2}}{c_{B,h1}}\right) \quad (\text{E-16})$$

The concentration of the species A and B at the two interfaces are found by assuming that the partial pressure of species A is equal to its saturated vapor pressure at the temperature of the interface  $\frac{P_v(T_{h1})}{P_{tot}} = c_{A,h1}$ . This allows us to write  $x_B = x_B(T)$ .

In order to combine the heat and the mass transfer, Eqs. (E-16) and (Eq. (69) in section 3.2), the Taylor series expansion of Eq. (E-16) is needed:

$$\text{In general: } f(x_0 + \Delta x) = f(x_0) + \left.\frac{df}{dx}\right|_{x=x_0} \cdot \Delta x + \text{HOT}$$

Specifically for the natural logarithm:

$$\ln(1 + \Delta x) \cong \Delta x \quad (\text{E-17})$$

$$\begin{aligned} \ln\left(\frac{f(x_0 + \Delta x)}{f(x_0)}\right) &\cong \ln\left(\frac{f(x_0)}{f(x_0)} + \frac{1}{f(x_0)} \cdot \left.\frac{df}{dx}\right|_{x=x_0} \Delta x + H.O.T.\right) \\ &= \ln\left(1 + \frac{1}{f(x_0)} \cdot \left.\frac{df}{dx}\right|_{x=x_0} \Delta x + H.O.T.\right) \end{aligned} \quad (\text{E-18})$$

Combining Eqs. (E-17) and (E-18) yields:

$$\ln\left(\frac{f(x_0 + \Delta x)}{f(x_0)}\right) \cong \frac{1}{f(x_0)} \cdot \frac{df}{dx}\bigg|_{x=x_0} (x_2 - x_1)$$

Apply this to the following part of Eq. (E-16) results in:

$$\ln\left(\frac{x_{B,h2}}{x_{B,h1}}\right) \cong \frac{1}{x_{B,h1}} \cdot \frac{dx_B}{dT}\bigg|_{T=T_{h1}} (T_{h2} - T_{h1})$$

$$x_B + x_A = 1 \quad \rightarrow \quad \frac{dx_B}{dT} = -\frac{dx_A}{dT}$$

Inserting this in Eq. (E-16) leads to:

$$N_A = \frac{cD_{AB}}{L} \ln\left(\frac{x_{B,h2}}{x_{B,h1}}\right) = \frac{cD_{AB}}{L} \left(-\frac{1}{x_{B,h1}} \cdot \frac{dx_A}{dT}\bigg|_{T=T_{h1}} (T_{h2} - T_{h1})\right) \quad (\text{E-19})$$

The temperature difference can be found from the heat transfer equation. This derivation has been shown in section 3.1, and resulted in Eq. (69). Combining both results leads to Eq. (E-20) and ultimately to Eq. (E-21).

$$N_A = \frac{cD_{AB}}{L} \frac{1}{x_{B,h1}} \cdot \frac{dx_A}{dT}\bigg|_{T=T_{h1}} \cdot \left(-\frac{N_A \cdot \Delta H_s}{k_{ice}} \cdot 2d + \frac{\dot{q}''}{k_{ice}} 2d\delta\right) \quad (\text{E-20})$$

$$N_A = \left(-\frac{cD_{AB}}{L} \frac{1}{x_{B,h1}} \cdot \frac{dx_A}{dT}\bigg|_{T=T_{h1}} \cdot \frac{N_A \cdot \Delta H_s}{k_{ice}} \cdot 2d\right) + \left(\frac{cD_{AB}}{L} \frac{1}{x_{B,h1}} \cdot \frac{dx_A}{dT}\bigg|_{T=T_{h1}} \cdot \frac{\dot{q}''}{k_{ice}} 2d\delta\right)$$

$$N_A \cdot \left(1 + \frac{cD_{AB}}{L} \frac{1}{x_{B,h1}} \cdot \frac{dx_A}{dT}\bigg|_{T=T_{h1}} \cdot \frac{\Delta H_s}{k_{ice}} \cdot 2d\right) = \left(\frac{cD_{AB}}{L} \frac{1}{x_{B,h1}} \cdot \frac{dx_A}{dT}\bigg|_{T=T_{h1}} \cdot \frac{\dot{q}''}{k_{ice}} 2d\delta\right)$$

$$N_A = \frac{\left( \frac{cD_{AB}}{L} \frac{1}{x_{B,h1}} \cdot \left( \frac{dx_A}{dT} \right)_{T=T_{h1}} \right) \cdot \frac{\dot{q}''}{k_{ice}} \cdot 2d\delta}{\left( 1 + \frac{cD_{AB}}{L} \frac{1}{x_{B,h1}} \cdot \left( \frac{dx_A}{dT} \right)_{T=T_{h1}} \right) \cdot \frac{\Delta H_s}{k_{ice}} \cdot 2d} = \frac{\delta}{\left( \frac{1}{\frac{2cD_{AB}d\dot{q}''}{L \cdot x_{B,h1}k_{ice}} \left( \frac{dx_A}{dT} \right)_{T=T_{h1}}} + \frac{\Delta H_s}{\dot{q}''} \right)}$$

$$N_A = \frac{\delta}{\left( \frac{L \cdot x_{B,h1}k_{ice}}{2cD_{AB}d\dot{q}'' \left( \frac{dx_A}{dT} \right)_{T=T_{h1}}} + \frac{\Delta H_s}{\dot{q}''} \right)} \quad (\text{E-21})$$

21)

Applying  $\dot{\delta} = -\frac{N_A}{\rho_s}$  results in:

$$\dot{\delta} = -\frac{\delta}{\left( \frac{L \cdot x_{B,h1}k_{ice}\rho_s}{2cD_{AB}d\dot{q}'' \left( \frac{dx_A}{dT} \right)_{T=T_{h1}}} + \frac{2\Delta H_s\rho_s}{\dot{q}''} \right)} \quad (\text{E-22})$$

Solving this first order ODE leads to

$$\delta(t) = \delta_0 \exp \left( \frac{-t}{\left( \frac{L \cdot x_{B,h1}k_{ice}\rho_s}{2cD_{AB}d\dot{q}'' \left( \frac{dx_A}{dT} \right)_{T=T_{h1}}} + \frac{\Delta H_s\rho_s}{\dot{q}''} \right)} \right) \quad (\text{E-23})$$

This means that the solution of the combined heat and mass transfer problem can be solved in one expression. A 1/e decrease in the difference in layer thickness will be achieved every  $\tau$  minutes, where  $\tau$  is given by:

$$\tau = \frac{L \cdot x_{B,h1} k_{ice} \rho_s}{2cD_{AB} d \dot{q}'' \left. \frac{dx_A}{dT} \right)_{T=T_{h1}}} + \frac{\Delta H_s \rho_s}{\dot{q}''} \quad (\text{E-24})$$

The temperature-dependent gradient in the concentration of species A can be replaced by the gradient of the saturated vapor pressure over the solid by applying the ideal gas law:

$$\frac{x_{B,h1}}{c \left. \frac{dx_A}{dT} \right)_{T=T_{h1}}} = \frac{c_{B,h1}}{c \left. \frac{dc_A}{dT} \right)_{T=T_{h1}}} = \frac{P_{B,h1} R_{gas} T}{P \left. \frac{dP_A}{dT} \right)_{T=T_{h1}}}$$

This leads to the final result of Eq. (E-25), as quoted by Hoffer and Foreman<sup>52</sup>:

$$\tau = \frac{L \cdot k_{ice} \cdot \rho_s \cdot R_{gas} \cdot T \cdot P_{B,h1}}{2 \cdot D_{AB} \cdot d \cdot \dot{q}'' \cdot P \cdot \left. \frac{dP_A}{dT} \right)_{T=T_{h1}}} + \frac{\Delta H_s \rho_s}{\dot{q}''} \quad (\text{E-25})$$

Similarly to the previous case, the diffusion coefficient needs to be adjusted to the temperature and pressure in the vapor space (see Eqs. E-7 and E-8)

## COMPARISON OF THE TWO MODELS FOR DT LAYERING

In the two papers analyzed previously, the authors calculated the redistribution rates for DT in the presence of <sup>3</sup>He. The results from the two models are compared next. In contrast to the Stefan flow model (second case), for the simple diffusion model (first case), the redistribution time (for a 1/e improvement) could not be found explicitly. In order to compare the two models a certain layering scenario needed to be assumed. The speed of the interface under certain input parameters has been computed using both models.

The properties of the two species, DT and <sup>3</sup>He are found using Souers<sup>57</sup>. The temperature dependent vapor pressure of DT is given in Eq. (E-6)<sup>57</sup>. The total pressure can be computed adding the partial pressure of the DT and the partial pressure of <sup>3</sup>He, which depends on the age of the tritium.

$$\ln P_{v,DT} = 10.821 - \frac{150.34}{T} + 2.2389 \cdot \ln T \quad (\text{E-26})$$

$$P_{v,DT} = 50061 \cdot \exp\left(-\frac{150.34}{T} + 2.2389 \cdot \ln T\right) \quad (\text{E-27})$$

$$\frac{d}{dx} \exp(f(x)) = \exp(f(x)) \cdot \frac{d}{dx} f(x)$$

$$\frac{dP}{dT} = 50061 \cdot \exp\left(-\frac{150.34}{T} + 2.2389 \cdot \ln T\right) \cdot \left(\frac{150.34}{T^2} + 2.2389 \frac{1}{T}\right) \quad (\text{E-28})$$

$$n_{DT,fill} = \frac{P_{fill}}{R_{gas} T_{fill}}$$

$$n_{3He} = \frac{1}{2} n_{DT,fill} \left(1 - \exp\left(-\frac{t}{\tau}\right)\right)$$

$$\tau_{tritium} = \frac{\ln 2}{t_{1/2,tritium}}; \quad t_{1/2,tritium} = 12.3 \text{ years}$$

$$P_{3He} = n_{3He} R_{gas} T$$

$$P_{3He} = \frac{1}{2} \left(\frac{P_{Fill}}{T_{fill}}\right) T \left[1 - \exp\left(-\frac{t}{156080}\right)\right] \quad (\text{E-29})$$

For the case presented in fig. E-1, the speed of the interface has been computed using both models. The layer non-uniformity has been arbitrarily chosen to be one half of the equilibrium thickness. Using the geometry described in Bernat et al.<sup>51</sup>, the radius of the sphere is 15mm and the equilibrium thickness is 1.547 mm. With increasing concentration of the non-participating gas (<sup>3</sup>He) in the vapor phase between the two interfaces, the solutions of the heat and mass transfer equations from the two models become closer. This can be explained by a decreasing absolute <sup>3</sup>He flux as the total concentration of <sup>3</sup>He increases.

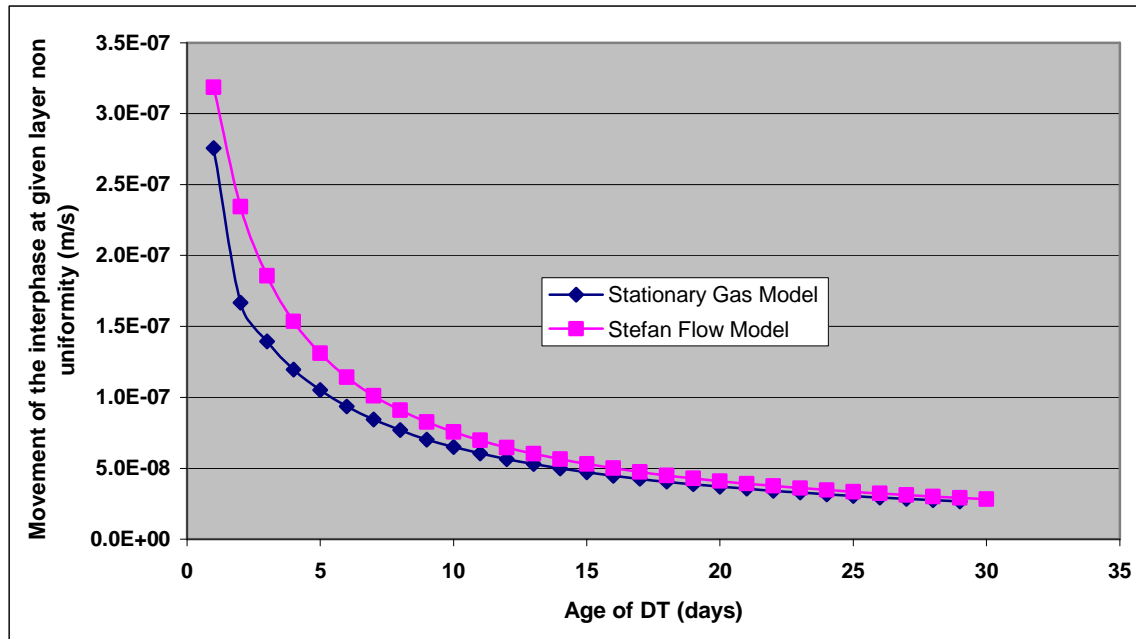


Figure E-1: Speed of interface movement towards equilibrium calculated from the two models as a function of tritium age. With increasing age of the tritium, the  $^3\text{He}$  density increases, slowing the diffusion process. In this case, the layer non-uniformity  $\delta$  was assumed to be one half of the equilibrium thickness  $d$ .

#### ESTIMATE THE TRITIUM AGE FOR WHICH THE LAYERING MODEL GIVES GOOD RESULTS WITHOUT CONSIDERING THE PRESENCE OF THE NON-PARTICIPATING GAS

After showing a significant influence of the  $^3\text{He}$  on the layering speed in the case studied in the literature, we posed the question of the validity of the model output from our 2-D layering model excluding the effects of a non-participating gas species. The effects of the  $^3\text{He}$  do not have to be considered when layering pure deuterium (since there will be no tritium, and hence no  $^3\text{He}$ ), as will be done in the MPLX, but ultimately it would be important to know the limit of the applicability of the model to DT layering studies. Thus, the increasing influence of the  $^3\text{He}$  was assessed in order to set an age limit above which the layering model would need to be expanded to account for the  $^3\text{He}$ .

Since the Stefan flow model as derived in 1-D in the previous section can give the increase in layering time in one simple equation, Eq. (E-25), it was used in this analysis. Tab. E-1 shows the numerical values used in this analysis, which ultimately results in fig. 4.9. The increase in layering time per day is initially (almost) constant, since the half life of the tritium is large compared to the time scales considered here (12.3 years compared to a few weeks). The quantitative result is an increase of the layering time (Eq. E-25 first term on the right hand side) by about 105 s per day depending on the fill fraction, the target geometry and the layering temperature

(parameters from tab. E-1 were used to estimate the increase in layering time from Eq. (E-25).

Table E-1  
Parameters used in the analysis of the increase in layering time due to the accumulation of  $^3\text{He}$  in a HAPL size target.

Symbol	Value used	Units
$P_{v,DT} (19.65 \text{ K})$	18 727	Pa
$\left. \frac{dP_{v,DT}}{dT} \right)_{T=19.65 \text{ K}}$	9425	Pa/K
$P_{fill}$	$1.1721 \times 10^8$	Pa
$T_{fill}$	295	K
L	$3.20 \times 10^{-3}$	m
D	$4.00 \times 10^{-4}$	m
$\dot{q}''$	50 000	W/m <sup>3</sup>
$k_{ice}$	0.303	W/m-K
$\rho_s$	50400	Mols/m <sup>3</sup>
$R_{gas}$	8.314	J/mol-K
$D_{AB}$	$\frac{0.110242}{P_{tot}}$	m <sup>2</sup> /s
$\Delta H_s$	$78.6 \times 10^6$	J/m <sup>3</sup>
<b>From above parameters:</b> $\frac{d\tau}{dt}$	105	s/day

#### EXPERIMENTAL MASS REDISTRIBUTION EXPERIMENTS USING WATER AS A SURROGATE (IN THE PRESENCE OF AIR AS A NONPARTICIPATING GAS)

While developing the layering model (see section 3) possible validation experiments were evaluated. The complexity of the process of filling and cooling the shells without bursting or crushing them drove us to consider other options to layering deuterium filled shells.

As one of these options, the possibility of layering pure water injected into a PAMS (polyalphamethylstyrene) shell was investigated. The water would be filled into the shell by drilling, filling and sealing it with UV glue. In order to test the model's

capabilities to predict mass redistribution while the shell would be exposed to a non-uniform heat flux, it was proposed to glue the filled shell to the end of a needle and insert it into a cooling gas stream. However, after filling half of the shell's volume with water, the other half would be filled with air, which would act as a non-participating gas, similar to the  $^3\text{He}$  in the previous section. By applying the 1-D model presented in the previous section and using the appropriate values for water (see tab. 3.3), the layering times in this experiment could be estimated.

Due to the relatively low vapor pressure over ice (compared to DT), very low partial pressures of air will largely influence the layering times. While not being fully applicable as a model validation case, it seemed interesting to conduct a set of experiments for a single stationary PAMS shell containing water and a vapor-air mixture to observe experimentally the effect of non-participating gas on ice layering.

As a first step, a preliminary computation yielded values for the partial pressure of the gas that would lead to a situation in which both terms on the right hand side of Eq. (E-25) would be of the same order. In that way, the temperature and the diffusion restriction on the mass redistribution would be of the same order.

Depending on the exact geometry and temperature, it was concluded (as can be seen from fig. 4.9) that the partial pressure of the air and the vapor pressure over ice at the inner surface temperature have to be of the same order of magnitude ( $\sim 600$  Pa at freezing point). In order to achieve a value of non-participating gas pressure that far below the atmospheric pressure, the shell would need to be filled and plugged with UV glue and the excess air evacuated by permeation in vacuum. The pressure in the shell was determined by Eq. (E-30) as the permeation rate of nitrogen through the PAMS shell had been measured in a prior experiment. Knowing the permeation rate and the time the shell had been exposed to vacuum, the pressure inside the shell could be computed. The minimum pressure of the air in the shell is ultimately determined by the minimum pressure on the outside of the shell, which has to be high enough to provide enough cooling power to the shell to counteract the volumetric heating. We determined that the gas pressure had to be of the order of 1/10 of an atmosphere in order to give enough cooling.

The same setup as the one presented in section 3.5.5 was used as a heating apparatus, shining filtered IR-light onto the shell. The measured volumetric heat flux was slightly higher than the one reported in the cuvette experiment, mainly because of the reduced volume and the use of reflectors to get multiple passes of the light through the water. We measured this heat flux to be 0.20 W/cc.

$$P = \Delta P \cdot \exp\left(-\frac{t}{\tau_{Perm}}\right) \quad (\text{E-30})$$

$$\tau_{Perm} = 54 \text{ hrs} \quad (\text{measured in separate experiment})$$

For water and air as binary mixture, the following diffusion coefficient was used<sup>66</sup>:

$$D_{AB} = \frac{1}{P_{tot}} (P_{crit,A} P_{crit,B})^{\frac{1}{3}} (T_{crit,A} T_{crit,B})^{\frac{5}{12}} \left( \frac{1}{M_A} + \frac{1}{M_B} \right)^{\frac{1}{2}} a_{diff} \cdot \left( \frac{T}{\sqrt{T_{crit,A} T_{crit,B}}} \right)^{b_{diff}} \quad (\text{E-31})$$

Once the air (nitrogen) pressure in the shell was reduced to satisfactory levels (after pumping for five days, the pressure in the shell was ~0.1 atm), a circulating gas stream of nitrogen at a pressure of ~0.1 atm and a temperature of ~270 K was used to cool the system down to ~ 272.5 K. The IR light was turned on and the mass redistribution was initiated.

In order to determine the layering time based on the 1-D Stefan flow theory, the system properties needed to be found. Theoretically, applying Eq. (E-25) (see tab. E-2, Eq. (E-31) and Eqs. (E-32) for the numerical values of the properties) leads to a layering time of about 8.5 days (1/e improvement), which is fairly long, but lies within a reasonable time frame. (The values of the coefficients A, B, and C in Eq. (E-32), are given in tab. 3.3, for the diffusion of water through a non-polar gas  $a_{diff} = 3.640 \times 10^{-4}$  and  $b_{diff} = 2.334$ ).

$$P_{v,H_2O}(T) = \left[ A + B \cdot T_{Celsius} + C \cdot T_{Celsius}^2 \right] \cdot \exp\left(\frac{-6150}{T_{Kelvin}}\right) \quad (\text{in mbar}) \quad (\text{E-32a})$$

$$\frac{dP_{v,H_2O}}{dT} = \left[ \left( A + B \cdot T_C + C \cdot T_C^2 \right) \cdot \left( \frac{6150}{T_K^2} \right) + (B + 2 \cdot C \cdot T_C) \right] \cdot \exp\left(\frac{-6150}{T_{Kelvin}}\right) \quad (\text{E-32b})$$

This leads to the following theoretical result:

$$\tau_3 = \frac{L \cdot k_{ice} \cdot \rho_s \cdot R \cdot T \cdot P_{B,h1}}{2 \cdot D_{AB} \cdot d \cdot \dot{q}'' \cdot P \cdot \left. \frac{dP_A}{dT} \right|_{T=T_{h1}}} = 207 \text{ hrs} \quad (\text{E-33})$$

It was the goal of this experiment, to qualitatively verify the influence of the non-participating gas on the layering mechanism. Fig. E-2 shows a side by side comparison of two pictures taken 90 hrs apart.

Table E-2: Parameters used in computing the influence of air as a non-participating gas on the layering time in an ice layering experiment.

	$H_2O$ -layering at 272 K	Units
$T_\infty$	270.3	K
$\Delta H_s$	$2.5 \times 10^9$	J/m <sup>3</sup>
$M$	0.018	Kg/mol
$\rho_{solid}$	50928	Mols/m <sup>3</sup>
$\dot{q}''$	0.20	W/cc
$k_{ICE}$	2.25	W/(m-K)
$P_{v,H_2O}(272.5 K)$	578.8	Pa
$\left. \frac{dP_{v,H_2O}}{dT} \right)_{T=272.5K}$	44.17	Pa/K
$P_{air}$	10100	Pa
$L$	$2.00 \times 10^{-3}$	m
$d$	$4.00 \times 10^{-4}$	m
$R_{gas}$	8.314	J/mol-K
$D_{AB}$	$1.99 \times 10^{-4}$	m <sup>2</sup> /s

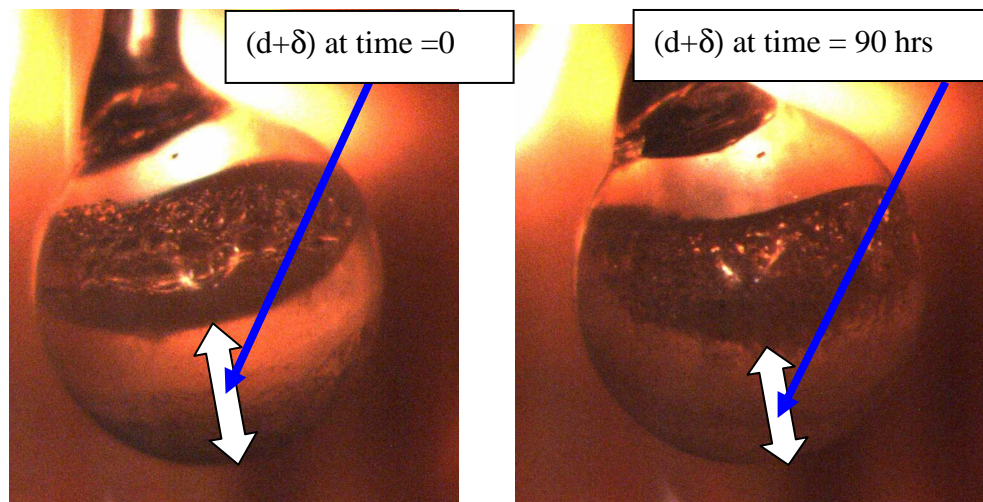


Figure E-2: Ice layering progress over the course of 90 hours. The measurement of the layer thickness on the thick layer on the bottom can be used as an indication of the length of the (1/e)-layering period.

The results from these pictures can be used to compute the layering time observed in the experiment by applying Eq. (E-34).

$$\tau = -\frac{90hrs}{\ln \frac{\delta_{r1}}{\delta_0}} = 295 hrs \quad (E-34)$$

This is in reasonable accordance with the calculated result (8.5 days of 204 hours), considering that the pressure of the nitrogen in the shell was an estimate based on permeation rate calculations. In addition, a fairly large error in the volumetric heat is expected in this experiment, as the optical properties of the PAMS shell show a slight absorption in the wavelength applied, and the effectiveness of the reflectors is unknown. Further, the gas flow rate used to cool the shell could not be determined, and with that, the variation in heat transfer coefficient along the surface from the leading edge of the particle could only be estimated (although the influence of the heat flux non-uniformity is not expected to have a big influence on the outcome that early in the layering phase).

The influence of the increasing nitrogen pressure on the layering time is shown in fig. E-3. For air at room pressure, the layering time would be increased to ~2000 hours (~80 days). However, once the nitrogen pressure was reduced to about 0.1 atm (80 torr), the increase in total layering time due to the nonparticipating gas is reduced to a few days.

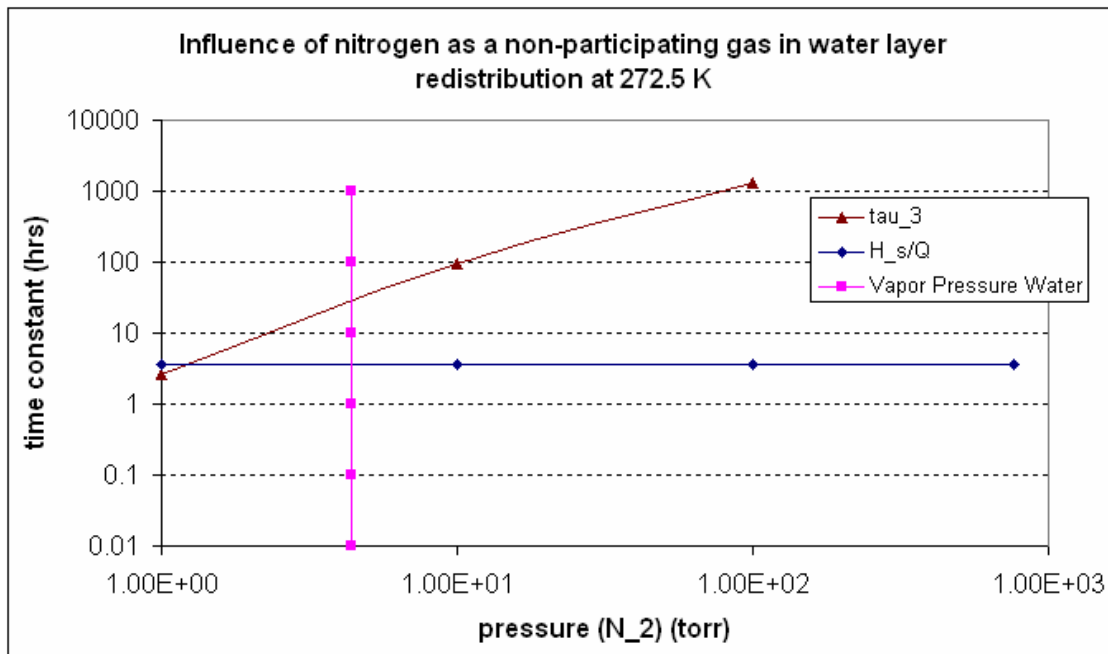


Figure E-3: Influence of an increase in partial pressure of the nitrogen on the ice layering time.

## APPENDIX F – MPLX Hardware

In this section, the MPLX hardware is presented along with a short explanation of the operation of the system.

Two vacuum chambers are mounted on a table and are connected by a steel bellows as shown in fig. F-1. Each chamber contains an inner copper shield, which can be cooled with liquid nitrogen. Inside the vacuum chambers runs a closed loop of 2.54 cm outer diameter (1 inch) plumbing containing cryogenic helium.

The chamber on the right hand side in fig. F-1 contains a cryogenic blower and two cryo-coolers. This part of the system is referred to as the helium-plant. The two cryo-coolers are used to cool two sets of coiled copper tubing, acting as heat exchangers cooling the helium stream. In fig. F-2, the vacuum dome and the cold shield of the helium plant have been removed, showing the two copper heat exchangers, the blower and part of the plumbing. This chamber also contains a trim heater, which allows temperature control of the gas stream with a PID controller.

The chamber on the left hand side in fig. F-1 contains the fluidized bed, the permeation fill station, the IR heating device and the optical characterization system. The system is cooled by forcing cooled helium through the closed-loop plumbing system that connects to all the parts which need to be cooled.



Figure F-1:  
MPLX experimental setup. The system consists of two vacuum domes, one mounted on top of the table, one mounted below. Liquid nitrogen hoses connect to the copper shields located on the inside of the vacuum domes.



Figure F-2:  
Inside of the bottom chamber after removing the vacuum dome. This reveals the cryogenic blower, the two copper heat exchangers and the plumbing connecting the components.

In fig. F-3, the vacuum dome and cold shield of the fluidized bed side of the system have been removed, showing the vertically mounted glass tube containing the gas-filled hollow spheres. A distributor plate is located at the bottom inlet of the bed, providing a shelf for the shells and causing a uniform flow field of the helium through the bed. A single shell can be isolated from the rest of the fluidized bed by a vacuum needle. Two orthogonally mounted cameras, equipped with microscopic lenses are able to record images of the (partially) layered sphere for characterization of the layer uniformity.

The fluidized bed has been operated with empty shells at temperatures as low as 10 K, the functionality of the vacuum pickup mechanism, the temperature control and the control of the fluidizing gas flow speed has been tested and verified.



Figure F-3:

Fluidized bed consisting of a vertically mounted glass tube. The shells will be placed on the frit mounted on the bottom of the glass tube. Though view ports in the vacuum dome, the fluidization can be monitored. Using a vacuum needle in the gas stream, a single particle can be held stationary for visual inspection of the layer formation.

Following successful initial cryogenic tests, additional hardware was installed to the system in order to add the capability to gas-fill the shells. The filling process is done by slowly permeating the deuterium gas into the shells. Knowing the buckle strength of the shells and the permeation rate of the gas through the shell wall, the system pressure needs to be increased accordingly from vacuum to the final fill pressure (1100 atm). By increasing the pressure in the permeation cell by 75 psi every hour it was determined that the pressure difference between the cell and the inside of the shell would be below the buckle strength of 13.6 atm (200 psi).

The section of the permeation cell containing the shells needs to be installed in such a way that the helium loop can be used to cool that section to below triple point temperature of deuterium (18.7 K). Fig. F-4 shows a bypass loop that was installed to bypass the fluidized bed, providing cooling power to the permeation cell. The

permeation cell consists of a length of high strength tubing with a small grid mounted to the bottom to keep the shells in place.

The controlled step-wise pressurization of the system is performed by a syringe pump, shown in figure F-5. Since multiple strokes of the syringe pump are needed to increase the system pressure from the supply bottle pressure (136 atm, 2000 psi) to the final fill pressure (1100 atm), while the system pressure is not allowed to change by more than 75 psi, two high resolution and high accuracy pressure sensors are used to equalize the pressure in the pump and in the system before each stroke.

Once filled and cooled, the shells need to be transferred to the fluidized bed for layering. This done by a pneumatic transfer system shown in fig. F-4. The cold helium stream initially used to cool the system to cryogenic temperatures can be diverted to flow through a ball valve mounted outside the chamber, upward through the permeation cell, through a second ball valve outside the chamber, back into the cryostat and connecting to the to top of the fluidized bed. The helium stream flow velocity through the high pressure plumbing is fast enough to move the shells, and fast enough to pass the shells the room temperature sections of the plumbing without heating them past the critical point.

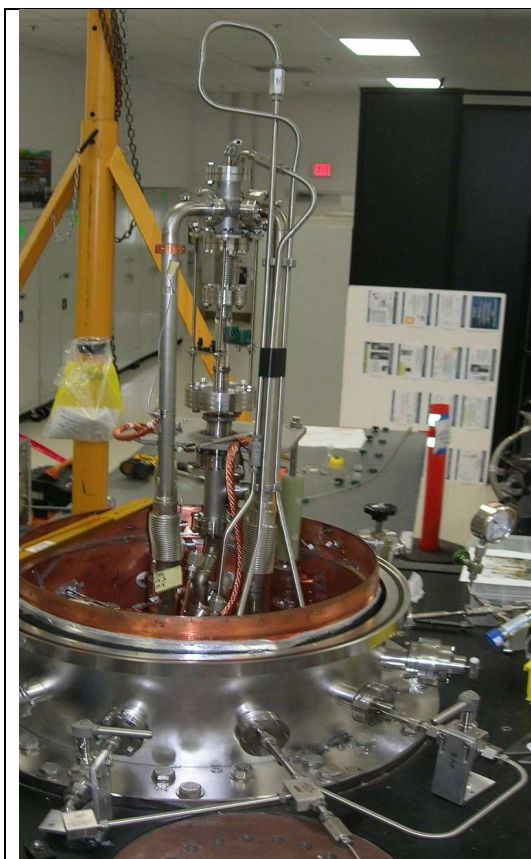


Figure F-4:

High pressure filling system added to the fluidized bed loop. The shells will be placed and filled at room temperature and pressures up to 1100 atm. After cooling to temperatures lower than the triple point, the shells will be transferred to the glass bed by the cold helium gas stream. Once in the bed, the shells are layered under IR irradiation.

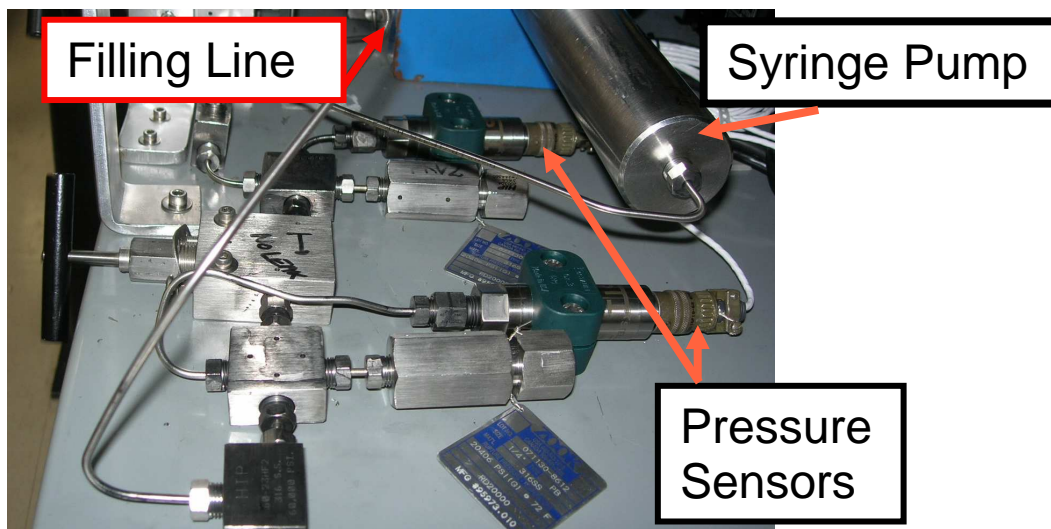


Figure F-5: Syringe pump used to slowly increase the pressure during the filling process, and to control the pressure in the permeation cell during the cool down. Two high resolution pressure sensors are used to control the pressure increase after the volume of the pump needed to be refilled (at the beginning of each stroke).

After transferring the shells into the bed, the helium flow is directed upward through the glass tube, fluidizing the particles in the bed. While fluidized, the particles are irradiated with filtered IR light, the wavelength of which is adjusted to the absorption spectrum of deuterium to provide volumetric heating. The heating system, depicted in fig. F-6, consists of three IR filaments, operating at  $\sim 1000$  K, a copper wave guide to direct the light beam into the bed, and a bandpass filter which narrows the light spectrum to wavelengths  $\sim 3.1$   $\mu\text{m}$ . Copper wires, connected to the liquid nitrogen shield are installed to protect the IR-emitters and the filter from overheating in vacuum.

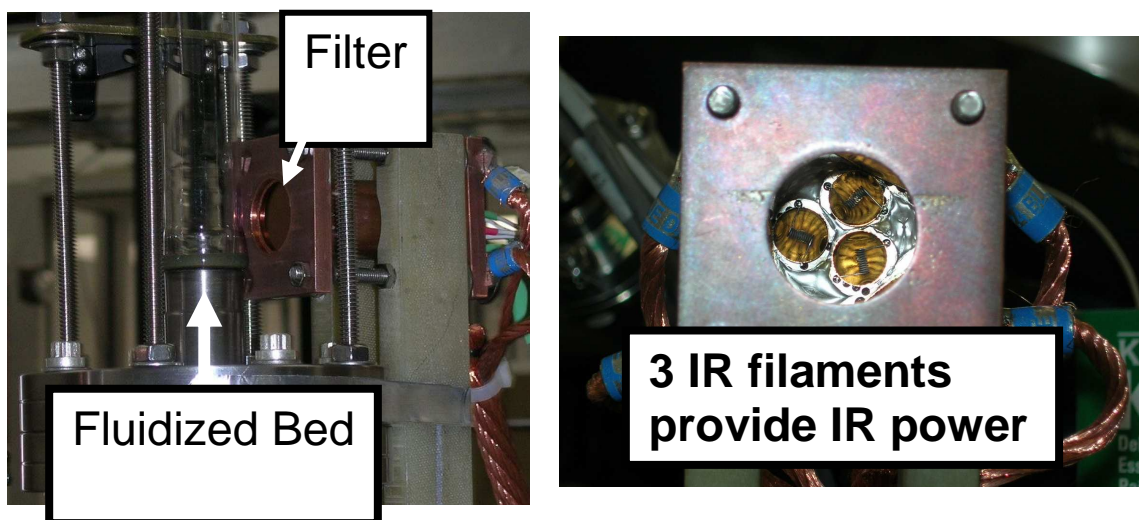


Figure F-6: IR heating system consisting of three IR filaments.

## APPENDIX G – Influence of the tangential drag force induced by the gas in the fluidized bed

In the fluidized bed model described in section 2 (Lupsbe), the motion of the particles in the bed is computed by adding all forces acting on the particle and then solving Newton's second law of linear motion and the corresponding equation for the angular acceleration.

In this analysis, the drag force induced by the upward flowing (fluidizing) gas was applied on the center of the spherical particle in the direction of the gas flow. Its magnitude was computed applying an established empirical relation<sup>29, 42</sup> as a function of the void fraction in the volume surrounding the particle and the specified inlet gas velocity. The tangential forces acting on the surface of a spinning particle were not taken into account based on the justification described below.

In order to simplify the equations for a spinning sphere, a cylinder of geometry similar to the particles in question was considered, and the influence of a tangential drag force due to the viscous gas surrounding the object was analyzed.

The azimuthal component of Navier Stokes equation is given by:

$$\frac{\delta U_{\theta}}{\delta t} = \nu \frac{\delta}{\delta r} \left( \frac{1}{r} \cdot \frac{\delta}{\delta r} (r \cdot U_{\theta}) \right) \quad (\text{G-1})$$

The boundary conditions for the analysis are given as follows, where  $\omega$  is the spin rate of the particle and  $R$  the radius of the particle:

$$U_{\theta}(r = R) = 2\pi\omega, \text{ and } U_{\theta}(r = \infty) = 0 \quad (\text{G-2})$$

Assuming steady state (since we are looking at a snapshot), one can re-write Eq. (G-1):

$$0 = \frac{\delta}{\delta r} \left( \frac{1}{r} \cdot \frac{\delta}{\delta r} (r \cdot U_{\theta}) \right) \quad (\text{G-3})$$

Integrating twice and applying the boundary conditions leads to

$$U_{\theta}(r) = \frac{2\pi R^2 \omega}{r} \quad (\text{G-4})$$

The shear force in the fluid is then given by ( $\mu$  representing the viscosity of the surrounding fluid):

$$\tau_{z\theta} = \mu \left[ r \frac{\delta}{\delta r} \left( \frac{U_\theta}{r} \right) \right] = \mu \left[ r \frac{\delta}{\delta r} \left( \frac{-2\pi R^2 \omega}{r^2} \right) \right] = -\frac{4\mu\pi\omega}{r^2} \quad (\text{G-5})$$

This leads to the following shear force on the surface of the cylinder (at  $r=R$ )

$$\tau_{z\theta} = -4\pi\mu\omega \quad (\text{G-6})$$

This shear force acts on the entire surface of the particle. In order to compute the surface of the object, it is assumed that the cylinder has the same height as its diameter (leading to a surface area of  $4\pi R^2$  disregarding the top and the bottom plate). This leads to a torque of:

$$T_{z\theta} = -16\pi\mu\omega R^3 \quad (\text{G-7})$$

The equation of angular acceleration is (where  $I$  is the mass moment of inertia):

$$\dot{\omega} = \frac{T}{I} = \frac{-16\pi\mu R^3}{I} \omega \quad (\text{G-8})$$

This first order ODE leads to

$$\omega(t) = \omega_0 \exp\left(-\frac{16\pi\mu R^3}{I} t\right) \quad (\text{G-9})$$

This means, that the target experiences an exponential decline in angular velocity with a time constant of

$$\Omega = \frac{I}{16\pi\mu R^3} \quad (\text{G-10}).$$

By inserting the values from table 2.5, one can compute a time constant for gas induced particle spin deceleration of 7.5 seconds.

This is fairly long compared to the average time between collisions of the order of 1/10 seconds (computed by the FB model). This means that the spin of the particle is not affected significantly by the gas in the time between collisions, which justifies the modeling assumptions of excluding the tangential forces acting on the surface of a spinning particle.

## 7. References

1. The High Average Power Laser Program, Meeting Archives from 1999 - present <http://aries.ucsd.edu/HAPL/MEETINGS/>
2. J.D. Sethian et al., "*Fusion Energy with Lasers, Direct Drive Targets, and Dry Wall Chambers*". Nucl. Fusion, Vol. 43, 1693, 2003.
3. W.R. Meier, A.R. Raffray, I.N. Sviatoslavsky, "*Systems Modeling for Laser IFE*". J.Phys. IV France Vol. 133, 833, 2006.
4. A.J. Martin, R.J. Simms, R.B. Jacobs, "*Beta energy driven uniform deuterium-tritium ice layer in reactor-size cryogenic inertial fusion targets*". J.Vac.Sci.Technol. A, Vol. 6, Issue 3, 1988.
5. D.R. Harding et al., "*Forming cryogenic targets for direct-drive experiments*", Physics of Plasmas, Vol. 13, 2006.
6. C.M. Chen, T. Norimatsu et al, "*Heating uniformity of a microwave discharge plasma to redistribute a solid fuel layer inside a cryogenic target for inertial confinement fusion*", J. Vac. Sci. Technol. A, Vol. 13, No. 6, 1995.
7. C.M. Chen, T. Norimatsu et al. "*Redistribution of solid fuel in inertial confinement fusion target by plasma*", J. Vac. Sci. Technol. A, Vol 11, No. 3, 1993.
8. E.R. Mapoles et. al., "*Smoothing of deuterium-tritium ice by electrical heating of the saturated vapor*", Physical Review E, Vol. 55, No. 3, 1996.
9. E.R. Koresheva, "*Possible approaches to fast quality control of IFE targets*", Nuclear Fusion, Vol 46. 2006.
10. I.V. Alexandrova et al. "*An efficient method of fuel ice formation in moving free-standing ICF/IFE targets* ", Journal of Physics D: Applied Physics, Vol 37, 2004.
11. N.B. Alexander et al. "*Mass Production for Inertial Fusion Energy*". HAPL project review, Albuquerque, NM. April 9<sup>th</sup>, 2003.
12. P.N. Rowe, "*Fluidization*", Academic Press, New York, 1971

13. N.B. Alexander, K.-J. Boehm et al. "*Progress towards Mass Production Layering*." Presentation given at the 15<sup>th</sup> Laser IFE program workshop at General Atomics, San Diego, CA, August 8<sup>th</sup>-9<sup>th</sup>, 2006
14. N.B. Alexander et al. "*Cryogenic Fluidized Bed for Layering of IFE Capsules*". Presentation given at the 17<sup>th</sup> TOFE Meeting, Albuquerque, NM, Nov 13-15, 2006.
15. N.B. Alexander et al. "Mass Production in Laser IFE", Presentation given at the 4<sup>th</sup> US/JP workshop of IFE Target Fabrication, Injection and Tracking. San Diego, CA, March 5<sup>th</sup> and 6<sup>th</sup>, 2007.
16. N.B. Alexander, K.-J. Boehm et al. "*Progress in Mass Production Layering Demonstrations*" Presentation given at the HAPL program meeting in Washington, DC, October 31<sup>st</sup>, 2007.
17. L. Carlson. "*A Method for Characterizing and Improving the Damage Resistance of the Outer Metallic Coating on IFE Targets*" submitted in partial satisfaction of the requirements for the degree Master of Science, UC San Diego, 2008
18. J. K. Hoffer, J.D. Sheliak, and D.A. Geller. "*Solid DT Studies*", Presentation given at the HAPL program meeting at the Naval Research Laboratories, Washington, DC, Dec. 5-6, 2002.
19. S. Warr et al. "*Tracking the translational and rotational motion of granular particles: use of high speed photography and image processing.*" Powder Technol. 81, 1994.
20. S. Ergun and A.A. Orning. "*Fluid Flow through randomly packed columns and fluidized beds*", Ind. Eng. Chem. 41, 6, 1948.
21. T.B. Anderson and R. Jackson. "*A fluid mechanical description of fluidized beds*", I&EC Fundam. 6, 1967.
22. D. Gidaspow, "*Multiphase Flow and Fluidization*", Academic Press, San Diego, 1994.
23. P.A. Cundall and O.D.L. Struck, "*A discrete numerical model for granular assemblies*", Geotechnique, Vol. 29, No. 1, 1979.
24. B.H. Xu and A.B. Yu, "*Numerical simulation of the gas-solid flow in a fluidized bed by combining discrete particle method with computational fluid dynamics*", Chemical Engineering Science, Vol. 52, No. 16, 1997.

25. Y.Tsuji et al. "*Lagrangian numerical simulation of plug flow of cohesionless particles in a horizontal pipe*", Powder Technology, vol. 71, 1992.
26. B.P.B. Hoormans et al. , "*Discrete particle simulation of bubble and slug formation in a two dimensional gas-fluidized bed : a hard sphere approach*", Chem. Engng Sci, 51, 1996.
27. Y.Tsuji et al. "Discrete particle simulation of two-dimensional fluidized bed", Powder Technology, Vol 77, 1993.
28. D. Gera, Y.Tsuji, et al., "*Computer simulation of bubbles in large-particle fluidized beds* ", Powder Technology, Vol 98, 1998
29. R. DiFelice, "*The voidage function for fluid-particle interaction systems*", Int. J. Multiphase Flow, 20, 153. 1994.
30. J.F. Richardson, W.N. Zaki, "*The sedimentation of a suspension of uniform spheres under conditions of viscous flow*", Chem Eng. Sci. 3, 65. 1954.
31. S. Pannala et al. "*Simulation of Gas-particle Flows in a Vertical Riser With a Square Cross Section*", AIChE Annual Meeting, San Francisco, Nov. 16-21, 2003. See also [www.mfix.org](http://www.mfix.org).
32. T.-W. Pan, D.D. Joseph et al. "*Fluidization of 1204 spheres: simulation and experiment*", J. Fluid Mech. Vol. 451. 2002.
33. M.P. Allen, "*Computer Simulation of Liquids*". Oxford, 1987.
34. D.S. Boyalakuntla, "*Simulation of Granular and Gas-Solid Flows Using Discrete Element Method*", PhD Thesis submitted to Carnegie Mellon University, 2003.
35. D. Janezic, "*Implicit Runge-Kutta Method for Molecular Dynamics Integration*", J.Chem. Inf. Comput. Sci., Vol. 33. 1993.
36. C.W. Gear, "*The Numerical Integration of Ordinary Differential Equations*", Mathematics of Computation, Vol 21. No. 98. 1967.
37. C.W. Gear, "*Numerical Initial Value Problems in Ordinary Differential Equations*". Prentice Hall, Englewood Hills, N.J. 1971.
38. D. Volfson, L.S. Tsimring, "*Partially fluidized shear flows: Continuum theory and molecular dynamics simulations*", Physical Review E, Vol. 68, 2003.

39. S. Dorbolo, D. Volfson, L.S. Tsimring and A. Kudrolli, “*Dynamics of a Bouncing Dimer*”, Physical Review Letters, Vol. 95, 2005.
40. D. Baraff, “*An Introduction to Physically Based Modeling: Rigid Body Simulation I and II*”. 1997  
(<http://www.cs.cmu.edu/~baraff/sigcourse/notesd2.pdf>)
41. J. Schaefer, S. Dippel, D.E. Wolf, “*Force Schemes in Simulations of Granular Materials*”, J. Phys. I France, Vol 6, 1996.
42. L.G. Gibilaro, “*Fluidization Dynamics*”, Butterworth-Heinemann, Oxford, 2001.
43. Merrit and Bacon, Meth. Enzymol. 277, pp 505-524, 1997.
44. FFmpeg is a collection of software libraries that can record, convert and stream digital audio and video in numerous formats. <http://ffmpeg.mplayerhq.hu/>.
45. T.M. Flynn, “*Cryogenic Engineering*”, Dekker, New York, 2005.
46. F.P. Incropera, D.P. DeWitt, “*Introduction to Heat Transfer*”, Wiley, New York, 2002.
47. L.J. Atherton, “*Targets for the National Ignition Campaign*”, Presentation to Fifth International Conference on Inertial Fusion Sciences and Applications.Kob, Japan, September 11<sup>th</sup>, 2007.
48. D. Kuni and O. Levenspiel, “*Fluidization Engineering*”, Wiley, New York, 1969.
49. W.H. Press et al., “*Numerical Recipes*”, Cambridge University Press, New York, 1986.
50. G.M. Rios, J.L. Baxerras and H. Gilbert, in “*Fluidization*”, Eds. J.R. Grace and J.M. Madsen, 529, Plenum Press, New York (1980)
51. T.P. Bernat, E.R. Mapoles, J.J. Sanchez, “*Temperature- and Age-Dependence of Redistribution Rates of Frozen Deuterium-Tritium*”, Inertial Confinement Fusion, ICF Quarterly Report, Vol 1, No 2, Jan-Mar 1991.
52. J.K. Hoffer and L.R. Foreman, “*The effects of exchange gas temperature and pressure on the beta-layering process in solid deuterium-tritium fusion fuel*”, Physica B, 165&166 (1990).
53. H.S. Udaykumar and W. Shyy, “*A Grid Supported Marker Particle Scheme for Interface Tracking*”, Numerical Heat Transfer B, 27, 1995.

54. W.J. Minkowycz, E.M. Sparrow, J.Y. Murthy, “*Handbook of Numerical Heat Transfer*”, 2<sup>nd</sup> Edition, J. Wiley, Hoboken, N.J. 2006.
55. H.S. Udaykumar, R Mittal and Wei Shyy, “*Computation of Solid-Liquid Phase Fronts in the Sharp Interface Limit on Fixed Grids*”, *Journal of Computational Physics*, 153, 1999.
56. K.-J. Boehm and A.R. Raffray, “*Transient thermo-mechanical behavior of a direct-drive target during injection in an inertial fusion energy chamber*”, *Fusion Engineering and Design*, 82, 3, 2007.
57. P.C. Souers, “*Hydrogen Properties for Fusion Energy*”, University of California Press, Berkeley, 1986.
58. T. Bewley, “*Numerical Renaissance: Simulation, Optimization, & Control*”, Renaissance Press, San Diego, CA, 2009.
59. J. G. Collier, “*Convective Boiling and Condensation*”, McGraw-Hill, London, 1972.
60. D.R. Harding et al., “*Cryogenic DT Foam Targets*”, Presentation given to the HAPL program meeting in Santa Fe, NM, April 9<sup>th</sup>, 2009.
61. M. Kaviany, *Principles of Convective Heat Transfer*, 2<sup>nd</sup> Edition, Springer, New York, 2001.
62. S.G. Warren, “*Optical constants of ice from the ultraviolet to the microwave*”, *Applied Optics*, Vol. 23, No. 8, 1984.
63. <http://www.holsoft.nl/physics/ocmain.htm>, Online Database for the properties of water. 2007.
64. L.-S. Fan, C. Zou, *Principles of Gas-Solid Flows*, Cambridge University Press, New York, 1998.
65. I. Pop and D.B. Ingham, *Convective Heat Transfer – Mathematical and Computational Modeling of Viscous Fluids and Porous Media*, Elsevier Science Ltd., Oxford, 2001.
66. R.B. Bird, W.E. Stewart and E.N. Lightfoot, *Transport Phenomena*, Wiley, New York, 1980.
67. R.S. Figliola, D.E. Beasley, “*Theory and Design for Mechanical Measurements*”. 4<sup>th</sup> Edition, Wiley, 2006.

68. A. C. Ugural and S. K. Fenster, *Advanced Strength and Applied Elasticity*, Prentice Hall PTR, Upper Saddle River, New Jersey, 2003.

## 8. Bibliography

S.-C. Liang et al., “*Effects of Particle Arrangements on the Drag Force of a particle in the Intermediate Flow Regime*“, Int. J. Multiphase Flow, Vol 22, No. 2, 1996.

L. Zeng et. al., “*Wall-induced forces on a rigid sphere at finite Reynolds number*“, J. Fluid Mech., Vol. 536, 2005.

W.J. Stronge, “*Rigid Body Collisions with Friction*“, Proc.: Math. and Phys. Sciences, Vol. 431, No. 1881, 1990.

C.T. Crowe, *Multiphase Flow Handbook*, CRC Press, Boca Raton, FL, 2006.

T.-Y. Wang and C. Kleinststeuer, “*Local skin friction and heat transfer in combined free-forces convection from a cylinder or sphere to a power-law fluid*“, Int. J. Heat and Fluid Flow, 9, 2, 1988.

I. Pop, T. Watanabe, H. Taniguchi, “*Laminar Boundary Layer Flow and Heat Transfer along a moving Cylinder with Suction and Injection*“, Technische Mechanik 15, 2, 1995.